Universität Hamburg
DER FORSCHUNG | DER LEHRE | DER BILDUNG

Artifact Reduction for Radon-based Image Reconstruction in Magnetic Particle Imaging with an FFL Scanner

Dissertation with the aim of achieving a doctoral degree at the Faculty of Mathematics, Informatics and Natural Sciences

Department of Mathematics
of Universität Hamburg

submitted by

Stephanie Elisabeth Blanke

2023 in Hamburg

Accepted as dissertation by the Department of Mathematics of Universität Hamburg based on the evaluations by:

Prof. Dr. Christina Brandt (Universität Hamburg)
Prof. Dr. Bernadette Hahn-Rigaud (Universität Stuttgart)

Date of the oral defense: 14.03.2024

Acknowledgment

Before we dive into the exciting topic of magnetic particle imaging, I would like to express my gratitude. First of all, I would like to thank my supervisor Christina Brandt, who not only supported me thematically, but also took an interest in her working group outside of the topic. In this context, I would also like to thank my working group for the joint activities and exchanges. Additionally, there is the RTG 2583 and, more generally, the people from the 15th as well as 1st floor. Thank you for shared workshops, lunches, coffee breaks, and not to forget shared cake. Many thanks to the studentchapter, MINGZ, and our bouldering group for the joint activities that helped keeping the head up. Furthermore, thank you Lena and Christine for our unforgettable writing retreat. Moreover, I feel very thankful to Lena, Marija, Tessa, and Tram for proofreading as well as the people from the UKE for showing me an actual scanner and providing me with magnetic field measurements. I hope I haven't forgotten anyone, but to be on the safe side: I am very happy about everyone I met during my time as a doctoral student.

Finally, I want to say thank you to my family, friends, and especially my now legally married husband for their support and patience. Thank you!

I further acknowledge the support by the Deutsche Forschungsgemeinschaft (DFG) within the Research Training Group RTG 2583 "Modeling, Simulation and Optimization of Fluid Dynamic Applications".

Kurzfassung

Magnetic particle imaging (MPI) ist ein Tracer-basiertes medizinisches Bildgebungsverfahren mit dazugehöriger Erstveröffentlichung im Jahr 2005. Ausgehend von der nicht-linearen Magnetisierungsantwort des Tracers auf sich verändernde Magnetfelder, ermöglicht MPI die quantitative Rekonstruktion der räumlichen Verteilung injizierter Partikel. Damit die notwendigen Informationen in den entsprechenden Spannungsmessungen enthalten sind, werden Magnetfelder verwendet, die eine feldfreie Region aufweisen. Mit dem spezifischen Verlauf der Magnetisierungskurve tragen nur Teilchen in der Nähe dieser zum Messsignal bei, während alle weiteren in magnetischer Sättigung verweilen. Für die Datengenerieung wird das Sichtfeld abgetastet, indem die sensitive Zone entlang von bestimmten Trajektorien verschoben wird. Es gibt zwei verschiedene Formen, wie das Niedrigfeld gewählt werden kann. Daraus resultieren der FFP bzw. der FFL Scanner, bei denen ein feldfreier Punkt (FFP) bzw. eine feldfreie Linie (FFL) das Zentrum dieses Niedrigfelds bildet. In dieser Arbeit betrachten wir das FFL Abtastschema. Dabei wird diese Line translatiert und rotiert, sodass die Messgeometrie denen in der Computertomographie ähnelt. Beide generieren Daten entlang von Linien. Für ein idealisiertes Setting wurde bereits gezeigt, dass die MPI Daten auf die Radon Transformation der Teilchenkonzentration zurückgeführt werden können. Das Ziel dieser Arbeit ist es, diese Beziehung für realistischere Annahmen zu verallgemeinern.
Wir betrachten zwei verschiedene Trajektorien, entlang derer die FFL bewegt wird. Zum einen betrachten wir eine sequentielle und zum anderen eine simultane Translation und Rotation der Linie. Da der Vorwärtsoperator eine Zeitableitung enthält und für das simultane Abtastschema die FFL ihre Bewegungsrichtung während der Messung ändert, sorgt diese zusätzliche Zeitabhängigkeit für zusätzliche Terme in der Signalgleichung, wenn die Ableitung ausgeführt wird. Gleichermaßen ergeben sich Zusatzterme, wenn dynamische Konzentrationen und Magnetfeldungenauigkeiten zugelassen werden. Wir beschreiben sich zeitlich verändernde Teilchenkonzentrationen mittels diffeomorpher Deformation einer Referenzkonzentration. Diesen Ansatz übertragen wir auf den Fall der Magnetfeldungenauigkeiten. Diese Vorgehensweise stützt sich auf der Annahme, dass die Datengenerierung entlang von Linien für dynamische Phantome und die Datengenerierung entlang von Kurven für statische Phantome in gewisser Weise miteinander verbunden sind. Da das ideale Feld berechnet und das tatsächliche Feld gemessen werden kann, verwenden wir Bildregistrierungsmethoden, um einen verbindenden Diffeomorphismus zu bestimmen. Für die verschiedenen Annahmen leiten wir angepasste Vorwärtsmodelle und Verbindungen zur Radon Transformation her. Wir schätzen die Zusatzterme mittels der Messparameter ab und basierend auf der totalen Variation rekonstruieren wir simultan Teilchenkonzentration und Radondaten. Wir untersuchen numerische Resultate für synthetische Daten.

Abstract

Magnetic particle imaging (MPI) is a tracer-based medical imaging modality whose first publication dates back to 2005. Relying on the non-linear magnetization response of the tracer material to changing magnetic fields, it allows for quantitative reconstruction of the spatial distribution of injected particles. Encoding of this information into corresponding voltage measurements is guaranteed by applying fields featuring a field-free region. Due to the specific shape of the magnetization curve, only those particles in close vicinity to this area are contributing to the signal, while all other particles stay in magnetic saturation. The low-field volume is moved along dedicated trajectories in order to scan the field of view. There are two different choices available for the shape of the low-field volume. This gives the FFP respectively FFL scanner, where a field-free point (FFP) respectively a field-free line (FFL) centers the low-field volume. In this work, we will concentrate on the FFL encoding scheme. Considering translation and rotation of the line, the scanning geometry resembles those in computerized tomography. Both generate data along lines. For an idealized setting it was already shown that MPI data can be traced back to the Radon transform of the particle concentration. The goal of our work is to generalize this relation to different setups aiming for more realistic assumptions.

We consider two scanning geometries. One bases on sequential and one on simultaneous translation and rotation of the line. The forward operator for MPI contains a time derivative. Thus, as the simultaneous line rotation changes its moving direction, the additional time dependence results in additional terms in the signal equation, when executing the derivative. Likewise, additive components occur, when allowing dynamic particle concentrations and magnetic field imperfections. We treat time-varying tracer distributions based on diffeomorphic template deformation. We transfer this approach to field imperfections, as we assume that generating data along straight lines for moving phantoms and generating data along deformed lines for static phantoms are somehow connected. Since the ideal magnetic field can be computed and the actual field can be measured, we apply image registration techniques to determine a connecting diffeomorphism. For the different setup assumptions, we derive adapted versions of the forward model, state relations to the Radon transform, estimate the additional parts in terms of measurement parameters, and jointly reconstruct particle concentration and Radon data by means of total variation regularization. We give numerical results for synthesized data.

Contents

Nomenclature

Abbreviations and mathematical symbols used within this thesis are listed below.

Abbreviations

BV	Bounded variation
CT	Computerized tomography
EIT	Electrical impedance tomography
FAIR	Flexible algorithms for image registration
FBP	Filtered backprojection
FFL	Field-free line
FFP	Field-free point
FOV	Field of view
LDDMM	Large deformation diffeomorphic metric mapping
LFV	Low-field volume
MPI	Magnetic particle imaging
PAT	Photoacoustic tomography
PDE	Partial differential equation
PET	Positron emission tomography
PNS	Peripheral nerve stimulation
PSNR	Peak-signal-to-noise ratio
RESESOP	Regularizing sequential subspace optimization
SHC	Spherical harmonics coefficient
SNR	Signal-to-noise ratio
SPECT	Single-photon emission computerized tomography
SSIM	Structural similarity
TV	Total variation

Mathematical Symbols

$\lvert\cdot\rvert$	Absolute value
$\lvert\Omega\rvert$	Size of a domain Ω
$\mathrm{BV}(\Omega), \mathrm{BV}(\Omega, \mathbb{R})$	Space of functions of bounded variation on domain $\Omega \subset \mathbb{R}^2$
Δ	Laplace operator
δ	Dirac-δ-distribution
$\delta_{\mathcal{C}}$	Indicator function with respect to a set $\mathcal{C}$
Γ	Diffeomorphic deformation function
Λ	Excitation function
$\lfloor\cdot\rfloor$	Floor function
$\mathbb{C}$	Complex numbers
$\mathbb{K}$	$\mathbb{K} \in \{\mathbb{R}, \mathbb{C}\}$
$\mathbb{N}$; $\mathbb{N}_0$	Natural numbers; including zero

$\mathbb{R}$; $\mathbb{R}^+$; $\mathbb{R}_0^+$; $\overline{\mathbb{R}}$	Real numbers; positive; non-negative; extended by $+\infty$
1_Ω	Characteristic function on Ω
$\mathbf{E}$	Electric field strength
$\mathbf{e}_\varphi, \mathbf{e}_t, \mathbf{e}_\varphi^\perp, \mathbf{e}_t^\perp$	Unit vectors perpendicular respectively parallel to the FFL
$\mathbf{H}$; $\mathbf{H}_\mathrm{S}$; $\mathbf{H}_\mathrm{D}$	Magnetic field strength; selection field; drive field
$\mathbf{M}$	Magnetization
$\mathbf{R}^\varphi, \mathbf{R}^t$	Rotation matrix regarding rotation within xy-plane
$\mathcal{A}^*$	Adjoint of an operator $\mathcal{A}$
$\mathcal{C}$	$\mathcal{C} := \{(c, v) \in \mathcal{D} :\ c \geq 0,\ v \geq 0\}$
$\mathcal{D}$	$\mathcal{D} := L_2(B_R, \mathbb{R}) \times L_2(Z_R, \mathbb{R})$ or $\mathcal{D} := L_2(B_R, \mathbb{R}) \times L_2(Z_T \times \mathbb{R}, \mathbb{R})$
$\mathcal{F}, \hat{f}$	Fourier transform of a function f
$\mathcal{F}^{-1}$	Inverse Fourier transform
$\mathcal{L}$	Langevin function
$\mathcal{L}(X, Y)$	Space of linear and bounded operators between normed spaces X and Y
$\mathcal{N}^\perp(\mathcal{A})$	Orthogonal complement of the null space of an operator $\mathcal{A}$
$\mathcal{R}$	Radon transform
$\mathcal{S}'$	Space of tempered distributions
$\mathcal{S}, \mathcal{S}(\mathbb{R}^n), \mathcal{S}(\mathbb{R}^n, \mathbb{K})$	Schwartz space
μ_0	Magnetic permeability of free space
$\nabla \times \mathbf{g}$	Rotation of a differentiable vector field
$\|\cdot\|_X$	Norm with respect to the underlying space X
$\|\cdot\|_2$	Euclidean norm
$\overline{\mathbf{m}}$	Mean magnetic moment
$\overline{x}$	Convex conjugate of an element $x \in \mathbb{C}$
$\langle \cdot, \cdot \rangle_X$	Inner product with respect to the underlying space X
$\mathrm{supp}(f)$	Support of f
$\mathrm{div}(\mathbf{g}), \nabla \cdot \mathbf{g}$	Divergence of a differentiable vector field $\mathbf{g}$
$\mathrm{dom}(J)$	Domain of J
$\mathrm{TV}(\cdot)$	TV semi-norm
A	Drive peak amplitude
B_R	Open ball with radius $R > 0$ around the origin in $\mathbb{R}^n$
C^1	Space of continuously differentiable functions
C^∞; C_0^∞	Space of infinitely often differentiable functions; with compact support
$f * g$	Convolution of mappings f and g
f_d; f_s; f_rot	Drive frequency; sampling frequency; rotation frequency
G	Gradient strength
k_B	Boltzmann constant
$L_p, L_p(\mathbb{R}^n), L_p(\mathbb{R}^n, \mathbb{K})$	Lebesgue spaces
$L_p(\mathcal{M}), L_p(\mathcal{M}, X)$	Lebesgue-Bochner spaces with $(\mathcal{M}, \mu)$ finite measure space and X Banach space
m	Magnetic moment of a single particle
P_l^m	Associated Legendre polynomials of degree $l \in \mathbb{N}_0$ and order $0 \leq m \leq l$
p_{lm}	Solid harmonics $p_{lm} = r^l Y_{lm}$
S^n	Unit sphere in $\mathbb{R}^{n+1}$
S_R^n	Sphere with radius $R > 0$ around the origin in $\mathbb{R}^{n+1}$

T_m, U_m	Chebyshev polynomials of the first and second kind
T_p	Particle temperature
X^n	n-dimensional space
$x_n \rightharpoonup x$	Weak convergence
Y_{lm}	Spherical harmonics of degree $l \in \mathbb{N}_0$ and order $m \in \{-l, \dots, l\}$
Z	$S^1 \times \mathbb{R}$
Z_R	$S^1 \times [-R, R]$
Z_T	$[0, 2\pi] \times [0, T]$

1. Introduction

Tomographic imaging devices revolutionized medical diagnostics and have become an indispensable part of everyday clinical practice. Enabling non-invasive detection of e.g. cancerous cells or blood vessel stenosis, it is no question that research is being conducted worldwide and across disciplines to develop new and foster existing methods. Points of consideration comprise spatial and temporal resolution as well as safety issues. Within this thesis, we focus on magnetic particle imaging. It is a still rather new tracer-based imaging modality, allowing for the quantitative reconstruction of the particle distribution within the object under investigation. Like the well-known computerized tomography (CT), the FFL scanner generates data along lines. Thereby, the patient is exposed to magnetic fields and, to great advantage, not to ionizing radiation. For an idealized setting, assuming static particle concentrations and ideal magnetic fields, a relation between the MPI-FFL forward operator and the Radon transform has already been derived. In practice, however, the phantoms move and magnetic field imperfections occur. Neglecting this fact may lead to severe image artifacts that make reliable diagnostics impossible. We build on the previously mentioned result to target artifact reduction for Radon-based image reconstruction in magnetic particle imaging with an FFL scanner.

1.1. Outline of the thesis

We start with a recapitulation of some results and concepts from functional analysis, optimization theory, the space of functions of bounded variation, and spherical harmonics. These preliminaries are summarized in Chapter 2. Mathematically, magnetic particle imaging is described via an ill-posed linear inverse problem. For reliable reconstruction, that is to prevent that small measurement noise results in huge image deviations, suitable regularization methods are mandatory. We recall the notion of ill-posedness and regularization in Chapter 3. We review the example of Tikhonov regularization in its variational formulation and according existence, stability, and consistency results. Furthermore, we introduce dynamic inverse problems. In this course, we briefly consider the motion model and the deformable template approach to describe the phantom dynamics. Chapter 4 is dedicated to computerized tomography. We explain the imaging principle, define the Radon transform of a function, and visualize the data as well the scanning geometry. We picture the data inconsistencies for objects varying over time during scanning and recall a variant of the Radon transform obtained via expressing the time dependence of the phantom in terms of diffeomorphic motion functions. We state the important Fourier slice theorem, basing on this an inversion formula for the Radon transform, as well as the filtered backprojection reconstruction. Regarding affine organ movement and using the already mentioned diffeomorphic functions, adapted versions of the Fourier slice theorem and the inversion formula are recapitulated for the dynamic setting. In comparison to existing works, we slightly change the results by incorporating an additional function so as to simultaneously treat the mass and intensity preservation assumption. Afterwards, in Chapter 5, we introduce magnetic particle imaging. We review the physical principles MPI bases on as well as the derivation of a forward model. We explain the signal generation and how information about the particles' positions is encoded in the data. Specifically, we recall the forward operator for an FFL scanner using the Langevin theory of paramagnetism. We image the scanning geometry, derive

a link between the MPI-FFL forward operator and the Radon transform in three dimensions for idealized setup assumptions, and show that, under the supposition that the particles are located within a plane, this result reduces to a corresponding known theorem for two dimensions. We recapitulate a sequential reconstruction of Radon data and particle concentration by means of Wiener deconvolution. In contrast, we suggest a simultaneous determination of particle distribution and Radon data, applying total variation regularization. We further give according existence, stability, and consistency results. We present and compare numerical results for both approaches. After this introductory part of the thesis, we go on with considerations regarding different setup assumptions, aiming to approach stepwise a more realistic setting. We start with regarding a different scanning geometry in Chapter 6, accelerating data acquisition via allowing joint rotation and translation of the FFL. Afterwards, we consider dynamic particle concentrations in Chapter 7 and we close with examining magnetic field imperfections in Chapter 8. For all these settings, we derive the according MPI-FFL forward operator and transfer the correspondence to the Radon transform to one with possibly adapted versions of the Radon transform, e.g. integrating along curves rather than lines in case of dynamic concentrations. Due to the additional time dependencies, we obtain additive components in the forward model. We adapt our reconstruction approach by updating the corresponding model and state numerical results for a proof-of-concept. We consider synthetic data and compare results neglecting the setting adaptions with those incorporating them, confirming the necessity of proper inclusion in the image determination. Otherwise, severe artifacts occur disguising the phantom and possible diseases.

2. Preliminaries

In this chapter, we gather useful definitions and results being used within this thesis. Thereby, we address aspects regarding functional analysis, optimization theory, functions of bounded variation, and spherical harmonics.

2.1. Functional analysis

We first recapitulate the definition of Lebesgue and Schwartz spaces. Moreover, we state the definition of Fourier transforms and convolutions. Please consult [49] and [144] for further details.

Let in the following $\mathbb{K} \in \{\mathbb{R}, \mathbb{C}\}$. The Lebesgue spaces are defined below.

Definition and Theorem 2.1. *Let $1 \leq p < \infty$. The Lebesgue spaces $L_p = L_p(\mathbb{R}^n) = L_p(\mathbb{R}^n, \mathbb{K})$ consist of all measurable functions $f : \mathbb{R}^n \to \mathbb{K}$ such that*

$$\|f\|_{L_p} := \left(\int_{\mathbb{R}^n} |f(\mathbf{r})|^p \, \mathrm{d}\, \mathbf{r} \right)^{\frac{1}{p}}$$

is bounded. Together with these norms, they form Banach spaces. The L_2-space equipped with the inner product

$$\langle f, g \rangle_{L_2} := \int_{\mathbb{R}^n} f(\mathbf{r}) \overline{g(\mathbf{r})} \, \mathrm{d}\, \mathbf{r}$$

gives a Hilbert space.

Similarly, the Lebesgue-Bochner spaces are introduced for Banach space valued functions. Therefore, let $(\mathcal{M}, \mu)$ denote a finite measure space and X be a Banach space. We refer to [40] and [93].

Definition and Theorem 2.2. *Let $1 \leq p < \infty$. The Lebesgue-Bochner spaces $L_p(\mathcal{M}, X)$ consist of all strongly μ-measurable functions $f : \mathcal{M} \to X$ such that*

$$\|f\|_{L_p, X} := \left(\int_{\mathcal{M}} \|f(\mathbf{r})\|_X^p \, \mathrm{d}\, \mu \right)^{\frac{1}{p}} \tag{2.1}$$

is bounded. Together with these norms, they form Banach spaces. We use the shorthand notation $L_p(\mathcal{M}) = L_p(\mathcal{M}, X)$ if X is clear from the context. For X being a Hilbert space, it holds that $L_2(\mathcal{M}, X)$ equipped with the inner product

$$\langle f, g \rangle_{L_2, X} := \int_{\mathcal{M}} \langle f, g \rangle_X \, \mathrm{d}\, \mu$$

is also a Hilbert space.

In the following, we drop the index X and simply write $\|\cdot\|_{L_p}$ also for the norm in the Lebesgue-Bochner space. It will be clear from the context which norm is meant.

Before introducing the so-called Schwartz space, we review the notion of a multi-index.

Definition 2.3. *Let* $\boldsymbol{\alpha} = (\alpha_1, \dots, \alpha_n)^T$ *with* $\alpha_i \in \mathbb{N}_0 := \mathbb{N} \cup \{0\}$, *for* $i = 1, \dots, n$, *and* $\mathbf{r} = (r_1, \dots, r_n)^T \in \mathbb{R}^n$ *with*

$$|\boldsymbol{\alpha}| := \sum_{i=1}^{n} \alpha_i, \quad \boldsymbol{\alpha}! := \prod_{i=1}^{n} \alpha_i, \quad \mathbf{r}^{\boldsymbol{\alpha}} := r_1^{\alpha_1} \cdots r_n^{\alpha_n}, \quad \mathrm{D}^{\boldsymbol{\alpha}} := \frac{\partial^{|\boldsymbol{\alpha}|}}{\partial r_1^{\alpha_1} \cdots \partial r_n^{\alpha_n}}.$$

Furthermore, let $\boldsymbol{\alpha} \leq \boldsymbol{\beta}$ *if and only if* $\alpha_i \leq \beta_i$, *for* $i = 1, \dots, n$. *Then,* $\boldsymbol{\alpha}$ *is called* ***multi-index****.*

Therewith, the Schwartz space can be defined. It consists of rapidly decreasing functions.

Definition 2.4.

(i) The ***Schwartz space*** $\mathcal{S} = \mathcal{S}(\mathbb{R}^n) = \mathcal{S}(\mathbb{R}^n, \mathbb{K})$ *contains all functions* $f \in C^\infty(\mathbb{R}^n, \mathbb{K})$ *such that*

$$\mathfrak{p}_{k,l}(f) := \sup_{\mathbf{r} \in \mathbb{R}^n} \left(1 + \|\mathbf{r}\|^k\right) \sum_{|\boldsymbol{\alpha}| \leq l} |\mathrm{D}^{\boldsymbol{\alpha}} f(\mathbf{r})|$$

is bounded for all $k, l \in \mathbb{N}_0$ *and multi-indices* $\boldsymbol{\alpha} \in \mathbb{N}_0^n$.

(ii) Convergence in $\mathcal{S}$ *is defined as*

$$f_j \xrightarrow[j \to \infty]{\mathcal{S}} f \quad \Longleftrightarrow \quad \lim_{j \to \infty} \mathfrak{p}_{k,l}(f_j - f) = 0, \text{ for all } k, l \in \mathbb{N}_0.$$

(iii) A functional $T : \mathcal{S} \to \mathbb{K}$ *is sequentially continuous, if*

$$f_j \xrightarrow[j \to \infty]{\mathcal{S}} f \quad \Longrightarrow \quad T f_j \xrightarrow[j \to \infty]{} T f.$$

(iv) The set of all linear and sequentially continuous functionals $T : \mathcal{S} \to \mathbb{K}$ *is denoted as* $\mathcal{S}'$. *The elements of* $\mathcal{S}'$ *are called* ***tempered distribution****.*

Example 2.5 (Dirac-δ-distribution)**.** *The dirac-δ-distribution* $\delta_{\mathbf{a}} : \mathcal{S} \to \mathbb{K}$ *is determined via*

$$\delta_{\mathbf{a}}(f) := f(\mathbf{a}).$$

In accordance to [144], for $\mathbf{a} \in \mathbb{R}^n$ *we write*

$$\int_{\mathbb{R}^n} f(\mathbf{r}) \delta_{\mathbf{a}}(\mathbf{r}) \, \mathrm{d}\, \mathbf{r} = f(\mathbf{a})$$

and introduce the shorthand notation $\delta := \delta_{\mathbf{0}}$.

Next, we dedicate ourselves towards the definition of Fourier transforms.

Definition and Proposition 2.6. *The* ***Fourier transform*** $\mathcal{F} : \mathcal{S} \to \mathcal{S}$ *is given by*

$$\mathcal{F} f(\boldsymbol{\xi}) := \widehat{f}(\boldsymbol{\xi}) := (2\pi)^{-\frac{n}{2}} \int_{\mathbb{R}^n} e^{-i \mathbf{r} \cdot \boldsymbol{\xi}} f(\mathbf{r}) \, \mathrm{d}\, \mathbf{r}.$$

This mapping is continuous and bijective with continuous inverse $\mathcal{F}^{-1} : \mathcal{S} \to \mathcal{S}$ *determined via*

$$\mathcal{F}^{-1} \widehat{f}(\mathbf{r}) := (2\pi)^{-\frac{n}{2}} \int_{\mathbb{R}^n} e^{i \mathbf{r} \cdot \boldsymbol{\xi}} \widehat{f}(\boldsymbol{\xi}) \, \mathrm{d}\, \boldsymbol{\xi}.$$

The Fourier transform $\mathcal{F}$ *and its inverse* $\mathcal{F}^{-1}$ *are isometric isomorphisms, which follows from Parseval's identity*

$$\|\mathcal{F} f\|_{L_2} = \|f\|_{L_2} = \left\|\mathcal{F}^{-1} f\right\|_{L_2}.$$

A simple computation gives the following formula for Fourier transforms applied to shifting operators $T^{\mathbf{z}} f(\mathbf{r}) := f(\mathbf{r}+\mathbf{z})$.

Lemma 2.7. *It holds for $f, g \in \mathcal{S}$*

$$\mathcal{F}\left(T^{\mathbf{z}} f\right)(\boldsymbol{\xi}) = e^{i\mathbf{z}\cdot\boldsymbol{\xi}} \mathcal{F} f(\boldsymbol{\xi}).$$

Finally, after defining the convolution mapping, we present a useful result stating that the Fourier transform converts the convolution into a multiplication.

Definition 2.8. *For $f, g \in \mathcal{S}$ the **convolution** $f * g$ is defined as*

$$(f * g)(\mathbf{r}) := \int_{\mathbb{R}^n} f(\mathbf{r}-\mathbf{y}) g(\mathbf{y}) \, \mathrm{d}\mathbf{y}.$$

Theorem 2.9. *It holds for $f, g \in \mathcal{S}$*

$$\widehat{(f * g)} = (2\pi)^{\frac{n}{2}} \hat{f}\, \hat{g}.$$

Remark 2.10. *The Fourier transform $\mathcal{F} : \mathcal{S} \to \mathcal{S}$ can be extended to an isometric isomorphism $\mathcal{F} : L_2 \to L_2$ called Fourier-Plancherel transform since $\mathcal{S} \subseteq L_2$ is dense.*

2.2. Optimization theory

We now review some helpful notions and results regarding optimization theory abstracted from [28] and [150].

Let $J : X \to \overline{\mathbb{R}} := \mathbb{R} \cup \{\infty\}$ be a functional mapping into the extended real numbers. For convenience, we assume X to be a real Hilbert space. By introducing the *indicator function*

$$\delta_{\mathcal{C}}(x) := \begin{cases} 0, & \text{for } x \in \mathcal{C}, \\ \infty, & \text{for } x \notin \mathcal{C}, \end{cases}$$

for a subset $\mathcal{C} \subset X$, every constrained minimization problem $\min_{x \in \mathcal{C}} J(x)$ can be written as an unconstrained problem by replacing the objective functional by $J(x) + \delta_{\mathcal{C}}(x)$. Thus, without loss of generality, we only regard unconstrained minimization problems

$$\min_{x \in X} J(x). \tag{2.2}$$

We first recall definitions of important properties of J.

Definition 2.11. *The **effective domain** of $J : X \to \overline{\mathbb{R}}$ is defined as*

$$\mathrm{dom}(J) := \{x \in X : \ J(x) < \infty\}.$$

*Further, J is called **proper** if $\mathrm{dom}(J) \neq \emptyset$.*

Definition 2.12. *The functional $J : X \to \overline{\mathbb{R}}$ is called **coercive** if $\lim_{n\to\infty} \|x_n\|_X = \infty$ implies*

$$\lim_{n\to\infty} J(x_n) = \infty.$$

Definition 2.13. *The functional $J : X \to \overline{\mathbb{R}}$ is **(weakly) sequentially lower semicontinuous** if*

$$J(x) \leq \liminf_{n\to\infty} J(x_n)$$

for all (weakly) converging sequences $\{x_n\}_{n\in\mathbb{N}}$ with (weak) limit $x \in X$.

Example 2.14.

- *The norm $\|\cdot\|_X$ is weakly sequentially lower semicontinuous.*
- *The indicator function $\delta_{\mathcal{C}}$ of a closed set $\mathcal{C}$ is sequentially lower semicontinuous.*

In order to analyze functions on (weak) sequential lower semicontinuity or create corresponding mappings, the lemma below is very useful.

Lemma 2.15. *Let $F : X \to \overline{\mathbb{R}}$ be (weakly) sequentially lower semicontinuous. Then, the following functionals are also (weakly) sequentially lower semicontinuous*

- *γF for $\gamma \geq 0$,*
- *$F + G$ for (weakly) sequentially lower semicontinuous $G : X \to \overline{\mathbb{R}}$,*
- *$\phi \circ F$ for monotonically increasing and sequentially lower semicontinuous $\phi : \overline{\mathbb{R}} \to \overline{\mathbb{R}}$,*
- *$F \circ \Phi$ for (weakly) sequentially continuous $\Phi : Y \to X$ with Banach space Y.*

Using these terms and definitions, we can state an existence result for (2.2).

Theorem 2.16. *Assuming J to be bounded from below, proper, coercive, and weakly sequentially lower semicontinuous, the minimization problem (2.2) has a solution $x^* \in dom(J)$.*

Proof. The proof is standard and follows the direct method in the calculus of variations (cf. pp. 264 f. in [28]).

1. Since J is bounded from below and proper, existence of a minimizing sequence $\{x_n\}_{n\in\mathbb{N}}$ with $J(x_n) < \infty$ for all $n \in \mathbb{N}$ and

   $$\lim_{n\to\infty} J(x_n) = \inf_{x\in X} J(x) \in \mathbb{R}.$$

   can be concluded.

2. From the coercivity of J, boundedness of this minimizing sequence is inferred. Thus, since X was assumed to be a Hilbert space, existence of a subsequence $\{x_{n_k}\}_{k\in\mathbb{N}}$ such that $x_{n_k} \rightharpoonup x^*$ for $k \to \infty$ and some $x^* \in X$ is given.

3. The weak lower semicontinuity of J finally implies the minimizing property of x^*

   $$\inf_{x\in X} J(x) \leq J(x^*) \leq \liminf_{k\to\infty} J(x_{n_k}) = \inf_{x\in X} J(x).$$

□

To conclude this section, we briefly consider convex minimization problems. These play a special role, since convexity has a lot of nice properties that are particularly advantageous when dealing with non-smooth functionals.

Definition 2.17.

- *A set $\mathcal{C} \subset X$ is called **convex** if for all $x, y \in \mathcal{C}$ and $\lambda \in [0,1]$ it holds $\lambda x + (1-\lambda) y \in \mathcal{C}$.*
- *The functional $J : X \to \overline{\mathbb{R}}$ is called **convex** if for all $x, y \in X$ and $\lambda \in [0,1]$ it holds*

$$J(\lambda x + (1-\lambda) y) \leq \lambda J(x) + (1-\lambda) J(y).$$

*Moreover, J is **strictly convex** if for $x \neq y$ and $\lambda \in (0,1)$ it holds*

$$J(\lambda x + (1-\lambda) y) < \lambda J(x) + (1-\lambda) J(y).$$

Example 2.18.

- *The norm $\|\cdot\|_X$ is convex.*
- *The squared norm $\|\cdot\|_X^2$ is strictly convex.*
- *The indicator function $\delta_{\mathcal{C}}$ of a convex set $\mathcal{C}$ is convex.*

As in the case of (weak) sequential lower semicontinuity, the next lemma provides information concerning the investigation of whether a functional is convex.

Lemma 2.19. *Let $F : X \to \overline{\mathbb{R}}$ be (strictly) convex. Then, the following functionals are also (strictly) convex*

- *γF for $\gamma > 0$,*
- *$F + G$ for convex $G : X \to \overline{\mathbb{R}}$,*
- *$\phi \circ F$ for convex and on the range of F (strictly) increasing $\phi : \overline{\mathbb{R}} \to \overline{\mathbb{R}}$,*
- *$F \circ \Phi$ for linear (and injective) $\Phi : Y \to X$ with a normed space Y.*

Lemma 2.20. *Let $J : X \to \overline{\mathbb{R}}$. If J is weakly sequentially lower semicontinuous, then it is also sequentially lower semicontinuous. These properties are equivalent for convex J.*

For the existence result for convex optimization problems, we refer e.g. to Theorem 6.31 in [28] or Theorem 2.19 in [150].

Theorem 2.21. *Assuming J to be proper, convex, coercive, and sequentially lower semicontinuous, the minimization problem (2.2) has a solution $x^* \in \mathrm{dom}(J)$. If J is moreover strictly convex, x^* is the unique solution.*

2.3. Functions of bounded variation

Functions of bounded variation are of further interest for image reconstruction, as they allow discontinuities in the structure of the unknowns.

Following [179], we define the space of functions of bounded variation (BV) on a domain $\Omega \subset \mathbb{R}^2$ as

$$\mathrm{BV}(\Omega) = \mathrm{BV}(\Omega, \mathbb{R}) = \{c \in L_1(\Omega, \mathbb{R}) : \ \mathrm{TV}(c) < \infty\},$$

with total variation (TV)

$$\mathrm{TV}(c) := \sup\left\{\int_\Omega c(\mathbf{r})\,\mathrm{div}(\boldsymbol{\rho})(\mathbf{r})\,\mathrm{d}\mathbf{r} :\ \boldsymbol{\rho}\in\mathcal{G}\right\}$$

and $\mathcal{G} := \left\{C_0^\infty(\Omega,\mathbb{R}^2),\ \|\boldsymbol{\rho}(\mathbf{r})\|_2 \le 1 \text{ for all } \mathbf{r}\in\Omega\right\}$. If $c\in C^1(\Omega)$, it follows by integration by parts [1]

$$\mathrm{TV}(c) = \int_\Omega \|\nabla c(\mathbf{r})\|_2\,\mathrm{d}\mathbf{r} = \left\|\|\nabla c\|_2\right\|_{L_1}.$$

There are various ways to define total variation. In the above definition, the Euclidean norm $\|\cdot\|_2$ was applied to $\boldsymbol{\rho}$ resulting in an isotropic total variation. Diverse, possibly anisotropic versions of TV can be obtained by replacing the Euclidean with other vector norms while keeping the BV space unchanged [39]. The following is extracted from [1]. Together with the norm $\|\cdot\|_{\mathrm{BV}} := \|\cdot\|_{L_1} + \mathrm{TV}(\cdot)$ the space $\mathrm{BV}(\Omega)$ forms a Banach space and it holds for bounded Ω

$$\mathrm{BV}(\Omega) \subset L_2(\Omega) \subset L_1(\Omega).$$

Next, we restate some important properties of the TV semi-norm. We will use these results later on to show existence of a minimizer with respect to an objective functional including a total variation term.

Theorem 2.22 (Theorem 2.3 in [1]). *The total variation is weakly sequentially lower semicontinuous regarding the L_2 topology.*

Theorem 2.23 (Theorem 2.4 in [1]). *The total variation semi-norm is convex.*

Theorem 2.24 (Theorem 2.5 in [1]). *Regard a* BV*-bounded set of functions $\mathcal{C}$, i.e. $\|c\|_{\mathrm{BV}} \le B$ for all $c\in\mathcal{C}$ and some $B>0$. Then, $\mathcal{C}$ is bounded and relatively weakly compact in $L_2(\Omega)$.*

In order to show the previous theorem, the *Poincaré-Wirtinger inequality* stated below was used.

Lemma 2.25 (Poincaré-Wirtinger inequality (p. 1221 in [1])). *For $c\in\mathrm{BV}(\Omega)$, it holds*

$$\|c-\bar{c}\|_{L_2} \le C\ \mathrm{TV}(c), \quad \bar{c} := \frac{1}{|\Omega|}\int_\Omega c(\mathbf{r})\,\mathrm{d}\mathbf{r} \tag{2.3}$$

for some constant $C>0$.

Finally, it was shown that the total variation is BV-coercive. Remember that coercivity was one of the characteristics within the existence results, Theorem 2.16 and 2.21.

Lemma 2.26 (Lemma 4.1 in [1]). *Let $A: L_2(\Omega)\to Y$ be a bounded and linear functional on a Hilbert space Y such that $A1_\Omega \neq 0$ with 1_Ω denoting the characteristic function on Ω. Then, it holds for $g\in Y$ that $\|Ac-g\|_Y^2 + \gamma\,\mathrm{TV}(c)$ with $\gamma>0$ is* BV*-coercive.*

For more information concerning TV we recommend to consult, for instance, [1] and [39].

2.4. Spherical harmonics

To conclude the preliminary section, we introduce the spherical harmonic functions. Among other things, these can be used to model magnetic fields, as described in Appendix A. Please be referred to [30] as well as [31].

Consider the spherical coordinates $\mathbf{r} = (x, y, z)^T = r\,(\sin\vartheta\cos\varphi, \sin\vartheta\sin\varphi, \cos\vartheta)^T$.

Definition and Proposition 2.27. *The normalized real-valued* ***spherical harmonics*** Y_{lm} *of degree* $l \in \mathbb{N}_0$ *and order* $m \in \{-l, \dots, l\}$ *are defined as*

$$Y_{lm}(\vartheta, \varphi) := \begin{cases} \sqrt{2} K_l^m \cos(m\varphi)\, P_l^m(\cos\vartheta), & m > 0, \\ K_l^0 P_l^0(\cos\vartheta), & m = 0, \\ \sqrt{2} K_l^{|m|} \sin(|m|\,\varphi)\, P_l^{|m|}(\cos\vartheta), & m < 0. \end{cases} \tag{2.4}$$

Thereby, leaving out the often incorporated Condon-Shortly phase $(-1)^m$*, the* P_l^m *denote the associated Legendre polynomials*

$$P_l^m(x) := \frac{1}{2^l l!} \left(1 - x^2\right)^{\frac{m}{2}} \frac{d^{l+m}}{dx^{l+m}} \left(x^2 - 1\right)^l, \quad 0 \le m \le l. \tag{2.5}$$

Moreover, for the choice

$$K_l^m := \sqrt{\frac{(2l+1)}{4\pi} \frac{(l-m)!}{(l+m)!}}, \tag{2.6}$$

the spherical harmonics (2.4) *form an orthonormal basis regarding the square-integrable functions on the unit sphere* $S^2 := \left\{\mathbf{r} \in \mathbb{R}^3 : \|\mathbf{r}\| = 1\right\}$ *in* $\mathbb{R}^3$ *in view of*

$$\langle f, g \rangle_{L_2} = \int_{S^2} f(\mathbf{r})\, g(\mathbf{r})\, \mathrm{d}\,\mathbf{r} = \int_0^{2\pi} \int_0^{\pi} f(\vartheta, \varphi)\, g(\vartheta, \varphi) \sin\vartheta\, \mathrm{d}\,\vartheta\, \mathrm{d}\,\varphi.$$

Remark 2.28. *In some cases, it might be beneficial to choose* K_l^m *such that the maximum of the spherical harmonics is normalized to one. This gives the Schmidt quasi-normalization*

$$K_l^m = \sqrt{\frac{(l-m)!}{(l+m)!}}. \tag{2.7}$$

Lemma 2.29. *Exploiting the spherical harmonics from the last definition, the polynomials* p_{lm} *of degree* $l \in \mathbb{N}_0$ *and order* $m \in \{-l, \dots, l\}$

$$p_{lm}(r, \vartheta, \varphi) := r^l Y_{lm}(\vartheta, \varphi)$$

give a basis for the space of homogeneous harmonic polynomials of degree l *in* $\mathbb{R}^3$*. That is, for the space of polynomials* p *such that the Laplace equation* $\Delta p = 0$ *is fulfilled and* p *can be written as a linear combination of monomials* $\mathbf{r}^{\boldsymbol{\alpha}}$ *with multi-indices* $\boldsymbol{\alpha} \in \mathbb{N}_0^3$ *such that* $|\boldsymbol{\alpha}| = l$*.*

The table below summarizes the spherical harmonics of degree $l \le 2$.

Table 2.1.: Spherical harmonics of degree $l \leq 2$.

l	m	$Y_{lm}(\vartheta, \varphi)$	$p_{lm}(x, y, z)$
0	0	1	1
1	-1	$\sin\vartheta \sin\varphi$	y
1	0	$\cos\vartheta$	z
1	1	$\sin\vartheta \cos\varphi$	x
2	-2	$\frac{\sqrt{3}}{2} \sin^2\vartheta \sin 2\varphi$	$\sqrt{3}xy$
2	-1	$\sqrt{3} \sin\vartheta \cos\vartheta \sin\varphi$	$\sqrt{3}yz$
2	0	$\frac{1}{2}\left(3\cos^2\vartheta - 1\right)$	$z^2 - \frac{1}{2}x^2 - \frac{1}{2}y^2$
2	1	$\sqrt{3} \sin\vartheta \cos\vartheta \cos\varphi$	$\sqrt{3}xz$
2	2	$\frac{\sqrt{3}}{2} \sin^2\vartheta \cos 2\varphi$	$\frac{\sqrt{3}}{2}\left(x^2 - y^2\right)$

3. Inverse Problems

This chapter deals with the interaction of cause and impact of measurable effects. The physical principles relating both are summarized in a forward model $\mathcal{A} : X \to Y$ mapping the set of parameters X to the set of data Y. The *direct problem* describes the generation of data $g = \mathcal{A}c$ for given c. The more demanding task of reconstructing the quantity $c \in X$ from determined measurements $g \in Y$ is called the *inverse problem*, which we denote by $(\mathcal{A}, X, Y)$.

Proper study of inverse problems is of great interest, as they occur in various applications. A large field comprises medical tomographic imaging techniques visualizing inner structures of the patient's body slice by slice, thus enabling diagnostics, treatment planning, and monitoring. Widely known examples are single-photon emission computerized tomography (SPECT), positron emission tomography (PET), magnetic resonance imaging (MRI), electrical impedance tomography (EIT), photoacoustic tomography (PAT), computerized tomography, and more recently magnetic particle imaging. We recommend to consult [50] for insights into numerous medical imaging schemes. For a comprehensive collection of works aiming at the mathematical treatment of imaging tasks, we refer to [164].
Tomographic methods can be classified into two groups depending on whether the image is formed based on properties of the tissue itself or of a tracer material injected into the object under investigation. Note that tracer usage is not exclusive for the second type, it could additionally be applied e.g. for contrast enhancement. Techniques associated to the first category deliver morphological information, whereas those from the second group give quantitative results regarding the tracer distribution convenient for functional imaging. Hence, hybrid scanners combining principles and therewith informational content from each category are of beneficial interest. For further aspects as well as a feature comparison with respect to different imaging modalities, we refer to [113].

Let us now give further insights into those two schemes relevant within this thesis, namely CT and MPI. Computerized tomography relies on tissue-based and magnetic particle imaging on tracer-based properties.

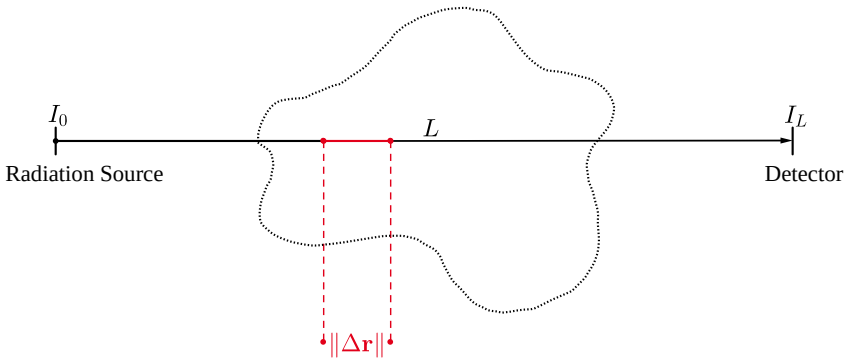

Figure 3.1.: Visualization of the imaging principle of CT: A radiation source emits an X-Ray L with initial intensity I_0. After traversing the specimen, the attenuated intensity I_L is measured via a detector panel. An exemplary distance traveled $\|\Delta\mathbf{r}\|$ is marked in red.

Example 3.1. *The first example we regard is computerized tomography, a well-known imaging modality whose invention opened many research topics and which inhabits great benefits for medical diagnostics. Based on the fact that different tissue types absorb radiation to varying extents, CT can be applied to give morphological knowledge about inner structures of an object under investigation. To this end, as visualized in Figure 3.1 the intensity loss of X-rays traversing the specimen is measured. Gathering data for a suitable amount of radiation source positions and X-ray directions then enables reconstruction of the tissue density $c \geq 0$ correlating to the attenuation coefficient. The intensity loss can be expressed in terms of the distance covered $\|\Delta \mathbf{r}\|$ as*

$$\Delta I(\mathbf{r}) = I(\mathbf{r} + \Delta \mathbf{r}) - I(\mathbf{r}) = -c(\mathbf{r}) \|\Delta \mathbf{r}\| I(\mathbf{r}). \tag{3.1}$$

The X-ray spreads in good accordance along a straight line L. Let I_0 denote the initial intensity and I_L the intensity measured at the detector. Considering $\|\Delta \mathbf{r}\| \to 0$ in (3.1) and integrating along the line L, the corresponding forward model

$$\mathcal{A}c(L) = \int_L c(\mathbf{r}) \, \mathrm{d}\mathbf{r} = \ln\left(\frac{I_0}{I_L}\right) = g(L) \tag{3.2}$$

is obtained. Hence, the inverse problem in CT consists of reconstructing the density c from knowledge of its line integrals g. The forward operator $\mathcal{A}$ is the so-called Radon transform. We advise to view [144] for mathematical prospects of CT. We will consider this example in more detail in Chapter 4.

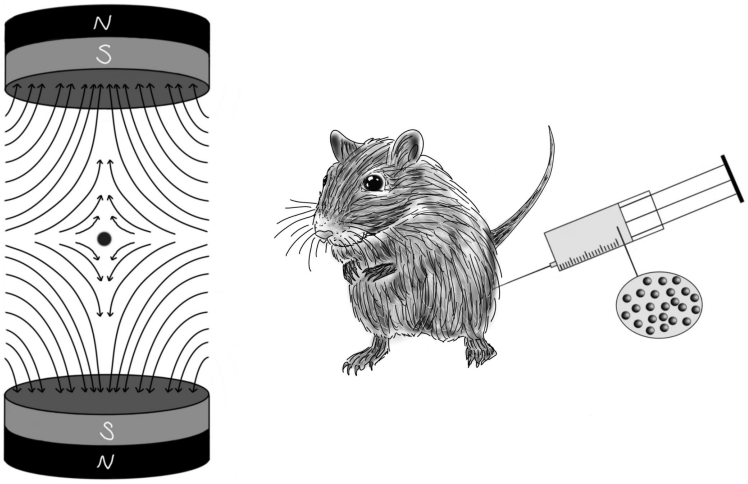

Figure 3.2.: Visualization of the imaging principle of MPI: Magnetic tracer material is injected into the specimen (right). For measurements, magnetic fields (indicated by the arrows) featuring a low-field volume (indicated by the black dot) are applied (left).

Example 3.2. *The second example we regard is magnetic particle imaging. In contrast to computerized tomography, MPI is a preclinical tracer-based imaging modality, i.e. the generated data do not rely on properties of the specimen itself but on characteristics of the injected material. As the name implies, magnetic particles are chosen as tracer. Applying changing magnetic fields to these particles results in a change in magnetization, which can be measured in the matter of voltage signals induced in dedicated receive coils. According to Faraday's law of induction the inverse problem regarding MPI can be formulated as*

$$\mathcal{A}c(t) = \int_{\mathbb{R}^3} c(\mathbf{r}) \, s(\mathbf{r}, t) \, \mathrm{d}\mathbf{r} = g(t).$$

Thereby, s denotes the space- and time-dependent system function gathering all components linking the particle concentration $c \geq 0$ with the measured voltage signal g. We refer to [113] for a detailed overview of various aspects concerning MPI. Within this thesis, we refer to Chapter 5 for an adequate introduction to MPI.

While the underlying physical principles differ for the different methods, in each case images are obtained by solving an inverse problem. This points out the importance and necessity of accurate investigations within this field of research, which resulted in corresponding highly developed theory and methods. Consider ([52], [96], [108], [142], [155]) to name only a few examples from the vast set of literature for inverse problems in general.

We now consider some basic concepts regarding inverse problems. In the following, for convenience, let X and Y be Hilbert spaces. The problem $(\mathcal{A}, X, Y)$ can be categorized depending on the properties of $\mathcal{A}$.

Definition 3.3 (Definition 1.5.2 in [155]). *An inverse problem is called **well-posed** if the following conditions are satisfied.*

(i) For all $g \in Y$ there exists a solution to the equation $\mathcal{A}c = g$.

(ii) This solution is unique.

(iii) The inverse operator $\mathcal{A}^{-1} : Y \to X$ is continuous.

*If one of these conditions is not fulfilled, the problem $(\mathcal{A}, X, Y)$ is called **ill-posed**.*

The notion of well-posedness was introduced by Hadamard [73]. Commonly, inverse problems are ill-posed, usually due to violation of condition *(iii)* guaranteeing that the solution to $\mathcal{A}c = g$ depends continuously on the data. If $\mathcal{A}^{-1}$ exists but is not continuous, small errors in the data g may lead to huge deviations in the reconstruction c. Among other things, due to device inaccuracies or environmental effects on the measurement system, in real-world applications noisy data is the rule instead of the exception. Thus, stabilization methods limiting the influence of noise to the reconstruction are indispensable for reliable determination of c. For the remainder, let $g^\epsilon \in Y$ denote data contaminated by measurement noise and let $\epsilon > 0$ determine the noise level such that $\|g - g^\epsilon\|_Y \leq \epsilon$.

Definition 3.4 (Definition 3.1.1 in [155]). *Let $\mathcal{A} \in \mathcal{L}(X, Y)$ and $\{R_t\}_{t>0}$ be a family of continuous operators from Y to X satisfying $R_t 0 = 0$. If there exists a mapping $\gamma : (0, \infty) \times Y \to (0, \infty)$ such that for all $c \in \mathcal{N}(\mathcal{A})^\perp$ it holds*

$$\sup\left\{ \left\| c - R_{\gamma(\epsilon, g^\epsilon)} g^\epsilon \right\|_X : \; g^\epsilon \in Y, \; \|\mathcal{A}c - g^\epsilon\|_Y \leq \epsilon \right\} \longrightarrow 0 \quad \text{for } \epsilon \to 0,$$

*the pair $\left(\{R_t\}_{t>0}, \gamma\right)$ is called a **regularization (method)** for determining c. If each R_t is linear, it is further called a **linear** regularization. The mapping γ is named **parameter choice** and chosen to be oriented such that*

$$\sup\left\{ \gamma(\epsilon, g^\epsilon) : \; g^\epsilon \in Y, \; \|g - g^\epsilon\|_Y \leq \epsilon \right\} \longrightarrow 0 \quad \text{for } \epsilon \to 0.$$

*The corresponding value $\gamma(\epsilon, g^\epsilon)$ is called **regularization parameter**. If γ only depends on ϵ it is denoted as an **a priori**, otherwise as an **a posteriori** parameter choice.*

The idea of the above definition is to replace the task of solving the ill-posed problem by solving associated well-posed approximations. A lot of effort has been put into the development of elaborated

regularization methods allowing stable reconstruction of the searched-for quantity c. A name that must be mentioned in this context is Tikhonov. His pathbreaking works ([174], [175], [176], [177]) initiated further research in this direction. Examples comprise the introduction of the truncated singular value decomposition ([7], [86]), the approximate inverse ([128], [172]), iterative methods ([5], [62], [100]) like Landweber ([85], [121]) or regularizing sequential subspace optimization (RESESOP) ([171], [188]), variational techniques ([35], [165]), and in the last years data-driven approaches [4]. Many regularization methods are variants, combinations, or special cases from one another. Hence, oftentimes they inherit features from different reconstruction techniques and would fit into more than one category. For an overview, we refer to [52]. Furthermore, for a survey on topical schemes we recommend to consult [11]. The latter also gives an historical placement of different regularization approaches.

Based on [96] we review the important example of Tikhonov regularization in its variational formulation. Thereby, a regularized solution c_γ^ϵ of $(\mathcal{A}, X, Y)$ is determined via solving

$$\min_{c\in\mathcal{C}} \left\{ J_\gamma^{g^\epsilon}(c) := F(c, g^\epsilon) + \gamma P(c) \right\} \tag{3.3}$$

with *Tikhonov functional* $J_\gamma^{g^\epsilon} : X \to \overline{\mathbb{R}}$. Here, the regularization parameter $\gamma > 0$ balances the weighting of the *fidelity term* $F(c, g^\epsilon)$ and a non-negative *regularization term* $P(c)$. The fidelity term monitors the closeness of measured data g^ϵ and modeled data $\mathcal{A}c$. The regularization term endorses solutions featuring specific a priori known properties, like sparsity or piecewise constancy, via penalizing those c not complying to these characteristics. Additional constraints on the minimizer, such as non-negativity, can further be incorporated by the choice of the *feasibility set* $\mathcal{C} \subset X$ assumed to be convex and closed.
Next, we recall results aiming at the well-posedness of (3.3) choosing $F(c, g^\epsilon) := \|\mathcal{A}c - g^\epsilon\|_Y^p$, i.e.

$$\min_{c\in\mathcal{C}} \left\{ J_\gamma^{g^\epsilon}(c) := \|\mathcal{A}c - g^\epsilon\|_Y^p + \gamma P(c) \right\}. \tag{3.4}$$

To this end, we first review the definitions of *H-property* and *P-minimizing* solution.

Definition 3.5 (cf. Definition 3.1 in [96]). *A functional $P : X \to \overline{\mathbb{R}}$ has the* ***H-property*** *on X if for any sequence $\{c_n\}_{n\in\mathbb{N}} \subset X$ it holds*

$$c_n \rightharpoonup c \text{ and } P(c_n) \to P(c) \implies c_n \to c$$

for $n \to \infty$ and some $c \in X$.

For instance, norms on Hilbert spaces satisfy the H-property (see Remark 3.3 in [96]).

Definition 3.6 (Definition 3.2 in [96]). *An element $c^P \in X$ fulfilling*

$$\mathcal{A}c^P = g \text{ and } P\left(c^P\right) \le P(c), \quad \text{for all } c \in \{c \in \mathcal{C} : \mathcal{A}c = g\}$$

is called ***P-minimizing*** *solution.*

For the remainder of this section, we assume (cf. Assumption 3.1 in [96]) that

- the functional $J_\gamma^{g^\epsilon}$ is coercive;
- the functional P is proper and weakly sequentially lower semicontinuous;
- the forward operator $\mathcal{A}$ is linear and bounded, that is $\mathcal{A} \in \mathcal{L}(X, Y)$.

Therewith, the results below are valid. We resist from giving the proofs, these can be found in [96].

Theorem 3.7 (Theorem 3.3 in [96]). *There exists a P-minimizing solution to $\mathcal{A}c = g$.*

Concerning the well-posedness respectively the regularization property of (3.4), we demonstrate the next three theorems.

Theorem 3.8 (Theorem 3.1 in [96]). ***Existence.*** *For all $\gamma > 0$ there exists a solution to (3.4).*

As discussed earlier, a continuous dependence of minimizer c_γ^ϵ on the data g^ϵ is indispensable to guarantee that small deviations stay small. This is ensured by the upcoming theorem.

Theorem 3.9 (Theorem 3.2 in [96]). ***Stability.*** *Consider a sequence $\{g_n^\epsilon\}_{n\in\mathbb{N}} \subset Y$ satisfying $\lim_{n\to\infty} \|g_n^\epsilon - g^\epsilon\|_Y = 0$. Moreover, let $c_\gamma^{g_n^\epsilon} \in \mathcal{C}$ be a minimizer to $J_\gamma^{g_n^\epsilon}$. Then, there exists a subsequence converging weakly to a minimizer $c_\gamma^{g^\epsilon}$ of $J_\gamma^{g^\epsilon}$. If the solution $c_\gamma^{g^\epsilon}$ is unique, the sequence $\left\{c_\gamma^{g_n^\epsilon}\right\}_{n\in\mathbb{N}} \subset \mathcal{C}$ itself converges weakly to $c_\gamma^{g^\epsilon}$. In case the functional P meets the H-property, the convergence is even strong.*

The last statement finally concerns convergence of approximated solutions to true solutions for decreasing noise level ϵ.

Theorem 3.10 (Theorem 3.4 in [96]). ***Consistency.*** *Consider a sequence $\{g^{\epsilon_n}\}_{n\in\mathbb{N}} \subset Y$ of noisy data satisfying $\lim_{n\to\infty} \{\epsilon_n := \|g^{\epsilon_n} - g\|_Y\} = 0$. Let the regularization parameter $\gamma_n \equiv \gamma(\epsilon_n)$ fulfill*

$$\lim_{n\to\infty} \frac{\epsilon_n^p}{\gamma_n} = 0 \quad \textit{and} \quad \lim_{n\to\infty} \gamma_n = 0.$$

Then, the sequence $\left\{c_{\gamma_n}^{g^{\epsilon_n}}\right\}_{n\in\mathbb{N}} \subset \mathcal{C}$ of corresponding minimizer contains a subsequence, which converges weakly to a P-minimizing solution c^P. In case the P-minimizing solution c^P is unique, the sequence itself converges weakly to c^P. The convergence is strong for P having the H-property.

With the ongoing investigation of inverse problems, various aspects and setting assumptions have aroused further interest. Consider for example the inclusion of inaccuracies in the forward model stemming e.g. from discretization, simplifying assumptions, or usage of approximations instead of the exact version, when they feature valuable mathematical properties. For MPI, proper modeling of the complex particle dynamics is still an open problem facing great challenges ([111], [139]). Incorporation of operator uncertainties in the reconstruction might help to relax the demands on an accurate model while maintaining reconstruction quality. We exemplary refer to ([18], [34], [170]) for works dealing with operator uncertainties. Furthermore, in [17] the previously mentioned RESESOP method was accordingly adapted and tested for dynamic computerized tomography. Thereby, the time dependence of the tissue density was interpreted as model inaccuracy.
Investigation of dynamic inverse problems became a field of research in its own. In the next section, we give a brief overview with respect to imaging tasks. Moreover, we refer to Subsections 4.1.2 as well as 4.2.2 for a few considerations regarding dynamic CT and to Chapter 7 for the case of MPI allowing time-varying particle concentrations.

Please note that some of the references mentioned earlier already targeted recent developments in inverse problems (e.g. [4], [11]). Additionally, we want to point out the special issue on modern challenges in imaging [84].

3.1. Dynamic inverse problems in imaging

Initially, it was assumed that the searched-for quantity c is static during measurements. However, in practical applications this might not be true. Consider, for instance, organ movements like the beating heart or expansion and compression of the lungs while breathing. Additionally, blood flow visualization and instrument tracking result intrinsically in time-dependent inverse problems. It is thus self-evident that reconstruction methods have to be adapted to meet the special requirements of dynamic inverse problems. Prior information need to be taken into account in order to reduce or prevent motion artifacts blocking reliable diagnostics. In this section, we first introduce the general setting and then outline different research directions. We conclude with two descriptions of the object's dynamics, namely motion model and deformable templates. In view of this thesis, it is worth keeping the latter in mind, as we will use this method in the context of dynamic MPI.

Based on [89] we formalize the setting of dynamic inverse problems via

$$\mathcal{A}\left(c\left(\cdot,t\right),t\right)\left(\cdot,t\right) = g\left(\cdot,t\right), \quad t \in [0,T]\,. \tag{3.5}$$

Thereby, $T > 0$ denotes the total time required for data acquisition. Independently of each other, time dependencies may occur at different positions within the above formula. These are indicated by color and correspond to time dependencies in the

- solution $c\left(\cdot,t\right) \in X$, as for tracer material flowing with the blood stream;
- forward operator $\mathcal{A}\left(\cdot,t\right)$, consider the case that physical properties linking cause and impact change with time, e.g. due to heating of measurement devices;
- data $g\left(\cdot,t\right) \in Y$, as with MPI, where the voltage signal is generated by a change in magnetization with respect to time.

The critical and *new* time dependence is the one of the searched-for solution resulting in inconsistent and highly undersampled data sets. Just recently, in [40] two notions of ill-posedness, namely pointwise and uniform ill-posedness, and according regularization of dynamic inverse problems were proposed.

One of the first works aiming at dynamic inverse problems were ([168], [169]). They adapted the reconstruction process by adding a temporal smoothness assumption. The approach is quite general, requires no further knowledge of the motion itself and can therefore be used for a wide range of applications if the movement is not too strong. Within the past years, there was a high increase in available methods. Many of them base on classical regularization techniques being adapted to suit the increased demands stemming from the additional degree of freedom due to allowing time variance. Within the next paragraph, we aim to give a glimpse on different categories of regularization techniques and points to be considered with respect to dynamic inverse problems. Again, a lot of works are multifaceted and while being assigned here to one specific class, they may fit into others as well.
To start with, we refer to the special issue on modeling, regularization and numerical aspects of time-dependent problems [124]. Furthermore, for a collection of works and a survey paper concerning dynamic inverse problems in imaging, we point to [102] and [89]. The latter is dedicated to the extensive group of variational approaches, which can be further divided into those exploiting a motion model, a deformable template, or those not relying on any of these. Examples for works using motion models based on partial differential equations (PDEs) are ([36], [37], [48], [122], [130]).

Template motivated papers are given by ([42], [43], [123]), and ([55], [132]) do not exploit precise knowledge of the motion. The same holds for [32] using shearlets and [145] using level-set methods. While the aforementioned approaches either consider joint image and motion reconstruction or do not depend on further motion information, there are also methods assuming the dynamics as given ([77], [104]) in conjunction with dedicated motion estimation techniques ([79], [82], [106], [125]). Further categories regarding methods aiming at dynamic inverse problems are analytic ([44], [47], [105], [158]), iterative ([19], [95], [99], [180]), and deep learning ([88], [118], [147], [151]) based approaches.
For literature specifically aiming at dynamic MPI, we refer to Chapter 7 and for further aspects in the context of dynamic CT to the next chapter.

We close this section by reviewing two of the mentioned approaches. The first one incorporates information about the object's dynamics in terms of a *motion model*, the second one in terms of a *deformable template*. In either case, we suppose that the motion can be modeled using a time-dependent parameterization. If not indicated differently, we refer to [89] for the remainder of this section.

Let Θ be the set of parameters and assume the existence of a mapping $t \mapsto \theta_t \in \Theta$ and a motion model $\Psi_{\theta_t} : X \to X$ such that (3.5) can be rewritten as the constrained inverse problem

$$\mathcal{A}\left(c\left(\cdot,t\right),t\right)\left(\cdot,t\right) = g\left(\cdot,t\right) \quad \text{s.t.} \quad \Psi_{\theta_t}\left(c\left(\cdot,t\right)\right) = 0, \quad t \in [0,T]\,. \tag{3.6}$$

Both the time-varying image $t \mapsto c\left(\cdot,t\right) \in X$ as well as the time-dependent motion parameter $t \mapsto \theta_t \in \Theta$ need to be determined based on the measured data $t \mapsto g\left(\cdot,t\right) \in Y$. Being able to model the phantom dynamics via a motion model as in (3.6) restricts the set of solutions since therewith the course of the time development of c is predefined. Hence, incorporating the corresponding constraint simplifies the problem and may already operate as regularization. However, solving (3.6) remains a complex task requiring appropriate consideration. The strict constraint can be relaxed via including the motion model Ψ_{θ_t} in terms of a penalty term.
As noted earlier, PDE-based motion models have been used to deal with dynamic inverse problems. Prominent examples in this context are given by the *optical flow* [91] constraint

$$\Psi_{\boldsymbol{\nu}}\left(c\left(\cdot,t\right)\right) := \frac{\partial c}{\partial t}\left(\cdot,t\right) + \nabla c\left(\cdot,t\right) \cdot \boldsymbol{\nu}\left(\cdot,t\right) \tag{3.7}$$

assuming intensity preservation and the *continuity equation*

$$\Psi_{\boldsymbol{\nu}}\left(c\left(\cdot,t\right)\right) := \frac{\partial c}{\partial t}\left(\cdot,t\right) + \nabla \cdot \left(c\left(\cdot,t\right)\boldsymbol{\nu}\left(\cdot,t\right)\right)$$

assuming mass preservation. The parameterization $t \mapsto \theta_t \in \Theta$ is given by a sufficiently regular velocity field $\theta_t := \boldsymbol{\nu}\left(\cdot,t\right)$.

Another option to model the object's dynamics is to link each state of the phantom $c\left(\cdot,t\right)$ to a static template $c_0 \in X$ via parameterized deformation operators $\mathcal{W}_{\theta_t} : X \to X$ for $\theta_t \in \Theta$. To this end, assume existence of a fixed family $\{\mathcal{W}_{\theta_t}\}_{\theta_t \in \Theta}$ of those mappings such that (3.5) can be rewritten as

$$\mathcal{A}\left(\mathcal{W}_{\theta_t}\left(c_0\right),t\right)\left(\cdot,t\right) = g\left(\cdot,t\right), \quad t \in [0,T]\,. \tag{3.8}$$

Again, both the time-varying image $t \mapsto c\left(\cdot,t\right) \in X$ as well as the time-dependent parameterization $t \mapsto \theta_t \in \Theta$ need to be determined based on the measured data $t \mapsto g\left(\cdot,t\right) \in Y$. Similar to the motion

model setting, using deformable templates may already operate as regularization and simplifies the problem. Nevertheless, solving (3.8) stays challenging and needs a proper reconstruction method. A special case is when deformation operators can be expressed by diffeomorphisms. Thereby, we consider two cases based on the underlying constraint. More precisely, we regard existence of parameterized diffeomorphisms Γ_{θ_t} acting on the image domain such that

$$\mathcal{W}_{\theta_t}(c_0) := c_0 \circ \Gamma_{\theta_t} \tag{3.9}$$

for the setting of intensity preservation and for mass preservation

$$\mathcal{W}_{\theta_t}(c_0) := (c_0 \circ \Gamma_{\theta_t}) \left|\det \mathrm{D}\, \Gamma_{\theta_t}\right|. \tag{3.10}$$

An upcoming question is how to determine the parameterization θ_t and the according diffeomorphisms. Many approaches are inspired by image registration and shape theory. To name a few, in [43] they build on the concept of large deformation diffeomorphic metric mappings (LDDMM) and [71] considers metamorphosis. We refer to [193] for a comprehensive introduction into the framework of shapes and diffeomorphisms including the two approaches just named. We would also like to mention optimal transport ([161], [183]). Thereby, a mapping is sought that transforms an initial density into a specified final density. The searched-for transport function is optimal in the sense that it minimizes a certain characteristic quantity.

The methodologies of motion models and deforming templates are somehow interconnected. A deformation operator may motivate a certain motion model and vice versa. In case of PDE-based motion models, this connection was especially illustrated in ([42], [43], [89]).

4. Computerized Tomography

Basic Principle: Computerized tomography allows for the reconstruction of inner structures by exploiting the varying absorption rates of different tissues with respect to radiation.

We dedicate this chapter towards the well-known modality *X-ray computerized tomography* in the framework of medical imaging. Nevertheless, there are many other application fields. Some insights regarding CT were already given in Example 3.1. We recommend to consult [144] for details concerning the mathematical treatment of CT that go beyond our presentation.

One of the early contributions that opened the path for the invention of CT is [152] authored by Johann Radon. He investigated the determination of a function by its line integrals and is name giver of the Radon transform.
A major breakthrough for the establishment of CT was reached by scanning a living human for the first time. Dating back to 1972 at the Atkinson Morley's Hospital in London, this proved the capability of computerized tomography to differentiate between healthy and diseased tissue [92]. The clinical relevance was consolidated. For his seminal work with respect to the evolution of CT and building such a scanner, Godfrey N. Hounsfield was awarded the Nobel Prize in Physiology and Medicine in 1979 together with Allan M. Cormack. A biography of the latter is given by [181].

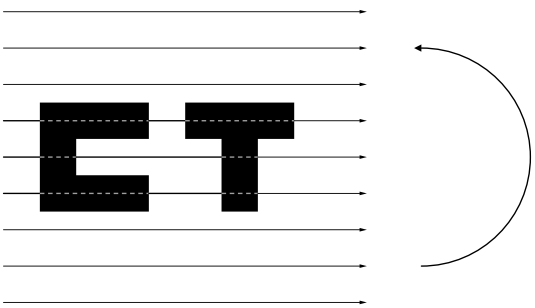

Figure 4.1.: Visualization of the parallel scanning geometry: The phantom is irradiated by a set of parallel X-rays. Data is acquired for evenly distributed directions by rotating radiation source and detector panel after each measurement.

Ever since, a variety of different scanners was constructed differing e.g. based on the sampling pattern. For the fan beam scanning geometry, the patient is circled by a radiation source emitting a fan beam of X-rays. We regard the *parallel scanning geometry* already used in the early days of CT. Thereby, the specimen is irradiated by a number of equidistant, aligned X-rays. Data is acquired for evenly distributed angles by rotating radiation source and detector accordingly (see Figure 4.1). The two geometries mentioned above collect data for one slice through the object at a time. Implementation examples capturing data for a whole volume at once are spiral and multi-slice CT (see [98]). The former gathers data via simultaneously rotating the X-ray source and shifting the patient tabletop, resulting in a helical trajectory of the radiation source relative to the patient.

Outline of the chapter: In Section 4.1, we derive a forward model for CT regarding both static as well as time-varying tissue densities. In the dynamic setting, the forward operator is attained based on diffeomorphic motion functions. Afterwards, Section 4.2 concerns the derivation of an inversion formula. Again, the static and the dynamic case are considered separately.

4.1. Forward model

We recapitulate forward models for computerized tomography regarding static and dynamic objects one after the other. Thereby, we focus our attention on the parallel scanning geometry visualized in Figure 4.1. Reconstructing the object's inner structure in slices allows restriction to two dimensional considerations. For the classical static setting we refer to [144], for time-dependent densities according references are given within the subpart itself.

4.1.1. Static object

Let $c : \mathbb{R}^2 \to \mathbb{R}_0^+ := \mathbb{R}^+ \cup \{0\}$ be a non-negative, time-invariant density distribution. Example 3.1 presented that the inverse problem in computerized tomography consists in determining the density c from information about its line integrals (cf. (3.2)). To illustrate the acquired data, Figure 4.2 shows line integral values for a number of rays for two different scanning directions. It also points out the necessity of having access to data for a number of source positions. Single measurements only give the accumulated intensity loss per line, which could have originated from various density distributions. For instance, the data for a single measurement can always be generated by a constant phantom whose shape is determined by the area enclosed by the line integral value distribution. Increasing the number of scanning directions, decreases the number of possible solutions.

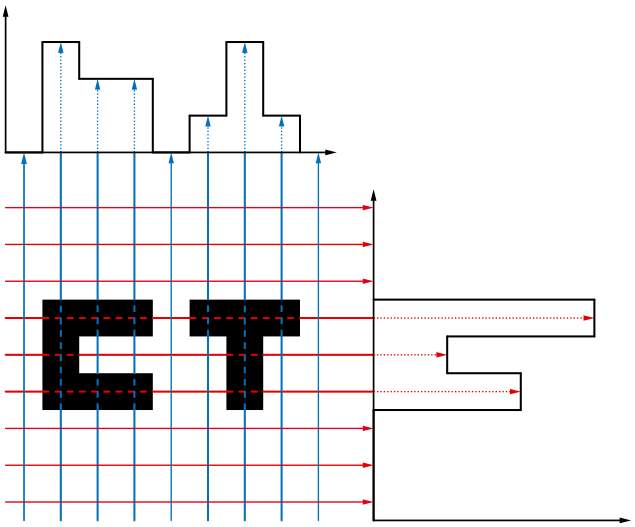

Figure 4.2.: Visualization of the acquired data: The data, i.e. the corresponding line integral values, are shown on the right and at the top of the figure for two different scanning directions, which are indicated by red and blue color respectively.

Let $S^1 := \left\{\mathbf{r} \in \mathbb{R}^2 : \|\mathbf{r}\| = 1\right\}$ denote the unit sphere in $\mathbb{R}^2$. Further, we set $Z := S^1 \times \mathbb{R}$.

Definition 4.1. *The* ***Radon transform*** *of a function $c \in \mathcal{S}\left(\mathbb{R}^2\right)$ evaluated at $(\boldsymbol{\theta}, s) \in Z$ is defined as*

$$\mathcal{R}c(\boldsymbol{\theta}, s) := \int_{\mathbb{R}} c\left(s\boldsymbol{\theta} + t\boldsymbol{\theta}^{\perp}\right) \mathrm{d}\, t = \int_{L(\boldsymbol{\theta},s)} c(\mathbf{r}) \,\mathrm{d}\,\mathbf{r} = \int_{\mathbb{R}^2} c(\mathbf{r})\delta\left(\mathbf{r}\cdot\boldsymbol{\theta} - s\right) \mathrm{d}\,\mathbf{r} \tag{4.1}$$

with dirac-δ-distribution $\delta = \delta_{\mathbf{0}}$ introduced in Example 2.5 and

$$L(\boldsymbol{\theta}, s) := \left\{\mathbf{r} \in \mathbb{R}^2 : \; s = \mathbf{r} \cdot \boldsymbol{\theta}\right\} \tag{4.2}$$

defining the line orthogonal to $\boldsymbol{\theta}$ and with signed distance s to the origin.

Therewith, the forward operator in CT is given by the *Radon transform* mapping a function to the set of its line integrals. Existence of the inverse Radon transform would imply the possibility to determine inner structures of an object by CT measurements. However, the inverse problem

$$\mathcal{R}c = g$$

is ill-posed and regularization methods are necessary for a stable reconstruction. Before we have a closer look at the reconstruction task (Section 4.2), we recall some properties of the Radon transform following directly from its definition (4.1). The Radon transform $\mathcal{R}$ of the density c is

- even, that is $\mathcal{R}c(-\boldsymbol{\theta}, -s) = \mathcal{R}c(\boldsymbol{\theta}, s)$, as

$$L(-\boldsymbol{\theta}, -s) = \left\{\mathbf{r} \in \mathbb{R}^2 : \; -s = -\mathbf{r} \cdot \boldsymbol{\theta}\right\} = \left\{\mathbf{r} \in \mathbb{R}^2 : \; s = \mathbf{r} \cdot \boldsymbol{\theta}\right\} = L(\boldsymbol{\theta}, s);$$

- linear as the integral is linear by itself;
- contained in $\mathcal{S}(Z)$ for $c \in \mathcal{S}\left(\mathbb{R}^2\right)$. Thereby, the space $\mathcal{S}(Z)$ is defined via restricting functions in $\mathcal{S}\left(\mathbb{R}^3\right)$ to Z.

The first property (evenness) demonstrates that it is sufficient to gather data covering a half circle. Lastly, one other feature is captured by the Lemma below (cf. [144], pp. 12 f.). For a derivation, please refer to the reference given.

Lemma 4.2. *Let $c \in \mathcal{S}\left(\mathbb{R}^2\right)$. The Radon transform $\mathcal{R}c \in \mathcal{S}(Z)$ can be extended to $\left(\mathbb{R}^2 \setminus \{0\}\right) \times \mathbb{R}$ as a function homogeneous of degree (-1)*

$$\mathcal{R}c\left(\lambda\boldsymbol{\theta}, \lambda s\right) = \lambda^{-1}\mathcal{R}c\left(\boldsymbol{\theta}, s\right)$$

for $(\boldsymbol{\theta}, s) \in Z$ and $\lambda > 0$. For this extension, derivatives concerning the first variable can be determined as

$$\mathrm{D}_{\boldsymbol{\theta}}^{\mathbf{k}}\mathcal{R}c = (-1)^{|\mathbf{k}|}\frac{\partial^{|\mathbf{k}|}}{\partial s^{|\mathbf{k}|}}\mathcal{R}\left(\mathbf{r}^{\mathbf{k}}c\right)$$

with multi-index $\mathbf{k}$.

As shown in Figure 4.3, the line $L(\boldsymbol{\theta}, s)$ can also be specified by the angle φ between x-axis and regarded X-ray. On that account, we parameterize the normal vector $\boldsymbol{\theta} \in S^1$ as follows

$$\boldsymbol{\theta}\left(\varphi\right) = \begin{pmatrix} -\sin\varphi \\ \cos\varphi \end{pmatrix} =: \mathbf{e}_{\varphi}, \quad \varphi \in [0, 2\pi].$$

Because of this parameterization, throughout this work, we will use both terms $\mathcal{R}c\left(\mathbf{e}_{\varphi}, s\right)$ respectively $\mathcal{R}c\left(\boldsymbol{\theta}, s\right)$ as well as $\mathcal{R}c\left(\varphi, s\right)$ depending on which notion is more convenient in the particular situation.
Notice that usually the X-ray orientation is determined by the angle between x-axis and normal vector $\mathbf{e}_{\varphi}$. Yet, we use the deviating notation above in order to match the one we apply for practical reasons in the remaining chapters, which focus on magnetic particle imaging. Hence, compared to common CT literature an angle shift of $\frac{\pi}{2}$ appears in the definition of φ. This was also remarked in [114].

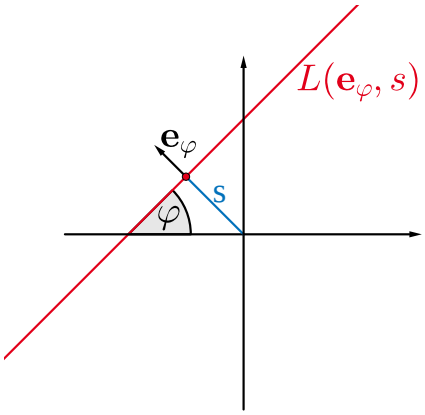

Figure 4.3.: Visualization of the X-ray parameterization: The X-ray $L(\mathbf{e}_\varphi, s)$ is uniquely determined by the signed distance s to the origin and the normal vector $\mathbf{e}_\varphi$, which itself is set by the angle φ between x-axis and X-ray.

So far, everything has been considered in a continuous setting. In practice, however, the scanning process can be executed only for a finite number of source positions. This leads us to the final remark of this subsection, namely how we assume that the data is sampled.

Remark 4.3. *For $p, q \in \mathbb{N}$, let measurements be executed for p different scanning directions and $2q+1$ signed distances to the origin determined by*

$$\begin{aligned} \varphi_k &:= (k-1)\,\frac{\pi}{p}, \quad k = 1, \dots, p, \\ s_l &:= (q+1-l)\,\frac{s_{\max}}{q}, \quad l = 1, \dots, 2q+1, \end{aligned}$$

*with $s_{\max} > 0$ denoting the maximum displacement. Corresponding data are sorted into a so-called **sinogram** $\mathbf{S} \in \mathbb{R}^{(2q+1)\times p}$. We suppose that $\mathbf{S}$ is filled according to $\mathbf{S} = (S_{lk})_{l=1,\dots,2q+1;k=1,\dots,p}$ and $S_{lk} = \mathcal{R}c\,(\varphi_k, s_l)$. We refer to Figure 4.4 for an illustration.*

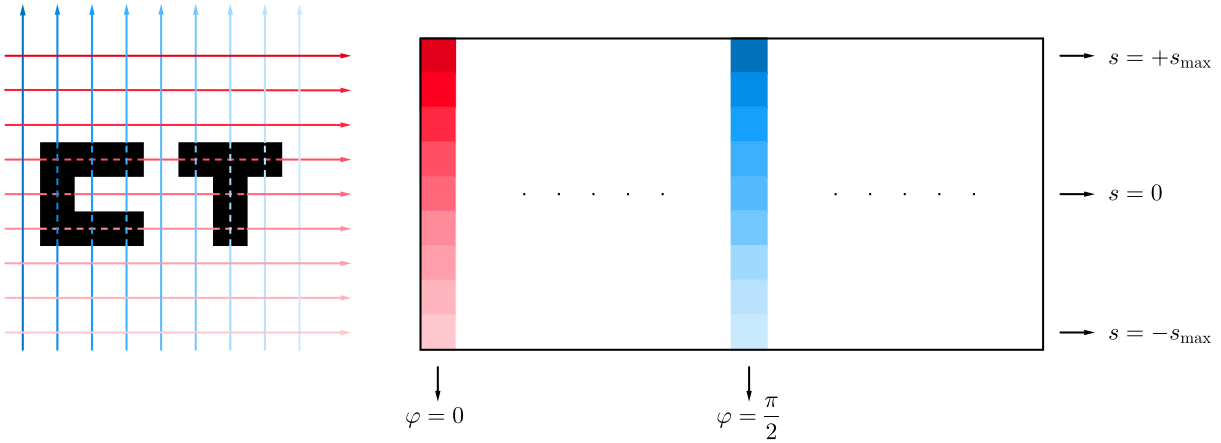

Figure 4.4.: Visualization of sorting the Radon data into a sinogram: Each column corresponds to an angle φ defining the scanning direction, while each row corresponds to a displacement s of the regarded X-ray to the origin.

Before we review the invertibility of the Radon transform for the static case in Subsection 4.2.1, we consider a forward model for time-varying specimens in the next paragraph.

4.1.2. Dynamic object

As noted in Section 3.1, the assumption of static objects is not satisfied for many applications. We already gave an overview concerning existing methods to reduce or even prevent motion artifacts. We therefore add only a few more references. In [156] gating is used to treat respiratory motion. In [129] it is proposed to estimate and compensate motion straight in sinogram space. Therewith, classical reconstruction approaches can be used. The authors of [81] and [83] investigate the information content of dynamic data relying on microlocal analysis. The accessible resolution for affine deformations in two dimensions is examined in [78]. Lastly, we refer to [24] for an overview, published in 2003, regarding conceptions in dynamic CT. The goal of the following part is to derive an adapted forward operator for moving objects. More precisely, on the grounds of [76], we recall the approach of using diffeomorphic motion functions linking the time-varying tissue density to a static reference phantom. This corresponds to the diffeomorphic deformable template framework introduced at the end of the previous chapter.

In the following, the time dependence is identified with an angle-dependence as the time-consuming part for CT consists in the rotation of source and detector [76]. Therewith, the Radon transform of a changing object $c(\cdot,\varphi) \in \mathcal{S}\left(\mathbb{R}^2\right)$, for all $\varphi \in [0,2\pi]$, is given by

$$\mathcal{R}c(\varphi,s) = \int_{\mathbb{R}^2} c(\mathbf{r},\varphi)\delta\left(\mathbf{r}\cdot\mathbf{e}_\varphi - s\right)\,\mathrm{d}\,\mathbf{r}. \tag{4.3}$$

The issue with dynamic specimen is that for different angles, measurements with respect to different states of the object are taken. This results in insufficient data for the individual states. As remedy, motion information can be incorporated via so-called *motion functions* connecting the time instances, thus, relating each data to one static reference density. We consider two distinct a priori assumptions, namely *intensity* and *mass preservation* [80] corresponding to (3.9) and (3.10) of the last chapter. In accordance to this, let $c_0 \in \mathcal{S}\left(\mathbb{R}^2\right)$ be the static *reference state* (the template) such that

$$\begin{aligned} &\textit{(intensity pres.)} && c\left(\mathbf{r},\varphi\right) &&= c_0\left(\Gamma_\varphi\mathbf{r}\right), && (4.4)\\ &\textit{(mass pres.)} && c\left(\mathbf{r},\varphi\right) &&= c_0\left(\Gamma_\varphi\mathbf{r}\right)\left|\det \mathrm{D}\,\Gamma_\varphi\mathbf{r}\right| && (4.5)\end{aligned}$$

with $\Gamma : \mathbb{R}^2\times[0,2\pi] \to \mathbb{R}^2$ and $\Gamma_\varphi\mathbf{r} := \Gamma(\mathbf{r},\varphi)$ being a diffeomorphism for each fixed $\varphi \in [0,2\pi]$. The reference density can, for instance, be chosen as one state of the object during data generation

$$c_0(\mathbf{r}) = c(\mathbf{r},\varphi_0)$$

for some reference angle $\varphi_0 \in [0,2\pi]$. We summarize expressions (4.4) and (4.5) as

$$c\left(\mathbf{r},\varphi\right) = c_0\left(\Gamma_\varphi\mathbf{r}\right)h_\varphi\left(\Gamma_\varphi\mathbf{r}\right)\left|\det \mathrm{D}\,\Gamma_\varphi\mathbf{r}\right| \tag{4.6}$$

via introducing

$$h_\varphi(\mathbf{y}) := \begin{cases} \left|\det \mathrm{D}\,\Gamma_\varphi^{-1}\mathbf{y}\right|, & \text{for } c \text{ as in (4.4)},\\ 1, & \text{for } c \text{ as in (4.5)}. \end{cases} \tag{4.7}$$

The just described concept of motion functions is visualized in Figure 4.5. The static phantom already shown in Figure 4.2 is depicted in black. On the right side, values of corresponding line integrals are presented for X-rays regarding $\varphi = 0$. Rotation of the radiation source gives the values

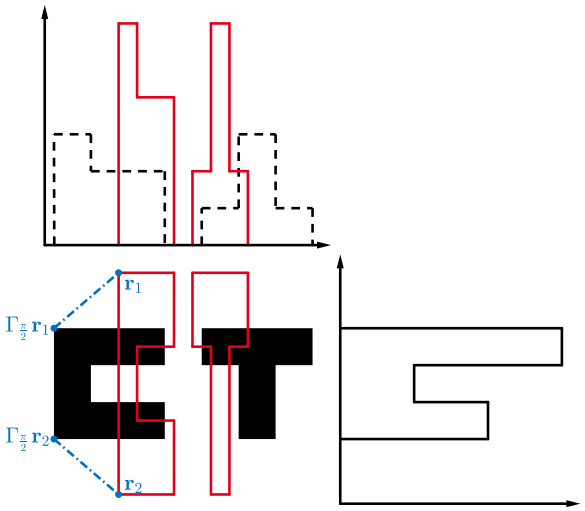

Figure 4.5.: Visualization of inconsistent data: The black phantom defines the reference state (phantom at $\varphi = 0$). Corresponding integral values are depicted at the right. At the top of the picture, data is imaged in red for the deformed specimen (indicated by red contours) at $\varphi = \frac{\pi}{2}$. For comparison, the black dashed lines are the measurements for the non-changing black phantom. Finally, the blue lines link positions within the object at these two angles.

at the top of the image. Thereby, the dashed black line illustrates data for an unchanged phantom, while the solid red line shows the integral values for the deformed object indicated by the red contours in the picture center. This demonstrates the data inconsistencies described before, namely that measurements relate to different states of the object resulting in incomplete data sets with respect to the different density distributions over time. The blue components show the connection of the reference object (black) and the current state (red). In this example, it holds $|\det \mathrm{D}\,\Gamma_\varphi \mathbf{r}| = 1$, i.e. both mass and intensity preservation are given and the motion of the object can be interpreted as a motion of its composing particles carrying the density value from $\Gamma_{\frac{\pi}{2}}\mathbf{r}_i$ to $\mathbf{r}_i$ with i indicating the considered particle. It holds (visualized for $i = 1, 2$)

$$c\left(\mathbf{r}_i, \frac{\pi}{2}\right) = c\left(\Gamma_{\frac{\pi}{2}}\mathbf{r}_i, 0\right) = c_0\left(\Gamma_{\frac{\pi}{2}}\mathbf{r}_i\right).$$

By inserting expression (4.6) into (4.3), the forward operator for dynamic CT with respect to the presented motion treatment can be obtained via substituting $\mathbf{y} := \Gamma_\varphi \mathbf{r}$

$$\begin{aligned}\mathcal{R}c(\varphi, s) &= \int_{\mathbb{R}^2} c_0\left(\Gamma_\varphi \mathbf{r}\right) h_\varphi\left(\Gamma_\varphi \mathbf{r}\right) \left|\det \mathrm{D}\,\Gamma_\varphi \mathbf{r}\right| \delta\left(\mathbf{r}\cdot\mathbf{e}_\varphi - s\right) \mathrm{d}\,\mathbf{r} \\ &= \int_{\mathbb{R}^2} c_0\left(\mathbf{y}\right) h_\varphi\left(\mathbf{y}\right) \delta\left(\Gamma_\varphi^{-1}\mathbf{y}\cdot\mathbf{e}_\varphi - s\right) \mathrm{d}\,\mathbf{y}.\end{aligned}$$

Definition 4.4. *Assume an angle dependent function $c(\cdot, \varphi) \in \mathcal{S}\left(\mathbb{R}^2\right)$, for all $\varphi \in [0, 2\pi]$, that can be linked to a reference function $c_0 \in \mathcal{S}\left(\mathbb{R}^2\right)$ as in (4.6). The adapted Radon transform of c_0 evaluated at $(\varphi, s) \in [0, 2\pi] \times \mathbb{R}$ is defined as*

$$\mathcal{R}^\Gamma c_0(\varphi, s) := \int_{C(\varphi,s)} c_0\left(\mathbf{y}\right) h_\varphi\left(\mathbf{y}\right) \mathrm{d}\,\mathbf{y} = \int_{\mathbb{R}^2} c_0\left(\mathbf{y}\right) h_\varphi\left(\mathbf{y}\right) \delta\left(\Gamma_\varphi^{-1}\mathbf{y}\cdot\mathbf{e}_\varphi - s\right) \mathrm{d}\,\mathbf{y} \tag{4.8}$$

with $C(\varphi, s) := \left\{\mathbf{y} \in \mathbb{R}^2 : s = \left(\Gamma_\varphi^{-1}\mathbf{y}\right)\cdot\mathbf{e}_\varphi\right\}$.

In comparison to the classical Radon transform, the adapted version $\mathcal{R}^\Gamma$ takes function values rather along curves $C(\varphi, s)$ instead of straight lines [76]. For illustration, we refer to Figure 4.6. The left picture 4.6a shows the reference state and X-rays traversing the object parallel to the x-axis. Image 4.6b gives the deformed phantom. The last sketch relates positions of particles at the current state with those according to the reference state. Thereby, particles distributed along the parallel black lines regarding the red phantom (deformed) are positioned along the red curves regarding the black phantom (reference).

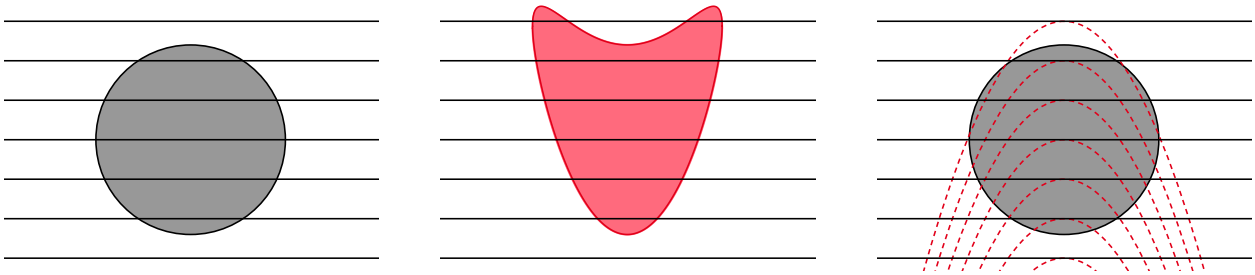

Figure 4.6.: Visualization of the dynamic Radon transform: Picture (a) shows the reference state and X-rays for $\varphi = 0$. Data regarding a deformed phantom for this angle, can be either determined via integrating the actual shape (red phantom in (b)) along straight lines, or by integrating the reference density along the dashed red curves in (c).

For affine motions, i.e. Γ_φ^{-1} is for all $\varphi \in [0, 2\pi]$ of the form

$$\Gamma_\varphi^{-1}\mathbf{y} = \mathbf{A}_\varphi \mathbf{y} + \mathbf{b}_\varphi, \quad \mathbf{A}_\varphi \in \mathbb{R}^{2\times 2},\ \det \mathbf{A}_\varphi \neq 0,\ \mathbf{b}_\varphi \in \mathbb{R}^2,$$

the adapted Radon transform $\mathcal{R}^\Gamma$ still integrates along straight lines. According to

$$\begin{aligned} C(\varphi, s) &= \left\{\mathbf{y} \in \mathbb{R}^2 : s = \left(\Gamma_\varphi^{-1}\mathbf{y}\right) \cdot \mathbf{e}_\varphi\right\} \\ &= \left\{\mathbf{y} \in \mathbb{R}^2 : s = \left(\mathbf{A}_\varphi \mathbf{y} + \mathbf{b}_\varphi\right) \cdot \mathbf{e}_\varphi\right\} \\ &= \left\{\mathbf{y} \in \mathbb{R}^2 : s - \mathbf{b}_\varphi \cdot \mathbf{e}_\varphi = \mathbf{y} \cdot \mathbf{A}_\varphi^* \mathbf{e}_\varphi\right\}, \end{aligned}$$

these lines are orthogonal to $\frac{\mathbf{A}_\varphi^* \mathbf{e}_\varphi}{\|\mathbf{A}_\varphi^* \mathbf{e}_\varphi\|}$ and have signed distance $\frac{s - \mathbf{b}_\varphi \cdot \mathbf{e}_\varphi}{\|\mathbf{A}_\varphi^* \mathbf{e}_\varphi\|}$ to the origin (cf. [76]).

Remark 4.5. *The operator $\mathcal{R}^\Gamma$ is in general not symmetric. Nevertheless, based on the symmetry property in the static case, only data for angles covering a half circle are measured in order to reduce measurement time and radiation exposure. Thus, using the same scanning process in the dynamic setting, the forward operator can be assumed to be even without changing the data and for convenience it is proposed $\mathcal{R}^\Gamma c_0(-\mathbf{e}_\varphi, -s) = \mathcal{R}^\Gamma c_0(\mathbf{e}_\varphi, s)$ (see [76]).*

As final note, we point out that even with incorporation of motion information and having access to measurements covering the whole angle range, the acquired data might be insufficient for reliable reconstruction. This is due to the fact that the object might change in such a way that the X-rays do not hit some regions of the phantom. Consider, for instance, a specimen continuously rotating in compliance with the source rotation. Then, for all angles the X-rays travel through the same parts of the object and effectively data for only one angle is available. Based on microlocal analysis, results have been derived investigating the information content of data with respect to different image artifacts ([81], [83]).

4.2. Reconstruction

Various reconstruction approaches for (dynamic) inverse problems are referenced in Chapter 3. Note that the underlying forward model for time-varying densities derived in the previous section

$$\mathcal{R}^{\Gamma} c_0 = g^{\Gamma}$$

reduces to the one for time-constant specimen $\mathcal{R}c = g$ by setting $\Gamma = \mathrm{Id}$. Thus, methods developed for time-dependent objects are applicable within the static case as well. In the following, we consider inversion formulas for both static and dynamic phantoms.

4.2.1. Static object

First, we recall an inversion formula for the classical Radon transform. Due to its ill-posedness, regularization techniques are mandatory for stable image reconstruction and, hence, for reliable diagnostics. Exemplary, we review the well-known filtered backprojection (FBP).

For the derivation of the inversion formula, the *Fourier slice theorem* is of major importance. It links the Fourier transform of the Radon data with the Fourier transform of the density itself.

Theorem 4.6 (Fourier Slice Theorem, Theorem 1.1 in [144]). *Let $c \in \mathcal{S}\left(\mathbb{R}^2\right)$. It holds for $\sigma \in \mathbb{R}$*

$$\widehat{\mathcal{R}c}(\boldsymbol{\theta}, \sigma) = (2\pi)^{\frac{1}{2}}\, \widehat{c}(\sigma\boldsymbol{\theta}).$$

Thereby, the Fourier transform with respect to the second argument is regarded.

Therefore, the searched-for image can essentially be obtained by applying the inverse Fourier transform to the transformed data.

Theorem 4.7 (cf. Theorem 2.1 in [144]). *The following inversion formula for the tissue density applies for $c \in \mathcal{S}\left(\mathbb{R}^2\right)$*

$$c(\mathbf{r}) = \frac{1}{2}(2\pi)^{-\frac{3}{2}} \int_{S^1} \int_{\mathbb{R}} e^{i\mathbf{r}\cdot(\sigma\boldsymbol{\theta})}\, \widehat{\mathcal{R}c}(\boldsymbol{\theta}, \sigma)\, |\sigma| \,\mathrm{d}\sigma \,\mathrm{d}\boldsymbol{\theta}. \tag{4.9}$$

Proof. The following is based on the proof of Theorem 2.1 in [144]. To obtain expression (4.9) the Definition 2.6 of the Fourier transform and its inverse is exploited

$$c(\mathbf{r}) = \mathcal{F}^{-1}\mathcal{F}\, c(\mathbf{r}) = (2\pi)^{-1} \int_{\mathbb{R}^2} e^{i\mathbf{r}\cdot\boldsymbol{\xi}}\, \widehat{c}(\boldsymbol{\xi}) \,\mathrm{d}\boldsymbol{\xi}.$$

Proceeding to polar coordinates $\boldsymbol{\xi} := \sigma\boldsymbol{\theta}$ and applying the Fourier slice theorem yields

$$\begin{aligned} c(\mathbf{r}) &= (2\pi)^{-1} \int_{S^1} \int_0^{\infty} e^{i\mathbf{r}\cdot(\sigma\boldsymbol{\theta})}\, \widehat{c}(\sigma\boldsymbol{\theta})\, \sigma \,\mathrm{d}\sigma \,\mathrm{d}\boldsymbol{\theta} \\ &= (2\pi)^{-\frac{3}{2}} \int_{S^1} \int_0^{\infty} e^{i\mathbf{r}\cdot(\sigma\boldsymbol{\theta})}\, \widehat{\mathcal{R}c}(\boldsymbol{\theta}, \sigma)\, \sigma \,\mathrm{d}\sigma \,\mathrm{d}\boldsymbol{\theta}. \end{aligned}$$

Finally, utilizing that the Radon and, thus, its Fourier transform are even, results in

$$c(\mathbf{r}) = \frac{1}{2}(2\pi)^{-\frac{3}{2}} \int_{S^1} \int_{\mathbb{R}} e^{i\mathbf{r}\cdot(\sigma\boldsymbol{\theta})}\, \widehat{\mathcal{R}c}(\boldsymbol{\theta}, \sigma)\, |\sigma| \,\mathrm{d}\sigma \,\mathrm{d}\boldsymbol{\theta}.$$

□

As already mentioned, regularization methods are inevitable for reliable reconstruction. A well-known method called *filtered backprojection* can be obtained by including a low-pass filter in the above formula. More precisely, in order to smooth the image, a filter $\widehat{\mathfrak{F}}\left(\frac{1}{\gamma}\cdot\right)$ with cut-off frequency $\gamma > 0$ is complemented to (4.9) (cf. [144], pp. 102 f.)

$$c_\gamma(\mathbf{r}) := \int_{S^1}\int_{\mathbb{R}} e^{i\mathbf{r}\cdot(\sigma\boldsymbol{\theta})}\,\widehat{\mathcal{R}c}(\boldsymbol{\theta},\sigma)\widehat{\Phi}_\gamma(\sigma)\,\mathrm{d}\sigma\,\mathrm{d}\boldsymbol{\theta}, \qquad \widehat{\Phi}_\gamma(\sigma) := \frac{1}{2}(2\pi)^{-\frac{3}{2}}\,|\sigma|\,\widehat{\mathfrak{F}}\left(\frac{|\sigma|}{\gamma}\right). \tag{4.10}$$

Thereby, the filter satisfies $0 \le \widehat{\mathfrak{F}} \le 1$ and $\widehat{\mathfrak{F}}(\lambda) = 0$ for $\lambda > 1$, i.e. $\widehat{\Phi}_\gamma(\sigma) = 0$ for $\sigma \notin [-\gamma,\gamma]$.

Example 4.8 (Shepp-Logan Filter, pp. 110 f. in [144]). *A prominent example is given by the Shepp-Logan filter*

$$\widehat{\mathfrak{F}}(\sigma) = \begin{cases} \operatorname{sinc}\left(\frac{\pi}{2}\sigma\right), & \sigma \le 1, \\ 0, & \sigma > 1, \end{cases} \quad\Longrightarrow\quad \Phi_\gamma(s) = \begin{cases} \frac{\gamma^2}{2\pi^4}, & s = \pm\frac{\pi}{2\gamma}, \\ \frac{\gamma^2}{2\pi^3}\frac{\frac{\pi}{2}-\gamma s\sin(\gamma s)}{\left(\frac{\pi}{2}\right)^2-\gamma^2 s^2}, & \text{otherwise.} \end{cases}$$

We will see that c_γ can be expressed in terms of the adjoint $\mathcal{R}^*$ of the Radon transform, which is given according to the next theorem.

Theorem 4.9 (pp. 13 f. in [144]). *The adjoint of the Radon transform is given as*

$$\mathcal{R}^* g(\mathbf{r}) = \int_{S^1} g(\boldsymbol{\theta}, \mathbf{r}\cdot\boldsymbol{\theta})\,\mathrm{d}\boldsymbol{\theta}.$$

Together with Theorem 2.9, formula (4.10) translates to

$$c_\gamma(\mathbf{r}) = \int_{S^1} (\Phi_\gamma * \mathcal{R}c)(\boldsymbol{\theta}, \mathbf{r}\cdot\boldsymbol{\theta})\,\mathrm{d}\boldsymbol{\theta} = \mathcal{R}^*(\Phi_\gamma * \mathcal{R}c)(\mathbf{r}). \tag{4.11}$$

This expression explains the name filtered backprojection. The filtering part is given in form of the convolution with Φ_γ. Note that while $\mathcal{R}c(\boldsymbol{\theta}, s)$ determines the integral of c along the line $L(\boldsymbol{\theta}, s)$, the adjoint $\mathcal{R}^* g(\mathbf{r})$ considers integrals in relation to all lines through $\mathbf{r}$. Thus, the application of the adjoint Radon transform gives the backprojection component. To further clarify the idea of the FBP scheme, we recall the theorem below.

Theorem 4.10 (Theorem 1.3 in [144]). *For all $c \in \mathcal{S}(\mathbb{R}^2)$ and $g \in \mathcal{S}(Z)$ it holds*

$$(\mathcal{R}^* g) * c = \mathcal{R}^*(g * \mathcal{R}c).$$

Thus, assuming that $\mathcal{R}^*\Phi_\gamma$ approximates the dirac-δ-distribution, it follows with (4.11) that

$$c_\gamma = R^*(\Phi_\gamma * \mathcal{R}c) = (\mathcal{R}^*\Phi_\gamma) * c \approx c.$$

For the remainder, we suppose the object under investigation to be contained within the circle B_R of radius $R > 0$ around the origin, i.e. we assume $\operatorname{supp}(c) \subseteq B_R := B_R(0) := \{\mathbf{r} \in \mathbb{R}^2 : \|\mathbf{r}\| < R\}$ with $\operatorname{supp}(c) := \overline{\{\mathbf{r} \in \mathbb{R}^2 : c(\mathbf{r}) \neq 0\}}$ (cf. support condition in [80]).

Theorem 4.11 (Theorem 1.6 in [144]). *The Radon transform (4.1) can be continuously extended to an operator mapping between L_2-spaces*

$$\mathcal{R} : L_2(B_R) \to L_2\left(Z_R := S^1 \times [-R, R]\right).$$

Remark 4.12. *For the sake of convenience, throughout this thesis we exploit the continuous extensions $c(\mathbf{r}) = 0$ for $\mathbf{r} \in \mathbb{R}^2 \setminus B_R$ and $\mathcal{R}c(\boldsymbol{\theta}, s) = 0$ for $(\boldsymbol{\theta}, s) \in Z \setminus Z_R$.*

4.2.2. Dynamic object

This paragraph deals with an inversion formula for the dynamic Radon transform regarding affine deformations as introduced in Section 4.1.2. We suppose the tissue density to be contained within a circle B_R of radius $R > 0$ around the origin for all time instances, i.e. for all angles $\varphi \in [0, 2\pi]$. Motivated by Theorem 4.11 and justified by the smoothing property of $\mathcal{R}^\Gamma$ as declared in [76], we consider $c_0 \in L_2(B_R)$ with continuous extension $c_0(\mathbf{r}) := 0$ for $\mathbf{r} \in \mathbb{R}^2 \setminus B_R$. If not mentioned differently, the following is abstracted from [76], adapted to our notation and with the minor adjustment of simultaneously considering the cases of mass and intensity conservation via incorporating h_φ, defined in (4.7).

First, we state the adjoint of the dynamic Radon transform.

Theorem 4.13 (cf. (3.2) in [76]). *The adjoint $\left(\mathcal{R}^\Gamma\right)^* : L_2([0, 2\pi] \times [-R, R]) \to L_2(B_R)$ of the adapted Radon transform $\mathcal{R}^\Gamma$ is given as*

$$\left(\mathcal{R}^\Gamma\right)^* g(\mathbf{y}) = \int_{[0,2\pi]} h_\varphi(\mathbf{y})\, g(\mathbf{e}_\varphi, \Gamma_\varphi^{-1}\mathbf{y} \cdot \mathbf{e}_\varphi)\, \mathrm{d}\varphi.$$

In the following, we restrict ourselves to affine motion functions such that Γ_φ^{-1} is for all $\varphi \in [0, 2\pi]$ determined by

$$\Gamma_\varphi^{-1}\mathbf{y} = \mathbf{A}_\varphi \mathbf{y} + \mathbf{b}_\varphi, \quad \mathbf{A}_\varphi \in \mathbb{R}^{2\times 2},\ \det \mathbf{A}_\varphi \neq 0,\ \mathbf{b}_\varphi \in \mathbb{R}^2.$$

In this setting, definition (4.7) transforms to

$$h_\varphi := h_\varphi(\mathbf{y}) = \begin{cases} |\det \mathbf{A}_\varphi|, & \text{for } c \text{ as in (4.4)}, \\ 1, & \text{for } c \text{ as in (4.5)}. \end{cases}$$

Remember that for affine motions the forward operator $\mathcal{R}^\Gamma$ integrates the density along lines orthogonal to $\frac{\mathbf{A}_\varphi^* \mathbf{e}_\varphi}{\|\mathbf{A}_\varphi^* \mathbf{e}_\varphi\|}$. Suppose that

$$\left\{ \frac{\mathbf{A}_\varphi^* \mathbf{e}_\varphi}{\|\mathbf{A}_\varphi^* \mathbf{e}_\varphi\|} : \varphi \in [0, 2\pi] \right\} = S^1,$$

i.e. data for every direction with respect to the reference state can be taken. Let the motion be smooth, that is, let $\mathbf{A}_\varphi$ and $\mathbf{b}_\varphi$ be componentwise continuously differentiable. As in practice only a finite number of measurements is available, this does not represent a limitation [81]. A smooth motion function matching the discrete evaluation points can be found by interpolation. Furthermore,

$$\tilde{j}(\varphi) := \left(\mathbf{A}_\varphi^* \mathbf{e}_\varphi\right)_1 \frac{\partial}{\partial \varphi}\left(\mathbf{A}_\varphi^* \mathbf{e}_\varphi\right)_2 - \left(\mathbf{A}_\varphi^* \mathbf{e}_\varphi\right)_2 \frac{\partial}{\partial \varphi}\left(\mathbf{A}_\varphi^* \mathbf{e}_\varphi\right)_1 \neq 0, \quad \text{for } \varphi \in [0, 2\pi] \tag{4.12}$$

shall be satisfied.

Like in the static case, before we state the inversion formula, we consider an adaption of the Fourier slice theorem.

Theorem 4.14 (cf. Theorem 4.1 in [76]). *Let $c_0 \in L_2(B_R)$. Application of the Fourier transform with respect to the second argument to the dynamic Radon transform results in*

$$\widehat{\mathcal{R}^\Gamma c_0}(\mathbf{e}_\varphi, \sigma) = (2\pi)^{\frac{1}{2}} h_\varphi e^{-i\sigma \mathbf{b}_\varphi \cdot \mathbf{e}_\varphi} \widehat{c_0}(\sigma \mathbf{A}_\varphi^* \mathbf{e}_\varphi).$$

Therewith, we finally recall the inversion formula for affine deformations.

Theorem 4.15 (cf. Theorem 4.2 in [76]). *The following inversion formula applies for* $c_0 \in L_2(B_R)$

$$c_0(\mathbf{r}) = \frac{1}{2}(2\pi)^{-\frac{3}{2}} \int_{[0,2\pi]} h_\varphi^{-1} \left|\tilde{j}(\varphi)\right| \int_{\mathbb{R}} e^{i\mathbf{r}\cdot\sigma\mathbf{A}_\varphi^*\mathbf{e}_\varphi}\, e^{i\sigma\mathbf{b}_\varphi\cdot\mathbf{e}_\varphi}\, \widehat{\mathcal{R}^\Gamma c_0}(\mathbf{e}_\varphi,\sigma)\,|\sigma|\,\mathrm{d}\sigma\,\mathrm{d}\varphi. \tag{4.13}$$

Proof. The proof works similar to the static case, that is to the proof of Theorem 4.7. Inclusion of the identity map $\mathrm{Id} = \mathcal{F}^{-1}\mathcal{F}$ yields

$$c_0(\mathbf{r}) = \mathcal{F}^{-1}\mathcal{F}\, c_0(\mathbf{r}) = (2\pi)^{-1} \int_{\mathbb{R}^2} e^{i\mathbf{r}\cdot\boldsymbol{\xi}}\, \widehat{c}_0(\boldsymbol{\xi})\,\mathrm{d}\boldsymbol{\xi}.$$

Substitution of $\boldsymbol{\xi} := j(\sigma,\varphi) := \sigma\mathbf{A}_\varphi^*\mathbf{e}_\varphi$ together with $\det \mathrm{D}\, j(\sigma,\varphi) = \sigma\,\tilde{j}(\varphi)$ (see (4.12)) gives

$$c_0(\mathbf{r}) = (2\pi)^{-1} \int_{[0,2\pi]} \int_0^\infty e^{i\mathbf{r}\cdot\sigma\mathbf{A}_\varphi^*\mathbf{e}_\varphi}\, \widehat{c}_0\left(\sigma\mathbf{A}_\varphi^*\mathbf{e}_\varphi\right)|\sigma|\left|\tilde{j}(\varphi)\right|\,\mathrm{d}\sigma\,\mathrm{d}\varphi.$$

Next, the adapted Fourier slice theorem 4.14 and the assumed evenness of $\mathcal{R}^\Gamma$, as noted in Remark 4.5, yield

$$c_0(\mathbf{r}) = \frac{1}{2}(2\pi)^{-\frac{3}{2}} \int_{[0,2\pi]} h_\varphi^{-1} \left|\tilde{j}(\varphi)\right| \int_{\mathbb{R}} e^{i\mathbf{r}\cdot\sigma\mathbf{A}_\varphi^*\mathbf{e}_\varphi}\, e^{i\sigma\mathbf{b}_\varphi\cdot\mathbf{e}_\varphi}\, \widehat{\mathcal{R}^\Gamma c_0}(\mathbf{e}_\varphi,\sigma)\,|\sigma|\,\mathrm{d}\sigma\,\mathrm{d}\varphi.$$

□

By introducing the *Riesz potential* $\widehat{\vartheta^{-1}f}(\sigma) := |\sigma|\,\widehat{f}(\sigma)$, the inversion formula (4.13) can be further transformed (see proof of Theorem 4.2 in [76]) to

$$\begin{aligned} c_0(\mathbf{r}) &= \frac{1}{2}(2\pi)^{-\frac{3}{2}} \int_{[0,2\pi]} h_\varphi^{-1} \left|\tilde{j}(\varphi)\right| \int_{\mathbb{R}} e^{i\mathbf{r}\cdot\sigma\mathbf{A}_\varphi^*\mathbf{e}_\varphi}\, e^{i\sigma\mathbf{b}_\varphi\cdot\mathbf{e}_\varphi}\, \widehat{\vartheta^{-1}\mathcal{R}^\Gamma c_0}(\mathbf{e}_\varphi,\sigma)\,\mathrm{d}\sigma\,\mathrm{d}\varphi \\ &= \frac{1}{4\pi} \int_{[0,2\pi]} h_\varphi^{-1} \left|\tilde{j}(\varphi)\right| \mathcal{F}^{-1}\left(e^{i\sigma\mathbf{b}_\varphi\cdot\mathbf{e}_\varphi}\, \widehat{\vartheta^{-1}\mathcal{R}^\Gamma c_0}\right)\left(\mathbf{e}_\varphi, \mathbf{r}\cdot\mathbf{A}_\varphi^*\mathbf{e}_\varphi\right)\mathrm{d}\varphi. \end{aligned}$$

Using the property of Fourier transforms regarding shifting operators, i.e. Lemma 2.7, together with Theorem 4.13 results in

$$\begin{aligned} c_0(\mathbf{r}) &= \frac{1}{4\pi} \int_{[0,2\pi]} h_\varphi^{-1} \left|\tilde{j}(\varphi)\right| \vartheta^{-1}\mathcal{R}^\Gamma c_0\left(\mathbf{e}_\varphi, \mathbf{r}\cdot\mathbf{A}_\varphi^*\mathbf{e}_\varphi + \mathbf{b}_\varphi\cdot\mathbf{e}_\varphi\right)\mathrm{d}\varphi \\ &= \frac{1}{4\pi}\left(\mathcal{R}^\Gamma\right)^*\left[h_\varphi^{-2}\left|\tilde{j}(\varphi)\right|\vartheta^{-1}\mathcal{R}^\Gamma c_0\right](\mathbf{r}). \end{aligned} \tag{4.14}$$

Remark 4.16. *Note that also the classical inversion formula (4.9) can be written in terms of the Riesz potential as*

$$c = \frac{1}{4\pi}\mathcal{R}^*\vartheta^{-1}\mathcal{R}c.$$

This is a direct consequence of (4.14) by choosing $\Gamma = Id$.

This chapter was dedicated to the introduction of the medical imaging scheme computerized tomography, considering both static and the more challenging case of time-varying objects. We now pass over to our main application of interest, namely magnetic particle imaging. We will see for a particular type of scanner that the geometry for MPI and CT is similar. The rest of this work is therefore focused on exploring a connection between the corresponding forward models, again for both static as well as dynamic specimen.

5. Magnetic Particle Imaging

Basic Principle: Magnetic particle imaging enables reconstruction of the spatial distribution of magnetic particles injected into the object under investigation via exploiting their non-linear magnetization response to changing magnetic fields.

In this chapter, we present the promising but still preclinical medical imaging modality *magnetic particle imaging*, introduced in Example 3.2, to some more extent. In contrast to the previous chapter, here we only regard static phantoms as we will consider time-dependent concentrations specifically in Chapter 7. We highly recommend to consult [113] and [115] for a detailed overview on MPI imaging principles, historical breakthroughs, as well as scanner types. Further review articles regarding magnetic particle imaging are e.g. given by [75] and [149].

MPI was established by Bernhard Gleich at the laboratory of Philips Research in Hamburg. The initial publication [63] by him and Jürgen Weizenecker, which appeared in 2005, has attracted attention across disciplines and led to the formation of dedicated research groups working to make MPI clinically applicable. In 2016, together with their team, Gleich and Weizenecker received the European Inventor Award in the category 'Industry' [1]. The authors of [191] managed to visualize a beating mouse heart based on first in vivo 3D measurements. This proved the ability of MPI to image living organisms. Bruker Biospin MRI GmbH and Magnetic Insight independently produced first commercial MPI scanners fostering investigations regarding the potential of this newly developed imaging concept.
Features such as high temporal and spatial resolution, quantifiability, and non-usage of ionizing radiation [113] make MPI auspicious for various applications comprising both imaging as well as treatment. Examples include cancer detection ([3], [194]), instrument tracking [74] and guidance [160], bolus ([97], [154], [186]) and cell ([33], [196]) tracking, magnetic hyperthermia ([90], [143]), as well as long term monitoring ([134], [153]). We refer to [13] for a review on applications and safety considerations with respect to the usage of magnetic nanoparticles.

MPI relies on the non-linear magnetization response of magnetic particles to changing magnetic fields. We will see that the magnetization curve features a highly sensitive area right around zero. Increasing the magnetic field strength eventually results in a saturation magnetization. This is exploited by applying a combination of a static selection field including a low-field volume (LFV) and a spatially constant but timely changing drive-field steering the LFV through the region of interest. Therewith, only particles in close vicinity to the LFV are contributing to the signal, while all others remain in magnetic saturation. Shifting the LFV allows gathering information for numerous positions within the field of view (FOV).
Various scanner implementations have been introduced since the invention of MPI aiming at enlarging the FOV, reducing the energy consumption, and so forth. Enlarging the field of view is important in order to be able to apply MPI to human-sized objects. For instance, single-sided scanner were suggested ([148], [163]) allowing specimen of arbitrary size. The authors of [187] pro-

[1] https://www.epo.org/en/news-events/press-centre/press-release/2016/451588

posed traveling wave MPI using a new low energy gradient system for field generation. A modular simulation framework for MPI is presented in [103].
As mentioned in Example 3.2, MPI does not rely on properties of the object itself and thus does not yield any morphological information. An advantage is that MPI offers high contrast images due to missing tissue background signals. Nevertheless, in order to locate the particle concentration within the body, additional scans with a different imaging modality become necessary. Therefore, hybrid scanning devices are extremely beneficial as they prevent repositioning of the phantom while providing both quantitative information on the tracer concentration and morphological insights. Hybrid MPI-MRI imaging instrumentation is presented in [59] and [184]. The first hybrid MPI-CT scanner is introduced in [185].
As mentioned above, a selection field featuring a so-called low-field volume is applied to the region of interest to ensure that spatial information about the particles' positions is encoded in the data. This gives rise to another differentiation of MPI devices based on the shape of the LFV. The initial publication [63] used a field-free point. Later, a field-free line [190] was suggested, which is the encoding scheme we will consider in this work.
The first FFL devices were developed by [12] and [66]. The former enabled electromagnetic line rotation and translation. The latter introduced an x-space projection MPI scanner, with FFL motion perpendicular to itself. Insights regarding a small-bore field-free line imager are available at [136] presenting the open-source project OS-MPI. The scanning geometries for the FFL scanner and CT are very similar. Thus, the aforementioned hybrid MPI-CT scanner becomes even more attractive. A Fourier slice theorem for the MPI-FFL setting was proven in [114]. Especially, they were able to trace back MPI data to the Radon transform of the particle concentration for an idealized setting. Likewise, this link was shown in [31] based on their 3D model, which is valid for changing fields approximately parallel to their velocity field. Therewith, we are now able to formulate the goal of this thesis. Namely, we aim to investigate the connection of MPI and Radon data for different setup assumptions covering dynamic particle concentrations (Chapter 7) and magnetic field imperfections (Chapter 8). This enables access to theory and methods from the well-known computerized tomography. The authors of [119] stated the first experimental results for projection reconstruction and proved practicability of FBP reconstruction in the context of MPI.

Outline of the chapter: Section 5.1 deals with the derivation of the forward model for magnetic particle imaging first in general and afterwards for the specific case of field-free line scanning. We state a link between MPI and Radon data in three dimensions and obtain the corresponding result of [114] by restriction to a two dimensional setting. Afterwards, following the just mentioned work by Tobias Knopp et al., we review the sequential reconstruction of Radon data and particle concentration in Section 5.2. In contrast, we propose a joint reconstruction of particle concentration and corresponding Radon data by means of total variation regularization. We consider existence, stability, and consistency results for this approach and conclude with stating first numerical results comparing the presented reconstruction schemes.

5.1. Forward model

In order to describe magnetic particle imaging mathematically, we now derive the according inverse problem $\mathcal{A}c = g$. To this end, we need to specify the data acquisition process as well as the physical properties and principles relating the searched-for particle distribution c with the data g, which correspond to voltage signals detected in dedicated receive coils.

5.1.1. General scanner

Unless otherwise mentioned, we refer to [113] for the following introduction of the general signal equation.

As starting point, we regard the tracer being injected into the patient's body. It consists of particles in the nanometer range featuring a magnetic core and a non-magnetic coating. Appropriate choice of the coating allows negligence of particle-particle interactions for clinical particle concentrations and prevents agglomeration. The performance of MPI is firmly linked to the suitability of the used tracer. It effects characteristics like spatial resolution and sensitivity. In addition, the particles must be biocompatible. Experience and availability of contrast agents from MRI are useful. In particular, clinically approved tracer are needed to move MPI from its preclinical stage into clinical trials. Therefore, MRI tracer that are suitable for MPI, such as Resotran® [87], are of great interest, also in view of hybrid systems combining both techniques. Nevertheless, the study of specially tuned magnetic particles can enhance the quality of MPI results [56]. In [131] the performance of a self-synthesized tracer is compared to commercial ones from MRI. For further aspects regarding tracer, we refer e.g. to [9].
The reaction of a single particle to an applied field is determined by its magnetic moment $\mathbf{m}_i$. The reaction of a collection of N particles is then set by the sum of their magnetic moments. Accordingly, the magnetization $\mathbf{M}$ is defined as the sum of all magnetic moments per volume ΔV

$$\mathbf{M} := \frac{1}{\Delta V} \sum_{i=1}^{N} \mathbf{m}_i.$$

The effect of an external magnetic field $\mathbf{H}$ on the particles' magnetization is visualized in Figure 5.1 for varying field strengths. Without applying a magnetic field, the particles' magnetic moments are oriented randomly on the basis of Brownian motion. Exposing the tracer material to a magnetic field, their moments start to align with this external field resulting in a non-zero magnetization pointing in the same direction. Starting from zero, the magnetization changes rapidly with increasing magnetic field strength. Eventually, the curve flattens out and enters the saturation area. This can be explained considering again the magnetic moments of the particles. With increasing field strength, more and more magnetic moments are oriented according to the outer field until finally every moment will point in the same direction. Thus, further increasing the field strength will not change the magnetization. This will be exploited to encode spatial information of the tracer material in the data.
The magnetization $\mathbf{M}$ depends linearly on the concentration c

$$\mathbf{M} = c\,\overline{\mathbf{m}}, \quad c := \frac{N}{\Delta V}, \quad \overline{\mathbf{m}} := \frac{1}{N} \sum_{i=1}^{N} \mathbf{m}_i, \tag{5.1}$$

linked via the mean magnetization $\overline{\mathbf{m}}$. For continuous considerations ΔV is set to be infinitesimal small. Regarding a discrete setting it corresponds to the voxel volume.

So far, we have been concerned with the reconstruction goal, i.e. determining the particle distribution c, and first associated physical properties. Next, we clarify how these properties can be exploited to construct a data acquisition scheme resulting in measurements containing sufficient information for reliable recovery of c. Therewith, we can derive both the given data g and the forward model A of the inverse problem describing MPI.

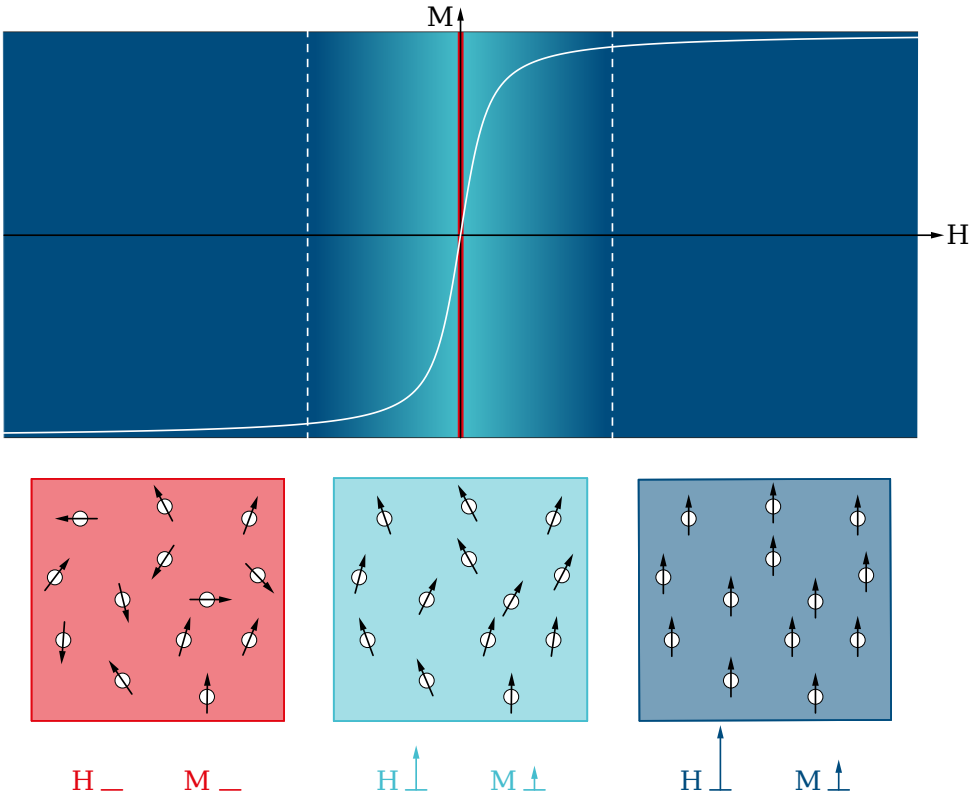

Figure 5.1.: Visualization of the alignment of magnetic moments in an applied field (inspired by Figure 2.4 in [53]): The upper image shows the signed modulus of the magnetization $\mathbf{M}$ in dependence of the signed modulus of the applied magnetic field strength $\mathbf{H}$. The sign is related to the direction of the magnetic field. The red color indicates a zero field, turquoise represents a low-field region where the magnetization is highly sensitive, and dark blue corresponds to an increased magnetic field strength resulting in saturation magnetization. The lower part of the figure shows the orientation of the magnetic moments, which become more and more aligned with the applied magnetic field as its field strength increases (from left to right) until all moments point in the same direction.

Magnetic particle imaging builds on the theory of electrodynamics, which itself builds on the Maxwell equations. One of these is *Faraday's law of induction*

$$\nabla \times \mathbf{E} = -\frac{\partial \mathbf{B}}{\partial t} \tag{5.2}$$

stating that a temporal change in the magnetic flux density $\mathbf{B}$ results in a spatial change in the electric field strength $\mathbf{E}$ and vice versa. This mutual interference can be tracked by measuring the induced voltage via a receive coil e.g. made of a single wire loop surrounding an area S (Figure 5.2). Transforming (5.2) into integral form creates the corresponding connection to the voltage signal u

$$u(t) = \oint_{\partial S} \mathbf{E}(\mathbf{l}, t) \cdot \mathrm{d}\,\mathbf{l} = -\frac{\mathrm{d}}{\mathrm{d}t} \int_S \mathbf{B}(\mathbf{r}, t) \cdot \mathrm{d}\,\mathbf{A}. \tag{5.3}$$

The magnetic flux density $\mathbf{B} = \mu_0 (\mathbf{M} + \mathbf{H})$ is related to the magnetization $\mathbf{M}$ and the magnetic field strength $\mathbf{H}$ via the permeability of free space $\mu_0 = 4\pi \cdot 10^{-7}\,\mathrm{TA^{-1}m}$. Inserting this relation into (5.3) results in

$$u(t) = -\mu_0 \frac{\mathrm{d}}{\mathrm{d}t} \int_S \mathbf{M}(\mathbf{r}, t) \cdot \mathrm{d}\,\mathbf{A} - \mu_0 \frac{\mathrm{d}}{\mathrm{d}t} \int_S \mathbf{H}(\mathbf{r}, t) \cdot \mathrm{d}\,\mathbf{A} =: u^M(t) + u^H(t). \tag{5.4}$$

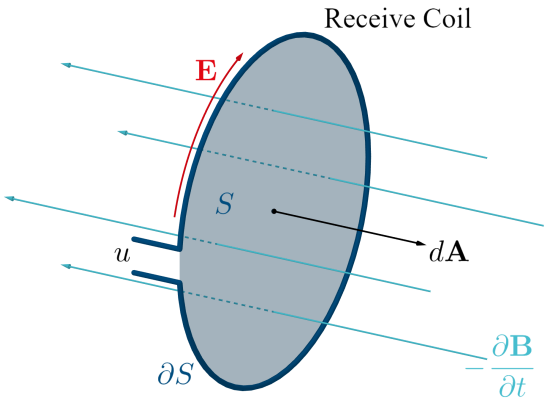

Figure 5.2.: Visualization of Faraday's law of induction (cf. Figure 2.13 in [113]): A changing magnetic field (turquoise) generates an electric field (red). The corresponding induced voltage signal u is measured via a single loop receive coil (dark blue) with surface S.

For details concerning the fundamentals of electrodynamics, we refer to [70]. Remember that the magnetization depends linearly on the particle concentration. Hence, equation (5.4) links a physical instance, which can be measured, to our reconstruction goal and a possible choice for the data is to set $g = u$. However, the voltage signal stems not only from the particles' magnetization response to the excitation field. The applied field itself influences the measurements by the additional component u^H. Further, due to practical constraints on the analog-to-digital converter and as the direct feedthrough of the excitation field is orders of magnitudes higher than the particle signal, it is not possible to clear the total voltage u by simply subtracting the induced signal resulting from an empty measurement. Thus, the signal originating from the outer field needs to be removed *before* conversion to digital. This can be accomplished by regarding the signal in Fourier space and choosing a time-dependent excitation field with small bandwidth, e.g. a sinusoidal signal leading to a spectrum containing only a single frequency. Due to the non-linear magnetization response, the particle induced signal is built by a broad range of harmonics and utilizing a band-stop filter before digitization allows it to be accessed alone. Note that application of the band-stop filter not only removes the direct feedthrough of the excitation field but also the first harmonic of the particle signal. For the sake of simplicity, in the remainder we assume $g = u^M$ keeping the actual signal filtering within the data acquisition process in mind. Please consult [113] for further aspects and insights.

After we have specified which quantity c we are looking for based on given data g, we finally aim to define the forward operator $\mathcal{A}$ connecting both. According to the law of reciprocity, the particle induced voltage signal can be determined equivalently as

$$u^M(t) = -\mu_0 \frac{\mathrm{d}}{\mathrm{d}t} \int_{\mathbb{R}^3} \mathbf{M}(\mathbf{r},t) \cdot \mathbf{p}(\mathbf{r}) \,\mathrm{d}\mathbf{r} \overset{(5.1)}{=} -\mu_0 \frac{\mathrm{d}}{\mathrm{d}t} \int_{\mathbb{R}^3} c(\mathbf{r})\, \overline{\mathbf{m}}(\mathbf{r},t) \cdot \mathbf{p}(\mathbf{r}) \,\mathrm{d}\mathbf{r} \tag{5.5}$$

with receive coil sensitivity $\mathbf{p}$. Hence, we set

$$\mathcal{A}c(t) := -\mu_0 \int_{\mathbb{R}^3} c(\mathbf{r}) \frac{\partial}{\partial t} \overline{\mathbf{m}}(\mathbf{r},t) \cdot \mathbf{p}(\mathbf{r}) \,\mathrm{d}\mathbf{r} = u^M(t) = g(t)\,. \tag{5.6}$$

Thus, the system function introduced in Example 3.2 is given as $s(\mathbf{r},t) = \frac{\partial}{\partial t} \overline{\mathbf{m}}(\mathbf{r},t) \cdot \mathbf{p}(\mathbf{r})$. Let $T > 0$ be the total measurement time. Assuming the particle concentration $c : \mathbb{R}^3 \to \mathbb{R}_0^+$ and system function $s : \mathbb{R}^3 \times [0,T] \to \mathbb{R}$ to be square-integrable, equation (5.6) is well-defined. In the following, for convenience, we neglect the superscript and only write u for the particle signal.

Approaches for determining the system function can be categorized into two groups, measurement- and model-based. The measurement-based approach, used for instance in the first MPI publication [63], applies a calibration scan. Positioning a small delta probe of known concentration at each voxel position, the system matrix describing a discretized forward operator can be obtained. Since an MPI scan must be performed for each position of the delta probe, the measurement-based approach is time-consuming and memory-intensive. Importantly, even changing a single parameter would require a new calibration scan, making this approach severely cumbersome. However, it inherently incorporates the complex particle dynamics when being exposed to changing magnetic fields. The model-based approach (initiated by [117]), on the other hand, gives flexibility, as changes in the measurement setup and different grid sizes can be included without an arduous calibration scan. The development of models that accurately describe the complex particle dynamics is an ongoing challenge. Example works aiming to improve the modeling quality comprise ([2], [111], [189]). Furthermore, the authors of [101] relate modeling the system function to an inverse parameter identification problem and ([12], [45]) took relaxation effects into account. A survey paper regarding mathematical modeling of the signal chain is given by [109]. In [146] the RESESOP-Kaczmarz method introduced in [17] is considered for coping with model uncertainties.
In this work, we use the Langevin theory of paramagnetism to model the magnetization reaction. While still representing the state of the art, this is known to be no suitable model as it grounds on the assumption that particles are in thermal equilibrium. Considering the Langevin function

$$\mathcal{L}: \mathbb{R} \to [-1,1], \quad \mathcal{L}(\lambda) := \begin{cases} \coth(\lambda) - \frac{1}{\lambda} & , \lambda \neq 0, \\ 0 & , \lambda = 0, \end{cases} \tag{5.7}$$

according to [114] the mean magnetic moment can then be written in terms of the magnetic moment of a single particle m, the Boltzmann constant k_{B}, and the particle temperature T_p

$$\overline{\mathbf{m}}(\mathbf{r},t) = \overline{m}(\|\mathbf{H}(\mathbf{r},t)\|)\frac{\mathbf{H}(\mathbf{r},t)}{\|\mathbf{H}(\mathbf{r},t)\|}, \quad \overline{m}(H) = m\mathcal{L}\left(\frac{\mu_0 m}{k_{\mathrm{B}}T_p}H\right). \tag{5.8}$$

Next, we need to specify the data acquisition process in MPI. More precisely, the question is how to choose the magnetic fields in order to guarantee information about the particles' position to be encoded in the measurements. This makes it possible to determine not only the presence of magnetic material in the scanned area, but also its spatial distribution.

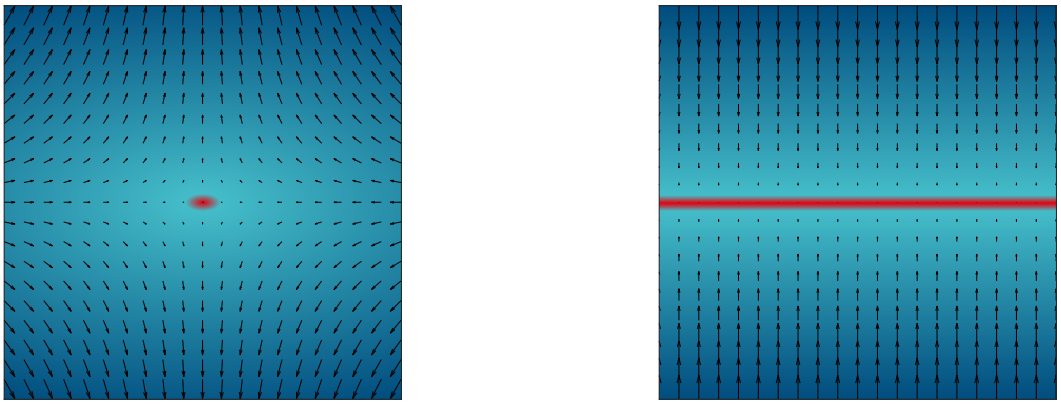

Figure 5.3.: Visualization of the selection field: Imaged is a selection field featuring a field-free point (left) or a field-free line (right) centering the low-field volume. Arrows specify the field direction and color indicates the modulus of the magnetic field strength. Strong red corresponds to zero field and values are increasing as color changes from red over turquoise to dark blue.

Exploiting the specific shape of the magnetization response, a suitable static, inhomogeneous *selection field* $\mathbf{H}_S$ is applied. This allows to distinct the particles' magnetic response to an additionally applied time-dependent, homogeneous *drive field* $\mathbf{H}_D$ in correspondence to their position within the field. Thereby, the field construction is based on the fact that particles levitated into magnetic saturation by the selection field react differently to a superimposed changing magnetic field than those located in a LFV, i.e. a highly sensitive region. Currently, two different choices for the selection field, visualized in Figure 5.3, are available. In its initial publication [63] a field featuring a *field-free point* centering the LFV was used. Later, in [190] using a *field-free line* instead was suggested. Note that the FFP cannot be radially symmetric considering all three dimensions as is explained by the Maxwell equations. For data acquisition, the LFV is moved through the FOV. The steering takes place via the time-varying drive field. MPI performance for several trajectories is investigated in [112] for an FFP and in [178] for an FFL scanner. In its original proposal [190], the FFL oscillates rapidly through the FOV while rotating slowly leading to a scanning geometry that looks like a rosette and is regarded in Chapter 6.

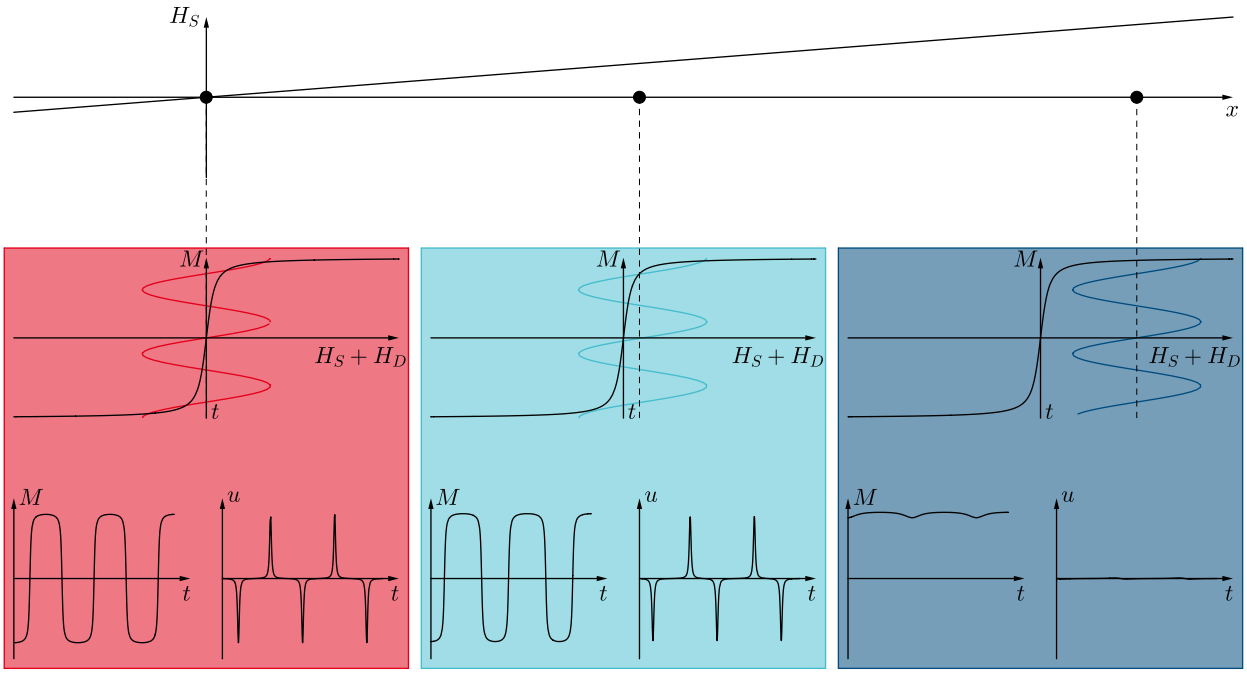

Figure 5.4.: Visualization of spatial encoding (inspired by Figure 2.11 in [53]): The top shows, in one dimension, a linear gradient selection field with a field-free point at the origin. The particle response to an additional sinusoidal excitation field is imaged at the bottom for three different particle positions within the selection field. For a particle located at the FFP, the positive and negative parts of the magnetization response are of the same magnitude and width (red box). Considering a particle in the positive magnetic field strength region, the negative components of the magnetization are narrower. As a result, the peaks of the voltage signal are no longer equidistant (turquoise box). A particle located within the positive saturation area, gives a positive magnetization signal that hardly changes (dark blue box). Since the voltage signal is proportional to the negative magnetization change, information about the location is encoded in the data. The voltage peaks differ in height and spacing as a function of location. Particles in magnetic saturation barely contribute to the voltage signal.

Figure 5.4 illustrates the generated signal of particles located at three different positions within the selection field (in one dimension) for a sinusoidal excitation field. Particles in magnetic saturation hardly contribute to the voltage signal. Shifting a particle in the direction of the FFP, the voltage peaks change in magnitude and spacing. Only particles in the FFP show equidistant peaks.

Considering the magnetic field along one axis, the FFP-based selection field can be described via $H_S(x) = -Gx$ with gradient strength G specifying the width of the low-field. Without loss of generality we assume $G > 0$. Adding a drive field $H_D(t) = A\cos(2\pi f_\mathrm{d}\, t)$ with drive peak amplitude $A > 0$, drive frequency $f_\mathrm{d} > 0$, and time $t \in [0, T]$, the total magnetic field is given as

$$H(x,t) = H_\mathrm{S}(x) + H_\mathrm{D}(t) = -Gx + A\cos(2\pi f_\mathrm{d}\, t)\,.$$

Computing the zeros gives the FFP position $\mathrm{FFP}(t) := \frac{A}{G}\cos(2\pi f_\mathrm{d}\, t)$, which oscillates in the interval $\left[-\frac{A}{G}, \frac{A}{G}\right]$. It becomes obvious that the choice of parameters A, G, and f_d influences important characteristics as FOV size, resolution, and scan time. One of the aspects to consider is that increasing the gradient strength G makes the LFV sharper, resulting in a higher resolution, but also fewer particles contribute to the signal, which reduces the signal-to-noise ratio (SNR). In addition, the size of the FOV is reduced. For static concentrations, the SNR can be increased at the expense of measurement time via averaging voltage signals obtained by multiple scans of the same setting, but the FOV size is limited by safety concerns regarding the choice of the drive peak amplitude. These comprise peripheral nerve stimulation (PNS) and heating ([23], [162], [166]). A typical FOV size concerning these limitations would be $10 \times 10 \times 5\ \mathrm{mm}^2$ for humans [22]. To make MPI applicable for clinical usage FOV enlargement is thus necessary. For this purpose, so-called focus fields were introduced, which enable an extended scanning area by capturing data patch-wise (e.g. [64], [167]). A further step towards clinical application is the presentation of a human-sized brain scanner [67].

In this work, we are devoted to field-free line magnetic particle imaging. Before we turn to this specific scanner type in the next section, we once more recommend to consult [113]. It not only describes the physical principles, but also imparts knowledge about practical implementation.

5.1.2. FFL scanner

Using a field-free line instead of an FFP for spatial encoding was first suggested in [190]. We refer to [29] and [53] for further information and practical insights. Since the FFL scanning scheme applies a larger LFV, more particles can contribute to the signal, which leads to an increase in SNR and thus sensitivity. Technical feasibility was proven in [54]. Another highly interesting property is that scanning geometries for the FFL scanner and computerized tomography look similar and well-established theory and reconstruction methods of CT may be applicable. We now transform the forward model (5.6) to this special case and state a first link to the Radon transform of the particle concentration.

Introducing the gradient matrix $\mathbf{G} \in \mathbb{R}^{3\times 3}$, the selection field can be modeled as $\mathbf{H}_\mathrm{S}(\mathbf{r}) = \mathbf{G}\,\mathbf{r}$. For example, the choice

$$\mathbf{G} = G\begin{pmatrix} 0 & 0 & 0 \\ 0 & -1 & 0 \\ 0 & 0 & 1 \end{pmatrix}$$

leads to an FFL along the x-axis as was imaged in Figure 5.3. Again, $G > 0$ denotes the gradient strength determining the width of the LFV. Applying the rotation matrix $\mathbf{R}^\varphi$ and further defining the orthonormal vectors $\mathbf{e}_\varphi$, $\mathbf{e}_\varphi^\perp$, and $\mathbf{e}_z$

$$\mathbf{R}^\varphi = \begin{pmatrix} \cos\varphi & -\sin\varphi & 0 \\ \sin\varphi & \cos\varphi & 0 \\ 0 & 0 & 1 \end{pmatrix}, \quad \mathbf{e}_\varphi = \begin{pmatrix} -\sin\varphi \\ \cos\varphi \\ 0 \end{pmatrix}, \quad \mathbf{e}_\varphi^\perp = -\begin{pmatrix} \cos\varphi \\ \sin\varphi \\ 0 \end{pmatrix}, \quad \mathbf{e}_z = \begin{pmatrix} 0 \\ 0 \\ 1 \end{pmatrix},$$

a selection field featuring an FFL through the origin within the xy-plane and angle φ to the x-axis can be expressed as (cf. [114])

$$\mathbf{H}_{\mathrm{S}}(\mathbf{r},\varphi) = \mathbf{R}^{\varphi}\,\mathbf{G}\,\mathbf{R}^{-\varphi}\,\mathbf{r} = -G\,(\mathbf{r}\cdot\mathbf{e}_{\varphi})\,\mathbf{e}_{\varphi} + G\,(\mathbf{r}\cdot\mathbf{e}_{z})\,\mathbf{e}_{z}.$$

Thereby, we exploited that for $\mathbf{r} = (x,y,z)^{T}$ it holds

$$\mathbf{R}^{\varphi}\,\mathbf{r} = -x\,\mathbf{e}_{\varphi}^{\perp} + y\,\mathbf{e}_{\varphi} + z\,\mathbf{e}_{z}, \quad (\mathbf{R}^{\varphi})^{-1}\,\mathbf{r} = \mathbf{R}^{-\varphi}\,\mathbf{r} = \left(-\mathbf{r}\cdot\mathbf{e}_{\varphi}^{\perp}, \mathbf{r}\cdot\mathbf{e}_{\varphi}, \mathbf{r}\cdot\mathbf{e}_{z}\right)^{T}. \tag{5.9}$$

The aforementioned *simultaneous line rotation*, which leads to a rosette-shaped scanning geometry, is examined in Chapter 6. In this section, we consider a *sequential line rotation*. During measurements the FFL is translated through the FOV and in between measurements the FFL is rotated such that its trajectory forms a star as can be seen in Figure 5.5a.

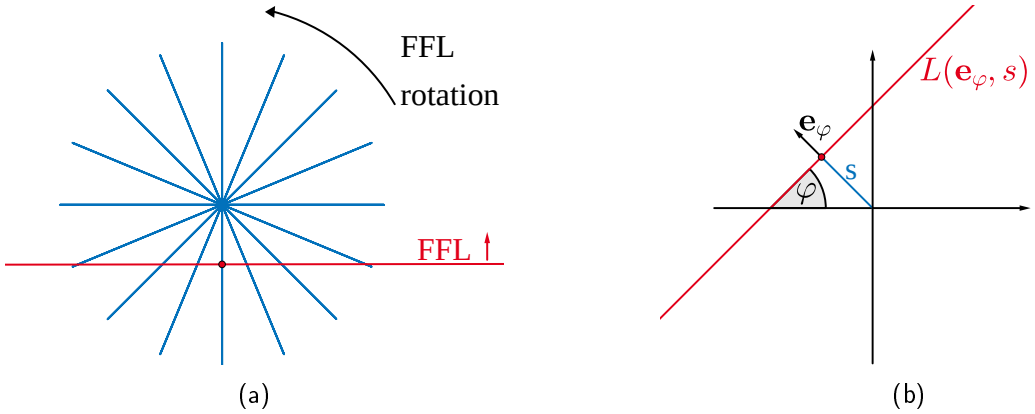

Figure 5.5.: Visualization of the sequential line rotation scanning geometry: (a) During measurement, the FFL is translated through the FOV. It is rotated between scans. (b) Line geometry. The FFL is uniquely defined by the angle φ between line and x-axis as well as the FFL's signed distance s to the origin.

This geometry can be achieved by superimposing an additional drive field

$$\mathbf{H}_{\mathrm{D}}(\varphi,t) = A\,\Lambda_{\varphi}(t)\,\mathbf{e}_{\varphi}$$

with drive peak amplitude $A > 0$ and excitation function $\Lambda_{\varphi}:\ [0,T] \to [-1,1]$ to the selection field. The measurement time per angle is fixed to be $T > 0$. The total magnetic field is thus

$$\mathbf{H}(\mathbf{r},\varphi,t) = (-G\,\mathbf{r}\cdot\mathbf{e}_{\varphi} + A\,\Lambda_{\varphi}(t))\,\mathbf{e}_{\varphi} + G\,(\mathbf{r}\cdot\mathbf{e}_{z})\,\mathbf{e}_{z} =: f_{\varphi}\,(\mathbf{r},t)\ \mathbf{e}_{\varphi} + f_{z}\,(\mathbf{r})\ \mathbf{e}_{z}. \tag{5.10}$$

Computation of the nulls results in the definition of the corresponding field-free line

$$\mathrm{FFL}\,(\varphi,t) = L\,(\mathbf{e}_{\varphi}, s_{\varphi,t}) = \left\{\mathbf{r}\in\mathbb{R}^{3}:\ \mathbf{r}\cdot\mathbf{e}_{\varphi} = s_{\varphi,t},\ \mathbf{r}\cdot\mathbf{e}_{z} = 0\right\}, \quad s_{\varphi,t} := \frac{A}{G}\,\Lambda_{\varphi}\,(t)\,,$$

visualized in Figure 5.5b. Please compare with (4.2) in the CT section.

Remark 5.1. *To obtain the star-shaped scanning geometry, we assume for fixed $\varphi \in [0,2\pi]$ that Λ_{φ} is continuous covering the entire interval $[-1,1]$ as well as it is either strictly monotonically increasing or decreasing on $(0,T)$.*

The results below are independent of this assumption and various scanning geometries can be created. Remember e.g. that the SNR can be increased by oscillating the FFL through the FOV rather than performing a single translation per angle. What we need, however, is that the excitation function is differentiable with respect to time. We denote the corresponding derivative as Λ'_φ.

Looking at Figure 5.5 with FFLs replaced by X-rays, similarities between the field-free line and the CT scanning geometry become obvious. While for CT a whole set of X-rays can be emitted, for MPI only one FFL per time step is available. Due to the geometric resemblance of the scanning processes and because only particles near the FFL contribute to the voltage signal, the question arose whether MPI-FFL data can be traced back to the Radon transform of the particle concentration. This would make the extensive results and methods of the well-known medical imaging technique CT accessible for the rather new modality MPI. We obtain the theorem below by introducing $c_z : \mathbb{R}^2 \to \mathbb{R}_0^+$ as

$$c_z(x,y) := c(x,y,z).$$

Theorem 5.2. *For magnetic fields as given in (5.10) as well as spatially homogeneous receive coil sensitivity* $\mathbf{p}(\mathbf{r}) = \mathbf{p}$*, signal equation (5.5) can be written as*

$$u(\varphi,t) = -\mu_0\, \mathbf{e}_\varphi \cdot \mathbf{p}\, \frac{\partial}{\partial t} \int_{\mathbb{R}} \left[k_z^1 * \mathcal{R}c_z(\mathbf{e}_\varphi,\cdot)\right](s_{\varphi,t})\, \mathrm{d}\, z - \mu_0\, \mathbf{e}_z \cdot \mathbf{p}\, \frac{\partial}{\partial t} \int_{\mathbb{R}} \left[k_z^2 * \mathcal{R}c_z(\mathbf{e}_\varphi,\cdot)\right](s_{\varphi,t})\, \mathrm{d}\, z, \tag{5.11}$$

with convolution kernels

$$k_z^1(s) := \frac{s}{\sqrt{s^2+z^2}}\, \overline{m}\left(G\sqrt{s^2+z^2}\right), \quad k_z^2(s) := \frac{z}{\sqrt{s^2+z^2}}\, \overline{m}\left(G\sqrt{s^2+z^2}\right).$$

Proof. We insert the specific field (5.10) into the mean magnetization modeled via the Langevin theory of paramagnetism (5.8). For convenience, we set $f_{\varphi,z}(\mathbf{r},t) := \sqrt{f_\varphi^2(\mathbf{r},t) + f_z^2(\mathbf{r})}$ and obtain

$$\overline{\mathbf{m}}(\mathbf{r},\varphi,t) = \overline{m}(\|\mathbf{H}(\mathbf{r},\varphi,t)\|)\, \frac{\mathbf{H}(\mathbf{r},\varphi,t)}{\|\mathbf{H}(\mathbf{r},\varphi,t)\|} = \overline{m}(f_{\varphi,z}(\mathbf{r},t))\, \frac{f_\varphi(\mathbf{r},t)\, \mathbf{e}_\varphi + f_z(\mathbf{r})\, \mathbf{e}_z}{f_{\varphi,z}(\mathbf{r},t)}.$$

Hence, the signal equation (5.5) transforms to

$$\begin{aligned} u(\varphi,t) =& -\mu_0 \frac{\partial}{\partial t} \int_{\mathbb{R}^3} c(\mathbf{r})\, \overline{\mathbf{m}}(\mathbf{r},\varphi,t) \cdot \mathbf{p}(\mathbf{r})\, \mathrm{d}\,\mathbf{r} \\ =& -\mu_0 \frac{\partial}{\partial t} \int_{\mathbb{R}^3} c(\mathbf{r})\, \frac{f_\varphi(\mathbf{r},t)}{f_{\varphi,z}(\mathbf{r},t)}\, \overline{m}(f_{\varphi,z}(\mathbf{r},t))\, \mathbf{e}_\varphi \cdot \mathbf{p}(\mathbf{r})\, \mathrm{d}\,\mathbf{r} \\ & -\mu_0 \frac{\partial}{\partial t} \int_{\mathbb{R}^3} c(\mathbf{r})\, \frac{f_z(\mathbf{r})}{f_{\varphi,z}(\mathbf{r},t)}\, \overline{m}(f_{\varphi,z}(\mathbf{r},t))\, \mathbf{e}_z \cdot \mathbf{p}(\mathbf{r})\, \mathrm{d}\,\mathbf{r}. \end{aligned}$$

Proceeding similar to [114], we assume a spatially homogeneous receive coil sensitivity $\mathbf{p}(\mathbf{r}) = \mathbf{p}$ and rotate the coordinate system such that the x-axis gets parallel to the FFL, i.e. we substitute $\mathbf{r}' = (v', s', z)^T := \mathbf{R}^{-\varphi}\, \mathbf{r}$, yielding

$$\begin{aligned} u(\varphi,t) =& -\mu_0\, \mathbf{e}_\varphi \cdot \mathbf{p}\, \frac{\partial}{\partial t} \int_{\mathbb{R}^3} c\left(\mathbf{R}^\varphi \mathbf{r}'\right)\, \frac{f_\varphi(\mathbf{R}^\varphi \mathbf{r}', t)}{f_{\varphi,z}(\mathbf{R}^\varphi \mathbf{r}', t)}\, \overline{m}\left(f_{\varphi,z}\left(\mathbf{R}^\varphi \mathbf{r}', t\right)\right)\, \mathrm{d}\,\mathbf{r}' \\ & -\mu_0\, \mathbf{e}_z \cdot \mathbf{p}\, \frac{\partial}{\partial t} \int_{\mathbb{R}^3} c\left(\mathbf{R}^\varphi \mathbf{r}'\right)\, \frac{f_z(\mathbf{R}^\varphi \mathbf{r}')}{f_{\varphi,z}(\mathbf{R}^\varphi \mathbf{r}', t)}\, \overline{m}\left(f_{\varphi,z}\left(\mathbf{R}^\varphi \mathbf{r}', t\right)\right)\, \mathrm{d}\,\mathbf{r}'. \end{aligned}$$

Exploiting (5.9), we redefine

$$\begin{aligned} f_z\left(\mathbf{R}^{\varphi}\mathbf{r}'\right) &= G\,\mathbf{R}^{\varphi}\mathbf{r}'\cdot\mathbf{e}_z = G\,z =: f_z, \\ f_{\varphi}\left(\mathbf{R}^{\varphi}\mathbf{r}',t\right) &= -G\,\mathbf{R}^{\varphi}\mathbf{r}'\cdot\mathbf{e}_{\varphi} + A\,\Lambda_{\varphi}(t) = -G\,s' + A\,\Lambda_{\varphi}(t) = G\,\left(s_{\varphi,t}-s'\right) =: f_{\varphi}\left(s',t\right), \\ f_{\varphi,z}\left(\mathbf{R}^{\varphi}\mathbf{r}',t\right) &= \sqrt{f_{\varphi}^2\left(\mathbf{R}^{\varphi}\mathbf{r}',t\right)+f_z^2\left(\mathbf{R}^{\varphi}\mathbf{r}'\right)} = G\sqrt{\left(s_{\varphi,t}-s'\right)^2+z^2} =: f_{\varphi,z}\left(s',t\right). \end{aligned}$$

Therewith, we arrive at

$$\begin{aligned} u\left(\varphi,t\right) = &-\mu_0\,\mathbf{e}_{\varphi}\cdot\mathbf{p}\,\frac{\partial}{\partial t}\int_{\mathbb{R}}\int_{\mathbb{R}}\int_{\mathbb{R}} c_z\left(-v'\,\mathbf{e}_{\varphi}^{\perp}+s'\,\mathbf{e}_{\varphi}\right)\,\frac{f_{\varphi}\left(s',t\right)}{f_{\varphi,z}\left(s',t\right)}\,\overline{m}\left(f_{\varphi,z}\left(s',t\right)\right)\,\mathrm{d}\,v'\,\mathrm{d}\,s'\,\mathrm{d}\,z \\ &-\mu_0\,\mathbf{e}_z\cdot\mathbf{p}\,\frac{\partial}{\partial t}\int_{\mathbb{R}}\int_{\mathbb{R}}\int_{\mathbb{R}} c_z\left(-v'\,\mathbf{e}_{\varphi}^{\perp}+s'\,\mathbf{e}_{\varphi}\right)\,\frac{f_z}{f_{\varphi,z}\left(s',t\right)}\,\overline{m}\left(f_{\varphi,z}\left(s',t\right)\right)\,\mathrm{d}\,v'\,\mathrm{d}\,s'\,\mathrm{d}\,z. \end{aligned}$$

Utilizing the Definition 4.1 of the Radon transform results in

$$\begin{aligned} u\left(\varphi,t\right) = &-\mu_0\,\mathbf{e}_{\varphi}\cdot\mathbf{p}\,\frac{\partial}{\partial t}\int_{\mathbb{R}}\int_{\mathbb{R}}\mathcal{R}c_z\left(\mathbf{e}_{\varphi},s'\right)\,\underbrace{\frac{\left(s_{\varphi,t}-s'\right)}{\sqrt{\left(s_{\varphi,t}-s'\right)^2+z^2}}\,\overline{m}\left(G\sqrt{\left(s_{\varphi,t}-s'\right)^2+z^2}\right)}_{k_z^1\left(s_{\varphi,t}-s'\right)}\,\mathrm{d}\,s'\,\mathrm{d}\,z \\ &-\mu_0\,\mathbf{e}_z\cdot\mathbf{p}\,\frac{\partial}{\partial t}\int_{\mathbb{R}}\int_{\mathbb{R}}\mathcal{R}c_z\left(\mathbf{e}_{\varphi},s'\right)\,\underbrace{\frac{z}{\sqrt{\left(s_{\varphi,t}-s'\right)^2+z^2}}\,\overline{m}\left(G\sqrt{\left(s_{\varphi,t}-s'\right)^2+z^2}\right)}_{k_z^2\left(s_{\varphi,t}-s'\right)}\,\mathrm{d}\,s'\,\mathrm{d}\,z. \end{aligned}$$

Exploiting Definition 2.8 this completes the proof. □

We examined the relation between MPI-FFL and Radon data for measurements within a plane. By analogously applying rotation matrices with respect to the other coordinate system defining planes and adapting the drive field accordingly, the FFL can be steered to any position within the $\mathbb{R}^3$. Additionally allowing simultaneous line rotation and translation, offers great freedom in the choice of the scanning trajectory. However, practical feasibility needs to be taken into account. It should be mentioned that the more time dependencies we allow in the choice of the sampling pattern, the more components we get within the signal equation when computing the time derivative.

Magnetic particle imaging is three dimensional by itself. Nevertheless, since for all our considerations we regard scanning geometries moving the FFL within the xy-plane, the problem can be reduced to a two dimensional setting (cf. [110]). To this end, we assume that all particles are located in the regarded plane such that we can express the tracer distribution as

$$c\left(x,y,z\right) = c_z\left(x,y\right)\delta\left(z\right).$$

Hence, exploiting $\overline{m}\left(-H\right) = -\overline{m}\left(H\right)$ the signal equation (5.11) simplifies to

$$u\left(\varphi,t\right) = -\mu_0\,\mathbf{e}_{\varphi}\cdot\mathbf{p}\,\frac{\partial}{\partial t}\left[\overline{m}\left(G\,\cdot\right) * \mathcal{R}c_{z=0}\left(\mathbf{e}_{\varphi},\cdot\right)\right]\left(s_{\varphi,t}\right). \tag{5.12}$$

For the remainder of this thesis, we consider this two dimensional setting. Therefore, we restrict the introduced matrices and basis vectors to suitable submatrices and subvectors

$$\mathbf{R}^{\varphi} = \begin{pmatrix}\cos\varphi & -\sin\varphi\\ \sin\varphi & \cos\varphi\end{pmatrix}, \quad \mathbf{e}_{\varphi} = \begin{pmatrix}-\sin\varphi\\ \cos\varphi\end{pmatrix}, \quad \mathbf{e}_{\varphi}^{\perp} = -\begin{pmatrix}\cos\varphi\\ \sin\varphi\end{pmatrix}. \tag{5.13}$$

Similar to before, it holds for $\mathbf{r} = (x, y)^T$

$$\mathbf{R}^{\varphi}\,\mathbf{r} = -x\,\mathbf{e}_{\varphi}^{\perp} + y\,\mathbf{e}_{\varphi}, \quad \left(\mathbf{R}^{\varphi}\right)^{-1}\,\mathbf{r} = \mathbf{R}^{-\varphi}\,\mathbf{r} = \left(-\mathbf{r}\cdot\mathbf{e}_{\varphi}^{\perp}, \mathbf{r}\cdot\mathbf{e}_{\varphi}\right)^T. \tag{5.14}$$

We obtain the two dimensional magnetic fields

$$\mathbf{H}(\mathbf{r}, \varphi, t) = \left(-G\,\mathbf{r}\cdot\mathbf{e}_{\varphi} + A\,\Lambda_{\varphi}(t)\right)\mathbf{e}_{\varphi}.$$

Therewith, the mean magnetization for an ideal FFL scanner can be written as

$$\overline{\mathbf{m}}\,(\mathbf{r}, \varphi, t) = \overline{m}\,\left(-G\,\mathbf{r}\cdot\mathbf{e}_{\varphi} + A\Lambda_{\varphi}(t)\right)\mathbf{e}_{\varphi}.$$

Voltage signals are not only measured in one receive coil, but in $L \in \mathbb{N}$ coils with sensitivity $\mathbf{p}_l : \mathbb{R}^2 \to \mathbb{R}^2$, for $l = 1, \ldots, L$. Usually L equals the regarded dimension, i.e. in our case $L = 2$. The receive coils are then chosen to be oriented orthogonal to each other. Please consult [113] for more information regarding receive coils and their sensitivity. For convenience, we define $Z_T := [0, 2\pi] \times [0, T]$. Like for tissue densities in Chapter 4, we assume the tracer material to be contained within the circle B_R of radius $R > 0$ around the origin, i.e. $\operatorname{supp}(c) \subset B_R \subset \mathbb{R}^2$ and consider the continuous extensions introduced in Remark 4.12 to be able to regard integrals over the whole $\mathbb{R}^2$.

Definition 5.3. *Define* $\mathcal{A}_l^{FFL} : L_2\left(B_R, \mathbb{R}_0^+\right) \to L_2\left(Z_T, \mathbb{R}\right)$ *to be*

$$\mathcal{A}_l^{FFL} c\,(\varphi, t) := -\mu_0 \int_{\mathbb{R}^2} c(\mathbf{r}) \frac{\partial}{\partial t} \overline{m}\,\left(-G\,\mathbf{r}\cdot\mathbf{e}_{\varphi} + A\Lambda_{\varphi}(t)\right)\mathbf{e}_{\varphi}\cdot\mathbf{p}_l\,(\mathbf{r})\;\mathrm{d}\,\mathbf{r}. \tag{5.15}$$

The forward operator for an MPI-FFL scanner is given as $\mathcal{A}^{FFL} : L_2\left(B_R, \mathbb{R}_0^+\right) \to L_2\left(Z_T, \mathbb{R}^L\right)$ *with* $\mathcal{A}^{FFL} c\,(\varphi, t) = \left\{\mathcal{A}_l^{FFL} c\,(\varphi, t)\right\}_{l=1,\ldots,L}$.

The forward operator is linear and bounded. Assume $\Lambda_{\varphi+\pi} = -\Lambda_{\varphi}$. Then, because $\overline{m}$ is odd and $\mathbf{e}_{\varphi+\pi} = -\mathbf{e}_{\varphi}$, it holds

$$\mathcal{A}_l^{\mathrm{FFL}} c\,(\varphi + \pi, t) = \mathcal{A}_l^{\mathrm{FFL}} c\,(\varphi, t)\,.$$

Hence, similar to CT it is adequate to gather data only for $\varphi \in [0, \pi]$. However, as already noted, further measurements can be taken to increase the SNR. Note that $\Lambda_{\varphi+\pi} = -\Lambda_{\varphi}$ is not necessary for the sufficiency of data covering a half circle, however, in this case it gets quite clear.

The above definition links the measured data $\mathbf{u} = \{u_l\}_{l=1,\ldots,L}$ with the searched-for particle distribution c. Therewith, the inverse problem we need to solve is

$$\mathcal{A}^{\mathrm{FFL}} c = \mathbf{u}.$$

According to [110], solving this problem might be less ill-posed than the one for an FFP scanner. Nevertheless, appropriate regularization methods are necessary for reliable reconstruction.
For the idealized setting considered here, i.e. straight lines centering the LFVs, magnetic fields being constant along lines parallel to this FFL, sequential line rotation, and static particle concentrations, we have already shown a relation between the voltage signal and the Radon data of the particle distribution in the three dimensional setting. Reduction to our two dimensional considerations, yields the following link between the forward operators of MPI-FFL and CT, which complies with the results of [31] and [114].

Theorem 5.4. *Given spatially homogeneous receive coil sensitivities* $\mathbf{p}_l(\mathbf{r}) = \mathbf{p}_l$*, the MPI-FFL forward operator with respect to the l-th receive coil* (5.15) *can be written as*

$$\mathcal{A}_l^{FFL} = \mathcal{K}_l \circ \mathcal{R} \tag{5.16}$$

with convolution operator $\mathcal{K}_l : L_2(Z, \mathbb{R}) \to L_2(Z_T, \mathbb{R})$*, for* $l \in \{1, \dots, L\}$*,*

$$\mathcal{K}_l f(\varphi, t) \quad = \quad -\mu_0 \, A\Lambda'_\varphi(t) \, \mathbf{e}_\varphi \cdot \mathbf{p}_l \left[\overline{m}'(G\,\cdot) * f(\mathbf{e}_\varphi, \cdot)\right] \left(\frac{A}{G}\Lambda_\varphi(t)\right).$$

Proof. The result follows directly from (5.12) computing

$$\frac{\partial}{\partial t}\left[\overline{m}(G\,\cdot) * \mathcal{R}c(\mathbf{e}_\varphi, \cdot)\right]\left(\frac{A}{G}\Lambda_\varphi(t)\right) = A\Lambda'_\varphi(t)\left[\overline{m}'(G\,\cdot) * \mathcal{R}c(\mathbf{e}_\varphi, \cdot)\right]\left(\frac{A}{G}\Lambda_\varphi(t)\right).$$

□

Using a sinusoidal excitation function, the FFL velocity decreases towards the edge of the FOV and reaches zero at inflection points. The last theorem therefore explains a potentially lower image quality with increasing distance from the origin (cf. [112]). Note that for particle diameters approaching infinity, the magnetization response becomes a step function. Accordingly, the derivative of the mean magnetization can be formulated via the dirac-δ-distribution and the forward operator is pointwise proportional to the Radon transform. However, choosing the particle size as large as practically possible is not reasonable since e.g. relaxation effects and specific applications constrain the diameter [113].

For the remainder of this thesis, we will always consider the field-free line encoding scheme. For the sake of simplicity, we will write briefly $\mathcal{A}_l$ refraining from indicating the choice of an FFL scanner. Next, we dedicate ourselves towards reconstruction of the particle concentration as well as corresponding Radon data. Let the excitation function Λ_φ be continuously differentiable for fixed $\varphi \in [0, 2\pi]$.

5.2. Reconstruction

Like for general inverse problems, there are many possible approaches to reconstruct the particle concentration. For the x-space formulation introduced in [65] for one dimensional FFP measurements, the reconstruction task can be formulated as a deconvolution. The signal equation can also be first discretized and written as matrix vector multiplication. Usually, this equation is regarded in Fourier space such that excitation signal components can be easily removed. For instance, according regularized normal equations can be solved iteratively. A popular method in MPI is to apply Kaczmarz approach due to its fast convergence as the system matrix rows are almost orthogonal [116]. Deep learning based image reconstruction is considered in [4]. For a further overview on existing methods to determine the particle concentration, we refer to [72] and [115].

The field-free line scanner is less explored than the FFP implementation. However, in [107] images obtained via inverse Radon transform based reconstruction are compared to results determined by applying Kaczmarz method for system matrix-based reconstruction regarding their open-sided FFL scanner prototype. Furthermore, similar to CT the Fourier slice theorem derived in [114] for the context of FFL-based MPI can be used to derive reconstruction methods. In the following, we review their procedure to determine the Radon data from MPI-FFL measurements. In contrast,

instead of reconstructing Radon data and particle concentration sequentially, we suggest a joint determination of both by means of total variation regularization inspired by [179].

5.2.1. Sequential reconstruction of Radon data and particle concentration

We follow the course of [114] to recover the Radon data from MPI measurements using a field-free line. Thus, we define $\overline{m}'_G(s) := -\mu_0 \overline{m}'(Gs)$ and $p_l^\varphi := \mathbf{e}_\varphi \cdot \mathbf{p}_l$. According to Theorem 5.4, the voltage signal induced in the l-th receive coil can then be written as

$$u_l(\varphi, t) \quad = \quad A\Lambda'_\varphi(t)\, p_l^\varphi \left[\overline{m}'_G * \mathcal{R}c\left(\mathbf{e}_\varphi, \cdot\right)\right] \left(\frac{A}{G}\Lambda_\varphi(t)\right).$$

The idea is to eliminate the factor in front of the convolution and apply deconvolution techniques afterwards. Since p_l^φ vanishes for receive coil sensitivities aligned parallel to the FFL, at least two receive coils with linear independent coil sensitivities $\mathbf{p}_1$ and $\mathbf{p}_2$ are required to prevent data loss with respect to this scanning direction.

Corollary 5.5 (Corollary 1 in [114]). *The receive channel normalized signal can be computed as*

$$u^p(\varphi, t) := A\Lambda'_\varphi(t) \left[\overline{m}'_G * \mathcal{R}c\left(\mathbf{e}_\varphi, \cdot\right)\right] \left(\frac{A}{G}\Lambda_\varphi(t)\right) = \frac{u_1(\varphi, t) + \sigma^\varphi u_2(\varphi, t)}{p_1^\varphi + \sigma^\varphi p_2^\varphi},\ \sigma^\varphi := \begin{cases} 1 & , p_1^\varphi p_2^\varphi > 0, \\ -1 & , p_1^\varphi p_2^\varphi \leq 0. \end{cases}$$

For the FFL speed normalization, the voltage signal is divided by the excitation function

$$\overline{u}^p(\varphi, t) := \frac{u^p(\varphi, t)}{A\Lambda'_\varphi(t)} = \left[\overline{m}'_G * \mathcal{R}c\left(\mathbf{e}_\varphi, \cdot\right)\right] \left(\frac{A}{G}\Lambda_\varphi(t)\right).$$

Thereby, time points need to be removed for which $\Lambda'_\varphi(t)$ is zero, which can only be the case at the boundary. Remember our assumptions regarding the star-shaped scanning geometry (Remark 5.1). The last step before deconvolution is the transformation of the time dependence into a space dependence. The signal equation can be expressed in terms of the displacement s of the FFL to the origin

$$\widetilde{u}^p(\varphi, s) := \left[\overline{m}'_G * \mathcal{R}c\left(\mathbf{e}_\varphi, \cdot\right)\right](s) = \overline{u}^p\left(\varphi, \Lambda_\varphi^{-1}\left(\frac{G}{A}s\right)\right), \quad s \in \left(-\frac{A}{G}, \frac{A}{G}\right).$$

The bounds of the interval can be included if $\Lambda'_\varphi(t)$ is non-zero on the whole interval $[0, T]$. To finally determine the Radon data, it is exploited that the Fourier transform of a convolution relates to the product of the Fourier transforms of the multipliers (cf. Theorem 2.9). For $\mathcal{F}(\overline{m}'_G(v)) \neq 0$ for all frequencies $v \in \mathbb{R}$ it holds

$$\mathcal{R}c(\varphi, \cdot) = \mathcal{F}^{-1}\left((2\pi)^{-\frac{1}{2}} \frac{\mathcal{F}\widetilde{u}^p(\varphi, \cdot)(v)}{\mathcal{F}\overline{m}'_G(v)}\right).$$

Deconvolution is again an ill-posed problem. Hence, it is proposed to apply Wiener deconvolution attenuating frequency parts with small SNR

$$\mathcal{R}^W c(\varphi, \cdot) = \mathcal{F}^{-1}\left((2\pi)^{-\frac{1}{2}} \frac{\mathcal{F}\widetilde{u}^p(\varphi, \cdot)(v)}{\mathcal{F}\overline{m}'_G(v)} \left(\frac{\left|\mathcal{F}(\overline{m}'_G(v))\right|^2}{\left|\mathcal{F}(\overline{m}'_G(v))\right|^2 + \frac{1}{\mathrm{SNR}(v)}}\right)\right). \tag{5.17}$$

5.2.2. Joint reconstruction of Radon data and particle concentration

Instead of sequentially reconstructing Radon data and particle concentration, inspired by [179] we suggest a joint reconstruction of both by means of total variation regularization. Starting with the work by Rudin, Osher, and Fatemi [159], proposing TV for image denoising, total variation became a popular approach in image reconstruction. Existence, stability, and consistency results with respect to the corresponding minimization problem were investigated in [1]. TV-based methods favor piecewise constant solutions and allow to reconstruct discontinuities, which correspond to edges in the image. We refer to [39] and [41] for an overview on theory and numerical methods for the computation of a TV regularized solution. Also for MPI, TV has already been applied to take a priori knowledge regarding the image structure into account ([8], [173], [195]). Considering an ideal FFL scanner, the authors of [94] compared the projection-based ansatz using the inverse Radon transform with a combination of the system-based ansatz and total variation regularization.

Let us assume $R < \frac{A}{G}$, that is the concentration is contained within the fully sampled region. Moreover, suppose the receive coils to be chosen such that $\mathbf{e}_\varphi \cdot \mathbf{p}_l \neq 0$ for at least one $l \in \{1, \dots, L\}$. Define $\mathcal{D} := L_2(B_R, \mathbb{R}) \times L_2(Z_R, \mathbb{R})$, which forms a Hilbert space with inner product

$$\langle \cdot, \cdot \rangle_{\mathcal{D}} := \langle \cdot, \cdot \rangle_{L_2(B_R,\mathbb{R})} + \langle \cdot, \cdot \rangle_{L_2(Z_R,\mathbb{R})} .$$

We propose to solve the optimization problem below to determine a regularized particle concentration c and Radon data v from noisy measurements u_l^ϵ, for $l = 1, \dots, L$, with noise level $\epsilon > 0$

$$\min_{(c,v)\in\mathcal{C}} \frac{1}{2} \sum_l \|\mathcal{K}_l v - u_l^\epsilon\|_{L_2}^2 + \frac{\omega}{2} \|\mathcal{R}c - v\|_{L_2}^2 + \gamma_1 \operatorname{TV}(c) + \gamma_2 P(v) . \tag{5.18}$$

The feasible set $\mathcal{C} := \{(c, v) \in \mathcal{D} : \ c \geq 0, \ v \geq 0\}$ accounts for the non-negativity of particle concentration c and Radon data v. The weighting parameter $\omega > 0$ balances the data fidelity term connecting v with the given data u_l^ϵ and the second term connecting tracer density c and Radon data v. The regularization parameters $\gamma_1, \gamma_2 > 0$ define the strength of penalization. Geometric a priori information is incorporated via the total variation acting on the concentration. The additional penalty term for the Radon data is not specified here. Throughout, we either choose it to be zero or as a sparsity constraint. Differently, e.g. directional TV regularization as used in [179] could be applied. In particular, various choices for both penalty terms are possible, which should be set according to problem specific properties.
Let $\mathcal{K} : L_2(Z, \mathbb{R}) \to L_2\left(Z_T, \mathbb{R}^L\right)$ with $\mathcal{K}v(\varphi, t) = \{\mathcal{K}_l v(\varphi, t)\}_{l=1,\dots,L}$. Further, let $\mathbf{u}^\epsilon = \{u_l^\epsilon\}_{l=1,\dots,L}$. Then, the data fidelity term can be expressed as (cf. (2.1))

$$\frac{1}{2} \sum_l \|\mathcal{K}_l v - u_l^\epsilon\|_{L_2}^2 = \frac{1}{2} \|\mathcal{K}v - \mathbf{u}^\epsilon\|_{L_2,\mathbb{R}^L}^2 .$$

Note that the concentration can also be determined directly via

$$\min_{c\geq 0} \frac{1}{2} \left\|\mathcal{A}^{\mathrm{FFL}} c - \mathbf{u}^\epsilon\right\|_{L_2,\mathbb{R}^L}^2 + \gamma_1 \operatorname{TV}(c) .$$

However, we decided to use (5.18) as it allows exploiting additional information on the Radon data. Furthermore, therewith the problem is divided into two smaller inverse problems with two forward operators integrating along lines instead of one integrating over a plane. Moreover, we are interested in Radon-based methods to keep the connection to the well-known CT.

To establish existence, stability, and consistency results, we rewrite (5.18) as the unconstrained optimization problem

$$\min_{(c,v)\in\mathcal{D}} \left\{ J_{\boldsymbol{\gamma}}^{\mathbf{u}^\epsilon}(c,v) := \frac{1}{2}\left\|\mathcal{K}v - \mathbf{u}^\epsilon\right\|_{L_2,\mathbb{R}^L}^2 + \frac{\omega}{2}\left\|\mathcal{R}c - v\right\|_{L_2}^2 + \gamma_1 \operatorname{TV}(c) + \gamma_2 P(v) + \delta_{\mathcal{C}}(c,v) \right\}$$

with indicator function $\delta_{\mathcal{C}}$ introduced in Section 2.2. We further exploited the shorthand form of the data fidelity term and set $\boldsymbol{\gamma} := (\gamma_1, \gamma_2)$. We make the following assumptions on the penalty function P.

Assumption 5.6. *Let $P : L_2(Z,\mathbb{R}) \to \mathbb{R}_0^+$ be proper, convex, and weakly sequentially lower semicontinuous.*

Therewith, the functional $J_{\boldsymbol{\gamma}}^{\mathbf{u}^\epsilon}$ satisfies useful properties regarding convex optimization.

Lemma 5.7. *Using Assumption 5.6, the objective functional $J_{\boldsymbol{\gamma}}^{\mathbf{u}^\epsilon} : \mathcal{D} \to \overline{\mathbb{R}}$ is*

(i) proper,

(ii) convex,

(iii) weakly sequentially lower semicontinuous,

(iv) coercive.

Proof. It is easy to see that $J_{\boldsymbol{\gamma}}^{\mathbf{u}^\epsilon}$ is proper and we only consider the remaining characteristics. By Theorem 2.22 and 2.23 the total variation is weakly sequentially lower semicontinuous and convex. Further, $\mathcal{K}$ and $\mathcal{R}$ are linear bounded operators and the feasible set $\mathcal{C}$ is closed and convex. Thus, $J_{\boldsymbol{\gamma}}^{\mathbf{u}^\epsilon}$ is jointly convex in (c,v) as per Example 2.18 and Lemma 2.19. It is further weakly sequentially lower semicontinuous as per Example 2.14 as well as Lemma 2.15 and 2.20. This proves assertions *(ii)* and *(iii)*. Since the Radon transform does not annihilate constant functions, it follows by Lemma 2.26 that

$$\|c\|_{\mathrm{BV}} \to \infty \quad \Longrightarrow \quad \frac{\omega}{2}\left\|\mathcal{R}c - v\right\|_{L_2}^2 + \gamma_1 \operatorname{TV}(c) \to \infty. \tag{5.19}$$

To show coercivity, assume

$$\|(c,v)\|_{\mathcal{D}}^2 = \|c\|_{L_2}^2 + \|v\|_{L_2}^2 \to \infty,$$

i.e. either $\|c\|_{L_2}$ or $\|v\|_{L_2}$ must tend towards infinity. Let us first consider $\|v\|_{L_2} \to \infty$. We regard $v \geq 0$, otherwise $J_{\boldsymbol{\gamma}}^{\mathbf{u}^\epsilon}(c,v) = \infty$ due to the indicator function. Moreover, since $R < \frac{A}{G}$ and due to Remark 5.1, we can find $t_{\pm R} \in (0,T)$ such that $\frac{A}{G}\Lambda_\varphi(t) \in [-R,R]$ and $\left|A\Lambda'_\varphi(t)\right| \geq \epsilon_R$ for all $t \in [t_{-R}, t_{+R}]$ and some $\epsilon_R > 0$. Exploiting the non-negativity of $\overline{m}'$ and that $\overline{m}'(0) > 0$, we estimate

$$\begin{aligned}
\|\mathcal{K}_l v\|_{L_2}^2 &= \int_0^{2\pi}\int_0^T \left| \mu_0\, A\Lambda'_\varphi(t)\, \mathbf{e}_\varphi \cdot \mathbf{p}_l \left[\overline{m}'(G\,\cdot) * v(\mathbf{e}_\varphi,\cdot)\right]\left(\frac{A}{G}\Lambda_\varphi(t)\right)\right|^2 \mathrm{d}\,t\,\mathrm{d}\,\varphi \\
&\geq \left(\mu_0\,\overline{m}'(0)\right)^2 G\,\epsilon_R \int_0^{2\pi} |\mathbf{e}_\varphi \cdot \mathbf{p}_l|^2 \int_{t_{-R}}^{t_{+R}} \left|\frac{A}{G}\Lambda'_\varphi(t)\right| \left| v\left(\mathbf{e}_\varphi, \frac{A}{G}\Lambda_\varphi(t)\right)\right|^2 \mathrm{d}\,t\,\mathrm{d}\,\varphi \\
&= \left(\mu_0\,\overline{m}'(0)\right)^2 G\,\epsilon_R \int_0^{2\pi} |\mathbf{e}_\varphi \cdot \mathbf{p}_l|^2 \int_{-R}^{R} |v(\mathbf{e}_\varphi, s)|^2 \,\mathrm{d}\,s\,\mathrm{d}\,\varphi.
\end{aligned}$$

Since $\mathbf{e}_\varphi \cdot \mathbf{p}_l \neq 0$ for at least one $l \in \{1,\dots,L\}$, we can find $p_L > 0$ such that $\sum_l |\mathbf{e}_\varphi \cdot \mathbf{p}_l|^2 \geq p_L$. Therewith, we compute with $C = \left(\mu_0\,\overline{m}'(0)\right)^2 G\,\epsilon_R\,p_L$

$$\|\mathcal{K}v\|_{L_2,\mathbb{R}^L}^2 = \sum_l \|\mathcal{K}_l v\|_{L_2}^2 \geq \left(\mu_0\,\overline{m}'(0)\right)^2 G\,\epsilon_R\,p_L \int_0^{2\pi}\int_{-R}^{R} |v(\mathbf{e}_\varphi, s)|^2 \,\mathrm{d}\,s\,\mathrm{d}\,\varphi = C\,\|v\|_{L_2}^2.$$

Therefore, we deduce that for $\|v\|_{L_2} \to \infty$, it holds $\frac{1}{2}\|\mathcal{K}v - \mathbf{u}^\epsilon\|^2_{L_2,\mathbb{R}^L} \to \infty$ and it directly follows that $J^{\mathbf{u}^\epsilon}_{\boldsymbol{\gamma}}(c,v) \to \infty$. Suppose now that $\|v\|_{L_2}$ is bounded and $\|c\|_{L_2} \to \infty$. Applying the Poincaré-Wirtinger inequality (2.3) we obtain

$$\begin{aligned}\|c\|_{L_2} &\leq \|c - \overline{c}\,1_{B_R}\|_{L_2} + \|\overline{c}\,1_{B_R}\|_{L_2} \leq C'\ \mathrm{TV}(c) + \sqrt{\pi R^2}\,|\overline{c}| \\ &= C'\ \mathrm{TV}(c) + \frac{1}{\sqrt{\pi R^2}}\|c\|_{L_1} \leq \max\left\{C', \frac{1}{\sqrt{\pi R^2}}\right\}\|c\|_{\mathrm{BV}}\end{aligned}$$

and thus, $\|c\|_{\mathrm{BV}} \to \infty$ if $\|c\|_{L_2} \to \infty$. Hence, by (5.19) the objective functional $J^{\mathbf{u}^\epsilon}_{\boldsymbol{\gamma}}$ is coercive yielding the last statement (iv). □

Therewith, the existence, stability, and consistency results of Chapter 3 can be transferred to our joint reconstruction method.

Theorem 5.8. ***Existence.*** *Using Assumption 5.6 the minimization problem (5.18) has a solution* $\left(c^{\mathbf{u}^\epsilon}_{\boldsymbol{\gamma}}, v^{\mathbf{u}^\epsilon}_{\boldsymbol{\gamma}}\right) \in \mathcal{C}$.

Proof. According to Lemma 5.7, we can apply Theorem 2.21 yielding the proposed existence. □

Note that we do not consider uniqueness. This is due to the fact that the Radon transform has non-trivial null space when only data for finite scanning directions is available [127].

Theorem 5.9. ***Stability.*** *Using Assumption 5.6, consider a sequence* $\{\mathbf{u}^\epsilon_n\}_{n\in\mathbb{N}}$ *satisfying* $\lim_{n\to\infty}\|\mathbf{u}^\epsilon - \mathbf{u}^\epsilon_n\|^2_{L_2,\mathbb{R}^L} = 0$. *Moreover, let* $\left(c^{\mathbf{u}^\epsilon_n}_{\boldsymbol{\gamma}}, v^{\mathbf{u}^\epsilon_n}_{\boldsymbol{\gamma}}\right)$ *be a minimizer to* $J^{\mathbf{u}^\epsilon_n}_{\boldsymbol{\gamma}}$. *Then, there exists a subsequence converging weakly to a minimizer* $\left(c^{\mathbf{u}^\epsilon}_{\boldsymbol{\gamma}}, v^{\mathbf{u}^\epsilon}_{\boldsymbol{\gamma}}\right)$ *to* $J^{\mathbf{u}^\epsilon}_{\boldsymbol{\gamma}}$.

Proof. The proof of Theorem 3.2 in [96] can be transferred to our joint reconstruction setting. Exploiting that for $n \in \mathbb{N}$ it holds

$$\frac{1}{2}\|\mathcal{K}v - \mathbf{u}^\epsilon\|^2_{L_2,\mathbb{R}^L} \leq \|\mathcal{K}v - \mathbf{u}^\epsilon_n\|^2_{L_2,\mathbb{R}^L} + \|\mathbf{u}^\epsilon - \mathbf{u}^\epsilon_n\|^2_{L_2,\mathbb{R}^L}$$

as well as that $\left(c^{\mathbf{u}^\epsilon_n}_{\boldsymbol{\gamma}}, v^{\mathbf{u}^\epsilon_n}_{\boldsymbol{\gamma}}\right)$ is assumed to be a minimizer to $J^{\mathbf{u}^\epsilon_n}_{\boldsymbol{\gamma}}$, it follows

$$\begin{aligned}J^{\mathbf{u}^\epsilon}_{\boldsymbol{\gamma}}\left(c^{\mathbf{u}^\epsilon_n}_{\boldsymbol{\gamma}}, v^{\mathbf{u}^\epsilon_n}_{\boldsymbol{\gamma}}\right) &\leq 2\,J^{\mathbf{u}^\epsilon_n}_{\boldsymbol{\gamma}}\left(c^{\mathbf{u}^\epsilon_n}_{\boldsymbol{\gamma}}, v^{\mathbf{u}^\epsilon_n}_{\boldsymbol{\gamma}}\right) + \|\mathbf{u}^\epsilon - \mathbf{u}^\epsilon_n\|^2_{L_2,\mathbb{R}^L} \\ &\leq 2\,J^{\mathbf{u}^\epsilon_n}_{\boldsymbol{\gamma}}\left(c^{\mathbf{u}^\epsilon}_{\boldsymbol{\gamma}}, v^{\mathbf{u}^\epsilon}_{\boldsymbol{\gamma}}\right) + \|\mathbf{u}^\epsilon - \mathbf{u}^\epsilon_n\|^2_{L_2,\mathbb{R}^L} \\ &\leq 4\,J^{\mathbf{u}^\epsilon}_{\boldsymbol{\gamma}}\left(c^{\mathbf{u}^\epsilon}_{\boldsymbol{\gamma}}, v^{\mathbf{u}^\epsilon}_{\boldsymbol{\gamma}}\right) + 2\,\|\mathbf{u}^\epsilon - \mathbf{u}^\epsilon_n\|^2_{L_2,\mathbb{R}^L}\end{aligned}$$

and the sequence $\left\{J^{\mathbf{u}^\epsilon}_{\boldsymbol{\gamma}}\left(c^{\mathbf{u}^\epsilon_n}_{\boldsymbol{\gamma}}, v^{\mathbf{u}^\epsilon_n}_{\boldsymbol{\gamma}}\right)\right\}_{n\in\mathbb{N}}$ is bounded. From the coercivity of $J^{\mathbf{u}^\epsilon}_{\boldsymbol{\gamma}}$ we also get the boundedness of $\left\{\left(c^{\mathbf{u}^\epsilon_n}_{\boldsymbol{\gamma}}, v^{\mathbf{u}^\epsilon_n}_{\boldsymbol{\gamma}}\right)\right\}_{n\in\mathbb{N}}$ and, therewith, the existence of a subsequence, which we denote the same, weakly converging to some $(c^*, v^*) \in \mathcal{C}$. The weak sequential lower semicontinuity of $J^{\mathbf{u}^\epsilon}_{\boldsymbol{\gamma}}$, the linearity and boundedness of $\mathcal{K}$ together with $\lim_{n\to\infty}\|\mathbf{u}^\epsilon - \mathbf{u}^\epsilon_n\|^2_{L_2,\mathbb{R}^L} = 0$ finally yields

$$J^{\mathbf{u}^\epsilon}_{\boldsymbol{\gamma}}(c^*, v^*) \leq \liminf_{n\to\infty} J^{\mathbf{u}^\epsilon_n}_{\boldsymbol{\gamma}}\left(c^{\mathbf{u}^\epsilon_n}_{\boldsymbol{\gamma}}, v^{\mathbf{u}^\epsilon_n}_{\boldsymbol{\gamma}}\right) \leq \liminf_{n\to\infty} J^{\mathbf{u}^\epsilon_n}_{\boldsymbol{\gamma}}\left(c^{\mathbf{u}^\epsilon}_{\boldsymbol{\gamma}}, v^{\mathbf{u}^\epsilon}_{\boldsymbol{\gamma}}\right) = J^{\mathbf{u}^\epsilon}_{\boldsymbol{\gamma}}\left(c^{\mathbf{u}^\epsilon}_{\boldsymbol{\gamma}}, v^{\mathbf{u}^\epsilon}_{\boldsymbol{\gamma}}\right),$$

i.e. (c^*, v^*) is a minimizer of $J^{\mathbf{u}^\epsilon}_{\boldsymbol{\gamma}}$. □

Theorem 5.10. ***Consistency.*** *Using Assumption 5.6, consider a sequence* $\{\mathbf{u}^{\epsilon_n}\}_{n\in\mathbb{N}}$ *of noisy data satisfying* $\lim_{n\to\infty}\left\{\epsilon_n := \|\mathbf{u} - \mathbf{u}^{\epsilon_n}\|_{L_2,\mathbb{R}^L}\right\} = 0$. *Let the regularization parameters* $\boldsymbol{\gamma}_n := (\gamma_{1,n}, \gamma_{2,n}) \equiv$

$(\gamma_1(\epsilon_n), \gamma_2(\epsilon_n))$ *fulfill*

$$\lim_{n\to\infty} \frac{\gamma_{2,n}}{\gamma_{1,n}} = 0, \quad \lim_{n\to\infty} \frac{\epsilon_n^2}{\gamma_{1,n}} = 0, \quad \textit{and} \quad \lim_{n\to\infty} \gamma_{1,n} = 0, \quad \lim_{n\to\infty} \gamma_{2,n} = 0.$$

Then, the sequence $\left\{\left(c_{\boldsymbol{\gamma_n}}^{\mathbf{u}^{\epsilon_n}}, v_{\boldsymbol{\gamma_n}}^{\mathbf{u}^{\epsilon_n}}\right)\right\}_{n\in\mathbb{N}} \subset \mathcal{C}$ *of minimizer to* $J_{\gamma_n}^{\mathbf{u}^{\epsilon_n}}$ *contains a subsequence converging weakly to a solution* $\left(c^\dagger, v^\dagger\right) \in \mathcal{C}$ *of*

$$\mathcal{K}v = \mathbf{u}, \quad \mathcal{R}c = v$$

with $c^\dagger$ *being a* TV*-minimizing solution to* $(\mathcal{K}\circ\mathcal{R})\,c = \mathbf{u}$.

Proof. We adapt the proof of Theorem 3.4 in [96] to our needs. Again, we have that for $n \in \mathbb{N}$ it holds

$$\frac{1}{2}\left\|\mathcal{K}v_{\boldsymbol{\gamma_n}}^{\mathbf{u}^{\epsilon_n}} - \mathbf{u}\right\|_{L_2,\mathbb{R}^L}^2 \le \left\|\mathcal{K}v_{\boldsymbol{\gamma_n}}^{\mathbf{u}^{\epsilon_n}} - \mathbf{u}^{\epsilon_n}\right\|_{L_2,\mathbb{R}^L}^2 + \left\|\mathbf{u} - \mathbf{u}^{\epsilon_n}\right\|_{L_2,\mathbb{R}^L}^2.$$

Utilizing that $\left(c_{\boldsymbol{\gamma_n}}^{\mathbf{u}^{\epsilon_n}}, v_{\boldsymbol{\gamma_n}}^{\mathbf{u}^{\epsilon_n}}\right)$ is a minimizer to $J_{\boldsymbol{\gamma_n}}^{\mathbf{u}^{\epsilon_n}}$, we infer

$$\begin{aligned} J_{\boldsymbol{\gamma_n}}^{\mathbf{u}}\left(c_{\boldsymbol{\gamma_n}}^{\mathbf{u}^{\epsilon_n}}, v_{\boldsymbol{\gamma_n}}^{\mathbf{u}^{\epsilon_n}}\right) &\le 2\, J_{\boldsymbol{\gamma_n}}^{\mathbf{u}^{\epsilon_n}}\left(c_{\boldsymbol{\gamma_n}}^{\mathbf{u}^{\epsilon_n}}, v_{\boldsymbol{\gamma_n}}^{\mathbf{u}^{\epsilon_n}}\right) + \left\|\mathbf{u} - \mathbf{u}^{\epsilon_n}\right\|_{L_2,\mathbb{R}^L}^2 \\ &\le 2\, J_{\boldsymbol{\gamma_n}}^{\mathbf{u}^{\epsilon_n}}\left(c^\dagger, v^\dagger\right) + \epsilon_n^2 \\ &\le 2\gamma_{1,n}\,\mathrm{TV}\left(c^\dagger\right) + 2\gamma_{2,n}\,P\left(v^\dagger\right) + 2\epsilon_n^2 \end{aligned}$$

and the sequence $\left\{J_{\boldsymbol{\gamma_n}}^{\mathbf{u}}\left(c_{\boldsymbol{\gamma_n}}^{\mathbf{u}^{\epsilon_n}}, v_{\boldsymbol{\gamma_n}}^{\mathbf{u}^{\epsilon_n}}\right)\right\}_{n\in\mathbb{N}}$ is bounded. From the coercivity of $J_{\boldsymbol{\gamma_n}}^{\mathbf{u}}$ we again deduce the boundedness of $\left\{\left(c_{\boldsymbol{\gamma_n}}^{\mathbf{u}^{\epsilon_n}}, v_{\boldsymbol{\gamma_n}}^{\mathbf{u}^{\epsilon_n}}\right)\right\}_{n\in\mathbb{N}}$. It follows the existence of a subsequence, which we denote the same, weakly converging to a $(c^*, v^*) \in \mathcal{C}$. It holds due to the linearity and boundedness of $\mathcal{K}, \mathcal{R}$ and the weak sequential lower semicontinuity of norms that

$$\begin{aligned} \frac{1}{2}\left\|\mathcal{K}v^* - \mathbf{u}\right\|_{L_2,\mathbb{R}^L}^2 + \frac{\omega}{2}\left\|\mathcal{R}c^* - v^*\right\|_{L_2}^2 &\le \liminf_{n\to\infty} \frac{1}{2}\left\|\mathcal{K}v_{\boldsymbol{\gamma_n}}^{\mathbf{u}^{\epsilon_n}} - \mathbf{u}\right\|_{L_2,\mathbb{R}^L}^2 + \frac{\omega}{2}\left\|\mathcal{R}c_{\boldsymbol{\gamma_n}}^{\mathbf{u}^{\epsilon_n}} - v_{\boldsymbol{\gamma_n}}^{\mathbf{u}^{\epsilon_n}}\right\|_{L_2}^2 \\ &\le 2\,\limsup_{n\to\infty}\left(\gamma_{1,n}\,\mathrm{TV}\left(c^\dagger\right) + \gamma_{2,n}\,P\left(v^\dagger\right) + \epsilon_n^2\right) = 0, \end{aligned}$$

i.e. $\mathcal{K}v^* = \mathbf{u}, \quad \mathcal{R}c^* = v^*$. Finally, we complete the proof by deriving from the weak sequential lower semicontinuity of the total variation (Theorem 2.22) that

$$\begin{aligned} \mathrm{TV}(c^*) &\le \liminf_{n\to\infty} \mathrm{TV}\left(c_{\boldsymbol{\gamma_n}}^{\mathbf{u}^{\epsilon_n}}\right) \le \limsup_{n\to\infty} \mathrm{TV}\left(c_{\boldsymbol{\gamma_n}}^{\mathbf{u}^{\epsilon_n}}\right) \le \limsup_{n\to\infty} \frac{1}{\gamma_{1,n}} J_{\boldsymbol{\gamma_n}}^{\mathbf{u}^{\epsilon_n}}\left(c_{\boldsymbol{\gamma_n}}^{\mathbf{u}^{\epsilon_n}}, v_{\boldsymbol{\gamma_n}}^{\mathbf{u}^{\epsilon_n}}\right) \\ &\le \limsup_{n\to\infty} \frac{1}{\gamma_{1,n}} J_{\boldsymbol{\gamma_n}}^{\mathbf{u}^{\epsilon_n}}\left(c^\dagger, v^\dagger\right) \le \lim_{n\to\infty}\left(\mathrm{TV}\left(c^\dagger\right) + \frac{\gamma_{2,n}}{\gamma_{1,n}} P\left(v^\dagger\right) + \frac{\epsilon_n^2}{\gamma_{1,n}}\right) = \mathrm{TV}\left(c^\dagger\right). \end{aligned}$$

□

5.2.3. Numerical results

Throughout this thesis, we consider numerical examples for synthetic data and different setup assumptions. Based on the simulation framework developed by Gael Bringout [29] available at `https://github.com/gBringout`, we implemented one adapted to our purposes. In this section, we give first reconstruction results for the idealized setting proposing static phantoms, ideal magnetic fields, and sequential line rotation. The corresponding magnetic fields can be modeled using a finite number of spherical harmonics as described in Appendix A.1. We compare our suggested joint reconstruction approach with the sequential image determination described in [114] and Paragraph 5.2.1.

Consider the semidiscrete setting regarding a finite number $p \in \mathbb{N}$ of FFL orientations specified by

$$\varphi_j := (j-1)\,\frac{\pi}{p}, \quad j = 1, \dots, p. \tag{5.20}$$

As already mentioned, the excitation function is usually chosen to be sinusoidal. According to this we define

$$\Lambda_{\varphi_j}(t) = \begin{cases} \cos(2\pi f_\mathrm{d} t), & j \text{ odd}, \\ -\cos(2\pi f_\mathrm{d} t), & j \text{ even}, \end{cases} \qquad j = 1, \dots, p, \quad t \in [0, T]$$

with drive frequency $f_\mathrm{d} > 0$ and $T = \frac{1}{2f_\mathrm{d}}$. Hence, initially the FFL is located parallel to the x-axis with displacement $\frac{A}{G}$ to the origin. It is then translated in orthogonal FFL direction until a signed distance $-\frac{A}{G}$ to the coordinate center is reached. After a small rotation, the line is moved back through the FOV. This sequential repetition of translation and rotation then indeed results in a star-shaped scanning geometry as was visualized in Figure 5.5a. Within our numerical investigations, we consider an instantaneous rotation.
The tracer material is modeled as a solution with 0.5 $\frac{\mathrm{mol}(\mathrm{Fe_3O_4})}{\mathrm{m}^3}$ concentration of magnetite with 30 nm core diameter and $\frac{0.6}{\mu_0}$ T saturation magnetization. We propose the particle distribution to be normalized to one and contained within the circle of radius $\frac{A}{G}$, i.e. the maximum FFL displacement, around the origin. For data generation, we divide the FOV $\left[-\frac{A}{G}, \frac{A}{G}\right] \times \left[-\frac{A}{G}, \frac{A}{G}\right]$ into 501×501 pixel. Since MPI is intrinsically three dimensional and the concentration is given per volume, these are actually implemented as $501 \times 501 \times 1$ voxel. In order to avoid inverse crime, reconstructions are executed on a coarser 201×201 grid. Moreover, we use the concentration based formulation of the forward model (5.15) for data simulation and the Radon-based formulation (5.16) for reconstruction. We simulate voltage signals induced in two orthogonal receive coils. The chosen receive coil sensitivities as well as further simulation parameters are summarized in Table 5.1.

Table 5.1.: Simulation parameters

Parameter	Explanation	Value	Unit
μ_0	magnetic permeability	$4\pi \cdot 10^{-7}$	$\mathrm{TA}^{-1}\mathrm{m}$
k_B	Boltzmann constant	$1.380650424 \cdot 10^{-23}$	JK^{-1}
T_p	particle temperature	310	K
G	gradient strength	4	$\mathrm{T}\,(\mathrm{m}\mu_0)^{-1}$
A	drive peak amplitude	0.015	$\mathrm{T}\mu_0^{-1}$
$\mathbf{p}_1$	sensitivity of the first receive coil	$[0.015/293.29, 0]^T$	m^{-1}
$\mathbf{p}_2$	sensitivity of the second receive coil	$[0, 0.015/379.71]^T$	m^{-1}
f_d	drive-field frequency	25	kHz
f_s	sampling frequency	8	MHz
p	amount of FFL directions	25	

We use standard methods for discretization and denote the resulting operators using bold letters. If not mentioned differently, we use composite trapezoidal rule and linear respectively bilinear interpolation if necessary. We approximate time derivatives via central and spatial derivatives via forward differences. Finally, we replace L_p-norms via the norms $\|\cdot\|_p$ in the respective l_p-space of

sequences. The above choice of parameters leads to

$$n_{\mathrm{s}} := \frac{f_{\mathrm{s}}}{2f_{\mathrm{d}}} + 1 = 161$$

data points per sampling direction, which are gathered equidistantly in time. Therefore, the corresponding FFL positions are not equidistant according to the choice of the excitation function. During the signal processing according to [114], summarized in Paragraph 5.2.1, we use cubic spline interpolation to determine the signal on an equidistant spatial grid before the deconvolution step. Note that for our method, introduced in Paragraph 5.2.2, no signal transformation is necessary.

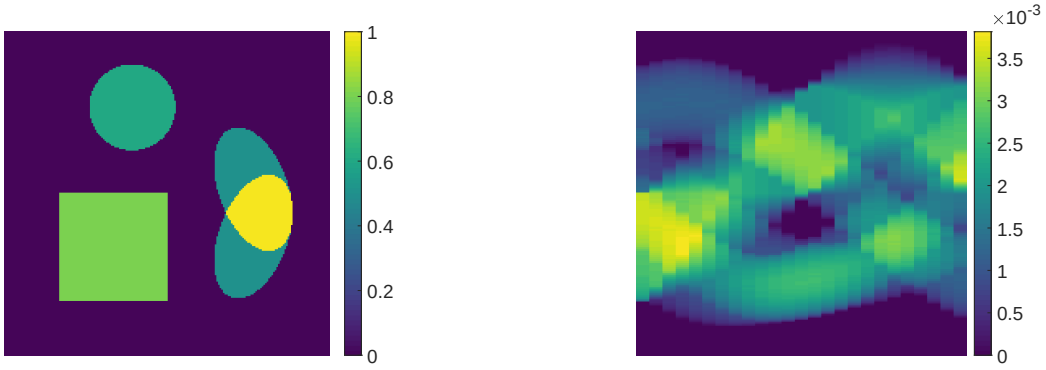

(a) (b)

Figure 5.6.: Phantom (a) and corresponding sinogram (b).

We consider simulated data generated for the phantom given in Figure 5.6a. Additionally to the phantom itself, we aim to reconstruct the corresponding sinogram for evenly distributed angles (5.20) as well as evenly distributed signed distances to the origin

$$s_l = \left(1 - 2\frac{l-1}{n_{\mathrm{s}}-1}\right)\frac{A}{G}, \quad l = 1, \ldots, n_{\mathrm{s}},$$

depicted in Figure 5.6b. First of all, using (5.17) respectively

$$\mathcal{R}^{\gamma}c(\varphi,\cdot) = \mathcal{F}^{-1}\left((2\pi)^{-\frac{1}{2}}\frac{\mathcal{F}\widetilde{u}^{p}(\varphi,\cdot)(v)}{\mathcal{F}\overline{m}'_{G}(v)}\left(\frac{\left|\mathcal{F}(\overline{m}'_{G}(v))\right|^{2}}{\left|\mathcal{F}(\overline{m}'_{G}(v))\right|^{2}+\gamma}\right)\right) \tag{5.21}$$

and choosing $\gamma = 1 \cdot 10^{-12}$ by visual inspection, we obtain the sinogram in Figure 5.7.

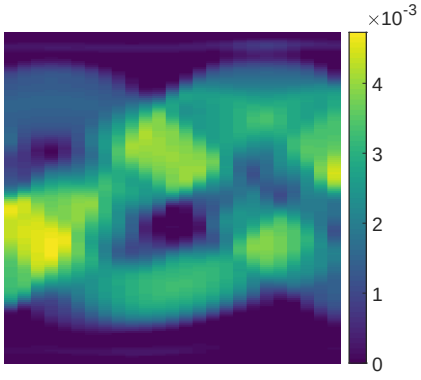

Figure 5.7.: Sinogram reconstruction using Wiener deconvolution (5.21) with $\gamma = 1 \cdot 10^{-12}$.

In [114] numerical results obtained by applying filtered backprojection to the previously determined Radon data were compared with results obtained by a system matrix-based Tikhonov regularized least-squares approach exploiting Kaczmarz for its solution. We restrict ourselves towards Radon-based approaches and give results using FBP. Thereby, since we assume the phantom to be contained within the circle of Radius $\frac{A}{G}$, we set all values outside this region to zero. The corresponding reconstruction is given in Figure 5.8a. All components of the phantom are clearly visible in the concentration reconstruction based on the Radon data determined by (5.21). However, the image is quite blurry and the background artifacts on the upper and lower part of the reconstructed sinogram (Figure 5.6b) are reflected in the circle contour in Figure 5.8a merging with the lower left corner of the square. The sharpness of the determined phantom and the intensity of the artifacts must be weighed up by the choice of γ. Smaller γ results in a sharper reconstruction at the cost of heavy artifacts obscuring the phantom. For comparison, Figure 5.8b gives the FBP reconstruction using computed exact Radon data, which shows clear contours of the shapes. While the sinogram is generated for 161 points per scanning direction, the number of angles ($p = 25$) is rather small. This results in streak artifacts visible in both FBP reconstructions.

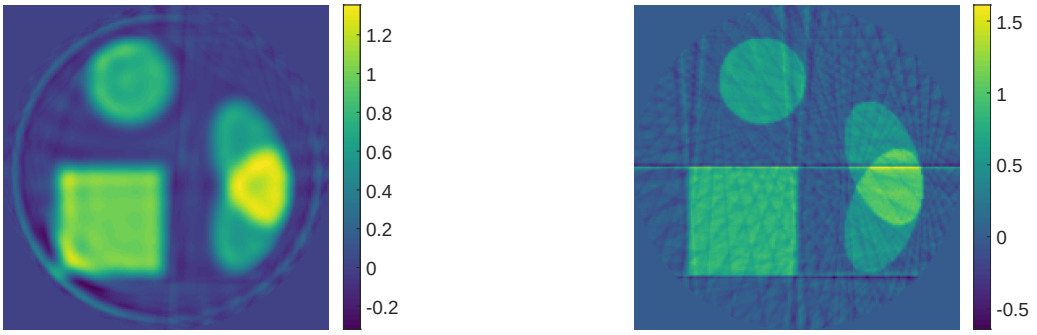

(a) (b)

Figure 5.8.: Phantom reconstruction using filtered backprojection for the sinogram obtained using Wiener deconvolution (a) and for computed exact Radon data (b).

Next, we consider results for our joint reconstruction approach (5.18). Let $\mathbf{K}$ and $\mathbf{R}$ denote the discretized forward mappings regarding MPI and CT. Moreover, let $\mathbf{u}$ denote finite data obtained via stacking measurements of both receive coils in one vector. Let u_∞ denote the maximum absolute data value regarding all time points and both receive coils. By setting

$$\widehat{\mathbf{u}} := \frac{\mathbf{u}}{u_\infty}, \quad \widehat{\mathbf{K}} := \frac{\mathbf{K}}{u_\infty},$$

we normalize the maximum absolute data value to one. We consider $P = 0$ and thus actively only regularize the concentration, which leads to the minimization problem

$$\min_{\mathbf{c}\geq 0, \mathbf{v}\geq 0} \frac{1}{2} \left\| \widehat{\mathbf{K}}\mathbf{v} - \widehat{\mathbf{u}} \right\|_2^2 + \frac{\omega}{2} \left\| \mathbf{R}\mathbf{c} - \mathbf{v} \right\|_2^2 + \gamma_1 \left\| \left\| \nabla \mathbf{c} \right\|_2 \right\|_1 . \tag{5.22}$$

To solve this problem, we use CVX, a package for specifying and solving convex programs ([68], [69]), together with the MOSEK solver [141]. By visual inspection, we determine a good choice for the parameters ω and γ_1. We then tune these by comparing solutions for $\omega \in \{1, 2, 4\} \cdot 10^4$ and $\gamma_1 \in \left\{0.1^{5.5-0.05i},\ i = 0, \ldots, 49\right\}$ based on their structural similarity (SSIM) value of the reconstructed particle concentration with the groundtruth phantom. Reconstructions regarding the choice of parameters yielding the highest SSIM value are given in Figure 5.9.

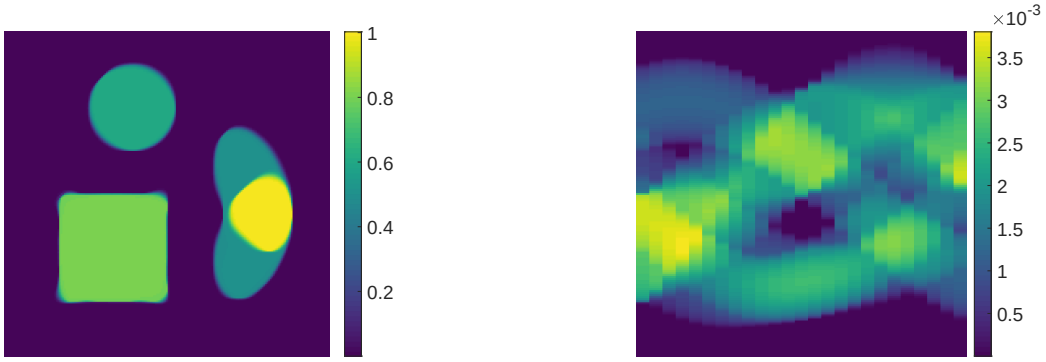

(a) (b)

Figure 5.9.: Reconstruction of phantom (a) and sinogram (b) based on (5.22) for the parameter choice $\omega = 2 \cdot 10^4$, $\gamma_1 = 0.1^{4.65}$, and according SSIM value $\mathrm{SSIM}(\mathbf{c}) = 0.9576$.

Both the considered particle distribution as well as the associated Radon data are well reconstructed. Furthermore, the streaking artifacts that appeared in the FBP reconstructions have completely disappeared as TV-based approaches endorse piecewise constant structures. However, the corners of the square are not sharply defined. An explanation can be e.g. missing information in the data or since we use an isotropic definition of the total variation favoring rounded edges (cf. [39] and Section 2.3). To conclude, we state results concerning added Gaussian noise (standard deviation: ca. 0.8% of u_∞) in Figure 5.10.

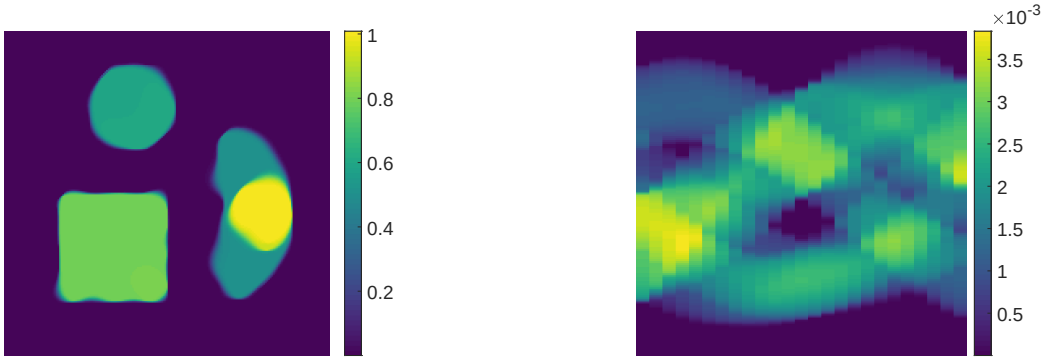

(a) (b)

Figure 5.10.: Reconstruction of phantom (a) and sinogram (b) applying (5.22) to noisy data. Parameters are chosen as $\omega = 4 \cdot 10^4$, $\gamma_1 = 0.1^{3.9}$, leading to an SSIM value $\mathrm{SSIM}(\mathbf{c}) = 0.8915$.

In real applications, the object might move and LFVs exhibit deformations. Hence, the next chapters deal with these non-ideal settings and aim to derive a similar relation between situation adapted MPI and Radon data. We start with introductory considerations and move on to simultaneous line rotation.

6. Simultaneous Line Rotation

This chapter also deals with MPI regarding static phantoms and ideal magnetic fields, i.e. straight lines centering the LFV. In contrast to Chapter 5, however, we here regard the scanning geometry suggested in the initial publication with respect to the FFL scanner [190]. The left image below (Figure 6.1a) recapitulates the *sequential line rotation* pattern discussed in the previous chapter. Remember that in this case the FFL is translated through the FOV followed by a rotation in between measurements. The translation and rotation procedure is repeated for different FFL orientations. Instead, for the *simultaneous line rotation* scheme translation and rotation are jointly executed resulting in an FFL trajectory forming a rosette (Figure 6.1b). Simultaneous rotation decreases the measurement time as data generation is not interrupted while rotating the FFL. For clinical applications short scanning times are crucial e.g. for avoiding inconsistent data sets due to time-varying concentrations. An open-source FFL implementation enabling continuous line rotation by mechanical movement of the corresponding magnets and shift coils for imaging the rat brain is presented in [137]. The authors of [31] and [114] proposed that the relation of the forward operator to the Radon transform stated in Theorem 5.4 can still be used for image reconstruction, if the rotation is sufficiently slow compared to the translation speed. The aim of this chapter is to examine this setting in more detail. Our results of this chapter have been published in [16].

Outline of the chapter: In Section 6.1, we adapt the forward model (5.15) by taking the additional time dependence resulting from the changed scanning geometry into account. Due to these new time dependencies and the time derivative within the model, the signal equation contains additive components. We link each of these to the Radon transform respectively a weighted version of the Radon transform and state corresponding upper bounds depending on the line translation or rotation velocity in Section 6.2. Afterwards, in Section 6.3, we modify our TV-based reconstruction approach according to the specified forward model and state corresponding numerical results for synthetic data in Section 6.4.

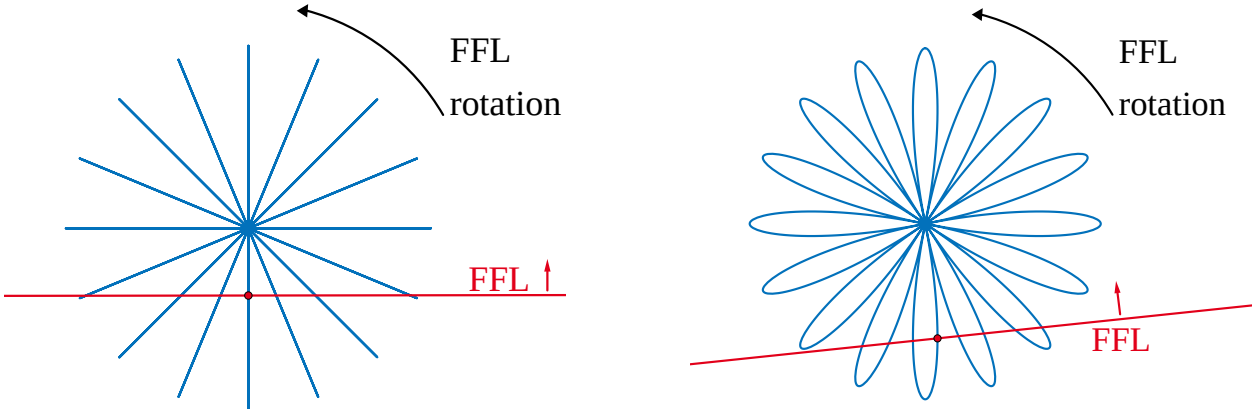

(a) Sequential line rotation

(b) Simultaneous line rotation

Figure 6.1.: Visualization of two different scanning geometries: (a) Sequential line translation and rotation. (b) Simultaneous line translation and rotation.

6.1. Forward model

First, we give a more general formulation of the Definition 5.15 of the MPI-FFL forward operator. To this end, we add a time dependence to the angle $\varphi : [0,T] \to [0,2\pi]$ and adapt the notation accordingly, namely we set $\mathbf{e}_t := \mathbf{e}_{\varphi(t)}$ as well as $\Lambda(t) := \Lambda_{\varphi(t)}(t)$. Note that $T > 0$ is now the total measurement time. Both Λ and φ are proposed to be differentiable with derivatives Λ' and φ'.

Definition 6.1. *Define* $\mathcal{A}_l : L_2\left(B_R, \mathbb{R}_0^+\right) \to L_2\left([0,T], \mathbb{R}\right)$ *to be*

$$\mathcal{A}_l c(t) := -\mu_0 \int_{\mathbb{R}^2} c(\mathbf{r}) \frac{\partial}{\partial t} \overline{m}\left(-G\,\mathbf{r}\cdot\mathbf{e}_t + A\Lambda(t)\right) \mathbf{e}_t \cdot \mathbf{p}_l(\mathbf{r})\,\mathrm{d}\,\mathbf{r}. \tag{6.1}$$

The forward operator for an MPI-FFL scanner is then given as $\mathcal{A} : L_2\left(B_R, \mathbb{R}_0^+\right) \to L_2\left([0,T], \mathbb{R}^L\right)$ *with* $\mathcal{A}c(t) = \{\mathcal{A}_l c(t)\}_{l=1,\dots,L}$.

This formulation of the forward model allows consideration of various scanning geometries. For example, sequential line rotation can be described via choosing $\varphi(t)$ to be piecewise constant. Regarding simultaneous line rotation, the angle φ determining the FFL direction changes with the corresponding translation. By introducing the line rotation frequency $f_{\mathrm{rot}} > 0$, the trajectory visualized in Figure 6.1b can be obtained by choosing the excitation function as $\Lambda(t) = \cos(2\pi f_{\mathrm{d}} t)$ and considering a temporally changing angle determined via $\varphi(t) := 2\pi f_{\mathrm{rot}} t$ (cf. [31]). Thereby, we propose that within a half line rotation, the FFL moves $(2n+1)$-times through the FOV

$$\frac{f_{\mathrm{d}}}{f_{\mathrm{rot}}} = 2n+1, \quad n \in \mathbb{N}.$$

This guarantees that after $t = \dfrac{1}{2f_{\mathrm{rot}}}$, that is $\varphi\left(\dfrac{1}{2f_{\mathrm{rot}}}\right) = \pi$, the FFL is back at its initial position. Therewith, as for CT and sequential line rotation, we motivate that gathering data within the angle range $[0,\pi]$ contains all required information.

Due to the additional time dependence, additional terms appear when determining the time derivative. Assuming that the FFL rotation is sufficiently slow compared to its translation, [114] and [31] supposed that Theorem 5.4 is still applicable. In what follows, we investigate this setting in more detail. We determine the supplementary components by executing the derivative and infer an analogue result to Theorem 5.4 by expressing these parts in terms of the Radon transform of the particle concentration.

6.2. Relation between MPI and Radon data

Like for $\mathbf{e}_t$, we adapt the notation in (5.13) towards $\mathbf{R}^t := \mathbf{R}^{\varphi(t)}$ as well as $\mathbf{e}_t^\perp := \mathbf{e}_{\varphi(t)}^\perp$. We further set $\mathbf{R}^{-t} := \left(\mathbf{R}^t\right)^{-1} = \mathbf{R}^{-\varphi(t)}$ and we define a weighted version of the Radon transform

$$\widetilde{\mathcal{R}}c(\mathbf{e}_t, s) := \int_{\mathbb{R}^2} c(\mathbf{r})\,\delta(\mathbf{r}\cdot\mathbf{e}_t - s)\,\mathbf{r}\cdot\mathbf{e}_t^\perp\,\mathrm{d}\,\mathbf{r}. \tag{6.2}$$

Exploiting (5.14) and rotating the coordinate system such that one axis is determined by $\mathbf{e}_t$ and the other one by $\mathbf{e}_t^\perp$ (see Figure 6.2), i.e. substituting $\mathbf{r}' := (v', s')^T := \mathbf{R}^{-t}\,\mathbf{r} = \mathbf{R}^{-t}(x,y)^T$, yields

$$\widetilde{\mathcal{R}}c(\mathbf{e}_t, s) = -\int_{\mathbb{R}} c\left(s\,\mathbf{e}_t - v'\,\mathbf{e}_t^\perp\right) v'\,\mathrm{d}\,v'.$$

Thus, $\widetilde{\mathcal{R}}$ determines the line integral for the function being weighted by the signed distance in line direction v' to the origin. It is therefore easy to see that this operator annihilates radially symmetrical functions, i.e. $c(\mathbf{r}) = c(\|\mathbf{r}\|)$.

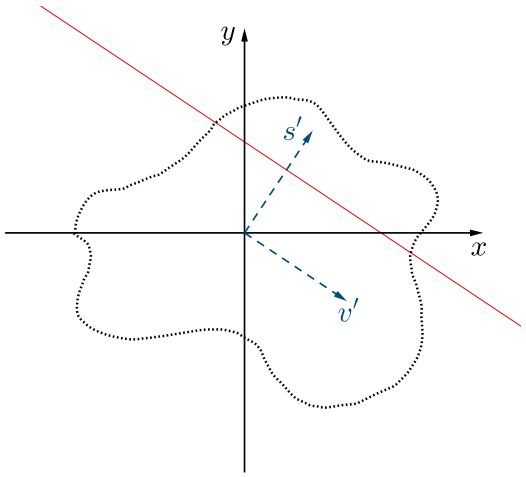

Figure 6.2.: Visualization of the rotation of the coordinate system such that one axis gets parallel to the FFL marked in red.

We now derive a relation between the Radon transform and the MPI-FFL forward operator (6.1) with a similar result as Theorem 5.4.

Theorem 6.2. *Given spatially homogeneous receive coil sensitivities, the MPI-FFL forward operator with respect to the l-th receive coil (6.1) can be written as*

$$\mathcal{A}_l = \mathcal{K}_{1,l} \circ \mathcal{R} + \mathcal{K}_{2,l} \circ \widetilde{\mathcal{R}} + \mathcal{K}_{3,l} \circ \mathcal{R}$$

with convolution operators $\mathcal{K}_{i,l} : L_2(Z, \mathbb{R}) \to L_2([0,T], \mathbb{R})$, *for* $i = 1,2,3$ *and* $l \in \{1, \dots, L\}$,

$$\begin{aligned}
\mathcal{K}_{1,l} f(t) &= -\mu_0 \, A\Lambda'(t) \, \mathbf{e}_t \cdot \mathbf{p}_l \, \overline{m}'(G\,\cdot) * f(\mathbf{e}_t, \cdot)(s_t), \\
\mathcal{K}_{2,l} f(t) &= \mu_0 \, G\varphi'(t) \, \mathbf{e}_t \cdot \mathbf{p}_l \, \overline{m}'(G\,\cdot) * f(\mathbf{e}_t, \cdot)(s_t), \\
\mathcal{K}_{3,l} f(t) &= -\mu_0 \, \varphi'(t) \, \mathbf{e}_t^{\perp} \cdot \mathbf{p}_l \, \overline{m}\,(G\,\cdot) * f(\mathbf{e}_t, \cdot)(s_t)
\end{aligned}$$

with $s_t := \dfrac{A}{G}\Lambda(t)$.

Proof. We start with executing the derivative in (6.1). Exploiting that $\mathbf{e}_t' = \varphi'(t)\,\mathbf{e}_t^{\perp}$ and that the receive coil sensitivities are proposed to be spatially homogeneous, we arrive at

$$\begin{aligned}
\mathcal{A}_l c(t) = &- \mu_0 \, A\Lambda'(t) \, \mathbf{e}_t \cdot \mathbf{p}_l \int_{\mathbb{R}^2} c(\mathbf{r}) \, \overline{m}'(-G\,\mathbf{r} \cdot \mathbf{e}_t + A\Lambda(t)) \, \mathrm{d}\,\mathbf{r} \\
&+ \mu_0 \, G\varphi'(t) \, \mathbf{e}_t \cdot \mathbf{p}_l \int_{\mathbb{R}^2} c(\mathbf{r}) \, \overline{m}'(-G\,\mathbf{r} \cdot \mathbf{e}_t + A\Lambda(t)) \, \mathbf{r} \cdot \mathbf{e}_t^{\perp} \, \mathrm{d}\,\mathbf{r} \\
&- \mu_0 \, \varphi'(t) \, \mathbf{e}_t^{\perp} \cdot \mathbf{p}_l \int_{\mathbb{R}^2} c(\mathbf{r}) \, \overline{m}\,(-G\,\mathbf{r} \cdot \mathbf{e}_t + A\Lambda(t)) \, \mathrm{d}\,\mathbf{r}.
\end{aligned}$$

As with the considerations regarding the weighted Radon transform and similar to [114], we transfer to a coordinate system with one axis being parallel to the field-free line, as visualized in Figure 6.2

and accomplished by substituting $\mathbf{r}' := (v', s')^T := \mathbf{R}^{-t}\,\mathbf{r}$. Based on (5.14) it holds

$$\begin{aligned}\mathrm{FFL}\left(\mathbf{e_t}, s'\right) &= L\left(\mathbf{e_t}, s'\right) = \left\{\mathbf{r} \in \mathbb{R}^2 :\ \mathbf{r}\cdot\mathbf{e}_t = s'\right\} = \left\{s'\,\mathbf{e}_t - v'\,\mathbf{e}_t^{\perp} :\ v' \in \mathbb{R}\right\} \\ &= \left\{\mathbf{R}^t \begin{pmatrix} v' \\ s' \end{pmatrix} :\ v' \in \mathbb{R}\right\}.\end{aligned}$$

We thus obtain

$$\begin{aligned}\mathcal{A}_l c\,(t) = &- \mu_0\, A\Lambda'\,(t)\ \mathbf{e}_t\ \cdot \mathbf{p}_l \int_{\mathbb{R}} \mathcal{R}c\left(\mathbf{e}_t, s'\right)\ \overline{m}'\left(-G\ s' + A\Lambda\,(t)\right)\,\mathrm{d}\,s' \\ &+ \mu_0\, G\varphi'\,(t)\ \mathbf{e}_t\ \cdot \mathbf{p}_l \int_{\mathbb{R}} \widetilde{\mathcal{R}}c\left(\mathbf{e}_t, s'\right)\ \overline{m}'\left(-G\ s' + A\Lambda\,(t)\right)\,\mathrm{d}\,s' \\ &- \mu_0\quad \varphi'\,(t)\ \mathbf{e}_t^{\perp} \cdot \mathbf{p}_l \int_{\mathbb{R}} \mathcal{R}c\left(\mathbf{e}_t, s'\right)\ \overline{m}\ \left(-G\ s' + A\Lambda\,(t)\right)\,\mathrm{d}\,s'.\end{aligned}$$

Hence, we finally get

$$\mathcal{A}_l = \mathcal{K}_{1,l} \circ \mathcal{R} + \mathcal{K}_{2,l} \circ \widetilde{\mathcal{R}} + \mathcal{K}_{3,l} \circ \mathcal{R}$$

completing the proof. □

Remark 6.3. *The sequential line rotation setting can be described by Definition 6.1 via choosing $\varphi\,(t)$ to be piecewise constant and neglecting the finite jumping points. In that case, operators $\mathcal{K}_{2,l}$ and $\mathcal{K}_{3,l}$ become zero mappings and Theorem 6.2 reduces to Theorem 5.4.*

Remark 6.4. *As in Theorem 5.2, we could have derived the more compact expression*

$$\mathcal{A}_l c\,(t) = -\mu_0\,\frac{\partial}{\partial t}\,\mathbf{e}_t \cdot \mathbf{p}_l\,[\overline{m}\,(G\,\cdot) * \mathcal{R}\,(\mathbf{e}_t, \cdot)]\left(\frac{A}{G}\Lambda\,(t)\right).$$

However, we are interested in the additional terms resulting from a sampling pattern where the FFL direction is time-dependent. Executing the time derivative in the above formula, gives the same result as in Theorem 6.2, validating our computation. This can be seen by exploiting Lemma 4.2 to obtain

$$\frac{\partial}{\partial t}\mathcal{R}c\,(\mathbf{e}_t, s) = -\varphi'\,(t)\,\frac{\partial}{\partial s}\mathcal{R}\left(\mathbf{r}\cdot\mathbf{e}_t^{\perp}\,c\right)(\mathbf{e}_t, s) = -\varphi'\,(t)\,\frac{\partial}{\partial s}\widetilde{\mathcal{R}}c\,(\mathbf{e}_t, s)$$

and applying integration by parts.

As shown in the last theorem, for all receive coils the according forward operator $\mathcal{A}_l$ can be divided into three parts $\mathcal{K}_{i,l}$, $i = 1, 2, 3$. Thereby, the third term incorporates the orientation change of the field-free line with respect to the receive coil sensitivity. For interpretation of the second term, we refer to the next chapter. Each component gives a convolution with the Radon transform respectively its weighted version defined in (6.2). While the first part $\mathcal{K}_{1,l}$ is analogue to the sequential setting regarded in the last chapter and scales with the translation speed $\Lambda'\,(t)$, the other two stem from the additional time dependence due to the simultaneous rotation and thus scale with the rotation speed $\varphi'\,(t)$ of the FFL. Hence, Theorem 6.2 supports the assumption of [31] and [114] that Theorem 5.4 can still be used in case $\varphi'\,(t)$ is small enough compared to $\Lambda'\,(t)$. For further confirmation regard the lemma below.

Lemma 6.5. *Let $R = \frac{A}{G}$, i.e. the concentration is contained within the fully sampled region. Assume $\varphi'\,(t) \neq 0$ for all $t \in [0, T]$. Then, it holds*

$$\left|\mathcal{K}_{1,l}\mathcal{R}c\,(t)\right| \ \geq\ \left|\frac{\Lambda'\,(t)}{\varphi'\,(t)}\right|\left|\mathcal{K}_{2,l}\widetilde{\mathcal{R}}c\,(t)\right|.$$

Proof. We have

$$\begin{aligned}\widetilde{\mathcal{R}}c\left(\mathbf{e}_t, s\right) &= \begin{cases} -\int_{-\sqrt{R^2-s^2}}^{\sqrt{R^2-s^2}} c\left(s\,\mathbf{e}_t - v'\,\mathbf{e}_t^{\perp}\right) v'\,\mathrm{d}\,v', & \text{for } s \leq R, \\ 0, & \text{for } s > R, \end{cases} \\ &\leq R\,\mathcal{R}c\left(\mathbf{e}_t, s\right).\end{aligned}$$

Therewith, we obtain

$$\begin{aligned}\left|\mathcal{K}_{1,l}\mathcal{R}c\left(t\right)\right| &= \left|\mu_0\, R G \Lambda'\left(t\right)\ \mathbf{e}_t \cdot \mathbf{p}_l\, \overline{m}'\left(G\,\cdot\right) * \mathcal{R}c\left(\mathbf{e}_t, \cdot\right)\left(s_t\right)\right| \\ &\geq \left|\mu_0 \quad G\Lambda'\left(t\right)\ \mathbf{e}_t \cdot \mathbf{p}_l\, \overline{m}'\left(G\,\cdot\right) * \widetilde{\mathcal{R}}c\left(\mathbf{e}_t, \cdot\right)\left(s_t\right)\right| \\ &= \left|\mu_0 \quad G\varphi'\left(t\right)\ \mathbf{e}_t \cdot \mathbf{p}_l\, \overline{m}'\left(G\,\cdot\right) * \widetilde{\mathcal{R}}c\left(\mathbf{e}_t, \cdot\right)\left(s_t\right)\right| \left|\frac{\Lambda'\left(t\right)}{\varphi'\left(t\right)}\right| \\ &= \left|\frac{\Lambda'\left(t\right)}{\varphi'\left(t\right)}\right| \left|\mathcal{K}_{2,l}\widetilde{\mathcal{R}}c\left(t\right)\right|.\end{aligned}$$

□

As mentioned earlier, to get a rosette trajectory as in Figure 6.1b, we set the excitation function $\Lambda\left(t\right) = \cos\left(2\pi f_{\mathrm{d}} t\right)$ and the time-varying angle $\varphi\left(t\right) := 2\pi f_{\mathrm{rot}} t$. In this case, it holds

$$\left|\frac{\Lambda'\left(t\right)}{\varphi'\left(t\right)}\right| = \frac{f_{\mathrm{d}}}{f_{\mathrm{rot}}} \left|\sin\left(2\pi f_{\mathrm{d}} t\right)\right|. \tag{6.3}$$

At each inflection point of the FFL, the first term $\mathcal{K}_{1,l}\mathcal{R}c$ reaches the value zero. According to Lemma 6.5 and (6.3), the associated time intervals in which this component can be exceeded by $\mathcal{K}_{2,l}\widetilde{\mathcal{R}}c$ are the smaller the larger the ratio $\frac{f_{\mathrm{d}}}{f_{\mathrm{rot}}}$ gets. As per [189], drive frequencies range around 1 kHz to 150 kHz and by [31] a typical upper bound for the rotation frequency is given by 100 Hz. Therewith, we estimate $\frac{f_{\mathrm{d}}}{f_{\mathrm{rot}}} \geq 10$. For radial symmetric concentrations, $\mathcal{K}_{2,l}\widetilde{\mathcal{R}}c$ vanishes.

Finally, we state bounds for $\left|\mathcal{K}_{2,l}\widetilde{\mathcal{R}}c\left(t\right)\right|$ and $\left|\mathcal{K}_{3,l}\mathcal{R}c\left(t\right)\right|$.

Lemma 6.6. *Let m denote the magnetic moment of a single particle, $\overline{m}'_{\infty} := \max_{\lambda\in\mathbb{R}} \overline{m}'\left(\lambda\right)$ and N_p the total amount of particles contained in the tracer injection. Then, it holds that*

$$\begin{aligned}\left|\mathcal{K}_{2,l}\widetilde{\mathcal{R}}c\left(t\right)\right| &\leq \mu_0\, G\, R\ \left|\varphi'\left(t\right)\right| \left|\mathbf{e}_t\ \cdot \mathbf{p}_l\right| \overline{m}'_{\infty}\ N_p, \\ \left|\mathcal{K}_{3,l}\mathcal{R}c\left(t\right)\right| &\leq \mu_0 \qquad \left|\varphi'\left(t\right)\right| \left|\mathbf{e}_t^{\perp} \cdot \mathbf{p}_l\right| m \quad N_p.\end{aligned} \tag{6.4}$$

Proof. From the proof of Theorem 6.2 we obtain

$$\begin{aligned}\left|\mathcal{K}_{2,l}\widetilde{\mathcal{R}}c\left(t\right)\right| &= \left|\mu_0\, G\, \varphi'\left(t\right)\ \mathbf{e}_t\ \cdot \mathbf{p}_l \int_{\mathbb{R}^2} c(\mathbf{r})\, \overline{m}'\left(-G\,\mathbf{r}\cdot\mathbf{e}_t + A\Lambda\left(t\right)\right)\ \mathbf{r}\cdot\mathbf{e}_t^{\perp}\,\mathrm{d}\,\mathbf{r}\right|, \\ \left|\mathcal{K}_{3,l}\mathcal{R}c\left(t\right)\right| &= \left|\mu_0 \quad \varphi'\left(t\right)\ \mathbf{e}_t^{\perp} \cdot \mathbf{p}_l \int_{\mathbb{R}^2} c(\mathbf{r})\, \overline{m}\ \left(-G\,\mathbf{r}\cdot\mathbf{e}_t + A\Lambda\left(t\right)\right)\mathrm{d}\,\mathbf{r}\right|.\end{aligned}$$

Therewith, it follows

$$\left|\mathcal{K}_{2,l}\widetilde{\mathcal{R}}c\left(t\right)\right| \leq \mu_0\, G\, R\ \left|\varphi'\left(t\right)\right| \left|\mathbf{e}_t\ \cdot \mathbf{p}_l\right| \overline{m}'_{\infty} \left|\int_{\mathbb{R}^2} c(\mathbf{r})\,\mathrm{d}\,\mathbf{r}\right| \leq \mu_0\, G\, R\ \left|\varphi'\left(t\right)\right| \left|\mathbf{e}_t\ \cdot \mathbf{p}_l\right| \overline{m}'_{\infty}\ N_p.$$

Furthermore, since the modulus of the mean magnetic moment is bounded by m (cf. Langevin model (5.7) and (5.8))

$$|\mathcal{K}_{3,l}\mathcal{R}c\,(t)| \;\leq\; \mu_0\,|\varphi'\,(t)|\left|\mathbf{e}_t^{\perp}\cdot\mathbf{p}_l\right| m\left|\int_{\mathbb{R}^2} c(\mathbf{r})\;\mathrm{d}\,\mathbf{r}\right| \leq \mu_0\,|\varphi'\,(t)|\left|\mathbf{e}_t^{\perp}\cdot\mathbf{p}_l\right| m\,N_p.$$

□

Note that using the Langevin model (5.8), it holds $\overline{m}'_{\infty} := \overline{m}'\,(0)$.

Remark 6.7. *For practical reasons, it might be convenient to state the upper bounds in terms of the maximal particle concentration $c_{\max}$ via exploiting $N_p \leq c_{\max}\pi R^2$.*

For time points for which the phantom is fully located within the saturation area on one side of the FFL, (6.4) applies approximately with equality. The estimates in the last Lemma can be computed beforehand to measurements, as all components are determined by the scanner setup and the choice of the injected tracer. Thus, these upper bounds can be determined and compared to the magnitudes of measured data in order to evaluate whether incorporation is needed. From the s-shape of the Langevin function, it follows that $|\mathcal{K}_{3,l}\mathcal{R}c\,(t)|$ is largest at turning points of the FFL, which are the zero crossings of $|\mathcal{K}_{1,l}\mathcal{R}c\,(t)|$.

6.3. Radon-based image reconstruction using TV regularization

For reconstruction, we use the same approach as presented in the last chapter (cf. (5.18)) and simply insert the updated forward model for simultaneous line rotation. Let $A_l : \mathcal{D} \to L_2\,([0,T],\mathbb{R})$ be for $l = 1,\ldots,L$ defined as

$$A_l\,(c,v) := \mathcal{K}_{1,l}v + \left(\mathcal{K}_{2,l}\circ\widetilde{\mathcal{R}}\right)c + \mathcal{K}_{3,l}v \tag{6.5}$$

with operators $\mathcal{K}_{i,l},\ i = 1,2,3$, introduced in Theorem 6.2. We then have that $A_l\,(c,\mathcal{R}c) = \mathcal{A}_l c$ for $c \geq 0$. Hence, we consider the following minimization problem for image c and Radon data v reconstruction from noisy measurements u_l^{ϵ}, for $l = 1,\ldots,L$, with noise level $\epsilon > 0$

$$\min_{(c,v)\in\mathcal{C}} \frac{1}{2}\sum_l \|A_l\,(c,v) - u_l^{\epsilon}\|_{L_2}^2 + \frac{\omega}{2}\,\|\mathcal{R}c - v\|_{L_2}^2 + \gamma_1\,\mathrm{TV}\,(c) + \gamma_2\,P\,(v)\,. \tag{6.6}$$

Remember that the feasible set $\mathcal{C} := \{(c,v)\in\mathcal{D} :\ c \geq 0,\ v \geq 0\}$ guarantees non-negativity of solutions. Introducing $A\,(c,v) = \{A_l\,(c,v)\}_{l=1,\ldots,L}$, the data fidelity term can be rewritten as

$$\frac{1}{2}\sum_l \|A_l\,(c,v) - u_l^{\epsilon}\|_{L_2}^2 = \frac{1}{2}\,\|A\,(c,v) - \mathbf{u}^{\epsilon}\|_{L_2,\mathbb{R}^L}^2$$

with $\mathbf{u}^{\epsilon} = \{u_l^{\epsilon}\}_{l=1,\ldots,L}$. We omit specification of existence, stability, and consistency results. For these, Lemma 5.7 needs to be proved for the new objective functional. Since only the data fidelity term has changed, but A_l is still linear and bounded, the only point of interest is the coercivity. This should be transferable from Paragraph 5.2.2 to the updated scanning geometry if the rotation speed is slow enough in comparison to the translation. In case of doubt, the penalty term acting on v can always be chosen in such a way that coercivity and thus all other results are guaranteed.

6.4. Numerical results

We now consider numerical results for synthetic data acquired using the same procedure as in the last chapter. Since we are now considering a continuously rotating FFL, we do not use an excitation function that changes sign for every other angle. Instead, a line that moves back and forth through the FOV can be modeled by choosing

$$\Lambda(t) = \cos(2\pi f_{\mathrm{d}} t).$$

Simulation parameters are set according to Table 5.1. Furthermore, we regard a line rotation frequency f_{rot} of 1 kHz. The total measurement time is determined to be $T = \frac{1}{2f_{\mathrm{rot}}}$. Therewith, we get a total of

$$2\frac{f_{\mathrm{d}}}{T} = \frac{f_{\mathrm{d}}}{f_{\mathrm{rot}}} = 25$$

passes of the FFL through the FOV covering angles in $[0, \pi]$. The number of sampling points per translation through the phantom is the same as for the numerical example with respect to sequential line rotation as we do not change drive or sampling frequency. Thus, we can compare results for simultaneous and sequential line rotation using this parameter choice. For comparison purposes, we consider the same phantom as for our sequential line rotation results in the last chapter. For convenience, we present concentration and sinogram filled angle by angle again in Figure 6.3.

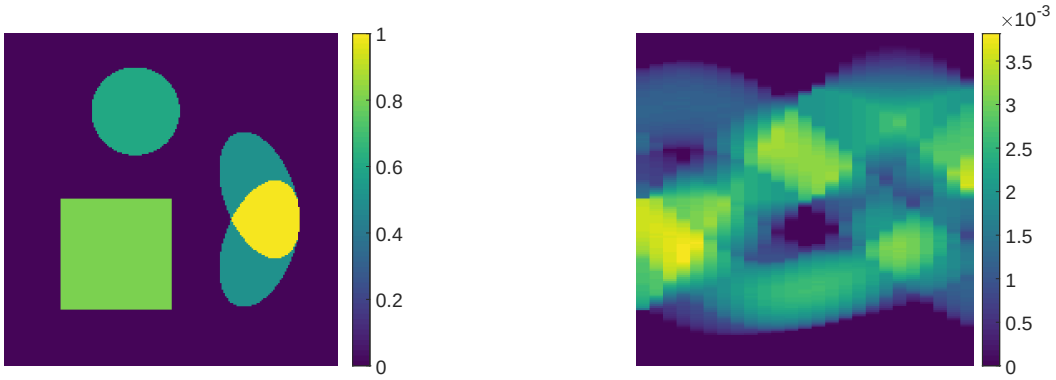

(a) (b)

Figure 6.3.: Phantom (a) and corresponding sinogram filled angle by angle (b).

We neglect the second part of the forward model, that is $\mathcal{K}_{2,l} \circ \widetilde{\mathcal{R}}$, such that the considered operator only depends on the Radon data. We justify this by our estimate in Lemma 6.5 and the specific choice of frequencies. Moreover, we refer to Figure 6.4 for an exemplary visualization of the negligible contribution of the second component to the voltage signal induced in the first receive coil. Thereby, normalizing the largest absolute data value regarding this coil

$$\widehat{\mathcal{K}}_{i,1} f(t) := \frac{\mathcal{K}_{i,1} f(t)}{\max_t \{|\mathcal{K}_{1,1} f(t)|\}}, \quad \text{for } i = 1, 2, 3,$$

the left image presents $\widehat{\mathcal{K}}_{1,1}\mathcal{R}c$ in relation to $\widehat{\mathcal{K}}_{3,1}\mathcal{R}c$. The image on the right shows $\widehat{\mathcal{K}}_{2,1}\widetilde{\mathcal{R}}c + \widehat{\mathcal{K}}_{3,1}\mathcal{R}c$ and $\widehat{\mathcal{K}}_{3,1}\mathcal{R}c$. Both components, which entered the model due to the additional time dependencies for simultaneous line rotation, are small compared to $\widehat{\mathcal{K}}_{1,1}\mathcal{R}c$. In particular, the second part is only recognizable when the main part reaches its highest values anyway. In contrast, the third term is largest for zero crossings of $\widehat{\mathcal{K}}_{1,1}\mathcal{R}c$. This term is easy to include in the reconstruction task as it directly links to the classical Radon transform itself. We see that the bound of Lemma 6.6 fits well.

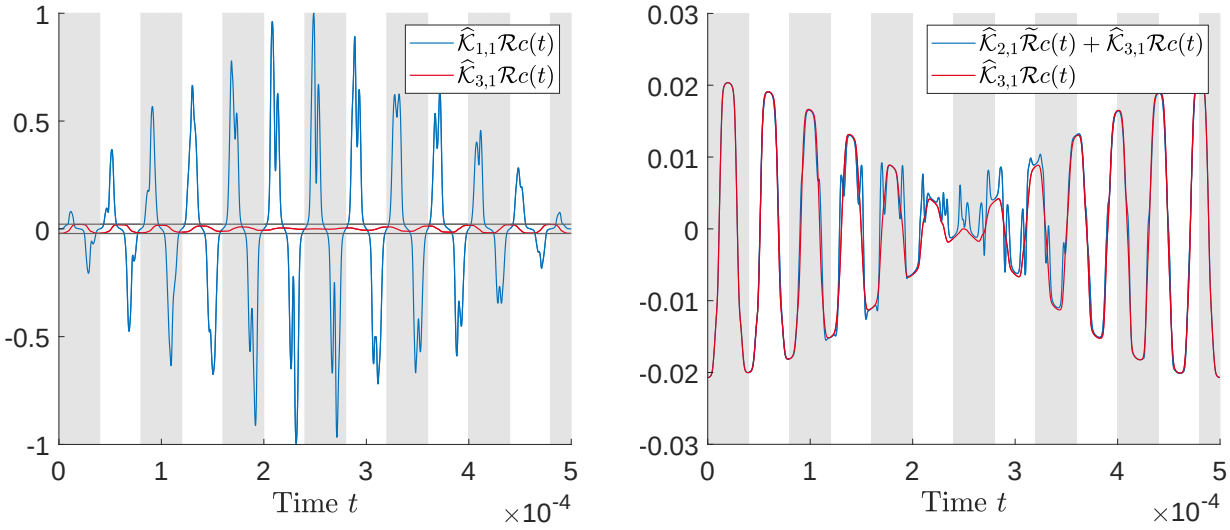

(a) (b)

Figure 6.4.: Comparison of the magnitudes of the forward model's components. (a) Given is $\widehat{\mathcal{K}}_{1,1}\mathcal{R}c$ (blue) in relation to $\widehat{\mathcal{K}}_{3,1}\mathcal{R}c$ (red) together with the bound determined in Lemma 6.6 (dark grey). (b) Given is $\widehat{\mathcal{K}}_{2,1}\widetilde{\mathcal{R}}c + \widehat{\mathcal{K}}_{3,1}\mathcal{R}c$ (blue) in comparison to $\widehat{\mathcal{K}}_{3,1}\mathcal{R}c$ (red) for the phantom in Figure 6.3a. Light gray color boxes in the background of the two plots, indicate periods of the drive field. The total measurement time is $12.5\frac{1}{f_\mathrm{d}} = \frac{1}{2f_\mathrm{rot}}$.

For the calculation of MPI data in a discretized setting, a sinogram filled angle by angle is required. Hence, to evaluate a discretized version of (6.5) for every sampling point, a sinogram composed of columns for each angle that the FFL assumes during scanning is needed. In case of rotating the FFL in between measurements, this condition is satisfied for the sinogram shown in Figure 6.3b. However, for simultaneous line rotation, the fine sinogram presented in Figure 6.5a would be necessary. Nevertheless, aiming at a problem size reduction, we opt for reconstruction of Radon data corresponding to the white dashed line in Figure 6.5a leading to the sinogram in Figure 6.5b. We assume that the corresponding additional error is negligible due to the shape of the convolution kernel with respect to the main contributing part $\widehat{\mathcal{K}}_{1,l}\mathcal{R}c$, which converges to the dirac-δ-distribution for particle diameters tending to infinity [113]. The use of regularization also ensures stability.

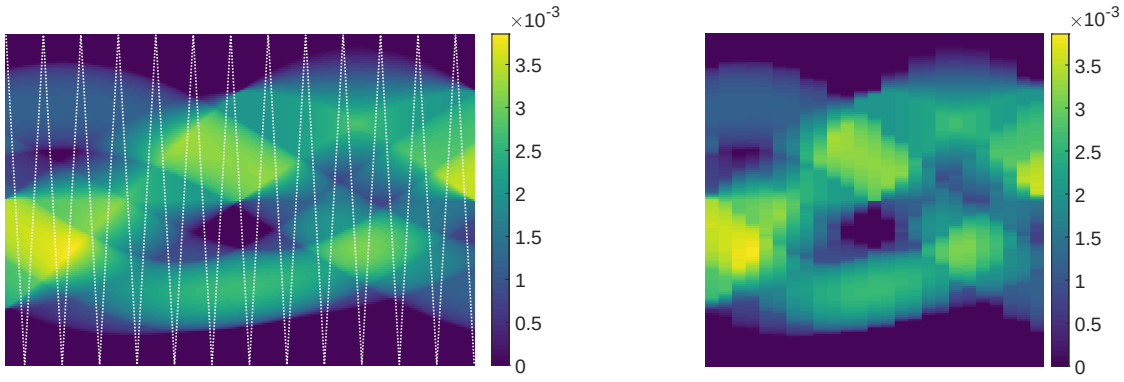

(a) (b)

Figure 6.5.: Sinogram for the phantom shown in Figure 6.3a with columns for each angle attained by the FFL during scanning (a) and adapted version filled following the dashed line on the left (b).

Consider discretizations of the Radon transform $\mathbf{R}_{\text{seq}}$ and $\mathbf{R}_{\text{sim}}$ such that $\mathbf{R}_{\text{seq}}\mathbf{c}$ gives the sinogram in Figure 6.3b and $\mathbf{R}_{\text{sim}}\mathbf{c}$ the one in Figure 6.5b. Let $\mathbf{K}_i$ denote a discretization of the forward model's components such that the resulting data $\mathbf{u}$ contains data for both receive coils stacked in one vector. As in Section 5.2.3, we scale simulated measurements and operators by dividing through the maximum absolute data value u_∞ with respect to all time points and both receive coils

$$\widehat{\mathbf{u}} := \frac{\mathbf{u}}{u_\infty}, \quad \widehat{\mathbf{K}}_i := \frac{\mathbf{K}_i}{u_\infty}, \quad i = 1, 3.$$

Incorporating only active regularization of the concentration by setting $P = 0$, we consider the variants of (6.6) specified in Table 6.1 for reconstruction. These comprise an approach neglecting the specific sampling pattern and using the same method as for sequential line rotation. The other approaches shall investigate results with and without including the third component.

Table 6.1.: Reconstruction methods

Method	**Regarded minimization problem**
$\mathcal{M}_1$	$\min\limits_{\mathbf{c}\geq 0, \mathbf{v}\geq 0} \frac{1}{2}\left\|\widehat{\mathbf{K}}_1\mathbf{v} - \widehat{\mathbf{u}}\right\|_2^2 + \frac{\omega}{2}\left\|\mathbf{R}_{\text{seq}}\mathbf{c} - \mathbf{v}\right\|_2^2 + \gamma_1 \left\|\left\|\nabla \mathbf{c}\right\|_2\right\|_1$
$\mathcal{M}_2$	$\min\limits_{\mathbf{c}\geq 0, \mathbf{v}\geq 0} \frac{1}{2}\left\|\widehat{\mathbf{K}}_1\mathbf{v} - \widehat{\mathbf{u}}\right\|_2^2 + \frac{\omega}{2}\left\|\mathbf{R}_{\text{sim}}\mathbf{c} - \mathbf{v}\right\|_2^2 + \gamma_1 \left\|\left\|\nabla \mathbf{c}\right\|_2\right\|_1$
$\mathcal{M}_3$	$\min\limits_{\mathbf{c}\geq 0, \mathbf{v}\geq 0} \frac{1}{2}\left\|\left(\widehat{\mathbf{K}}_1 + \widehat{\mathbf{K}}_3\right)\mathbf{v} - \widehat{\mathbf{u}}\right\|_2^2 + \frac{\omega}{2}\left\|\mathbf{R}_{\text{sim}}\mathbf{c} - \mathbf{v}\right\|_2^2 + \gamma_1 \left\|\left\|\nabla \mathbf{c}\right\|_2\right\|_1$

Like before, we use CVX ([68], [69]) together with the MOSEK solver [141] for determining solutions of the minimization problems. Also, we determine results for weighting parameters $\omega \in \{1, 2, 4\} \cdot 10^4$ and regularization parameters $\gamma_1 \in \left\{0.1^{5.5-0.05i},\ i = 0, \ldots, 49\right\}$ and give those results corresponding to the maximum structural similarity of the reconstructed particle concentration with respect to the groundtruth.

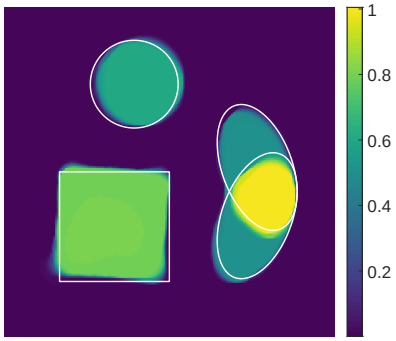

Figure 6.6.: Phantom reconstruction for simultaneous line rotation using method $\mathcal{M}_1$, neglecting the specific sampling pattern, and $\omega = 4 \cdot 10^4$, $\gamma_1 = 0.1^4$. The corresponding SSIM value is $\text{SSIM}(\mathbf{c}) = 0.7996$. Contours of the groundtruth are depicted in white.

A reconstruction result neglecting the specific sampling pattern via applying method $\mathcal{M}_1$, is stated in Figure 6.6. Contours of the groundtruth concentration are indicated in white. The phantom appears slightly rotated, which is self-evident as no information of the joint rotation and translation is exploited.

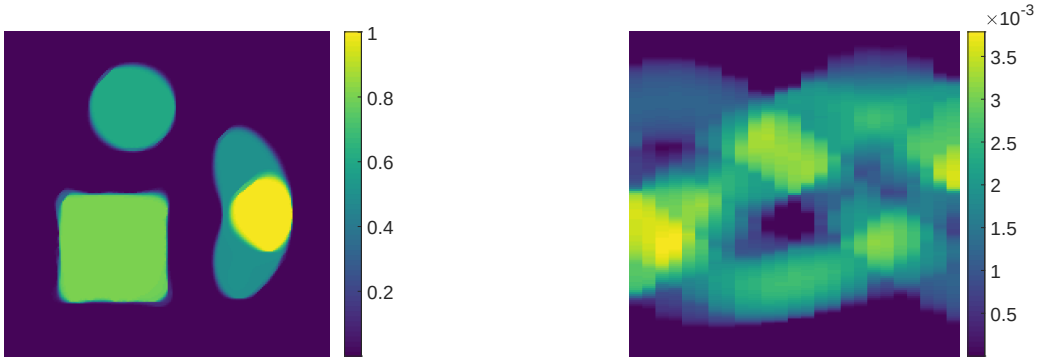

Reconstruction with respect to $\mathcal{M}_2$ and $\omega = 4 \cdot 10^4$, $\gamma_1 = 0.1^4$. SSIM $(\mathbf{c}) = 0.9070$

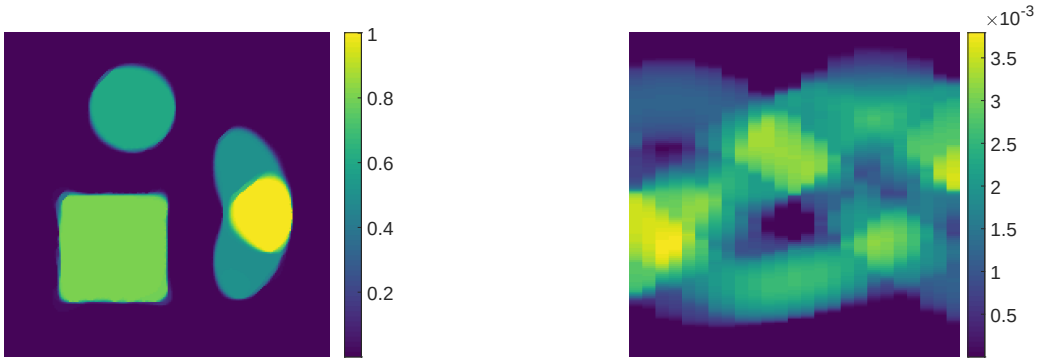

Reconstruction with respect to $\mathcal{M}_3$ and $\omega = 1 \cdot 10^4$, $\gamma_1 = 0.1^{4.5}$. SSIM $(\mathbf{c}) = 0.9304$

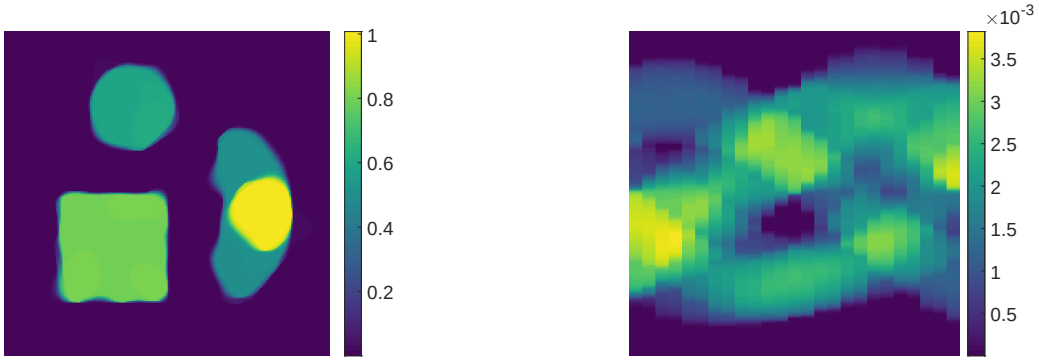

Reconstruction with respect to $\mathcal{M}_2$, noisy data, and $\omega = 4 \cdot 10^4$, $\gamma_1 = 0.1^4$. SSIM $(\mathbf{c}) = 0.8713$

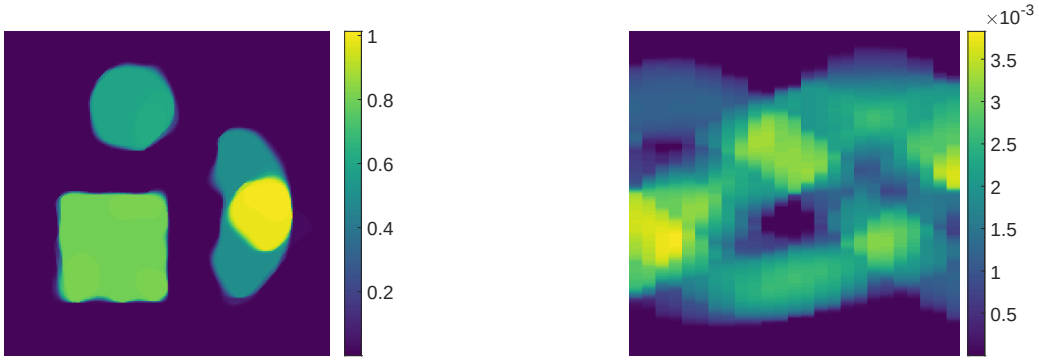

Reconstruction with respect to $\mathcal{M}_3$, noisy data, and $\omega = 4 \cdot 10^4$, $\gamma_1 = 0.1^{4.05}$. SSIM $(\mathbf{c}) = 0.8807$.

Figure 6.7.: Results for simultaneous line rotation using different reconstruction approaches.

Finally, we state results incorporating the specific sampling trajectory. We compare results including $\mathcal{K}_{3,l}\mathcal{R}$ in the reconstruction process, that is method $\mathcal{M}_3$, with those neglecting this term, i.e. method $\mathcal{M}_2$. With regard to Figure 6.4, we expect only minor differences. The according outcomes with and without added Gaussian noise (standard deviation: ca. 0.8% of u_∞) are presented in Figure 6.7. First of all, all reconstructions prove that we have removed the rotation artifacts by adapting the Radon transform to this measurement setting. Inclusion of the third component in the forward model leads to slightly higher values for structural similarity. For noisy data, the magnitude of $\mathcal{K}_{3,l}\mathcal{R}$ is close to the range of the added noise. Therefore, it is comprehensible that the increase in the SSIM value is lower compared to the noise-free setting. However, it is difficult to recognize differences when simply comparing images with the human eye.

6.5. Conclusion and outlook

We have generalized the MPI-FFL forward model to allow for different scanning trajectories. Due to the additional time dependencies via enabling simultaneous rotation and translation of the line, after executing the time derivative in the signal equation, the adapted forward operator is composed of different additive terms. We have defined bounds for these terms, which can be calculated before image reconstruction, as only parameters known from the measurement setup are required. In this way, it can be assessed whether the inclusion of the additional components is necessary or whether it is justifiable to neglect them. We investigated the new relation between the corresponding MPI measurements and the Radon transform of the particle concentration. Not every term is associated with the classic Radon transform itself, but one with a weighted version.
In this chapter, our main focus was on analyzing the rosette-shaped scanning geometry shown in Figure 6.1b, i.e. the drive frequency is a multiple of the rotation frequency. The larger the ratio of drive to rotation frequency, the closer the simultaneous and sequential rotation scheme. In our numerical results, we have considered a ratio of 25. We found that our reconstruction method including the specific trajectory is well suited for image reconstruction. Furthermore, in our examples, the utilization of the term $\mathcal{K}_1$, which connects to the operator $\mathcal{K}$ with respect to the sequential line rotation, was sufficient for the determination of particle concentration and Radon data.

Other scanning trajectories (cf. [178]) are interesting considerations for future investigations. A starting point could be the numerical analysis of the case that drive and rotation frequency are of the same order of magnitude or even show a reversed ratio in comparison to our examples. The weighting of the components of the forward model in relation to one another is then particularly interesting. This work continues with examinations regarding timely changing particle distributions. For the sake of clarity, we return to sequential scanning. We will see that for some motion the simultaneous line rotation can be interpreted to a certain extent as a kind of special case.

7. Dynamic Particle Concentrations

In this Chapter, we will consider a next step towards more realistic setup assumptions. We allow the particle concentration to vary with time. Due to the additional time dependence determining the time derivative gets again more cumbersome. Thus, for facility of inspection, we go back to the sequential line rotation scanning geometry in order to reduce the number of terms in the signal equation. We have summarized our findings in [15].

Since we already gave an overview on works regarding dynamic inverse problems in Chapter 3.1, we now restrict ourselves to dynamic approaches in MPI. For periodic dynamics, which may result e.g. from repetitive organ deformations like cardiac or pulmonary movement, the authors of [61] group the data with respect to the occurring phantom states. To this end, the motion frequency is determined based on the measurements. After this data processing, classic reconstruction schemes for static tracer distributions can be applied. An extension to multi-patch MPI is presented in [60]. In [26], the forward model is adapted to potentially fast and non-periodic dynamics. They also consider the relevance of this adjustment. To avoid motion and multi-patch artifacts, they presented a reconstruction approach based on expanding the tracer concentration using spline curves in [27]. Just recently, joint motion estimation and image reconstruction applying motion priors, which corresponds to the PDE-based model in Chapter 3.1, was considered in [25]. All these works assessed reconstruction examples for the FFP scanner, while we examine modeling and image determination for the FFL encoding scheme.
Motivated by our interest in Radon-based image reconstruction as well as the geometrical similarity of the FFL and CT scanning patterns, we model the time-varying particle concentrations via diffeomorphic motion functions, as presented for dynamic CT in Section 4.1.2. This approach allows us to relate the dynamic forward operator to an adapted Radon transform known (e.g. [80]) from dynamic CT. Regarding the FFP scanner implementation, in [51] a registration-based technique also led to a diffeomorphic transformation model for rigid motions and multi-patch MPI. While they consider image and motion estimation together, so far we assume that the dynamics are known. Nevertheless, we provide an outlook on possible strategies for the incorporation of motion determination.

Outline of the chapter: In Section 7.1, we begin with restating the motion model introduced for dynamic CT in Section 4.1.2 for MPI and accordingly adapt the forward model. We then derive the relation of this operator to Radon transforms modified with respect to the phantom dynamics in Section 7.2. Similar to the last section, the additional time dependencies result in additional components in the signal equation and we state bounds for these. Finally, in Section 7.4, we regard numerical results for synthetic data using our joint reconstruction approach incorporating motion information, as stated in Section 7.3. We present examples for both the intensity as well as the mass preservation assumption.

7.1. Forward model

First of all, we have to say that, in contrast to our former considerations, the time derivative in (5.5) does now operate on both the particle distribution as well as the mean magnetic moment

$$u(t) = -\mu_0 \int_{\mathbb{R}^3} \left(\overline{\mathbf{m}}(\mathbf{r},t) \frac{\partial}{\partial t} c(\mathbf{r},t) + c(\mathbf{r},t) \frac{\partial}{\partial t} \overline{\mathbf{m}}(\mathbf{r},t) \right) \cdot \mathbf{p}(\mathbf{r}) \, \mathrm{d}\mathbf{r}.$$

The authors of [60] assumed that the first part of the signal equation, which corresponds to the change in concentration with time, can be neglected. The authors of [27], on the other hand, incorporated both terms in modeling the voltage signal. To this end, they represented the particle distribution using spline curves. Via linking each state of the object to a static reference concentration by means of diffeomorphic motion functions, the dynamic inverse problem of determining the time-dependent concentration c can be transformed to the determination of a single reference state c_0 not depending on time and computation of the concentration derivative can be bypassed. In MPI, a single field-free line is steered through the FOV, whereas in CT a bunch of X-rays can be emitted at the same time. Hence, while in CT the time consuming part within the measurement process consists in the rotation of radiation source and detector panel and, thus, the time dependence was identified with an angle dependence, this is not the case in MPI and we consider tracer densities relying on time, angle, and space. When modeling the dynamic particle concentration, however, we proceed analogously to subsection 4.1.2 and make appropriate adjustments.

Recall that for sequential line rotation $T > 0$ denoted the scanning time needed for the FFL translation per angle. As before, we assume the following support condition for the particle distribution, now for each object state. Let $c(\cdot,\varphi,t) \in L_2\left(B_R, \mathbb{R}_0^+\right)$ for all $(\varphi,t) \in Z_T$ and, when convenient, regard the continuous extension $c(\cdot,\varphi,t) := 0$ for $\mathbf{r} \notin B_R$ (cf. Remark 4.12). We propose existence of a reference concentration $c_0 \in L_2\left(B_R, \mathbb{R}_0^+\right)$ and a motion function $\Gamma : \mathbb{R}^2 \times Z_T \to \mathbb{R}^2$ such that $\Gamma_{\varphi,t}\mathbf{r} := \Gamma(\mathbf{r},\varphi,t)$ is a diffeomorphism for all fixed $(\varphi,t) \in Z_T$ satisfying

$$\textit{(intensity pres.)} \qquad c(\mathbf{r},\varphi,t) = c_0(\Gamma_{\varphi,t}\mathbf{r}), \tag{7.1}$$

$$\textit{(mass pres.)} \qquad c(\mathbf{r},\varphi,t) = c_0(\Gamma_{\varphi,t}\mathbf{r}) \left|\det \mathrm{D}\,\Gamma_{\varphi,t}\mathbf{r}\right|. \tag{7.2}$$

Remember that c_0 could for example be chosen as one of the states the particle concentration attains during the measurement, i.e. for some reference time $t_0 \in [0,T]$ and angle $\varphi_0 \in [0,2\pi]$

$$c_0(\mathbf{r}) = c(\mathbf{r},\varphi_0,t_0).$$

Similar to before, we introduce the function

$$h_{\varphi,t}(\mathbf{y}) := \begin{cases} \left|\det \mathrm{D}\,\Gamma_{\varphi,t}^{-1}\mathbf{y}\right|, & \text{for } c \text{ as in (7.1)}, \\ 1, & \text{for } c \text{ as in (7.2)}, \end{cases}$$

in order to summarize the expressions concerning intensity and mass preservation in one formula

$$c(\mathbf{r},\varphi,t) = c_0(\Gamma_{\varphi,t}\mathbf{r})\, h_{\varphi,t}(\Gamma_{\varphi,t}\mathbf{r}) \left|\det \mathrm{D}\,\Gamma_{\varphi,t}\mathbf{r}\right|.$$

Significant movements in relation to magnetic particle imaging can be described in terms of these motion functions. Examples comprise instrument as well as bolus tracking ([74], [97], [186]). In these cases, it is even reasonable to assume affine motions. The reference concentration can be defined as the initial state of the particle distribution. Regarding instrument tracking, the starting

position of the tracer material relative to the marked device is known from the measurement setup and can be used to estimate c_0. Similarly, for bolus tracking, the initial state can be approximated from knowledge of the injection. Such advance information can be used to improve and accelerate reconstructions as well as to reduce the motion estimation problem.
By substituting $\mathbf{y} := \Gamma_{\varphi,t}\mathbf{r}$, all time dependencies can be shifted to quantities proposed to be known

$$\begin{aligned} u_l(\varphi,t) &= -\mu_0 \frac{\partial}{\partial t} \int_{\mathbb{R}^2} c(\mathbf{r},\varphi,t)\overline{m}\left(-G\,\mathbf{r}\cdot\mathbf{e}_\varphi + A\Lambda_\varphi(t)\right)\mathbf{e}_\varphi\cdot\mathbf{p}_l(\mathbf{r})\,\mathrm{d}\,\mathbf{r} \\ &= -\mu_0 \frac{\partial}{\partial t} \int_{\mathbb{R}^2} c_0\left(\Gamma_{\varphi,t}\mathbf{r}\right) h_{\varphi,t}\left(\Gamma_{\varphi,t}\mathbf{r}\right) \left|\det \mathrm{D}\,\Gamma_{\varphi,t}\mathbf{r}\right| \overline{m}\left(-G\,\mathbf{r}\cdot\mathbf{e}_\varphi + A\Lambda_\varphi(t)\right)\mathbf{e}_\varphi\cdot\mathbf{p}_l(\mathbf{r})\,\mathrm{d}\,\mathbf{r} \\ &= -\mu_0 \int_{\mathbb{R}^2} c_0(\mathbf{y}) \frac{\partial}{\partial t} h_{\varphi,t}(\mathbf{y})\,\overline{m}\left(-G\,\Gamma_{\varphi,t}^{-1}\mathbf{y}\cdot\mathbf{e}_\varphi + A\Lambda_\varphi(t)\right)\mathbf{e}_\varphi\cdot\mathbf{p}_l\left(\Gamma_{\varphi,t}^{-1}\mathbf{y}\right)\mathrm{d}\,\mathbf{y}. \end{aligned}$$

In order to ensure the above signal equation to be well-defined, we make the assumptions below.

Assumption 7.1. *Let $\Gamma_{\varphi,t}^{-1}$ and $\mathrm{D}\,\Gamma_{\varphi,t}^{-1}$ be differentiable with respect to time t. Further, we denote the corresponding partial derivatives as*

$$\left(\Gamma_{\varphi,t}^{-1}\right)' := \frac{\partial}{\partial t}\Gamma_{\varphi,t}^{-1}, \quad \left(\mathrm{D}\,\Gamma_{\varphi,t}^{-1}\right)' := \frac{\partial}{\partial t}\mathrm{D}\,\Gamma_{\varphi,t}^{-1}, \quad h'_{\varphi,t} := \frac{\partial}{\partial t}h_{\varphi,t}.$$

Finally, we assume the existence of constants $C_{\varphi,t},\ D_{\varphi,t} > 0$ such that for all $\mathbf{y}\in\mathbb{R}^2$ and $(\varphi,t)\in Z_T$, it holds

$$\left\|\left(\Gamma_{\varphi,t}^{-1}\right)'\mathbf{y}\right\| \le \frac{A}{G}C_{\varphi,t}, \quad \left|h'_{\varphi,t}(\mathbf{y})\right| \le D_{\varphi,t}.$$

Notice that Assumption 7.1 does not impose a restriction on actual applications. Speed and scope of the motion are inherently limited due to physiological constraints. Furthermore, only discrete measurements are available in practice, i.e. a smooth motion function matching the data at the discrete time points can be determined (see [81]). We formulate the forward operator for time-varying particle densities.

Definition 7.2. *Define $\mathcal{A}_l^\Gamma :\ L_2\left(B_R,\mathbb{R}_0^+\right) \to L_2\left(Z_T,\mathbb{R}\right)$ as*

$$\mathcal{A}_l^\Gamma c_0(\varphi,t) := -\mu_0 \int_{\mathbb{R}^2} c_0(\mathbf{y}) \frac{\partial}{\partial t} h_{\varphi,t}(\mathbf{y})\,\overline{m}\left(-G\,\Gamma_{\varphi,t}^{-1}\mathbf{y}\cdot\mathbf{e}_\varphi + A\Lambda_\varphi(t)\right)\mathbf{e}_\varphi\cdot\mathbf{p}_l\left(\Gamma_{\varphi,t}^{-1}\mathbf{y}\right)\mathrm{d}\,\mathbf{y}. \tag{7.3}$$

The forward operator for MPI-FFL scanner, allowing dynamic particle concentrations, is given by $\mathcal{A}^\Gamma :\ L_2\left(B_R,\mathbb{R}_0^+\right) \to L_2\left(Z_T,\mathbb{R}^L\right)$ with $\mathcal{A}^\Gamma c_0(\varphi,t) = \left\{\mathcal{A}_l^\Gamma c_0(\varphi,t)\right\}_{l=1,\dots,L}$.

Thus, the dynamic linear ill-posed inverse problem we aim to solve in this chapter is given by

$$\mathcal{A}^\Gamma c_0 = \mathbf{u}$$

with measured data $\mathbf{u} = \{u_l\}_{l=1,\dots,L}$ and forward operator $\mathcal{A}^\Gamma$. Knowledge of reference state and motion function then allows determination of the particle distribution at each time instance.

7.2. Relation between MPI and Radon data

We proceed similar to the last chapter in order to derive a connection between the MPI-FFL forward model (7.3) and the adapted version of the Radon transform (4.8) derived in Subsection 4.1.2. However, we have to make a simple adjustment since, as already mentioned, there is only one FFL per time instance and thus, we cannot identify time and angle. We therefore use the following

formulation for the dynamic Radon transform

$$\mathcal{R}^{\Gamma} c_0 (\varphi, t, s) := \int_{\mathbb{R}^2} c_0 (\mathbf{y})\, h_{\varphi,t} (\mathbf{y})\, \delta \left(\Gamma_{\varphi,t}^{-1} \mathbf{y} \cdot \mathbf{e}_{\varphi} - s \right) \mathrm{d}\, \mathbf{y}. \tag{7.4}$$

Comparable to the simultaneous line rotation setting, we additionally introduce a weighted version of $\mathcal{R}^{\Gamma}$, but this time more generally via inserting a bounded weight function $w_{\varphi,t} : \mathbb{R}^2 \to \mathbb{R}$

$$\mathcal{R}_w^{\Gamma} c_0 (\varphi, t, s) := \int_{\mathbb{R}^2} w_{\varphi,t} (\mathbf{y})\, c_0 (\mathbf{y})\, h_{\varphi,t} (\mathbf{y})\, \delta \left(\Gamma_{\varphi,t}^{-1} \mathbf{y} \cdot \mathbf{e}_{\varphi} - s \right) \mathrm{d}\, \mathbf{y}. \tag{7.5}$$

Therewith, the forward operator for MPI using a field-free line and allowing dynamic particle concentrations, can be reformulated as follows.

Theorem 7.3. *Given spatially homogeneous receive coil sensitivities, the MPI-FFL forward operator with respect to the l-th receive coil (7.3) can be written as*

$$\mathcal{A}_l^{\Gamma} = \mathcal{K}_{1,l} \circ \mathcal{R}^{\Gamma} + \mathcal{K}_{2,l} \circ \mathcal{R}_{\alpha}^{\Gamma} + \mathcal{K}_{3,l} \circ \mathcal{R}_{\beta}^{\Gamma} \tag{7.6}$$

with convolution operators $\mathcal{K}_{i,l} : L_2 (Z_T \times \mathbb{R}, \mathbb{R}) \to L_2 (Z_T, \mathbb{R})$, *for* $i = 1, 2, 3$ *and* $l \in \{1, \ldots, L\}$,

$$\begin{aligned}
\mathcal{K}_{1,l} f (\varphi, t) &= -\mu_0\, A \Lambda_{\varphi}' (t)\, \mathbf{e}_{\varphi} \cdot \mathbf{p}_l\, \overline{m}' (G \cdot) * f (\varphi, t, \cdot) (s_{\varphi,t}), \\
\mathcal{K}_{2,l} f (\varphi, t) &= \mu_0\, G\, \mathbf{e}_{\varphi} \cdot \mathbf{p}_l\, \overline{m}' (G \cdot) * f (\varphi, t, \cdot) (s_{\varphi,t}), \\
\mathcal{K}_{3,l} f (\varphi, t) &= -\mu_0\, \mathbf{e}_{\varphi} \cdot \mathbf{p}_l\, \overline{m}\, (G \cdot) * f (\varphi, t, \cdot) (s_{\varphi,t}),
\end{aligned}$$

with $s_{\varphi,t} := \dfrac{A}{G} \Lambda_{\varphi} (t)$ *as well as weight functions* $\alpha_{\varphi,t}, \beta_{\varphi,t} : \mathbb{R}^2 \to \mathbb{R}$

$$\alpha_{\varphi,t} (\mathbf{y}) = \left(\Gamma_{\varphi,t}^{-1} \right)' \mathbf{y} \cdot \mathbf{e}_{\varphi}, \quad \beta_{\varphi,t} (\mathbf{y}) = \frac{h_{\varphi,t}' (\mathbf{y})}{h_{\varphi,t} (\mathbf{y})}.$$

Proof. We start with the determination of the derivative in (7.3), which yields

$$\begin{aligned}
\mathcal{A}_l^{\Gamma} c_0 (\varphi, t) = &- \mu_0\, A \Lambda_{\varphi}' (t)\, \mathbf{e}_{\varphi} \cdot \mathbf{p}_l \int_{\mathbb{R}^2} c_0 (\mathbf{y})\, h_{\varphi,t} (\mathbf{y})\, \overline{m}' \left(-G\, \Gamma_{\varphi,t}^{-1} \mathbf{y} \cdot \mathbf{e}_{\varphi} + A \Lambda_{\varphi} (t) \right) \mathrm{d}\, \mathbf{y} \\
&+ \mu_0\, G\, \mathbf{e}_{\varphi} \cdot \mathbf{p}_l \int_{\mathbb{R}^2} c_0 (\mathbf{y})\, h_{\varphi,t} (\mathbf{y}) \left(\Gamma_{\varphi,t}^{-1} \right)' \mathbf{y} \cdot \mathbf{e}_{\varphi} \\
&\qquad \times \overline{m}' \left(-G\, \Gamma_{\varphi,t}^{-1} \mathbf{y} \cdot \mathbf{e}_{\varphi} + A \Lambda_{\varphi} (t) \right) \mathrm{d}\, \mathbf{y} \\
&- \mu_0\, \mathbf{e}_{\varphi} \cdot \mathbf{p}_l \int_{\mathbb{R}^2} c_0 (\mathbf{y})\, h_{\varphi,t}' (\mathbf{y})\, \overline{m}\, \left(-G\, \Gamma_{\varphi,t}^{-1} \mathbf{y} \cdot \mathbf{e}_{\varphi} + A \Lambda_{\varphi} (t) \right) \mathrm{d}\, \mathbf{y} \\
=: &- \mu_0\, \mathbf{e}_{\varphi} \cdot \mathbf{p}_l \Big(A \Lambda_{\varphi}' (t)\; I (\varphi, t) - G\, II (\varphi, t) + III (\varphi, t) \Big).
\end{aligned} \tag{7.7}$$

We investigate the integrals separately. Inspired by [114] and the last chapter, we introduce $\mathbf{R}^{-\varphi} \Gamma_{\varphi,t}^{-1} \mathbf{y} =: \mathbf{r}' =: (v', s')^T$ using the rotation matrix $\mathbf{R}^{\varphi}$ defined in (5.13). Remember that by (5.14) we get

$$\mathrm{FFL} \left(\mathbf{e}_{\varphi}, s' \right) = \left\{ \mathbf{r} \in \mathbb{R}^2 : \mathbf{r} \cdot \mathbf{e}_{\varphi} = s' \right\} = \left\{ s'\, \mathbf{e}_{\varphi} - v'\, \mathbf{e}_{\varphi}^{\perp} : v' \in \mathbb{R} \right\} = \left\{ \mathbf{R}^{\varphi} \begin{pmatrix} v' \\ s' \end{pmatrix} : v' \in \mathbb{R} \right\}.$$

Exploiting the definition of the adapted Radon transform (7.4), we get for the first integral in (7.7)

$$\begin{aligned} I(\varphi,t) &:= \int_{\mathbb{R}^2} c_0(\mathbf{y})\, h_{\varphi,t}(\mathbf{y})\, \overline{m}'\left(-G\,\Gamma_{\varphi,t}^{-1}\mathbf{y}\cdot\mathbf{e}_\varphi + A\Lambda_\varphi(t)\right)\mathrm{d}\,\mathbf{y} \\ &= \int_{\mathbb{R}^2} c_0\left(\Gamma_{\varphi,t}\mathbf{R}^\varphi\mathbf{r}'\right) h_{\varphi,t}\left(\Gamma_{\varphi,t}\mathbf{R}^\varphi\mathbf{r}'\right)\left|\det \mathrm{D}\,\Gamma_{\varphi,t}\left(\mathbf{R}^\varphi\mathbf{r}'\right)\right|\ \overline{m}'\left(-G\,\mathbf{R}^\varphi\mathbf{r}'\cdot\mathbf{e}_\varphi + A\Lambda_\varphi(t)\right)\mathrm{d}\,\mathbf{r}' \\ &= \int_{\mathbb{R}} \overline{m}'\left(-G\,s' + A\Lambda_\varphi(t)\right)\ \int_{\mathbb{R}^2} c_0\left(\Gamma_{\varphi,t}\mathbf{r}\right) h_{\varphi,t}\left(\Gamma_{\varphi,t}\mathbf{r}\right)\left|\det \mathrm{D}\,\Gamma_{\varphi,t}\mathbf{r}\right|\delta\left(\mathbf{r}\cdot\mathbf{e}_\varphi - s'\right)\mathrm{d}\,\mathbf{r}\,\mathrm{d}\,s' \\ &= \int_{\mathbb{R}} \mathcal{R}^\Gamma c_0\left(\varphi,t,s'\right)\overline{m}'\left(-G\,s' + A\Lambda_\varphi(t)\right)\mathrm{d}\,s' \\ &= \left[\overline{m}'\left(G\,\cdot\right) * \mathcal{R}^\Gamma c_0\left(\varphi,t,\cdot\right)\right]\left(\frac{A}{G}\Lambda_\varphi(t)\right). \end{aligned}$$

Proceeding similar for the other two integrals in (7.7), we arrive at

$$\begin{aligned} II(\varphi,t) &:= \int_{\mathbb{R}^2} c_0(\mathbf{y})\, h_{\varphi,t}(\mathbf{y})\left(\Gamma_{\varphi,t}^{-1}\right)'\mathbf{y}\cdot\mathbf{e}_\varphi\ \overline{m}'\left(-G\,\Gamma_{\varphi,t}^{-1}\mathbf{y}\cdot\mathbf{e}_\varphi + A\Lambda_\varphi(t)\right)\mathrm{d}\,\mathbf{y} \\ &= \int_{\mathbb{R}^2} c_0\left(\Gamma_{\varphi,t}\mathbf{R}^\varphi\mathbf{r}'\right) h_{\varphi,t}\left(\Gamma_{\varphi,t}\mathbf{R}^\varphi\mathbf{r}'\right)\left(\Gamma_{\varphi,t}^{-1}\right)'\left(\Gamma_{\varphi,t}\mathbf{R}^\varphi\mathbf{r}'\right)\cdot\mathbf{e}_\varphi\ \left|\det \mathrm{D}\,\Gamma_{\varphi,t}\left(\mathbf{R}^\varphi\mathbf{r}'\right)\right| \\ &\qquad \times \overline{m}'\left(-G\,\mathbf{R}^\varphi\mathbf{r}'\cdot\mathbf{e}_\varphi + A\Lambda_\varphi(t)\right)\mathrm{d}\,\mathbf{r}' \\ &= \int_{\mathbb{R}} \mathcal{R}_\alpha^\Gamma c_0\left(\varphi,t,s'\right)\overline{m}'\left(-G\,s' + A\Lambda_\varphi(t)\right)\mathrm{d}\,s' \\ &= \left[\overline{m}'\left(G\,\cdot\right) * \mathcal{R}_\alpha^\Gamma c_0\left(\varphi,t,\cdot\right)\right]\left(\frac{A}{G}\Lambda_\varphi(t)\right), \end{aligned}$$

as well as

$$\begin{aligned} III(\varphi,t) &:= \int_{\mathbb{R}^2} c_0(\mathbf{y})\, h'_{\varphi,t}(\mathbf{y})\,\overline{m}\left(-G\,\Gamma_{\varphi,t}^{-1}\mathbf{y}\cdot\mathbf{e}_\varphi + A\Lambda_\varphi(t)\right)\mathrm{d}\,\mathbf{y} \\ &= \int_{\mathbb{R}^2} c_0\left(\Gamma_{\varphi,t}\mathbf{R}^\varphi\mathbf{r}'\right) h_{\varphi,t}\left(\Gamma_{\varphi,t}\mathbf{R}^\varphi\mathbf{r}'\right)\frac{h'_{\varphi,t}\left(\Gamma_{\varphi,t}\mathbf{R}^\varphi\mathbf{r}'\right)}{h_{\varphi,t}\left(\Gamma_{\varphi,t}\mathbf{R}^\varphi\mathbf{r}'\right)}\left|\det \mathrm{D}\,\Gamma_{\varphi,t}\left(\mathbf{R}^\varphi\mathbf{r}'\right)\right| \\ &\qquad \times \overline{m}\left(-G\,\mathbf{R}^\varphi\mathbf{r}'\cdot\mathbf{e}_\varphi + A\Lambda_\varphi(t)\right)\mathrm{d}\,\mathbf{r}' \\ &= \int_{\mathbb{R}} \mathcal{R}_\beta^\Gamma c_0\left(\varphi,t,s'\right)\overline{m}\left(-G\,s' + A\Lambda_\varphi(t)\right)\mathrm{d}\,s' \\ &= \left[\overline{m}\left(G\,\cdot\right) * \mathcal{R}_\beta^\Gamma c_0\left(\varphi,t,\cdot\right)\right]\left(\frac{A}{G}\Lambda_\varphi(t)\right). \end{aligned}$$

Putting everything together, we finally obtain

$$\begin{aligned} \mathcal{A}_l^\Gamma c_0(\varphi,t) &= -\mu_0\,\mathbf{e}_\varphi\cdot\mathbf{p}_l\left(A\Lambda'_\varphi(t)\ I(\varphi,t) - G\,II(\varphi,t) + III(\varphi,t)\right) \\ &= \left[\mathcal{K}_{1,l}\circ\mathcal{R}^\Gamma + \mathcal{K}_{2,l}\circ\mathcal{R}_\alpha^\Gamma + \mathcal{K}_{3,l}\circ\mathcal{R}_\beta^\Gamma\right]c_0(\varphi,t). \end{aligned}$$

□

Via choosing $\Gamma_{\varphi,t} = \mathrm{Id}$, also static particle distributions can be modeled within the introduced framework. Moreover, in that case Theorem 7.3 reduces to Theorem 5.4.

Corollary 7.4. *Assume the existence of scalar functions* $\widetilde{\alpha}_{\varphi,t}, \widetilde{\beta}_{\varphi,t} : \mathbb{R} \to \mathbb{R}$ *satisfying*

$$\alpha_{\varphi,t}(\mathbf{y}) = \widetilde{\alpha}_{\varphi,t}\left(\Gamma_{\varphi,t}^{-1}\mathbf{y}\cdot\mathbf{e}_\varphi\right), \quad \beta_{\varphi,t}(\mathbf{y}) = \widetilde{\beta}_{\varphi,t}\left(\Gamma_{\varphi,t}^{-1}\mathbf{y}\cdot\mathbf{e}_\varphi\right).$$

Then, formula (7.6) simplifies to

$$\mathcal{A}_l^\Gamma = \mathcal{K}_l \circ \mathcal{R}^\Gamma. \tag{7.8}$$

Thereby, the operator $\mathcal{K}_l : L_2(Z_T \times \mathbb{R}, \mathbb{R}) \to L_2(Z_T, \mathbb{R})$ *is for* $l \in \{1, \dots, L\}$ *defined as*

$$\mathcal{K}_l f(\varphi, t) = \left[\mathcal{K}_{1,l} f + \mathcal{K}_{2,l}(\widetilde{\alpha}_{\varphi,t} f) + \mathcal{K}_{3,l}\left(\widetilde{\beta}_{\varphi,t} f\right)\right](\varphi, t).$$

Proof. Inserting the given scalar functions for $\alpha_{\varphi,t}$ respectively $\beta_{\varphi,t}$ into the definition of the weighted Radon transform (7.5), we simply obtain

$$\mathcal{R}_\alpha^\Gamma c_0(\varphi, t, s) = \widetilde{\alpha}_{\varphi,t}(s)\, \mathcal{R}^\Gamma c_0(\varphi, t, s), \quad \mathcal{R}_\beta^\Gamma c_0(\varphi, t, s) = \widetilde{\beta}_{\varphi,t}(s)\, \mathcal{R}^\Gamma c_0(\varphi, t, s).$$

Expression (7.8) then presents a direct consequence of the last theorem. □

Remark 7.5. *The third component* $\mathcal{K}_{3,l} \circ \mathcal{R}_\beta^\Gamma$ *in (7.6) depends on the chosen preservation assumption.*

- *Supposing mass conservation, we have* $h_{\varphi,t}(\mathbf{y}) = 1$. *It follows*

$$\beta_{\varphi,t}(\mathbf{y}) = \frac{h'_{\varphi,t}(\mathbf{y})}{h_{\varphi,t}(\mathbf{y})} = 0 \quad \Longrightarrow \quad \mathcal{K}_{3,l} \circ \mathcal{R}_\beta^\Gamma = 0.$$

- *Supposing intensity conservation, we have* $h_{\varphi,t}(\mathbf{y}) = \left|\det \mathrm{D}\, \Gamma_{\varphi,t}^{-1}\mathbf{y}\right|$. *It follows*

$$h'_{\varphi,t}(\mathbf{y}) = \frac{\partial}{\partial t}\left|\det \mathrm{D}\, \Gamma_{\varphi,t}^{-1}\mathbf{y}\right| = \frac{\det \mathrm{D}\, \Gamma_{\varphi,t}^{-1}\mathbf{y}\, \frac{\partial}{\partial t} \det \mathrm{D}\, \Gamma_{\varphi,t}^{-1}\mathbf{y}}{\left|\det \mathrm{D}\, \Gamma_{\varphi,t}^{-1}\mathbf{y}\right|}.$$

  Exploiting Jacobi's formula, we obtain

$$\frac{\partial}{\partial t} \det \mathrm{D}\, \Gamma_{\varphi,t}^{-1}\mathbf{y} = \det \mathrm{D}\, \Gamma_{\varphi,t}^{-1}\mathbf{y}\ \mathrm{tr}\left[\left(\mathrm{D}\, \Gamma_{\varphi,t}^{-1}\right)^{-1}(\mathbf{y})\ \left(\mathrm{D}\, \Gamma_{\varphi,t}^{-1}\right)'(\mathbf{y})\right],$$

  which finally results in

$$\begin{aligned}\beta_{\varphi,t}(\mathbf{y}) &= \frac{\frac{\partial}{\partial t}\left|\det \mathrm{D}\, \Gamma_{\varphi,t}^{-1}\mathbf{y}\right|}{\left|\det \mathrm{D}\, \Gamma_{\varphi,t}^{-1}\mathbf{y}\right|} = \frac{\det \mathrm{D}\, \Gamma_{\varphi,t}^{-1}\mathbf{y}\, \frac{\partial}{\partial t} \det \mathrm{D}\, \Gamma_{\varphi,t}^{-1}\mathbf{y}}{\left|\det \mathrm{D}\, \Gamma_{\varphi,t}^{-1}\mathbf{y}\right|^2} = \frac{\frac{\partial}{\partial t} \det \mathrm{D}\, \Gamma_{\varphi,t}^{-1}\mathbf{y}}{\det \mathrm{D}\, \Gamma_{\varphi,t}^{-1}\mathbf{y}} \\ &= \mathrm{tr}\left[\left(\mathrm{D}\, \Gamma_{\varphi,t}^{-1}\right)^{-1}(\mathbf{y})\ \left(\mathrm{D}\, \Gamma_{\varphi,t}^{-1}\right)'(\mathbf{y})\right] = \mathrm{tr}\left[\mathrm{D}\, \Gamma_{\varphi,t}\left(\Gamma_{\varphi,t}^{-1}\mathbf{y}\right)\ \left(\mathrm{D}\, \Gamma_{\varphi,t}^{-1}\right)'(\mathbf{y})\right].\end{aligned}$$

Let us now consider a specific set of dynamics, namely affine diffeomorphic motions, moreover satisfying Assumption 7.1. Then, the motion functions can be written in the form

$$\Gamma_{\varphi,t}^{-1}\mathbf{y} = \mathbf{A}_{\varphi,t}\mathbf{y} + \mathbf{b}_{\varphi,t}$$

with $\mathbf{b}_{\varphi,t} \in \mathbb{R}^2$, $\mathbf{A}_{\varphi,t} \in \mathbb{R}^{2\times 2}$ such that $\det \mathbf{A}_{\varphi,t} \neq 0$. Further, $\mathbf{b}'_{\varphi,t} \in \mathbb{R}^2$, $\mathbf{A}'_{\varphi,t} \in \mathbb{R}^{2\times 2}$ denote the corresponding partial derivatives with respect to time assumed to be bounded.
According to the previous remark, in case of mass conservation it always holds the nice property that $\beta_{\varphi,t} = 0$ decreasing the number of ingredients in the signal equation. Fortunately, for affine motions, things become easier also for the intensity preserving setting, as

$$\beta_{\varphi,t}(\mathbf{y}) = \mathrm{tr}\left[\mathbf{A}_{\varphi,t}^{-1}\, \mathbf{A}'_{\varphi,t}\right] =: \widetilde{\beta}_{\varphi,t} \tag{7.9}$$

is constant for fixed angle φ and time t and especially does not depend on the spatial variable $\mathbf{y}$.

However, even for affine motion model, the weighting function $\alpha_{\varphi,t}(\mathbf{y})$ can, in general, not be expressed as in Corollary 7.4. Nevertheless, we extract the spatially independent component

$$\alpha_{\varphi,t}(\mathbf{y}) = \left(\mathbf{A}'_{\varphi,t}\mathbf{y} + \mathbf{b}'_{\varphi,t}\right) \cdot \mathbf{e}_\varphi =: \mathbf{A}'_{\varphi,t}\mathbf{y} \cdot \mathbf{e}_\varphi + \widetilde{\alpha}_{\varphi,t}.$$

Thus, in total we arrive at the following formulation for the forward operator

$$\mathcal{A}_l^\Gamma = \mathcal{K}_l \circ \mathcal{R}^\Gamma + \mathcal{K}_{2,l} \circ \mathcal{R}^\Gamma_{\mathbf{A}'_{\varphi,t}\mathbf{y}\cdot\mathbf{e}_\varphi}.$$

Example 7.6. *Choose $a_{\varphi,t} \neq 0$ such that Assumption 7.1 is satisfied for the deformation*

$$\mathbf{A}_{\varphi,t} := \mathbf{R}^\varphi \begin{pmatrix} a_{\varphi,t} & 0 \\ 0 & 1 \end{pmatrix} \mathbf{R}^{-\varphi} \quad \Longrightarrow \quad \Gamma^{-1}_{\varphi,t}\mathbf{y} := \mathbf{A}_{\varphi,t}\mathbf{y} = a_{\varphi,t}\left(\mathbf{y}\cdot\mathbf{e}_\varphi^\perp\right)\mathbf{e}_\varphi^\perp + (\mathbf{y}\cdot\mathbf{e}_\varphi)\,\mathbf{e}_\varphi.$$

Therewith, the object is only distorted in directions orthogonal to the FFL translation. We compute for the time derivative

$$\mathbf{A}'_{\varphi,t}\mathbf{y} = a'_{\varphi,t}\left(\mathbf{y}\cdot\mathbf{e}_\varphi^\perp\right)\mathbf{e}_\varphi^\perp \quad \Longrightarrow \quad \alpha_{\varphi,t}(\mathbf{y}) = \mathbf{A}'_{\varphi,t}\mathbf{y}\cdot\mathbf{e}_\varphi = 0$$

and $\mathcal{K}_{2,l}\circ\mathcal{R}^\Gamma_\alpha = 0$. If a translation $\mathbf{b}_{\varphi,t}$ is also included in the movement, $\alpha_{\varphi,t}(\mathbf{y})$ is generally spatially independent, but only disappears for either a time-independent shift or for those translations that run parallel to the field-free line. At last, this example is especially appealing as here the dynamic Radon transform is directly linked to the classical static Radon transform

$$\begin{aligned}
\mathcal{R}^\Gamma c_0(\varphi,t,s) &= \int_{\mathbb{R}^2} c_0(\mathbf{y})\, h_{\varphi,t}(\mathbf{y})\, \delta\left(\mathbf{A}_{\varphi,t}\mathbf{y}\cdot\mathbf{e}_\varphi + \mathbf{b}_{\varphi,t}\cdot\mathbf{e}_\varphi - s\right) \mathrm{d}\,\mathbf{y} \\
&= \int_{\mathbb{R}^2} c_0(\mathbf{y})\, h_{\varphi,t}\, \delta\left(\mathbf{y}\cdot\mathbf{e}_\varphi + \mathbf{b}_{\varphi,t}\cdot\mathbf{e}_\varphi - s\right) \mathrm{d}\,\mathbf{y} \\
&= h_{\varphi,t}\, \mathcal{R}c_0(\varphi,t,s - \mathbf{b}_{\varphi,t}\cdot\mathbf{e}_\varphi)
\end{aligned}$$

with

$$h_{\varphi,t} := \begin{cases} |a_{\varphi,t}|, & \text{for } c \text{ as in (7.1)}, \\ 1, & \text{for } c \text{ as in (7.2)}. \end{cases}$$

We infer that for phantom translations in general and deformations restricted to directions perpendicular to the FFL movement, $\alpha_{\varphi,t}(\mathbf{y}) = \widetilde{\alpha}_{\varphi,t}$ does not depend on the spatial variable.

Example 7.7. *Choose $a_{\varphi,t} \neq 0$ such that Assumption 7.1 is satisfied for the rigid phantom rotation*

$$\Gamma^{-1}_{\varphi,t}\mathbf{y} = \mathbf{R}^{a_{\varphi,t}}\mathbf{y}.$$

A simple computation yields

$$\Gamma^{-1}_{\varphi,t}\mathbf{y}\cdot\mathbf{e}_\varphi = \mathbf{y}\cdot\mathbf{e}_{\varphi-a_{\varphi,t}}, \quad \det \mathrm{D}\,\Gamma^{-1}_{\varphi,t}\mathbf{y} = 1$$

and therewith

$$\alpha_{\varphi,t} = \left(\Gamma^{-1}_{\varphi,t}\right)'\mathbf{y}\cdot\mathbf{e}_\varphi = -a'_{\varphi,t}\,\mathbf{y}\cdot\mathbf{e}^\perp_{\varphi-a_{\varphi,t}}, \quad \beta_{\varphi,t} = 0.$$

Insertion into the definition of $\mathcal{R}^\Gamma$ as well as $\mathcal{R}^\Gamma_\alpha$ directly results in

$$\mathcal{R}^\Gamma c_0(\varphi,t,s) = \mathcal{R}c_0\left(\mathbf{e}_{\varphi-a_{\varphi,t}}, s\right), \quad \mathcal{R}^\Gamma_\alpha c_0(\varphi,t,s) = -\alpha'_{\varphi,t}\widetilde{\mathcal{R}}c_0\left(\mathbf{e}_{\varphi-a_{\varphi,t}}, s\right).$$

Comparison with Theorem 6.2 yields that rigid phantom rotations are highly correlated to the simultaneous line rotation setting. This observation is self-evident, as arithmetically it makes no difference whether we rotate the phantom or regard an oppositely rotating line. However, it is not equivalent as for line rotation the orientation of the magnetic field direction relative to the receive coil sensitivity changes, which is not the case for phantom rotation.

Remark 7.8. *The relation of the MPI-FFL forward operator to the dynamic Radon transform potentially enables access to the numerous results and techniques concerning computerized tomography. This includes fast reconstruction methods building on inversion formulas (cf. [76], [144]) or examination of the information contained in measurements using microlocal analysis (e.g. [81], [83], [120]). For instance, setting $a_{\varphi,t} = \varphi$ in the last example leads to severely insufficient data, because it contains information for only one angle, even if measurements are executed for numerous field-free line orientations.*

Analogous to the last chapter, we conclude this section by providing estimates for the, in comparison to the ideal case, additional terms $\mathcal{K}_{2,l} \circ \mathcal{R}^{\Gamma}_{\alpha}$ as well as $\mathcal{K}_{3,l} \circ \mathcal{R}^{\Gamma}_{\beta}$ for $l \in \{1, \dots, L\}$.

Lemma 7.9. *It holds that*

$$\left|\mathcal{K}_{1,l}\mathcal{R}^{\Gamma} c_0\left(\varphi, t\right)\right| \quad \geq \quad \left|\frac{\Lambda'_{\varphi}(t)}{C_{\varphi,t}}\right| \left|\mathcal{K}_{2,l}\mathcal{R}^{\Gamma}_{\alpha} c_0\left(\varphi, t\right)\right|.$$

Proof. Relying on Assumption 7.1, the weighted Radon transform can be bounded as follows

$$\begin{aligned}
\mathcal{R}^{\Gamma}_{\alpha} c_0\left(\varphi, t, s\right) &= \int_{\mathbb{R}^2} \alpha_{\varphi,t}\left(\mathbf{y}\right) c_0\left(\mathbf{y}\right) h_{\varphi,t}\left(\mathbf{y}\right) \delta\left(\Gamma^{-1}_{\varphi,t}\mathbf{y} \cdot \mathbf{e}_{\varphi} - s\right) \mathrm{d}\,\mathbf{y} \\
&\leq \int_{\mathbb{R}^2} \left\|\left(\Gamma^{-1}_{\varphi,t}\right)' \mathbf{y}\right\| c_0\left(\mathbf{y}\right) h_{\varphi,t}\left(\mathbf{y}\right) \delta\left(\Gamma^{-1}_{\varphi,t}\mathbf{y} \cdot \mathbf{e}_{\varphi} - s\right) \mathrm{d}\,\mathbf{y} \\
&\leq \frac{A}{G} C_{\varphi,t} \mathcal{R}^{\Gamma} c_0\left(\varphi, t, s\right).
\end{aligned}$$

This directly yields

$$\begin{aligned}
\left|\mathcal{K}_{1,l}\mathcal{R}^{\Gamma} c_0\left(\varphi, t\right)\right| &= \left|\mu_0\, \mathbf{e}_{\varphi} \cdot \mathbf{p}_l\, A\, \Lambda'_{\varphi}(t)\, \overline{m}'\left(G\,\cdot\right) * \mathcal{R}^{\Gamma} c_0\left(\varphi, t, \cdot\right)\left(s_{\varphi,t}\right)\right| \\
&\geq \left|\mu_0\, \mathbf{e}_{\varphi} \cdot \mathbf{p}_l\, G\, \frac{\Lambda'_{\varphi}(t)}{C_{\varphi,t}}\, \overline{m}'\left(G\,\cdot\right) * \mathcal{R}^{\Gamma}_{\alpha} c_0\left(\varphi, t, \cdot\right)\left(s_{\varphi,t}\right)\right| \\
&= \left|\frac{\Lambda'_{\varphi}(t)}{C_{\varphi,t}}\right| \left|\mathcal{K}_{2,l}\mathcal{R}^{\Gamma}_{\alpha} c_0\left(\varphi, t\right)\right|.
\end{aligned}$$

□

This lemma states that the size relation between $\mathcal{K}_{1,l}\mathcal{R}^{\Gamma}$ and $\mathcal{K}_{2,l}\mathcal{R}^{\Gamma}_{\alpha}$ correlates to the ratio between FFL translation velocity and speed of motion.

Lemma 7.10. *Define $\overline{m}'_{\infty} := \max_{\lambda \in \mathbb{R}} \overline{m}'\left(\lambda\right)$ and let c_{max} be the maximal particle concentration during measurements. Then, it holds that*

$$\begin{aligned}
\left|\mathcal{K}_{2,l}\mathcal{R}^{\Gamma}_{\alpha} c_0\left(\varphi, t\right)\right| &\leq \mu_0 \left|\mathbf{e}_{\varphi} \cdot \mathbf{p}_l\right| \overline{m}'_{\infty}\, A\, C_{\varphi,t}\, c_{\max} \pi R^2, \\
\left|\mathcal{K}_{3,l}\mathcal{R}^{\Gamma}_{\beta} c_0\left(\varphi, t\right)\right| &\leq \mu_0 \left|\mathbf{e}_{\varphi} \cdot \mathbf{p}_l\right| m \qquad D_{\varphi,t}\, c_{\max} \pi R^2.
\end{aligned}$$

Proof. Exploiting Assumption 7.1, we estimate based on the proof of Theorem 7.3

$$\begin{aligned}
\left|\mathcal{K}_{2,l}\mathcal{R}_\alpha^\Gamma c_0\left(\varphi,t\right)\right| &= \left|\mu_0\,\mathbf{e}_\varphi\cdot\mathbf{p}_l\,G\int_{\mathbb{R}^2} c_0\left(\mathbf{y}\right)h_{\varphi,t}\left(\mathbf{y}\right)\overline{m}'\left(-G\,\Gamma_{\varphi,t}^{-1}\mathbf{y}\cdot\mathbf{e}_\varphi+A\Lambda_\varphi(t)\right)\left(\Gamma_{\varphi,t}^{-1}\right)'\mathbf{y}\cdot\mathbf{e}_\varphi\,\mathrm{d}\,\mathbf{y}\right| \\
&\leq \mu_0\left|\mathbf{e}_\varphi\cdot\mathbf{p}_l\right|\,A\,C_{\varphi,t}\left|\int_{\mathbb{R}^2} c\left(\mathbf{r},\varphi,t\right)\,\overline{m}'\left(-G\,\mathbf{r}\cdot\mathbf{e}_\varphi+A\Lambda_\varphi(t)\right)\,\mathrm{d}\,\mathbf{r}\right| \\
&\leq \mu_0\left|\mathbf{e}_\varphi\cdot\mathbf{p}_l\right|\overline{m}'_\infty\,A\,C_{\varphi,t}\left|\int_{\mathbb{R}^2} c\left(\mathbf{r},\varphi,t\right)\,\mathrm{d}\,\mathbf{r}\right| \\
&\leq \mu_0\left|\mathbf{e}_\varphi\cdot\mathbf{p}_l\right|\overline{m}'_\infty\,A\,C_{\varphi,t}\,c_{\max}\pi R^2.
\end{aligned}$$

Remember that according to the Langevin model (5.7) and (5.8) the modulus of the mean magnetic moment is bounded by m. Hence, we determine

$$\begin{aligned}
\left|\mathcal{K}_{3,l}\mathcal{R}_\alpha^\Gamma c_0\left(\varphi,t\right)\right| &= \left|\mu_0\,\mathbf{e}_\varphi\cdot\mathbf{p}_l\int_{\mathbb{R}^2} c_0\left(\mathbf{y}\right)\overline{m}\left(-G\,\Gamma_{\varphi,t}^{-1}\mathbf{y}\cdot\mathbf{e}_\varphi+A\Lambda_\varphi(t)\right)h'_{\varphi,t}\left(\mathbf{y}\right)\,\mathrm{d}\,\mathbf{y}\right| \\
&\leq \mu_0\left|\mathbf{e}_\varphi\cdot\mathbf{p}_l\right|m\,D_{\varphi,t}\left|\int_{\mathbb{R}^2} c_0\left(\mathbf{y}\right)\,\mathrm{d}\,\mathbf{y}\right| \\
&\leq \mu_0\left|\mathbf{e}_\varphi\cdot\mathbf{p}_l\right|m\,D_{\varphi,t}\,c_{\max}\pi R^2.
\end{aligned}$$

□

Lemma 7.9 shows that $\mathcal{K}_{2,l}\circ\mathcal{R}_\alpha^\Gamma$ can be neglected for suitably slow phantom motion compared to the FFL translation. Moreover, for given bounds $C_{\varphi,t}, D_{\varphi,t}$ for velocity and extent of the object's dynamics, the estimates derived in Lemma 7.10 can be determined even prior to data generation as all further components are clear from the measurement setup. This can be used to decide which components of the forward model need to be included in the image reconstruction process.

7.3. Radon-based image reconstruction using TV regularization

In order to determine the reference concentration c_0, we now update our TV-based reconstruction method by inserting the adapted forward operators for MPI as well as CT with respect to the dynamic setting. Access to the motion functions Γ then enables calculation of the time-varying particle concentration for all other states. Let us redefine $\mathcal{D} := L_2\left(B_R,\mathbb{R}\right)\times L_2\left(Z_T\times\mathbb{R},\mathbb{R}\right)$ and $A_l^\Gamma : \mathcal{D}\to L_2\left(Z_T,\mathbb{R}\right)$ for $l=1,\ldots,L$ via

$$A_l^\Gamma\left(c_0,v^\Gamma\right) := \mathcal{K}_{1,l}v^\Gamma + \left(\mathcal{K}_{2,l}\circ\mathcal{R}_\alpha^\Gamma\right)c_0 + \left(\mathcal{K}_{2,l}\circ\mathcal{R}_\beta^\Gamma\right)c_0$$

using the operators $\mathcal{K}_{i,l},\ i=1,2,3$, and $\mathcal{R}_\alpha^\Gamma,\ \mathcal{R}_\beta^\Gamma$ introduced in Theorem 7.3. Therewith, it holds $A_l^\Gamma\left(c_0,\mathcal{R}^\Gamma c_0\right) = \mathcal{A}_l^\Gamma c_0$ in case $c_0\geq 0$. We regard the following minimization problem to jointly reconstruct the reference concentration c_0 and according dynamic Radon data $v^\Gamma := \mathcal{R}^\Gamma c_0$ from noisy measurements u_l^ϵ, for $l=1,\ldots,L$, with noise level $\epsilon>0$

$$\min_{\left(c_0,v^\Gamma\right)\in\mathcal{C}}\frac{1}{2}\sum_l\left\|A_l^\Gamma\left(c_0,v^\Gamma\right)-u_l^\epsilon\right\|_{L_2}^2+\frac{\omega}{2}\left\|\mathcal{R}^\Gamma c_0-v^\Gamma\right\|_{L_2}^2+\gamma_1\,\mathrm{TV}\left(c_0\right)+\gamma_2 P\left(v^\Gamma\right).$$

Again, the constraint $\left(c_0,v^\Gamma\right)\in\mathcal{C}$ guarantees non-negativity of both. We rewrite the data fidelity term like in the previous chapter as

$$\frac{1}{2}\sum_l\left\|A_l^\Gamma\left(c_0,v^\Gamma\right)-u_l^\epsilon\right\|_{L_2}^2=\frac{1}{2}\left\|A^\Gamma\left(c_0,v^\Gamma\right)-\mathbf{u}^\epsilon\right\|_{L_2,\mathbb{R}^L}^2$$

by setting $A^\Gamma\left(c_0, v^\Gamma\right) = \left\{A_l^\Gamma\left(c_0, v^\Gamma\right)\right\}_{l=1,\dots,L}$ with measurements $\mathbf{u}^\epsilon = \left(u_l^\epsilon\right)_{l=1,\dots,L}$. Moreover, in case the conditions in Corollary 7.4 are fulfilled, the forward model only depends on v^Γ since we then can write

$$\left[A_l^\Gamma\left(c_0, v^\Gamma\right)\right](\varphi, t) = \left[\mathcal{K}_{1,l} v^\Gamma + \mathcal{K}_{2,l}\left(\widetilde{\alpha}_{\varphi,t} v^\Gamma\right) + \mathcal{K}_{3,l}\left(\widetilde{\beta}_{\varphi,t} v^\Gamma\right)\right](\varphi, t)\,.$$

For existence, stability and consistency, we refer to Paragraph 5.2.2. Similar to the simultaneous line rotation considerations, the only interesting point is the coercivity. This should transfer from the ideal setting if the motion speed is suitably slow compared to the FFL translation. Additionally, coercivity can be enforced via choosing the penalty term acting on v accordingly.

7.4. Numerical results

We consider simulated data generated with respect to the sequential line rotation geometry described in Section 5.2.3. Notation and simulation parameters are presented in this section. Furthermore, we assume that the particle distribution is contained within a circle of radius $\frac{A}{G}$ around the origin for the entire measurement. For our numerical examples, we regard an affine motion

$$\Gamma_{\varphi_j,t}\mathbf{r} = \mathbf{A}_{\varphi_j,t}\mathbf{r} + \mathbf{b}_{\varphi_j,t}, \quad \Gamma_{\varphi_j,t}^{-1}\mathbf{y} = \mathbf{A}_{\varphi_j,t}^{-1}\left(\mathbf{y} - \mathbf{b}_{\varphi_j,t}\right),$$

defined for $j = 1, \dots, p$ and $t \in [0, T]$ via

$$\mathbf{A}_{\varphi_j,t} := \begin{pmatrix} a_{\varphi_j,t} & 0 \\ 0 & a_{\varphi_j,t} \end{pmatrix}, \quad a_{\varphi_j,t} := 0.8 + 0.2\cos\left(2\pi f\left(\frac{j-1}{2f_\mathrm{d}} + t\right)\right), \tag{7.10}$$

$$\mathbf{b}_{\varphi_j,t} := a_{\varphi_j,t}\begin{pmatrix} \Delta x - \left(\frac{j-1}{2f_\mathrm{d}} + t\right)\frac{2\Delta x}{(p-1)T} \\ 0 \end{pmatrix}. \tag{7.11}$$

Thereby, $f = 78$ kHz sets the deformation frequency and $\Delta x = 2$ mm gives the translation shift of the particle distribution at the beginning of data acquisition with respect to the reference state. Figure 7.1 shows the reference concentration together with Radon data proposing mass respectively intensity preservation. Imagine e.g. a bolus injection [154] or a labeled instrument like a catheter ([74], [160]).

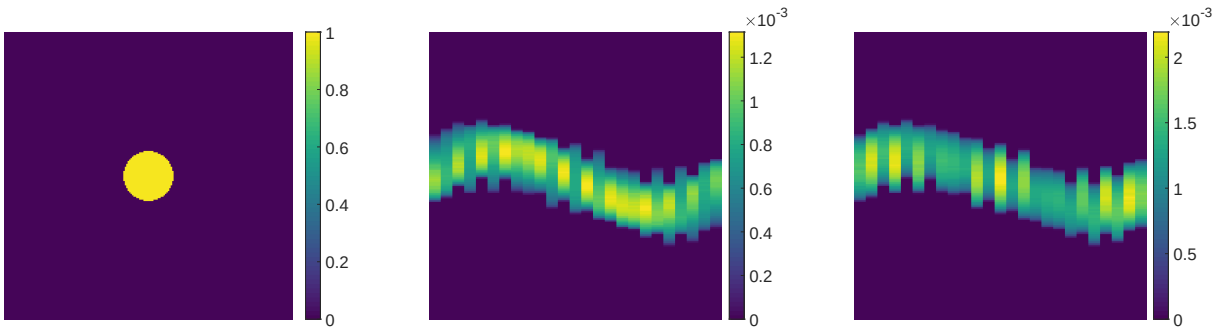

(a) (b) (c)

Figure 7.1.: Reference particle concentration (a) and sinograms assuming mass (b) respectively intensity (c) conservation.

For a continuously rotating FFL, a sinogram with columns filled angle by angle for each direction the line attains during measurement is required to properly evaluate discretizations of the forward

operator. Likewise, here one with each column corresponding to a fixed time-angle combination is needed. At the cost of modeling errors and in favor of a reduced problem size, we rather aim to reconstruct the sinogram with entries $\mathcal{R}^\Gamma c_0(\varphi_j, t_l, s_l)$ for $j = 1, \dots, p$ and $l = 1, \dots, n_\mathrm{s} = \frac{f_\mathrm{s}}{2f_\mathrm{d}} + 1$ as well as

$$\varphi_j = (j-1)\frac{\pi}{p}, \quad t_l = \frac{l-1}{f_\mathrm{s}}, \quad s_l = \left(1 - 2\frac{l-1}{n_\mathrm{s}-1}\right)\frac{A}{G}.$$

However, similar to the previous chapter, we propose the additional error to be sufficiently small to be controllable by means of TV-based regularization.
Note that exploiting (7.9) and relying to the proof of Corollary 7.4, we are able to write

$$\left(\mathcal{K}_{3,l} \circ \mathcal{R}^\Gamma_\beta c_0\right)(\varphi_j, t) = \widetilde{\beta}_{\varphi_j,t}\left(\mathcal{K}_{3,l} \circ \mathcal{R}^\Gamma c_0\right)(\varphi_j, t) =: \left(\widetilde{\mathcal{K}}_{3,l} \circ \mathcal{R}^\Gamma c_0\right)(\varphi_j, t).$$

Here, we have $\widetilde{\beta}_{\varphi_j,t} = 0$ assuming mass preservation and $\widetilde{\beta}_{\varphi_j,t} = \mathrm{tr}\left[\mathbf{A}^{-1}_{\varphi_j,t}\mathbf{A}'_{\varphi_j,t}\right] = 2\dfrac{a'_{\varphi_j,t}}{a_{\varphi_j,t}}$ in case of intensity conservation. Thus, the third component can be easily incorporated in the reconstruction process. For the same reasons as for simultaneous line rotation, we neglect the second term in what follows. Its share of the signal was insignificantly small compared to the other two signal components. Let $\mathbf{K}_1$ and $\widetilde{\mathbf{K}}_3$ denote a discretization of the forward model's components such that the resulting data $\mathbf{u}$ contains data for both receive coils stacked in one vector. Scaling by the maximum absolute data value u_∞ concerning all time points and both receive coils, we define

$$\widehat{\mathbf{u}} := \frac{\mathbf{u}}{u_\infty}, \quad \widehat{\mathbf{K}}_1 := \frac{\mathbf{K}_1}{u_\infty}, \quad \widehat{\widetilde{\mathbf{K}}}_3 := \frac{\widetilde{\mathbf{K}}_3}{u_\infty},$$

and consider the minimization problems determined in Table 7.1.

Table 7.1.: Reconstruction methods

Method	**Regarded minimization problem**
$\mathcal{M}_1$	$\min\limits_{\mathbf{c}_0 \geq 0, \mathbf{v}^\Gamma \geq 0} \frac{1}{2}\left\|\widehat{\mathbf{K}}_1\mathbf{v}^\Gamma - \widehat{\mathbf{u}}\right\|_2^2 + \frac{\omega}{2}\left\|\mathbf{R}\mathbf{c}_0 - \mathbf{v}^\Gamma\right\|_2^2 + \gamma_1\left\|\left\|\nabla\mathbf{c}_0\right\|_2\right\|_1 + \gamma_2\left\|\mathbf{v}^\Gamma\right\|_1$
$\mathcal{M}_2$	$\min\limits_{\mathbf{c}_0 \geq 0, \mathbf{v}^\Gamma \geq 0} \frac{1}{2}\left\|\widehat{\mathbf{K}}_1\mathbf{v}^\Gamma - \widehat{\mathbf{u}}\right\|_2^2 + \frac{\omega}{2}\left\|\mathbf{R}^\Gamma\mathbf{c}_0 - \mathbf{v}^\Gamma\right\|_2^2 + \gamma_1\left\|\left\|\nabla\mathbf{c}_0\right\|_2\right\|_1 + \gamma_2\left\|\mathbf{v}^\Gamma\right\|_1$
$\mathcal{M}_3$	$\min\limits_{\mathbf{c}_0 \geq 0, \mathbf{v}^\Gamma \geq 0} \frac{1}{2}\left\|\left(\widehat{\mathbf{K}}_1 + \widehat{\widetilde{\mathbf{K}}}_3\right)\mathbf{v}^\Gamma - \widehat{\mathbf{u}}\right\|_2^2 + \frac{\omega}{2}\left\|\mathbf{R}^\Gamma\mathbf{c}_0 - \mathbf{v}^\Gamma\right\|_2^2 + \gamma_1\left\|\left\|\nabla\mathbf{c}_0\right\|_2\right\|_1 + \gamma_2\left\|\mathbf{v}^\Gamma\right\|_1$

As always, we apply CVX ([68], [69]) together with the MOSEK solver [141] for determining solutions of these minimization problems. Unless otherwise specified, we calculate results for parameters $\omega \in \left\{2 \cdot 10^i,\ i = 1, \dots, 8\right\}$, $\gamma_1 \in \left\{0.1^{5-0.2i},\ i = 0, \dots, 19\right\}$, and $\gamma_2 = 0$. In contrast to the last chapter, we do not only regard the structural similarity but also the peak-signal-to-noise ratio (PSNR) for comparing the image reconstruction to the considered input phantom. The caption of the figures indicates whether the given results are obtained via a parameter choice based on SSIM or PSNR optimization. Complete information about the selected parameter values and the corresponding image quality measures are listed in special tables at the end of the sections. For static data using the method $\mathcal{M}_1$, that is static reconstruction using the classical Radon transform, we reach at its best an SSIM($\mathbf{c}_0$) value of 0.9882 ($\omega = 2 \cdot 10^5$, $\gamma_1 = 0.1^{2.8}$) and a PSNR($\mathbf{c}_0$) value of 31.91 ($\omega = 2 \cdot 10^6$, $\gamma_1 = 0.1^{3.6}$). These should serve as reference values for the possible image quality with respect to our reconstruction approach.

7.4.1. Mass preservation

In this section, we consider results for the motion defined in (7.10) and (7.11) assuming mass preservation. These motion functions describe a periodic expansion and contraction superimposed with a translation from left to right through the FOV as visualized in Figure 7.2. Consider, for instance, a particle distribution deforming due to respiration or an expanding and compressing bolus traveling within a blood vessel.

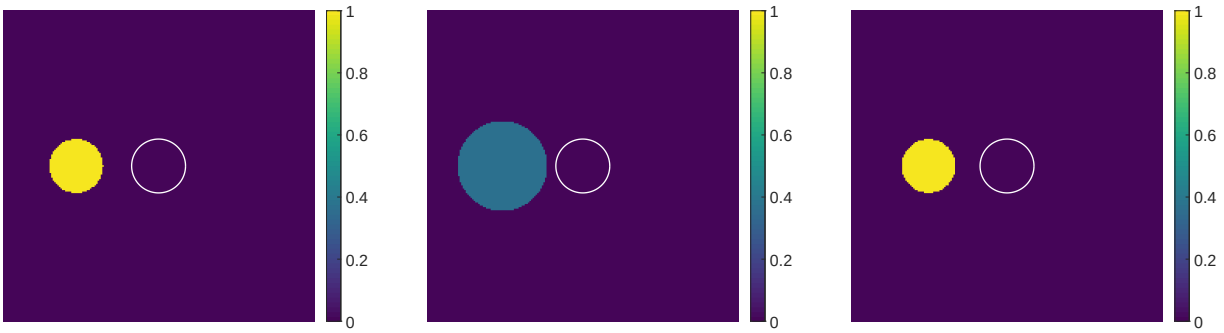

(a) (b) (c)

Figure 7.2.: Visualization of executed motion: Initially the specimen is located on the left side of the FOV (a). Simultaneously with being moved to the right side, the phantom expands until it reaches its maximum size (b). During further translation to the right, it contracts back until the next expansion cycle starts (c). Contours of the reference state are indicated by the white circle.

Application of method $\mathcal{M}_1$, that is ignoring the time dependence of the particle concentration, gives images suffering from severe motion artifacts. According deliverables are shown in Figure 7.3b for the SSIM- and Figure 7.3c for the PSNR-based parameter choice. Thereby, Figure 7.3a states a variant of Figure 7.3b enhancing the contrast by suppressing outliers via limiting the colorbar to the range of the groundtruth.

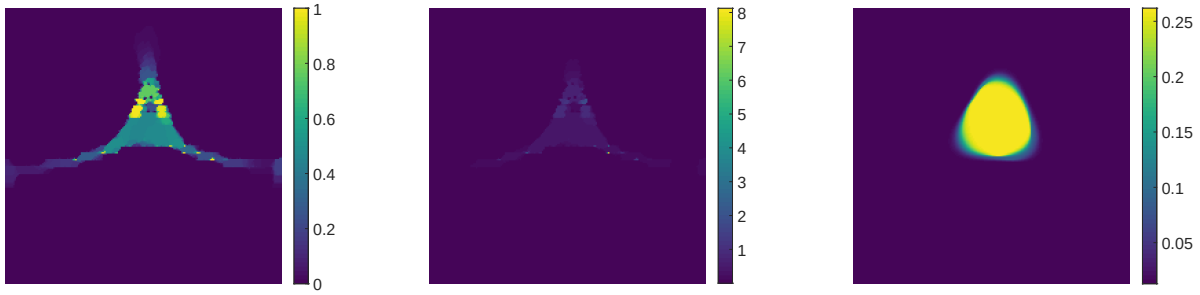

(a) SSIM($\mathbf{c}_0$) = 0.8603 (b) SSIM($\mathbf{c}_0$) = 0.8603 (c) PSNR($\mathbf{c}_0$) = 17.45

Figure 7.3.: Phantom reconstructions according to approach $\mathcal{M}_1$, neglecting the dynamics of the object. To improve the contrast, (a) shows a version of (b) where values greater than one are projected to one.

It is obvious that motion information need to be incorporated in the reconstruction process. With reference to Remark 7.5, we find that $\widehat{\widehat{\mathbf{K}}}_{3,l} = 0$ and thus methods $\mathcal{M}_2$ and $\mathcal{M}_3$ coincide. Corresponding results are depicted in Figure 7.4.

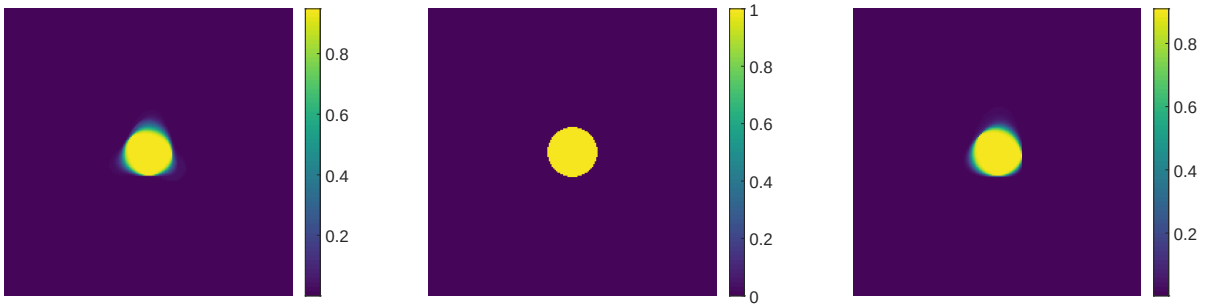

(a) SSIM($\mathbf{c}_0$) = 0.9685 (b) Groundtruth (c) PSNR($\mathbf{c}_0$) = 28.53

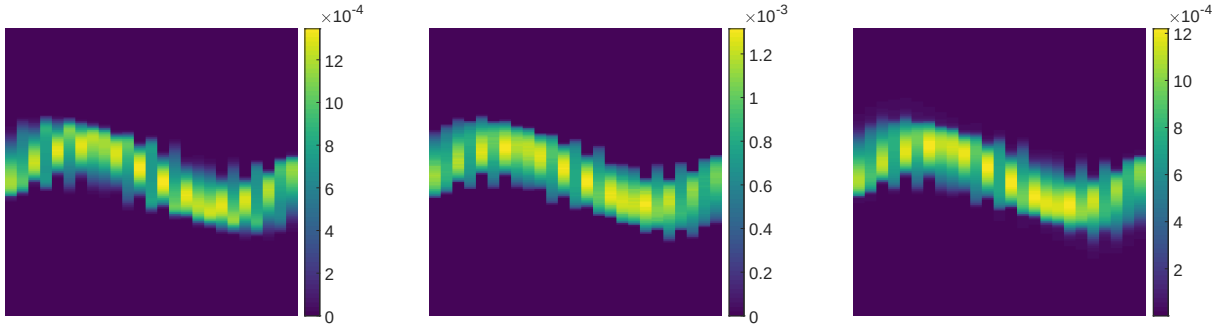

(d) SSIM($\mathbf{c}_0$) = 0.9685 (e) Groundtruth (f) PSNR($\mathbf{c}_0$) = 28.53

Figure 7.4.: Phantom (first row) and corresponding sinogram (second row) reconstructions applying method $\mathcal{M}_2$, incorporating motion information, compared to the groundtruth phantom (b) respectively sinogram (e).

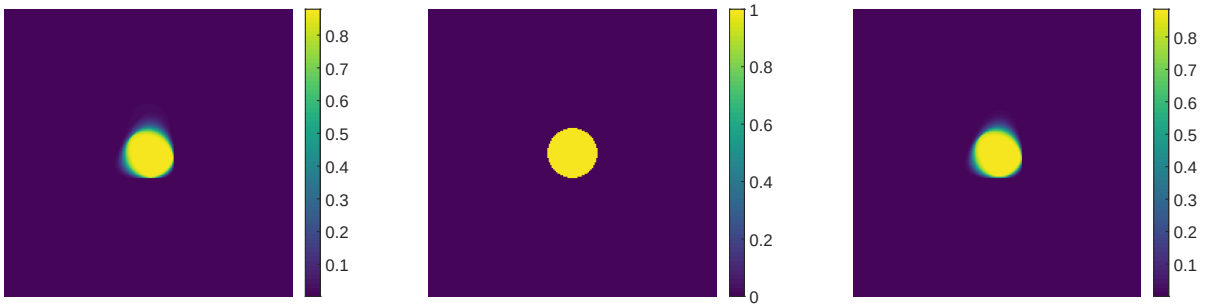

(a) PSNR($\mathbf{c}_0$) = 27.32 (b) Groundtruth (c) PSNR($\mathbf{c}_0$) = 27.53

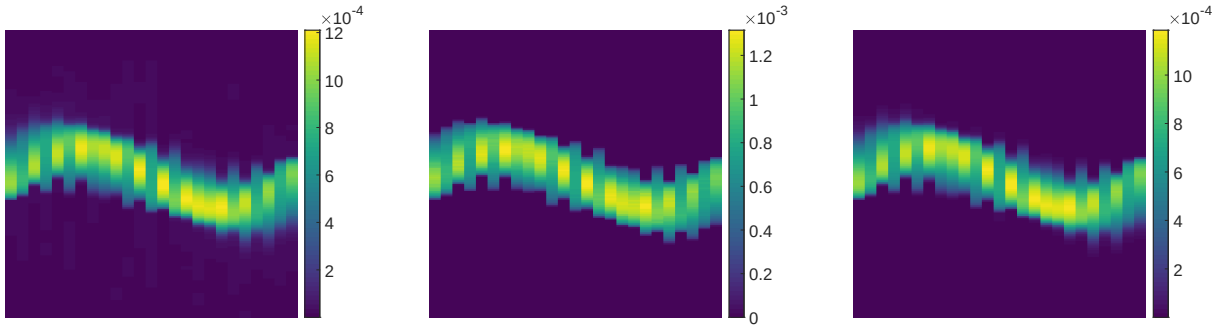

(d) PSNR($\mathbf{c}_0$) = 27.32 (e) Groundtruth (f) PSNR($\mathbf{c}_0$) = 27.53

Figure 7.5.: Comparison of the groundthruth phantom (b) to reconstructed images (first row) and groundtruth sinogram (e) to reconstructed sinograms (second row) applying $\mathcal{M}_2$ to noisy data without (left column) and with (right column) sparsity constraint on the Radon data.

Results for both, i.e. SSIM- and PSNR-based, parameter selections exhibit a similar image quality. The phantom still shows a slight blurring in the same directions as the static reconstruction. Nevertheless, the concentration and its Radon data are clearly recognizable, located at the right position with values in good accordance to the groundtruth. In summary, the motion artifacts are well prevented.
In addition, the application of $\mathcal{M}_2$ to data with added Gaussian noise (standard deviation: ca. 10% of u_∞) also works well, as can be seen in Figure 7.5. In this case, we do not contrast reconstructions with respect to SSIM- and PSNR-based parameter choices but we contrast results obtained with and without incorporation of an additional sparsity constraint on the Radon data. We abstain from executing a parameter search. Instead, we took those for the PSNR-based selection in the noise-free setting. While there is hardly any difference in the phantom reconstruction, the background noise in the reconstructed sinogram is avoided by setting $\gamma_2 > 0$.

Table 7.2.: Reconstruction parameters and image quality values

Figure	ω	γ_1	γ_2	SSIM($\mathbf{c}_0$)	PSNR($\mathbf{c}_0$)
7.3b	$2 \cdot 10^5$	$0.1^{3.6}$	0	0.8603	15.27
7.3c	$2 \cdot 10^1$	$0.1^{4.4}$	0	0.3335	17.45
7.4a + 7.4d	$2 \cdot 10^3$	$0.1^{3.6}$	0	0.9685	28.03
7.4c + 7.4f	$2 \cdot 10^6$	$0.1^{1.4}$	0	0.9477	28.53
7.5a + 7.5d	$2 \cdot 10^6$	$0.1^{1.4}$	0	0.8826	27.32
7.5c + 7.5f	$2 \cdot 10^6$	$0.1^{1.4}$	10	0.9730	27.53

7.4.2. Intensity preservation

We now consider the defined motion, but under the assumption of intensity conservation. To illustrate the motion, please refer back to Figure 7.2. Note that with intensity conservation, the concentration value is independent of the object's size.

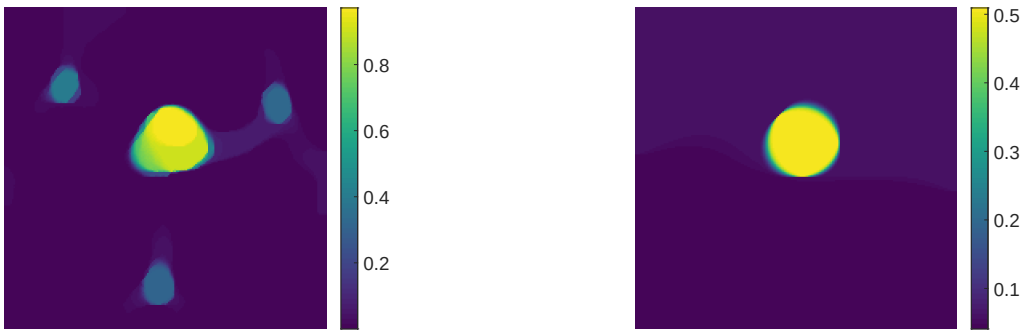

(a) SSIM($\mathbf{c}_0$) = 0.7684 (b) PSNR($\mathbf{c}_0$) = 16.95

Figure 7.6.: Phantom reconstructions according to $\mathcal{M}_1$, neglecting the dynamics of the object.

Results obtained by method $\mathcal{M}_1$, neglecting the dynamics of the particle concentration, are stated in Figure 7.6. While the PSNR-based parameter choice at least yields the correct shape but results in a delocalized phantom with incorrect size and concentration value, the SSIM-based choice leads to three additional circles in the reconstruction. These could be wrongly identified as three additional balls of lower concentration leading to severe misdiagnosis.

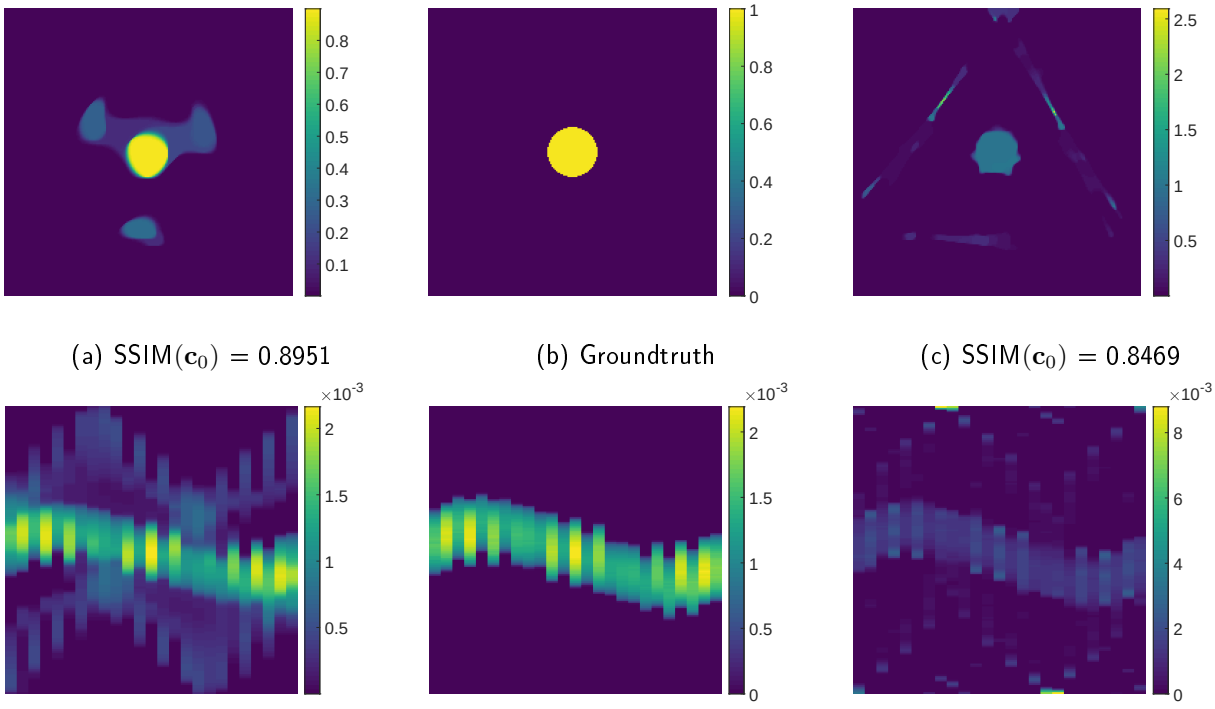

(a) SSIM($\mathbf{c}_0$) = 0.8951 (b) Groundtruth (c) SSIM($\mathbf{c}_0$) = 0.8469

(d) SSIM($\mathbf{c}_0$) = 0.8951 (e) Groundtruth (f) SSIM($\mathbf{c}_0$) = 0.8469

Figure 7.7.: Groundtruth phantom (b) and sinogram (e) compared to reconstructed phantoms (first row) and sinograms (second row) applying $\mathcal{M}_2$ (left column) or $\mathcal{M}_3$ (right column) for SSIM-based parameter choice.

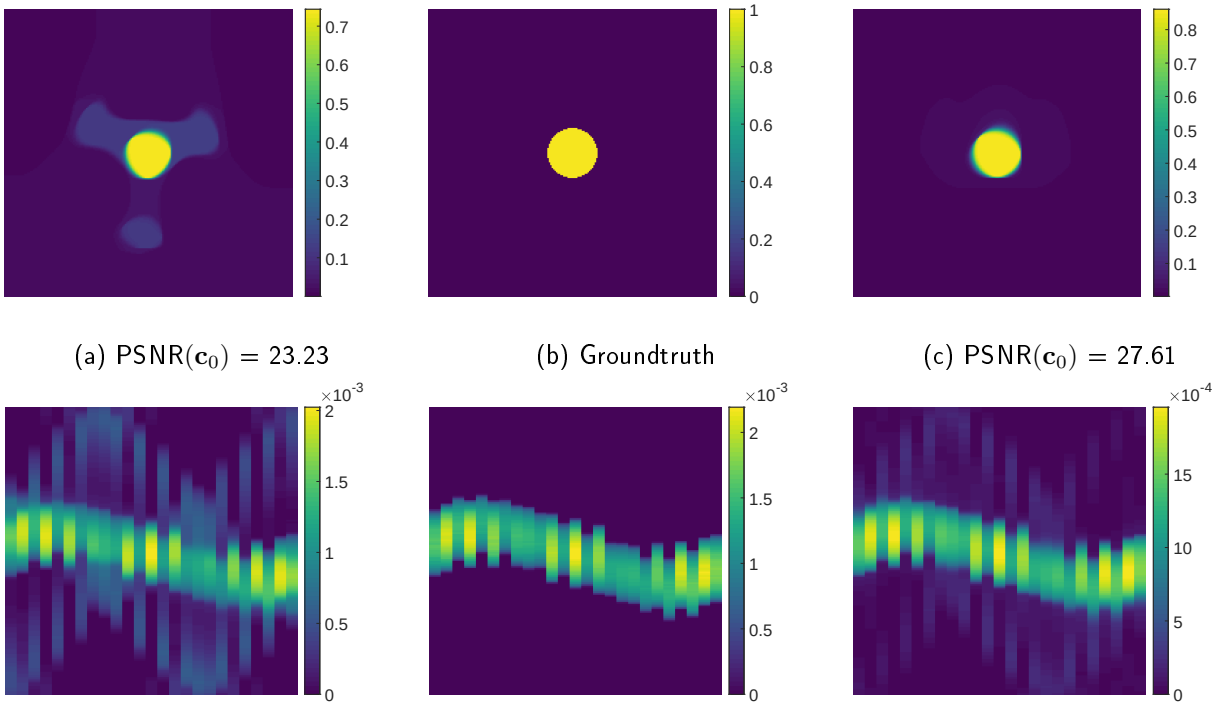

(a) PSNR($\mathbf{c}_0$) = 23.23 (b) Groundtruth (c) PSNR($\mathbf{c}_0$) = 27.61

(d) PSNR($\mathbf{c}_0$) = 23.23 (e) Groundtruth (f) PSNR($\mathbf{c}_0$) = 27.61

Figure 7.8.: Groundtruth phantom (b) and sinogram (e) compared to reconstructed phantoms (first row) and sinograms (second row) applying $\mathcal{M}_2$ (left column) or $\mathcal{M}_3$ (right column) for PSNR-based parameter choice.

Under the assumption of intensity conservation, the third component $\widehat{\widehat{\mathbf{K}}}_{3,l}$ does not vanish. We therefore compare results obtained by method $\mathcal{M}_2$, ignoring this term, with those by approach $\mathcal{M}_3$, including it. These results are presented in Figure 7.7 for a parameter choice based on the SSIM image quality measure. The three additional circles come closer to the actual phantom in the center. Moreover, size and position of the phantom fit better with the groundtruth than the results of method $\mathcal{M}_1$. The approach $\mathcal{M}_3$, which takes into account the additional term from the further time dependence, still contains artifacts. However, in this case, these are identifiable as those. Nevertheless, the contrast is reduced due to outliers, which could also explain the lower SSIM value in relation to $\mathcal{M}_2$ incorporating less information.
As presented in Figure 7.8, exploiting the PSNR-based parameter choice and applying approach $\mathcal{M}_3$ finally gives a well reconstructed reference state of the concentration. Nevertheless, the sinogram is still disturbed by background errors. One explanation for this could be that, despite the extension of the model by $\widehat{\widehat{\mathbf{K}}}_3$, the modeling inaccuracies resulting from the use of the reduced sinogram lead to these reconstruction errors.

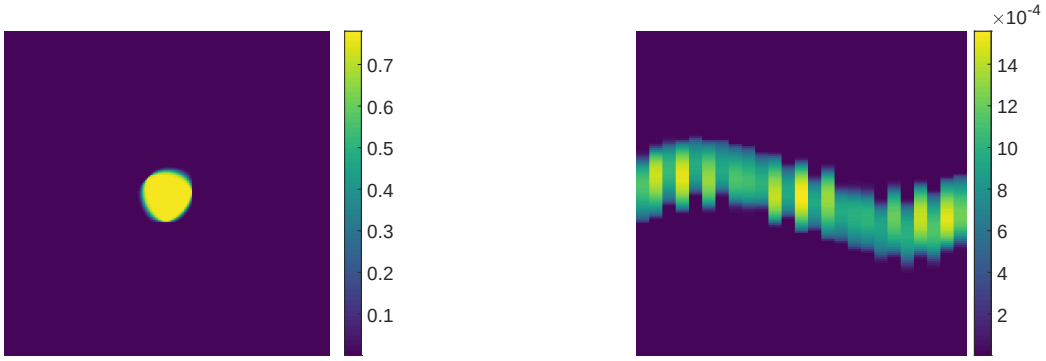

(a) SSIM($\mathbf{c}_0$) = 0.9726 (b) SSIM($\mathbf{c}_0$) = 0.9726

Figure 7.9.: Phantom and sinogram reconstruction applying method $\mathcal{M}_2$ with $\gamma_2 > 0$.

Figure 7.9 shows the potential of the supplementary sparsity constraint on the Radon data. The SSIM-based parameter choice using method $\mathcal{M}_2$, which formerly exhibited severe irritations in the sinogram and defective parts in the image, allows promising results when being used with $\gamma_2 > 0$, i.e. with sparsity constraint. Note that even better results can be expected, as we restrained from executing a parameter search and simply set ω and γ_1 like for the previous SSIM-based choice used for Figure 7.7.

Table 7.3.: Reconstruction parameters and image quality values

Figure	ω	γ_1	γ_2	SSIM($\mathbf{c}_0$)	PSNR($\mathbf{c}_0$)
7.6a	$2 \cdot 10^6$	$0.1^{2.6}$	0	0.7684	14.81
7.6b	$2 \cdot 10^4$	$0.1^{1.4}$	0	0.0468	16.95
7.7a + 7.7d	$2 \cdot 10^7$	$0.1^{1.4}$	0	0.8951	21.89
7.7c + 7.7f	$2 \cdot 10^2$	$0.1^{4.4}$	0	0.8469	19.58
7.8a + 7.8d	$2 \cdot 10^5$	$0.1^{1.2}$	0	0.4703	23.23
7.8c + 7.8f	$2 \cdot 10^5$	$0.1^{1.4}$	0	0.6096	27.61
7.9	$2 \cdot 10^7$	$0.1^{1.4}$	50	0.9726	23.22

7.5. Conclusion and outlook

In this chapter, we adapted the MPI-FFL forward operator for dynamic particle concentrations. Due to the geometric similarity of the FFL encoding scheme and CT, we describe the dynamics via diffeomorphic motion functions, as has successfully been done for dynamic CT. This approach allows shifting of the particle distribution's time dependence to the mean magnetization and thus, only components known from the measurement setup depend on time. Like for a simultaneously rotating FFL, we get additional parts in the forward operator, stemming from executing the time derivative. In particular, we found that the settings of simultaneous line rotation and phantom rotation are connected. Via suitable substitution of variables, all components can be linked to variants of the Radon transform. These comprise the version known from dynamic CT and further weighted adaptions. We derived estimates of these terms applicable for deciding whether incorporation within the reconstruction process is necessary. We presented numerical results for synthetic data, applying our usual TV-based joint reconstruction of particle concentration and Radon data. This time, we also stated results with respect to an additional sparsity constraint, acting on the sinogram, which was especially functional for the reduction of background artifacts. We considered examples for both mass and intensity preservation. For mass conservation, the signal equation is composed of two components in contrast to the three for intensity preservation. Comparison of results, neglecting and incorporating motion information in the image determination, pointed out the importance of appropriate reconstruction methods for reliable diagnostics. Our numerical results proved the operability of our method. Thus, it is worth proceeding with further research. This can e.g. include the reduction of the modeling error, we accepted by using the reduced sinogram. It would be interesting to combine our approach with inpainting techniques to come closer to the ideally required full sinogram for data computation. A major point of interest consists in motion estimation. For practical applicability, we need to determine the motion either before or jointly with image reconstruction. Fortunately, variational methods show great flexibility for incorporation of prior information and adapting the objective functional to specific applications. Starting points can be, for instance, techniques derived for dynamic CT or dynamic inverse problems in general. In [42], a simultaneous motion and image reconstruction, using a variational approach combined with diffeomorphic deformation functions, is presented, which would fit well to our setting. In contrast, we could also replace our joint reconstruction by first determining the dynamic Radon data and then applying corresponding motion estimation and compensation schemes. A proof-of-concept with respect to determining motion functions via solving the Navier-Cauchy equation is given in [82]. In general, PDEs play an important role for motion estimation, as was already pointed out in Section 3.1. Remember that MPI does not contain morphological information. Hence, it is typically applied in combination with an MRI or CT scan, providing knowledge about the tissue itself. These scans can be used to extract prior knowledge with respect to the particles' movements. In particular, to fuse MPI and e.g. MRI images, markers are exploited, which track the position of organs [160]. Information of these markers can be used to determine the organ's deformation (cf. [79]). This serves then as additional information or constraint for the determination of the particles' dynamics. Moreover, as also pointed out in Section 3.1, image registration and shape deformation [193] are of further interest for determining the motion functions.

Next, we transfer the considerations of this chapter, dealing with deformed phantoms, to the setting of static concentrations but deformed magnetic fields. We use image registration for the derivation of the corresponding deformation functions.

8. Magnetic Field Imperfections

So far, we considered ideal magnetic fields, i.e. the low-field volumes are centered by a straight line and the field is constant along lines parallel to this field-free line [114]. However, in practice we are confronted with field imperfections leading to deformed LFVs (e.g. [22], [29], [31], [192]) and therewith ignoring these circumstances within the reconstruction procedure results in disguising artifacts.

In [138] field imperfections regarding the selection, excitation, and receive coils were considered. They came to the conclusion that for Radon-based approaches artifact reduction methods are required. Hence, the last topic we aim to consider in this thesis regards artifact reduction for Radon-based image reconstruction in case of field deformations. We dedicate ourselves towards imperfections within the selection field. While for the system matrix based approach field imperfections are somehow intrinsically regarded due to the calibration scan, this is not the case for model-based considerations. The authors of [31] use spherical harmonics (cf. Section 2.4 and A.1) to model magnetic fields. Thereby, spherical harmonics coefficients (SHCs) for real fields can be obtained via a calibration process. In contrast to the ideal setting, more and higher degrees of spherical harmonics are required to properly express the real fields. In order to address the issue of artifact reduction, they introduce a new 3D model assuming that velocity and acceleration field are parallel. In the context of spherical harmonics, we additionally refer to [21]. In [192], selection field imperfections for the FFP scanner and x-space reconstruction are considered and reduced via unwarping methods relying on displacement maps. Warping is also regarded in [20] for artifact reduction. In the FFP multi-patch context, they suggest linking different system matrices via non-rigid transformations, which could be determined based on image registration. Instead, they then pursue a different approach starting from the magnetic fields. However, this goes in the direction we want to take. Namely, our goal is to connect ideal and deformed magnetic field via diffeomorphic deformation functions obtained using image registration techniques. The field imperfections are then included in the forward model, leading to a similar operator as for time-varying particle concentrations. The derivation of the link between MPI-FFL and Radon data and the updating of our reconstruction methods thus follow the same steps as in the last chapter dealing with dynamic MPI. Parts of our results have been published in [14].

Outline of the chapter: We are maintaining our usual structure. Hence, the first Section 8.1 is about adapting the forward model to the considered setting, that is incorporation of magnetic field imperfections via diffeomorphic functions. Afterwards, in Section 8.2, we state the relation between MPI-FFL and adapted Radon data. Since this setting is highly connected to the one of diffeomorphic motion functions, we keep it short and refrain from giving bounds of the additional component in the forward model. In Section 8.3, we review the image registration scheme we consider for linking ideal and real magnetic field. We close this chapter by stating numerical results in Section 8.4, applying again our joint reconstruction approach. We consider examples incorporating the exact deformation function and those incorporating an approximation obtained via registration. Furthermore, we check the possibility of describing real fields via ideal ones using diffeomorphisms. To this end, we apply the image registration scheme to measured fields and their corresponding computed ideal version.

8.1. Forward model

Thinking back to the Figure 4.6 in Chapter 4, we realized that the integration of a deformed object along straight lines and the integration of the non-deformed object along curves are equivalent. On that account, we approach magnetic field imperfections via transferring the diffeomorphic motion function ansatz regarding changing tracer distributions to this setting. More precisely, we assume the existence of a deformation function $\Gamma : \mathbb{R}^2 \times Z_T \to \mathbb{R}^2$ such that $\Gamma_{\varphi,t}\mathbf{r} := \Gamma(\mathbf{r}, \varphi, t)$ is a diffeomorphism for fixed $(\varphi, t) \in Z_T$, which approximately links the real magnetic field $\mathbf{H}^{\Gamma}$ to the ideal one $\mathbf{H}^{\text{ideal}}$

$$\mathbf{H}^{\Gamma}(\mathbf{r}, \varphi, t) \approx \mathbf{H}^{\text{ideal}}\left(\Gamma_{\varphi,t}^{-1}\mathbf{r}, \varphi, t\right). \tag{8.1}$$

Due to the similarity of these settings, i.e. dynamic phantoms and field deformations, we use the same notation. Hence, adapting the ideal forward model (5.15) accordingly, we obtain

Definition 8.1. *Define* $\mathcal{A}_l^{\Gamma} : L_2\left(B_R, \mathbb{R}_0^+\right) \to L_2\left(Z_T, \mathbb{R}\right)$ *to be*

$$\mathcal{A}_l^{\Gamma} c(\varphi, t) := -\mu_0 \int_{\mathbb{R}^2} c(\mathbf{r}) \frac{\partial}{\partial t} \overline{m}\left(-G\,\Gamma_{\varphi,t}^{-1}\mathbf{r} \cdot \mathbf{e}_{\varphi} + A\Lambda_{\varphi}(t)\right) \mathbf{e}_{\varphi} \cdot \mathbf{p}_l(\mathbf{r})\, \mathrm{d}\,\mathbf{r}. \tag{8.2}$$

The forward operator for MPI-FFL scanner in presence of imperfect fields satisfying (8.1) can be stated as $\mathcal{A}^{\Gamma} : L_2\left(B_R, \mathbb{R}_0^+\right) \to L_2\left(Z_T, \mathbb{R}^L\right)$ *with* $\mathcal{A}^{\Gamma} c(\varphi, t) = \left\{\mathcal{A}_l^{\Gamma} c(\varphi, t)\right\}_{l=1,\dots,L}$.

Again, we have to pose some conditions on the deformation function Γ to guarantee well-posedness of the previous definition.

Assumption 8.2. *Suppose that* $\Gamma_{\varphi,t}^{-1}$ *is differentiable with respect to time and let* $\left(\Gamma_{\varphi,t}^{-1}\right)' := \dfrac{\partial}{\partial t}\Gamma_{\varphi,t}^{-1}$ *denote the corresponding partial derivative. Moreover, propose for all* $\mathbf{r} \in \mathbb{R}^2$ *and* $(\varphi, t) \in Z_T$

$$\left\|\left(\Gamma_{\varphi,t}^{-1}\right)' \mathbf{r}\right\| \leq \frac{A}{G} C_{\varphi,t}.$$

for some $C_{\varphi,t} > 0$.

As before, this assumption states no restriction, since only a finite number of measurements are available and Γ describes the deviation of the real magnetic field to the ideal case, whereby the change over time should be small. The resulting inverse problem is given as

$$\mathcal{A}^{\Gamma} c = \mathbf{u}$$

with measured data $\mathbf{u} = \{u_l\}_{l=1,\dots,L}$ and forward operator $\mathcal{A}^{\Gamma}$.

8.2. Relation between MPI and Radon data

Comparing Definition 7.2 and 8.1, the connection between time-varying phantoms and field deformations is emphasized. Thus, the results of the last chapter directly transfer to this setting and we refrain from giving the proofs. A minor difference is that, in contrast to the dynamic case, we do not have to switch the time dependence from the concentration to the field description.

Theorem 8.3. *Given spatially homogeneous receive coil sensitivities, the MPI forward operator (8.2) with respect to the l-th receive coil can be written as*

$$\mathcal{A}_l^{\Gamma} = \mathcal{K}_{1,l} \circ \mathcal{R}^{\Gamma} + \mathcal{K}_{2,l} \circ \mathcal{R}_{\alpha}^{\Gamma}$$

with convolution operators $\mathcal{K}_{i,l} : L_2(Z_T \times \mathbb{R}, \mathbb{R}) \to L_2(Z_T, \mathbb{R})$, *for* $i = 1,2,3$ *and* $l \in \{1,\dots,L\}$,

$$\begin{aligned} \mathcal{K}_{1,l} f(\varphi,t) &= -\mu_0\, A\Lambda'_\varphi(t)\, \mathbf{e}_\varphi \cdot \mathbf{p}_l\, \overline{m}'(G\,\cdot) * f(\varphi,t,\cdot)(s_{\varphi,t}), \\ \mathcal{K}_{2,l} f(\varphi,t) &= \mu_0\, G \qquad \mathbf{e}_\varphi \cdot \mathbf{p}_l\, \overline{m}'(G\,\cdot) * f(\varphi,t,\cdot)(s_{\varphi,t}) \end{aligned}$$

with $s_{\varphi,t} := \dfrac{A}{G}\Lambda_\varphi(t)$ *as well as weight functions* $\alpha_{\varphi,t} : \mathbb{R}^2 \to \mathbb{R}$

$$\alpha_{\varphi,t}(\mathbf{r}) = \left(\Gamma_{\varphi,t}^{-1}\right)' \mathbf{r} \cdot \mathbf{e}_\varphi.$$

The above theorem transforms to the result for the ideal setting (Theorem 5.4) by choosing $\Gamma_{\varphi,t} = \mathrm{Id}$. Theoretically, Example 7.6 can also be applied to field imperfections. In practice, however, this does not make sense, as it is not possible to generate curved LFVs if restricting to field deformations parallel to the ideal FFL. For the same reason, the field transformations Γ will most likely not be described by affine functions. We refrain from transferring the estimates of Lemmas 7.9 and 7.10, as they are transferred one-to-one. Moreover, we assume that $\mathcal{K}_{2,l} \circ \mathcal{R}_\alpha^\Gamma$ is negligible, since the field deviations and especially the field changes with respect to time are most probably reasonably small. Hence, sticking to our Radon-based reconstruction scheme, we consider the minimization problem

$$\min_{(c,v)\in\mathcal{C}} \frac{1}{2}\sum_l \left\|\mathcal{K}_{1,l} v^\Gamma - u_l^\epsilon\right\|_{L_2}^2 + \frac{\omega}{2}\left\|\mathcal{R}^\Gamma c - v^\Gamma\right\|_{L_2}^2 + \gamma_1 \mathrm{TV}(c) + \gamma_2 P\left(v^\Gamma\right)$$

with noisy data u_l^ϵ, for $l = 1,\dots,L$, noise level $\epsilon > 0$, and the usual non-negativity constraint. An equivalent formulation of the fidelity term is given by

$$\frac{1}{2}\sum_l \left\|\mathcal{K}_{1,l} v^\Gamma - u_l^\epsilon\right\|_{L_2}^2 = \frac{1}{2}\left\|\mathcal{K}_1 v^\Gamma - \mathbf{u}^\epsilon\right\|_{L_2,\mathbb{R}^L}^2$$

with $\mathbf{u}^\epsilon = \{u_l^\epsilon\}_{l=1,\dots,L}$. Note that, differently from the previous chapters, we have decided to neglect the second component directly for the sake of simplicity. However, it could be included here in the same way as in the dynamic phantom considerations.

Next, we recapitulate some aspects regarding image registration. In particular, we summarize the technique we will rely on for our numerical investigations.

8.3. Image registration

Image registration plays an important role in medical imaging. Application fields comprise e.g. registration of images obtained via different scanner types. This is also of major interest for MPI in view of registering the particle distribution within the body by additional application of, for instance, MRI yielding morphological information. Furthermore, as stated earlier, image registration may be of great use for motion estimation and compensation by linking different states of a time-varying phantom. For magnetic particle imaging, the settings of dynamic concentrations and field deformations are strongly linked, as pointed out in the last section. Hence, we dedicate the following paragraph to image registration. Regard in this context the large deformation diffeomorphic metric mapping problem already mentioned in Section 3.1, we exemplary refer to [10]. See [182] for considerations concerning functions of bounded variation. The authors of [38] regard hyperelasticity as a regularizer. For an investigation of the description of diffeomorphic representations using geodesic interpolating splines, please refer to [135] and for learning based methods to ([6], [46], [126]). In this work, we consult a diffeomorphic image registration according to [133], which uses a Lagrangian

Gauss-Newton-Krylov solver for the LDDMM problem and whose implementation is available as an add-on to the flexible algorithms for image registration (FAIR) framework [140]. The following section is devoted to outline their method for the assumption of intensity preservation. Notice that their scheme is also available for mass conservation.

Let $\Omega \subset \mathbb{R}^d,\ d \in \{2,3\}$, denote the image domain. Let further $\mathfrak{T}, \mathfrak{R} : \Omega \to \mathbb{R}$ represent continuously differentiable and on Ω compactly supported *template* $\mathfrak{T}$ respectively reference $\mathfrak{R}$ images. In the following, we use the term *target* instead of reference image to avoid confusion with the reference concentration introduced in the last chapter. The LDDMM problem in variational formulation can be written as

$$\min_{\boldsymbol{\nu}, H} \mathfrak{D}\left(H\left(\cdot,1\right),\mathfrak{R}\right) + \gamma\, \mathfrak{S}\left(\boldsymbol{\nu}\right) \quad \text{s.t.} \quad \Psi_{\boldsymbol{\nu}}\left(H\left(\cdot,t\right)\right) = 0, \quad t \in [0,1]\,. \tag{8.3}$$

Thereby, $\mathfrak{D}$ measures the similarity between the image $H : \Omega \times [0,1] \to \mathbb{R}$ at final time point $t = 1$ and the target image $\mathfrak{R}$. The penalty term $\mathfrak{S}$ is added in order to pose a smoothness constraint on the velocity field $\boldsymbol{\nu} : \Omega \times [0,1] \to \mathbb{R}^d$. The regularization parameter $\gamma > 0$ can be used as controller to adjust the weighting between image fidelity and smoothness of the velocity field. Finally, $\Psi_{\boldsymbol{\nu}}$ determines the transformation model

$$\Psi_{\boldsymbol{\nu}}\left(H\left(\cdot,t\right)\right) = \begin{cases} \frac{\partial H}{\partial t}\left(\cdot,t\right) + \nabla H\left(\cdot,t\right) \cdot \boldsymbol{\nu}\left(\cdot,t\right) = 0, \\ H\left(\cdot,0\right) = \mathfrak{T}. \end{cases} \tag{8.4}$$

Please be referred to the PDE-based motion model (3.7) introduced in Section 3.1. As was already mentioned in that section, motion models and deforming templates are related to one another. Indeed, under certain regularity assumptions on the velocity field $\boldsymbol{\nu}$ as well as the template and target image, a diffeomorphism linking both can be derived exploiting the method of characteristics. This underlines the connection between motion estimation problems and image registration.
The constraint in (8.4) corresponds to the assumption of intensity preservation. Hence, it can be supposed that the template image is composed of particles positioned at $\mathbf{r}_0^p \in \Omega$ carrying the according intensity value over time until they reach their final position $\mathbf{r}_1^p$ forming the target image. This also connects to the description of motion via deformation functions as e.g. described in [76]. It thus holds for all $t \in [0,1]$ that

$$H\left(\Gamma_{\boldsymbol{\nu},t}^{-1}\mathbf{r}_0^p, t\right) = \mathfrak{T}\left(\mathbf{r}_0^p\right).$$

These particle trajectories, i.e. curves along which H is constant, result in the characteristics $t \mapsto \Gamma_{\boldsymbol{\nu},t}^{-1}\mathbf{r}_0^p$ fulfilling

$$\frac{\partial \Gamma_{\boldsymbol{\nu},t}^{-1}}{\partial t}\mathbf{r}_0^p = \boldsymbol{\nu}\left(\Gamma_{\boldsymbol{\nu},t}^{-1}\mathbf{r}_0^p\right) \quad \text{and} \quad \Gamma_{\boldsymbol{\nu},0}^{-1} = \mathrm{Id}.$$

Analogously, the transformation can be considered inversely. That is, starting from a position $\mathbf{r}_1^p$ at final time, the original image can be determined by following the particle's location backwards in time. For a given velocity field, the characteristics are determined exploiting a fourth order Runge-Kutta method and used to determine the deformed image by tracking them backwards in time. To this end, interpolation methods are required to calculate intensity values at off-gird points, since deformed and original grid differ. Thus, the searched-for approximation $H\left(\cdot,1\right)$ to the target image $\mathfrak{R}$ can be expressed in terms of the velocity field $\boldsymbol{\nu}$ and the minimization problem (8.3) reduces to

$$\min_{\boldsymbol{\nu}} \mathfrak{D}\left(H_{\boldsymbol{\nu}}\left(\cdot,1\right),\mathfrak{R}\right) + \gamma\, \mathfrak{S}\left(\boldsymbol{\nu}\right).$$

A discretize-then-optimize approach is pursued. To solve the discrete optimization problem an inexact Gauss-Newton-Krylov method is considered. Due to the non-convexity, a multilevel approach is suggested to increase robustness and decrease computation time.

In view of our application in mind, the image H corresponds to the magnetic field. In this setting, we actually do not connect different image states that existed but we link the actual field, which can be measured, to the desired ideal one, which practically never existed but can be calculated from the chosen parameter setting. Since we express the magnetic fields in terms of spherical harmonics, as outlined in Appendix A.1, they are composed of multivariate polynomials and hence especially continuously differentiable. Moreover, the magnetic fields are constrained to the bore of the field generating coils. Therefore, for arbitrary but fixed angle φ and time $t \in [0, T]$, real and ideal field can be represented as continuously differentiable and on some domain Ω compactly supported images. Note that the time dependence of the magnetic fields does not coincide with the time dependence of the images considered in this section, which was introduced to describe a step-wise transformation of the template into the target image.

8.4. Numerical results

For the numerical examples, we consider the same simulation framework as for the other chapters and refer to its introduction in Section 5.2.3. We regard the following time- and angle-independent field deformation function

$$\Gamma^{-1}\mathbf{r} := \Gamma_{\varphi,t}^{-1}\mathbf{r} = \Gamma_{\varphi,t}^{-1}\begin{pmatrix} x \\ y \end{pmatrix} = \begin{pmatrix} x \\ y - 50x^2 \end{pmatrix} \tag{8.5}$$

so that the second integral within the forward model is not only small, but even zero. As always, we denote a discretized version of the forward operator using bold letters $\mathbf{K}_1$ and $\mathbf{u}$ gives the data with respect to both receive coils gathered in one vector. In order to normalize the maximum absolute data value u_∞ concerning all time points and both receive coils, we set

$$\widehat{\mathbf{u}} := \frac{\mathbf{u}}{u_\infty}, \quad \widehat{\mathbf{K}}_1 := \frac{\mathbf{K}_1}{u_\infty}$$

and specify the regarded minimization problems in Table 8.1.

Table 8.1.: Reconstruction methods

Method	**Regarded minimization problem**
$\mathcal{M}_1$	$\min\limits_{\mathbf{c}\geq 0, \mathbf{v}^\Gamma \geq 0} \frac{1}{2}\left\|\widehat{\mathbf{K}}_1\mathbf{v}^\Gamma - \widehat{\mathbf{u}}\right\|_2^2 + \frac{\omega}{2}\left\|\mathbf{R}\mathbf{c} - \mathbf{v}^\Gamma\right\|_2^2 + \gamma_1 \left\|\|\nabla \mathbf{c}\|_2\right\|_1 + \gamma_2 \left\|\mathbf{v}^\Gamma\right\|_1$
$\mathcal{M}_2$	$\min\limits_{\mathbf{c}\geq 0, \mathbf{v}^\Gamma \geq 0} \frac{1}{2}\left\|\widehat{\mathbf{K}}_1\mathbf{v}^\Gamma - \widehat{\mathbf{u}}\right\|_2^2 + \frac{\omega}{2}\left\|\mathbf{R}^\Gamma\mathbf{c} - \mathbf{v}^\Gamma\right\|_2^2 + \gamma_1 \left\|\|\nabla \mathbf{c}\|_2\right\|_1 + \gamma_2 \left\|\mathbf{v}^\Gamma\right\|_1$

We aim to reconstruct phantom and sinogram depicted in Figure 8.1, which are the same we considered in Chapter 5 and 6. We compare results neglecting the field deformation (method $\mathcal{M}_1$) with those incorporating them (method $\mathcal{M}_2$). We further compare results using the exact deformation function (8.5) with those using image registration, as described in the last section, to determine a deformed grid. For simplicity, we apply the example "ELDDMM_2Ddisc2C_mbCurvatureST.m" for image registration. It is available within the LagLDDMM add-on [133] to the FAIR [140] package

https://github.com/C4IR/FAIR.m. To make it work for our setting, we need to scale the magnetic field such that its values are within similar range as those of template and target image in their example. After image registration, we undo the scaling and transfer the grid from their considered domain $\Omega = (0,1)^2$ to our FOV with length $2\frac{A}{G}$. We regard the phantom divided into 129×129 pixel. Therewith, applying their implementation works fine for our considerations, as we will see.

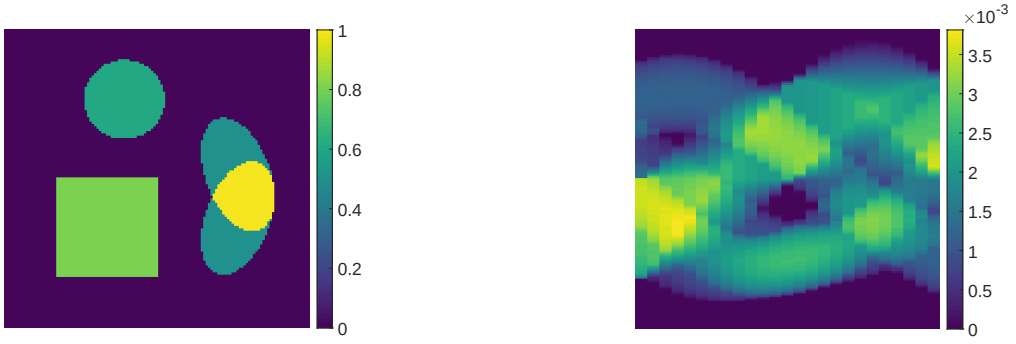

(a) (b)

Figure 8.1.: Phantom (a) and corresponding sinogram (b).

The non-scaled template and target fields are plotted in Figure 8.2 for the different resolution levels $(32 \times 32,\ 64 \times 64,\ 128 \times 128)$ regarded within the multilevel strategy. Note that we use the modulus of the magnetic field strengths for image registration.

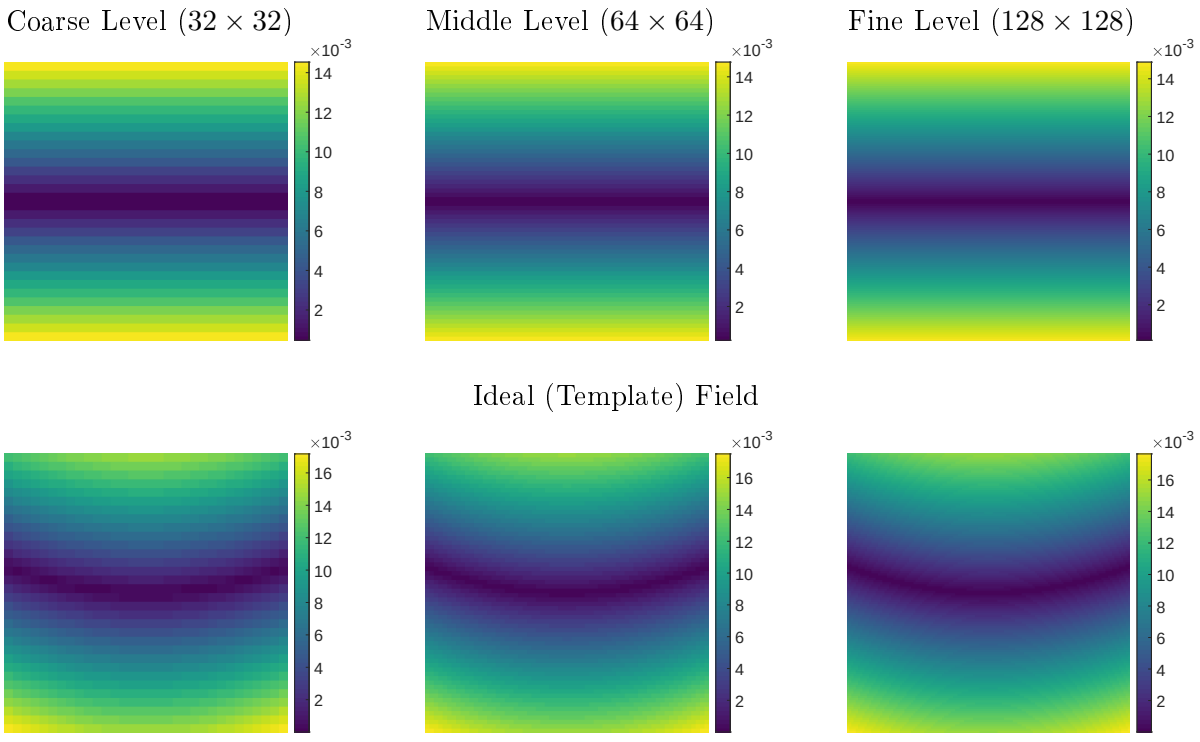

Figure 8.2.: Presented are the ideal and deformed fields with respect to different resolutions (coarse to fine from left to right with pixel numbers in brackets). With regard to image registration, the ideal field corresponds to the template and the deformed field to the target.

The image registration framework exploits padding and interpolation in order to ensure compactly supported and continuously differentiable functions. In the named example, the following is chosen as regularizer

$$\mathfrak{S}(\boldsymbol{\nu}) = \frac{1}{2}\int_0^1 \int_\Omega \sum_{k=1}^{2} |\Delta\nu_k(\mathbf{r},t)|^2 \,\mathrm{d}\mathbf{r}\,\mathrm{d}t.$$

However, the authors of [133] emphasize that the regularizer is a modular component.

Once more, we apply CVX ([68], [69]) together with the MOSEK solver [141] for determining solutions of these minimization problems. We determine reconstructions for the parameters $\omega \in \left\{2\cdot 10^i,\ i=1,\dots,8\right\}$, $\gamma_1 \in \left\{0.1^{9-0.25i},\ i=0,\dots,24\right\}$, and $\gamma_2 = 0$. Proceeding likewise as in the previous chapter dealing with time-varying particle concentrations, we extract those parameter choices maximizing the structural similarity or the peak-signal-to-noise ratio with respect to the groundtruth concentration respectively. The caption of the according reconstructions determines which image quality was used for the parameter choice and further information is gathered in a table at the end of the section. Please look back at Section 5.2.3 for results in the ideal setting and to Section 6.4 for results regarding simultaneous line rotation for this phantom.

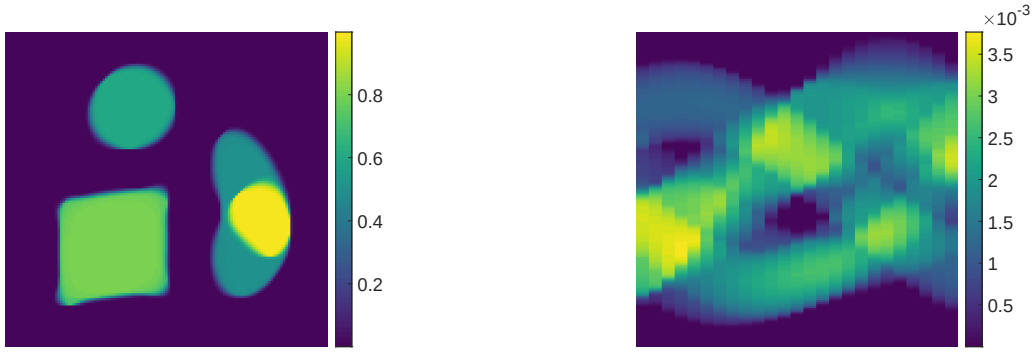

(a) (b)

Figure 8.3.: Phantom (a) and sinogram (b) reconstruction with respect to method $\mathcal{M}_1$, neglecting the field deformation. The structural similarity is $\mathrm{SSIM}(\mathbf{c}) = 0.8331$.

A reconstruction based on method $\mathcal{M}_1$, i.e. assuming ideal fields while data is determined for deformed fields, yields the concentration and sinogram depicted in Figure 8.3. We find that by proposing ideal fields the field deformation is transferred to the phantom, confirming the connection between phantom deformation and field deformation. Note that the concentration shape appears clear as we consider a constant deformation. If Γ depended on angle and time, the data set would be inconsistent and a blurred reconstruction as in the last chapter would be expected.
Applying method $\mathcal{M}_2$, incorporating the deformation in the reconstruction process, yields the images in Figure 8.4. The left column shows results using the exact deformation function (8.5), the right column makes use of the deformed grid obtained via the diffeomorphic image registration as previously described. In both cases, the concentration as well as the corresponding sinogram are well-reconstructed without deformation. We resist from additionally stating results for the PSNR-based parameter choice as they yield similar deliverables.

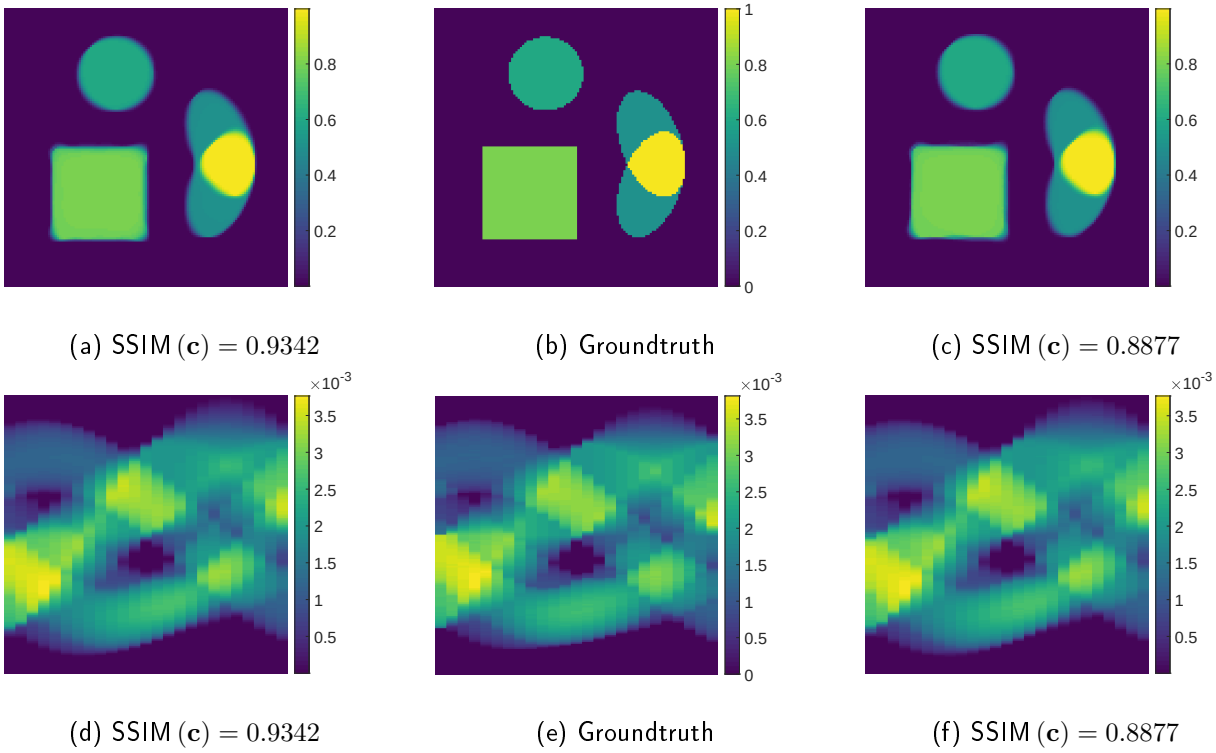

(a) SSIM $(\mathbf{c}) = 0.9342$ (b) Groundtruth (c) SSIM $(\mathbf{c}) = 0.8877$

(d) SSIM $(\mathbf{c}) = 0.9342$ (e) Groundtruth (f) SSIM $(\mathbf{c}) = 0.8877$

Figure 8.4.: Phantom (first row) and sinogram (second row) reconstructions according to method $\mathcal{M}_2$. The left column incorporates the exact deformation, the right column the one estimated via image registration.

We just presented a first proof-of-concept result for our approach to deal with magnetic field imperfections. However, for the regarded transformation (8.5), the corresponding field $\mathbf{H}^{\text{ideal}}\left(\Gamma_{\varphi,t}^{-1}\mathbf{r}, \varphi, t\right)$ does not satisfy the Maxwell conditions, that is it cannot be a real magnetic field. Therefore, we transform this field such that it is divergence- and rotation-free as proposed by (A.1). To this end, we first express it in terms of spherical harmonics. The coefficients for the ideal field are presented in Table A.1. To obtain the field described by the above defined deformation, we additionally need second order spherical harmonics. More precisely, we express $-x^2$ in terms of the polynomials p_{lm} defined in Lemma 2.29, that is

$$-x^2 = p_{2,0}(x, y, z) - \frac{1}{\sqrt{3}} p_{2,2}(x, y, z) - z^2.$$

The additional component z^2 does not matter for our considerations, as we regard the xy-plane and thus $z = 0$. Hence, by adding the black coefficients in Table 8.2 to the ideal field coefficients, we arrive at the field determined by our exact deformation function.
The field, however, is still not divergence- and rotation-free. Exploiting the explicit expression for spherical harmonics stated in Section A.2, we implemented a function that yields coefficients describing a divergence- and rotation-free field based on some input coefficients (if possible). Thereby, before transformation we add the red component in Table 8.2 to the spherical harmonics coefficients in order to guarantee that the Select Quad45 field is not changed back to its ideal version. Note that this component does not change the field within our two-dimensional formulation, as it scales again with z. Therewith, the coefficients in the previous table are transformed to those in Table 8.3.

Table 8.2.: Spherical harmonics coefficients used in addition to the ideal field's SHCs to describe fields deformed according to (8.5).

Coil Name	**H**		
	H_1	H_2	H_3
Select Maxwell		$c^2_{2,2} = \frac{25}{\sqrt{3}}G;\ c^2_{2,0} = -25\,G$	
Select Quad0		$c^2_{2,2} = \frac{25}{\sqrt{3}}G;\ c^2_{2,0} = -25\,G$	
Select Quad45	$c^1_{2,2} = -\frac{25}{\sqrt{3}}G;\ c^1_{2,0} = 25\,G$		$c^3_{2,1} = \frac{25}{\sqrt{3}}G$

Since some of the coefficients that we have added compared to the ideal field have thus been set to zero, we multiply all the remaining coefficients by two. Thus, the curvature of this deformation is comparable to the one we considered before.

Table 8.3.: Adapted spherical harmonics coefficients yielding a divergence- and rotation-free field.

Coil Name	**H**		
	H_1	H_2	H_3
Select Maxwell	$c^1_{2,-2} = \frac{25}{\sqrt{3}}G$	$c^2_{2,2} = \frac{25}{\sqrt{3}}G$	
Select Quad0	$c^1_{2,-2} = \frac{25}{\sqrt{3}}G$	$c^2_{2,2} = \frac{25}{\sqrt{3}}G$	
Select Quad45	$c^1_{2,2} = -\frac{25}{2\sqrt{3}}G;\ c^1_{2,0} = 25\,G$		$c^3_{2,1} = \frac{25}{\sqrt{3}}G$

We use these coefficients for modeling the magnetic fields and hence data simulation. Applying the classic reconstruction introduced for ideal fields, we gain the results presented in Figure 8.5. We obtain reconstructions exhibiting similar deformation artifacts as for our first example, where we included a diffeomorphic deformation and neglected it in the image determination. However, the results show background errors, which were not present in the previous setting. If we now incorporate the diffeomorphism (8.5) in the reconstruction, we obtain the results depicted in Figure 8.6. While the deformation is reduced, the background irritations are still present. Additionally, the shape of the phantom components do not fit. See for example the square, which rather appears as a rectangle in this reconstruction. Note that the deformation function in this case is only an approximation, as we have adapted the field to divergence- and rotation-free versions. The question is, whether the regarded fields can be linked to the ideal field via a diffeomorphism. Corresponding results, using a deformation function obtained by the described image registration framework are presented in Figure 8.7. This gives the best results. The background deviations are still present, but the shape matches the initial phantom. Considering these magnetic fields, we find varying results with respect to the SSIM- and PSNR-based parameter choice. The PSNR-based images appear smoother and by personal opinion are in better agreement to the groundtruth images. Reconstructions with reduced background noise obtained by adding a sparsity constraint on the Radon data are visualized in Figure 8.8. Please be referred to Table 8.4 for parameter choices and similarity values.

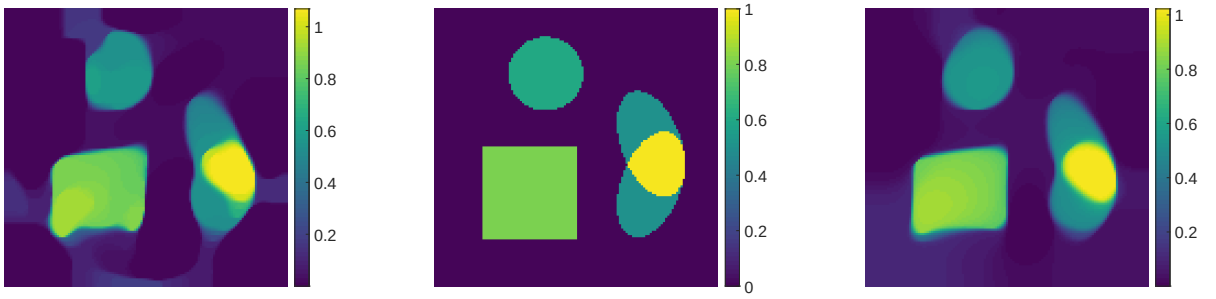

(a) SSIM $(\mathbf{c}) = 0.5537$ (b) Groundtruth (c) PSNR $(\mathbf{c}) = 17.24$

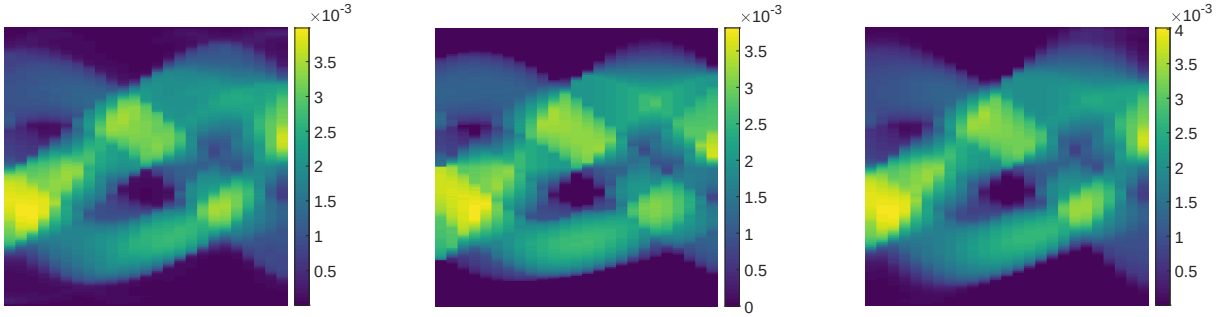

(d) SSIM $(\mathbf{c}) = 0.5537$ (e) Groundtruth (f) PSNR $(\mathbf{c}) = 17.24$

Figure 8.5.: Phantom (first row) and sinogram (second row) reconstructions using the approach $\mathcal{M}_1$. The left column shows results for SSIM-based and the right column for PSNR-based parameter choice.

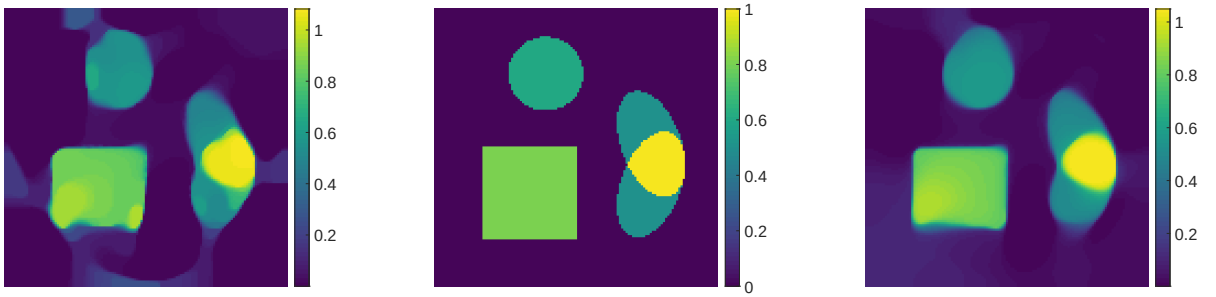

(a) SSIM $(\mathbf{c}) = 0.5801$ (b) Groundtruth (c) PSNR $(\mathbf{c}) = 18.54$

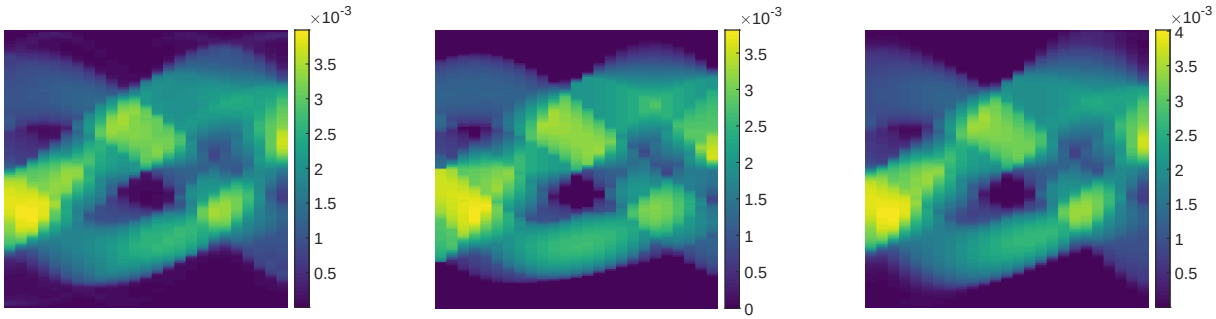

(d) SSIM $(\mathbf{c}) = 0.5801$ (e) Groundtruth (f) PSNR $(\mathbf{c}) = 18.54$

Figure 8.6.: Phantom (first row) and sinogram (second row) reconstructions using the approach $\mathcal{M}_2$ with the deformation function (8.5). The left column shows results for SSIM-based and the right column for PSNR-based parameter choice.

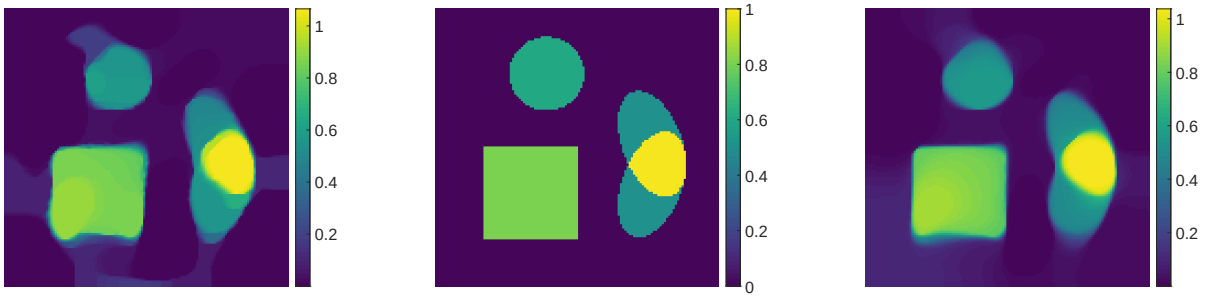

(a) SSIM $(\mathbf{c}) = 0.5995$ (b) Groundtruth (c) PSNR $(\mathbf{c}) = 19.92$

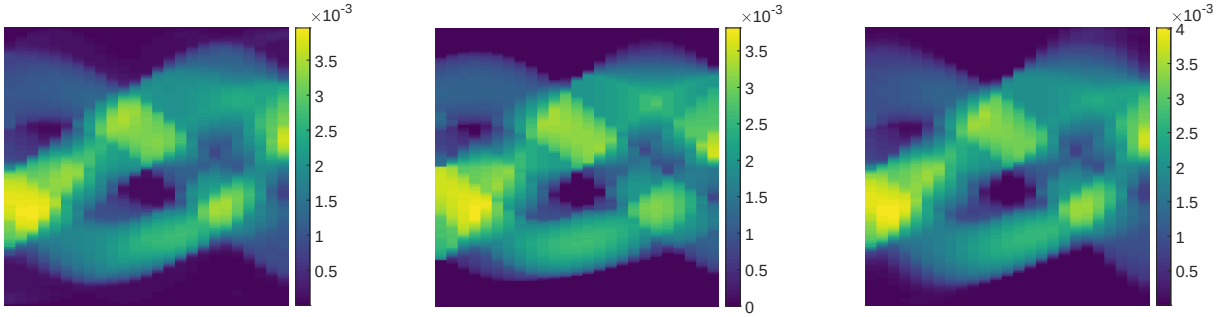

(d) SSIM $(\mathbf{c}) = 0.5995$ (e) Groundtruth (f) PSNR $(\mathbf{c}) = 19.92$

Figure 8.7.: Phantom (first row) and sinogram (second row) reconstructions using the approach $\mathcal{M}_2$ with deformation function generated via image registration. The left column shows results for SSIM-based and the right column for PSNR-based parameter choice.

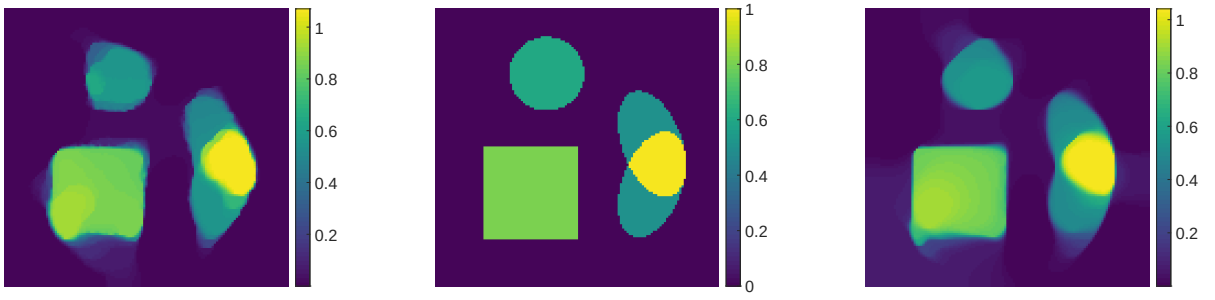

(a) SSIM $(\mathbf{c}) = 0.7242$ (b) Groundtruth (c) PSNR $(\mathbf{c}) = 19.96$

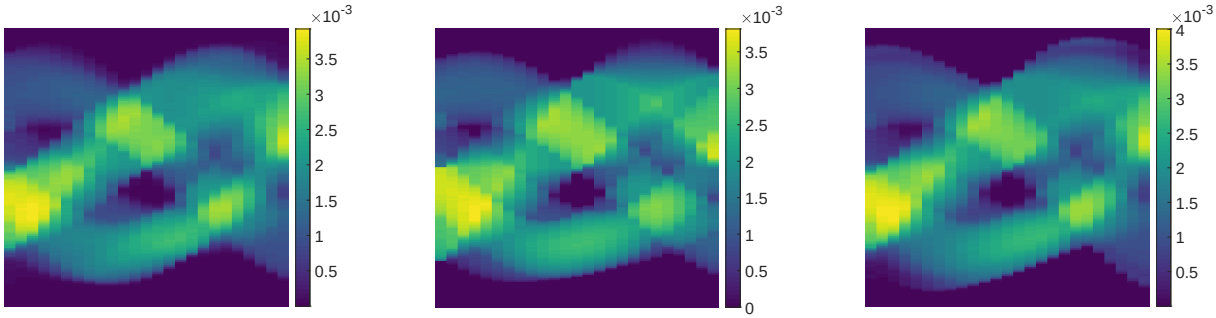

(d) SSIM $(\mathbf{c}) = 0.7242$ (e) Groundtruth (f) PSNR $(\mathbf{c}) = 19.96$

Figure 8.8.: Phantom (first row) and sinogram (second row) reconstructions using the approach $\mathcal{M}_2$ with sparsity constraint and deformation function generated via image registration. The left column shows results for SSIM-based and the right column for PSNR-based parameter choice.

We now want to investigate the background irritations and ideas to further improve image reconstruction. To this end, consider Figure 8.9.

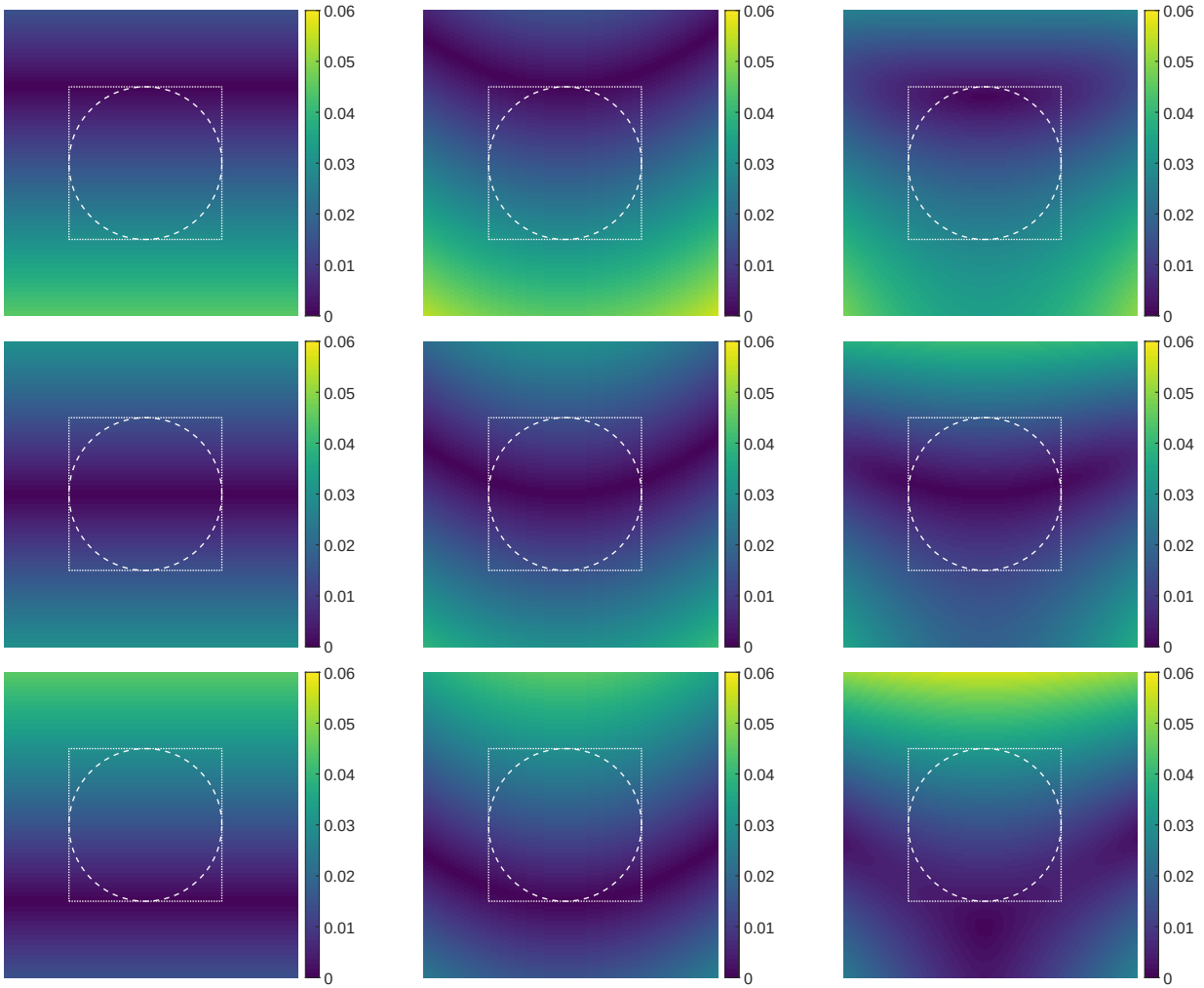

Figure 8.9.: Comparison of the ideal field (first column) with the fields deformed according to (8.5) (second column), and fields adapted to a divergence- and rotation-free version (third column), at different time steps (rows). The white dotted square shows our usual FOV and the dashed white circle represents the fully sampled region. The colorbar is fixed for better comparability.

Shown is the ideal magnetic field for different FFL positions in the first column. The second column gives the according fields for the deformation (8.5), and the third column those for the fields considered latest, i.e. the adaption to divergence- and rotation-free fields. Indicated by the dashed circle is the fully sampled region regarding ideal fields. For image registration, we considered the image sections in the second row limited by the dotted square. We added the square also in the first and third row for visualization purposes. We deduce that reconstructions can be improved by regarding an increased image section for image registration, as it can be seen that parts of the fields move to an area outside the dotted square. This cannot be described by diffeomorphisms derived with image sections constrained to the dotted square. In order to explain the lower image quality of reconstructions regarding the deformation described by Table 8.3, we compare the second and third column of the above figure. While the LFVs seem to be in good accordance when being located in the center of the FOV, this is not the case for outer regions. For the later fields, the low-field region appears compressed when located at the top of the FOV. It appears disconnected and shifted outside of the FOV, when located at the bottom. This explains the resolution and image quality

loss closer to the boundary in Figure 8.5 to 8.8. Thus, future investigations should include the specific shape of LFVs for realistic magnetic fields, as this directly links to reliability and usability of image reconstruction and gives insight of where to approach for image enhancement. Finally, it moreover is necessary to investigate whether the link between ideal and real magnetic fields can indeed be estimated by diffeomorphisms in practice. We do not assume an exact fit, keeping the disconnected LFV from our example in mind, however, a reasonable well matching approximation would be enough. As a first approach regarding real measured fields, we refer to Figure 8.10 and 8.11. Thereby, we take into account real measured fields that were provided to us and presented in ([57], [58]). Here, we further allow scaling of the magnetic fields to enable more flexibility, i.e.

$$\mathbf{H}^{\Gamma}(\mathbf{r},\varphi,t) \approx \lambda^{\mathrm{S}}_{\varphi,t}\,\mathbf{H}^{\mathrm{ideal}}_{\mathrm{S}}\left(\Gamma^{-1}_{\varphi,t}\mathbf{r},\varphi\right) + \lambda^{\mathrm{D}}_{\varphi,t}\,\mathbf{H}^{\mathrm{ideal}}_{\mathrm{D}}(\varphi,t) \tag{8.6}$$

with $\lambda^{\mathrm{S}}_{\varphi,t}, \lambda^{\mathrm{D}}_{\varphi,t} > 0$. This can easily be included in the modeling of the forward operator as well as in the image reconstruction if the scaling is assumed to be spatially independent. We find that the diffeomorphic image registration is well able to link the measured field with the computed ideal field. Note that we considered two dimensional registration for the depicted slices separately. In practice, three dimensional registration should be applied. However, LagLDDMM is capable of 3D image registration.

Table 8.4.: Reconstruction parameters and image quality values

Figure	ω	γ_1	γ_2	SSIM($\mathbf{c}$)	PSNR($\mathbf{c}$)
8.3	$2\cdot10^4$	$0.1^{4.25}$	0	0.8331	18.74
8.4a + 8.4d	$2\cdot10^3$	0.1^{5}	0	0.9342	26.36
8.4c + 8.4f	$2\cdot10^3$	$0.1^{4.75}$	0	0.8877	22.96
8.5a + 8.5d	$2\cdot10^4$	0.1^{4}	0	0.5537	16.57
8.5c + 8.5f	$2\cdot10^1$	$0.1^{5.25}$	0	0.3993	17.24
8.6a + 8.6d	$2\cdot10^4$	$0.1^{4.25}$	0	0.5801	17.43
8.6c + 8.6f	$2\cdot10^1$	$0.1^{5.75}$	0	0.4552	18.54
8.7a + 8.7d	$2\cdot10^5$	$0.1^{3.5}$	0	0.5995	18.82
8.7c + 8.7f	$2\cdot10^1$	$0.1^{5.5}$	0	0.4642	19.92
8.8a + 8.8d	$2\cdot10^5$	$0.1^{3.5}$	2.5	0.7242	18.76
8.8c + 8.8f	$2\cdot10^1$	$0.1^{5.5}$	0.4	0.5234	19.96

In summary, our new approach towards dealing with magnetic field imperfections gives promising results. Nevertheless, further investigations, especially in accordance with real measurements, are needed to provide a robust analysis.

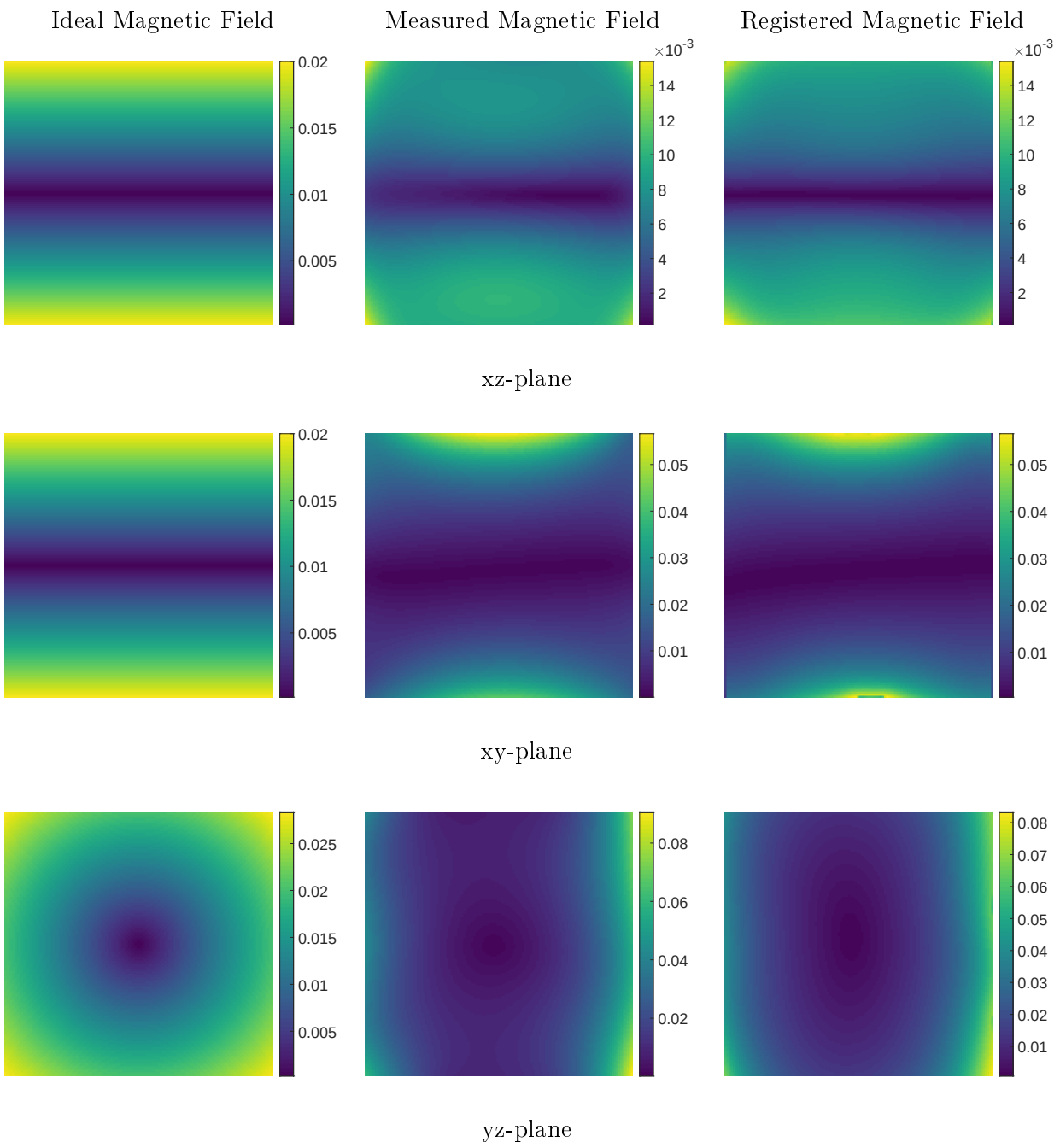

Figure 8.10.: Diffeomorphic image registration, which additionally allows scaling according to (8.6), applied to a real measured field, presented in ([57], [58]), featuring a horizontal FFL.

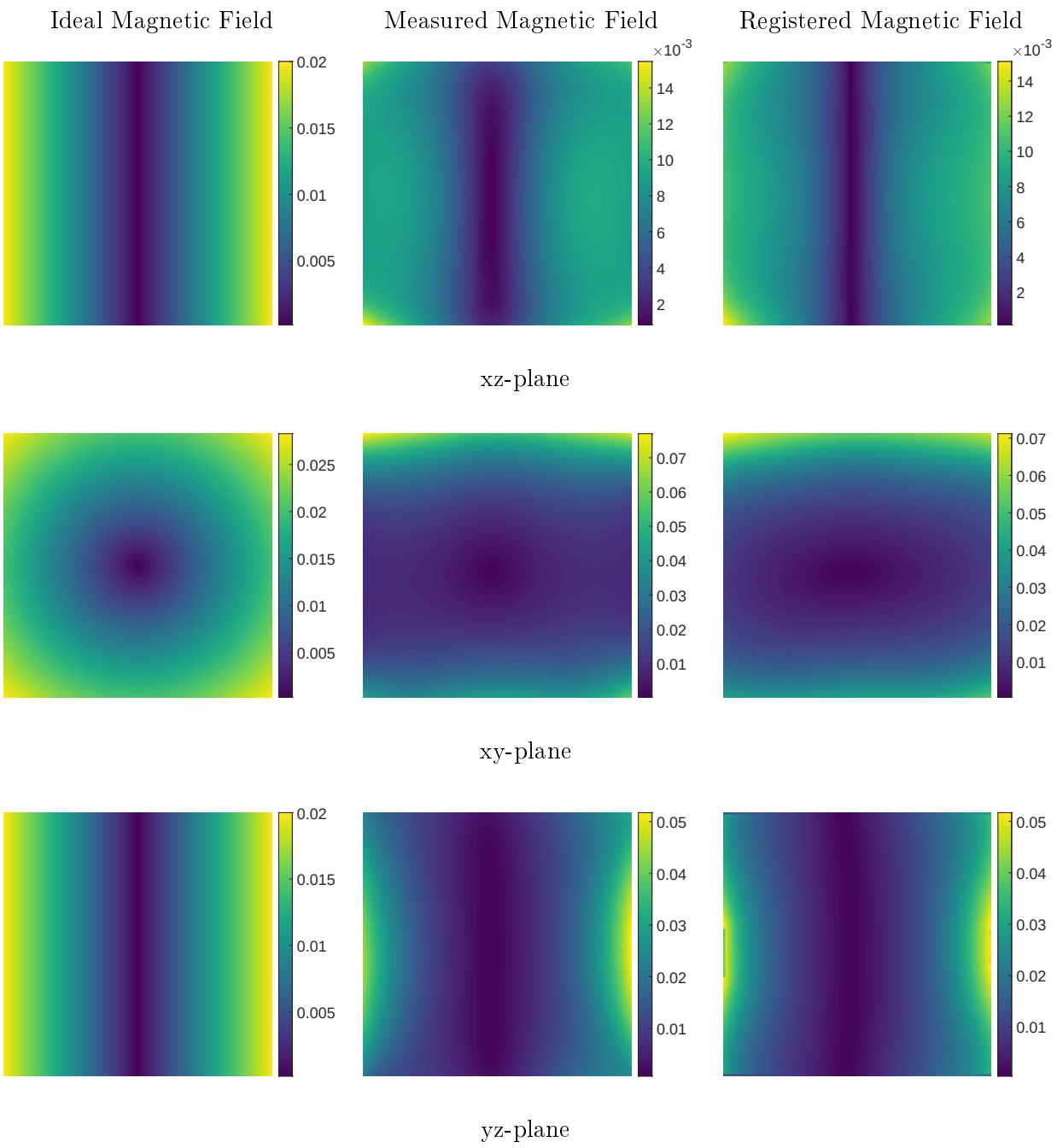

Figure 8.11.: Diffeomorphic image registration, which additionally allows scaling according to (8.6), applied to a real measured field, presented in ([57], [58]), featuring a vertical FFL.

8.5. Conclusion and outlook

We transferred the approach of dealing with dynamic particle concentrations to the setting of magnetic field imperfections. This grounds on the observation that integrating a static phantom along curves can be reinterpreted as integrating a deformed phantom along straight lines. We tested the functional capability on the basis of numerical results. More precisely, we considered magnetic fields deformed via a constant diffeomorphism. We were well able to reconstruct phantom and sinogram, using our usual simultaneous approach, for both exact incorporation of the deformation function and incorporating the approximated deformed grid based on diffeomorphic image registration applied to the modulus of magnetic field strengths. Since the resulting simulated magnetic field did not satisfy the Maxwell equations, we aimed to make our analysis more realistic by adapting the corresponding

spherical harmonics coefficients such that afterwards the fields are divergence- and rotation-free. We still were able to determine reconstructions in good accordance to the groundtruth. Nevertheless, by plotting the ideal field in comparison to the ideally deformed field (using the defined diffeomorphism) and to the divergence- and rotation-free field, showed that the image quality might be improved via including a larger image section for image registration, as parts of the fields moved out of the FOV. Furthermore, we observed that for the fields modeled by adapting the SHCs, the LFVs were contracted when located at the top of the FOV and teared apart at the bottom. Hence, for practical applications it should be examined on the one hand whether real and ideal field can indeed be linked via a diffeomorphic map, and on the other hand whether the information content of the data is reduced, as parts of the object might not be scanned by a LFV if it is shortened. Moreover, a possible resolution loss due smearing of real low-field volumes should be taken into account. As a first step towards real applications, we registered measured fields to computed ideal ones. Allowing additional scaling, which is easy to incorporate in modeling and reconstruction if it is spatially independent as it then can be pulled out of the voltage integral, we find that diffeomorphic image registration worked well for describing the measured fields in terms of the ideal one. These fields were presented in ([57], [58]) and thankfully provided to us. In our examples, we considered constant deformations. In practice, it might be necessary to execute image registration for different angle and time instances. Further future investigations might include considerations in 3D. Fortunately, the LagLDDMM approach [133] is also capable of 3D investigations and can be used for the according analysis. So far, we regarded the modulus of magnetic field strengths as input for image registration. It might be interesting to try registering the vector fields directly. In order to improve results, prior information as the requirement of the satisfaction of Maxwell equations can be exploited. Note that the considerations of this chapter are not only relevant for magnetic field imperfections but opens the possibility of various scanning geometries not restricted to applications utilizing an FFP or FFL. As a final remark, another point to consider is the possible occurrence of inaccuracies in the drive fields as well as receive coils.

9. Conclusion and Outlook

To conclude this work, let us recapitulate what we did and achieved. We started with introductory considerations, recalling fundamental notations and results from the fields of functional analysis, optimization theory, functions of bounded variation, as well as the definition of spherical harmonics. The latter can be used to model and simulate magnetic fields. In the ideal case a few SHCs are sufficient. For realistic magnetic fields, more and higher degrees become relevant. We continued with basic aspects of inverse problems in general and dynamic inverse problems in particular. Afterwards, we presented the two medical imaging techniques essential for our investigations, namely computerized tomography and magnetic particle imaging. For the special scanner type, applying a field-free line for spatial encoding, geometrical similarities between the scanning patterns of CT and MPI became obvious. Indeed, for an ideal setting, that is static phantoms, ideal fields, as well as sequential line rotation, it had already been shown that MPI-FFL data can be linked to the classical Radon transform. The goal of our work was to investigate artifact reduction for Radon-based image reconstruction in MPI using an FFL scanner. To this end, step by step, we considered different setup assumptions and aimed to transfer the mentioned relation from the ideal case to the updated settings. We started with considerations regarding a simultaneous line rotation, went on to dynamic particle concentrations, and ended with the examination of magnetic field imperfections. We find that all settings are somehow linked to the main part of this thesis, i.e. the examination of time-varying particle concentrations. The simultaneous line rotation links to the sequential one by assuming a rotating particle concentration. The field imperfections link to ideal fields in combination with deformed phantoms. It should be noted that this is not an equivalence, as the time dependencies are considered differently in the model, which leads to differences in the execution of the time derivative. For each setup, we were able to trace back MPI-FFL data to adapted versions of the Radon transform. These connections make the vast set of results regarding CT accessible. We decided to introduce a TV-based joint reconstruction of Radon data and particle concentration, which enables incorporation of both prior information about the phantom as well as the Radon data.

While our numerical results, using simulated data, showed promising results, future investigations require checking the applicability to real data in order to examine the reliability for clinical issues. To this end, it might be necessary to improve the magnetization model e.g. via incorporation of relaxation effects (cf. [12], [45]). Additionally, due to the great flexibility of variational regularization methods, we can enhance image reconstruction by adapting the objective functional. For instance, model uncertainties could be included like in [34]. Furthermore, the possibility to incorporate motion estimation directly in the image reconstruction process should be considered. At some point, however, the objective functional may become flooded with tasks and consideration should be given to outsourcing some of these to separate problem solvers. More points to consider comprise the elevation of the setting from two to three dimensions. We have taken an initial step in this direction by connecting the ideal MPI-FFL forward operator to the Radon transform in three dimensions and only then reducing it to 2D considerations for the sake of simplicity. To go on, our results could be transformed into Fourier space. Since all the links base on a convolution of the mean magnetization with the Radon transform, this might give helpful insights for the development of different reconstruction approaches. Being in Fourier space, it is then easily possible to extract

the particle response from the total signal including the direct feedthrough of the excitation function. Of further interest are investigations concerning the image quality with the first harmonic of the particle signal being removed. Finally, the combination of the settings we considered and the corresponding information content in the data could be examined with regard to e.g. contracted LFVs.

Bibliography

[1] R. Acar and C. R. Vogel. Analysis of bounded variation penalty methods for ill-posed problems. *Inverse problems*, 10(6):1217, 1994.

[2] H. Albers, T. Knopp, M. Möddel, M. Boberg, and T. Kluth. Modeling the magnetization dynamics for large ensembles of immobilized magnetic nanoparticles in multi-dimensional magnetic particle imaging. *Journal of Magnetism and Magnetic Materials*, 543:168534, 2022.

[3] H. Arami, E. Teeman, A. Troksa, H. Bradshaw, K. Saatchi, A. Tomitaka, S. S. Gambhir, U. O. Häfeli, D. Liggitt, and K. M. Krishnan. Tomographic magnetic particle imaging of cancer targeted nanoparticles. *Nanoscale*, 9(47):18723–18730, 2017.

[4] S. Arridge, P. Maass, O. Öktem, and C.-B. Schönlieb. Solving inverse problems using data-driven models. *Acta Numerica*, 28:1–174, 2019.

[5] A. B. Bakushinsky, M. Y. Kokurin, and A. Smirnova. *Iterative methods for ill-posed problems: An introduction*, volume 54. Walter De Gruyter, 2010.

[6] G. Balakrishnan, A. Zhao, M. R. Sabuncu, J. Guttag, and A. V. Dalca. Voxelmorph: a learning framework for deformable medical image registration. *IEEE transactions on medical imaging*, 38(8):1788–1800, 2019.

[7] D. M. Bates and G. Wahba. *A truncated singular value decomposition and other methods for generalized cross-validation.* University of Wisconsin, Department of Statistics, 1983.

[8] C. Bathke, T. Kluth, C. Brandt, and P. Maass. Improved image reconstruction in magnetic particle imaging using structural a priori information. *International Journal on Magnetic Particle Imaging*, 3(1), 2017.

[9] L. M. Bauer, S. F. Situ, M. A. Griswold, and A. C. S. Samia. Magnetic particle imaging tracers: State-of-the-art and future directions. *The journal of physical chemistry letters*, 6(13):2509–2517, 2015.

[10] M. F. Beg, M. I. Miller, A. Trouvé, and L. Younes. Computing large deformation metric mappings via geodesic flows of diffeomorphisms. *International journal of computer vision*, 61:139–157, 2005.

[11] M. Benning and M. Burger. Modern regularization methods for inverse problems. *Acta numerica*, 27:1–111, 2018.

[12] K. Bente, M. Weber, M. Graeser, T. F. Sattel, M. Erbe, and T. M. Buzug. Electronic field free line rotation and relaxation deconvolution in magnetic particle imaging. *IEEE transactions on medical imaging*, 34(2):644–651, 2014.

[13] C. Billings, M. Langley, G. Warrington, F. Mashali, and J. A. Johnson. Magnetic particle imaging: current and future applications, magnetic nanoparticle synthesis methods and safety measures. *International Journal of Molecular Sciences*, 22(14):7651, 2021.

[14] S. Blanke and C. Brandt. Dealing with field imperfections for field-free line magnetic particle imaging. In *Tomographic Inverse Problems: Mathematical Challenges and Novel Applications*, volume Report No. 21/2023. Mathematisches Forschungsinstitut Oberwolfach, 2023.

[15] S. Blanke and C. Brandt. Field-free line magnetic particle imaging: Radon-based artifact reduction with motion models. *arXiv preprint arXiv:2306.10722*, 2023.

[16] S. Blanke and C. Brandt. Radon-based image reconstruction for MPI using a continuously rotating FFL. In *Modeling, Simulation and Optimization of Fluid Dynamic Applications*, pages 93–111. Springer, 2023.

[17] S. E. Blanke, B. N. Hahn, and A. Wald. Inverse problems with inexact forward operator: Iterative regularization and application in dynamic imaging. *Inverse Problems*, 36(12):124001, 2020.

[18] I. R. Bleyer and R. Ramlau. A double regularization approach for inverse problems with noisy data and inexact operator. *Inverse Problems*, 29(2):025004, 2013.

[19] C. Blondel, R. Vaillant, G. Malandain, and N. Ayache. 3D tomographic reconstruction of coronary arteries using a precomputed 4D motion field. *Physics in Medicine & Biology*, 49(11):2197, 2004.

[20] M. Boberg, T. Knopp, and M. Möddel. Reducing displacement artifacts by warping system matrices in efficient joint multi-patch magnetic particle imaging. *International journal on magnetic particle imaging*, 6(2, Suppl 1):1–3, 2020.

[21] M. Boberg, T. Knopp, and M. Möddel. Unique compact representation of magnetic fields using truncated solid harmonic expansions. *arXiv preprint arXiv:2302.07591*, 2023.

[22] M. Boberg, T. Knopp, P. Szwargulski, and M. Möddel. Generalized MPI multi-patch reconstruction using clusters of similar system matrices. *IEEE transactions on medical imaging*, 39(5):1347–1358, 2019.

[23] J. Bohnert and O. Dössel. Effects of time varying currents and magnetic fields in the frequency range of 1 kHz to 1 MHz to the human body-a simulation study. In *2010 Annual International Conference of the IEEE Engineering in Medicine and Biology*, pages 6805–6808. IEEE, 2010.

[24] S. Bonnet, A. Koenig, S. Roux, P. Hugonnard, R. Guillemaud, and P. Grangeat. Dynamic X-ray computed tomography. *Proceedings of the IEEE*, 91(10):1574–1587, 2003.

[25] C. Brandt, T. Kluth, T. Knopp, and L. Westen. Dynamic image reconstruction with motion priors in application to 3D magnetic particle imaging. *arXiv preprint arXiv:2306.11625*, 2023.

[26] C. Brandt and C. Schmidt. Modeling magnetic particle imaging for dynamic tracer distributions. *Sensing and Imaging*, 22(1):1–24, 2021.

[27] C. Brandt and C. Schmidt. Motion compensation for non-periodic dynamic tracer distributions in multi-patch magnetic particle imaging. *Physics in Medicine & Biology*, 67(8):085005, 2022.

[28] K. Bredies and D. Lorenz. *Mathematical image processing*. Springer, 2018.

[29] G. Bringout. *Field free line magnetic particle imaging: Characterization and imaging device up-scaling*. PhD thesis, Universität zu Lübeck, 2016.

[30] G. Bringout and T. Buzug. A robust and compact representation for magnetic fields in magnetic particle imaging. *Biomed Tech*, 59:978–1, 2014.

[31] G. Bringout, W. Erb, and J. Frikel. A new 3D model for magnetic particle imaging using realistic magnetic field topologies for algebraic reconstruction. *Inverse Problems*, 36(12):124002, 2020.

[32] T. A. Bubba, T. Heikkilä, H. Help, S. Huotari, Y. Salmon, and S. Siltanen. Sparse dynamic tomography: A shearlet-based approach for iodine perfusion in plant stems. *Inverse Problems*, 36(9):094002, 2020.

[33] J. W. Bulte, P. Walczak, M. Janowski, K. M. Krishnan, H. Arami, A. Halkola, B. Gleich, and J. Rahmer. Quantitative "hot-spot" imaging of transplanted stem cells using superparamagnetic tracers and magnetic particle imaging. *Tomography*, 1(2):91–97, 2015.

[34] L. Bungert, M. Burger, Y. Korolev, and C.-B. Schönlieb. Variational regularisation for inverse problems with imperfect forward operators and general noise models. *Inverse Problems*, 36(12):125014, 2020.

[35] M. Burger. Variational regularization in inverse problems and machine learning. *arXiv preprint arXiv:2112.04591*, 2021.

[36] M. Burger, H. Dirks, L. Frerking, A. Hauptmann, T. Helin, and S. Siltanen. A variational reconstruction method for undersampled dynamic X-ray tomography based on physical motion models. *Inverse Problems*, 33(12):124008, 2017.

[37] M. Burger, H. Dirks, and C.-B. Schonlieb. A variational model for joint motion estimation and image reconstruction. *SIAM Journal on Imaging Sciences*, 11(1):94–128, 2018.

[38] M. Burger, J. Modersitzki, and L. Ruthotto. A hyperelastic regularization energy for image registration. *SIAM Journal on Scientific Computing*, 35(1):B132–B148, 2013.

[39] M. Burger and S. Osher. A guide to the TV zoo. In *Level set and PDE based reconstruction methods in imaging*, pages 1–70. Springer, 2013.

[40] M. Burger, T. Schuster, and A. Wald. Ill-posedness of time-dependent inverse problems in Lebesgue-Bochner spaces. *arXiv preprint arXiv:2310.08600*, 2023.

[41] V. Caselles, A. Chambolle, and M. Novaga. Total variation in imaging. *Handbook of mathematical methods in imaging*, 1(2):3, 2015.

[42] C. Chen. Spatiotemporal imaging with diffeomorphic optimal transportation. *Inverse Problems*, 37(11):115004, 2021.

[43] C. Chen, B. Gris, and O. Öktem. A new variational model for joint image reconstruction and motion estimation in spatiotemporal imaging. *SIAM Journal on Imaging Sciences*, 12(4):1686–1719, 2019.

[44] C. R. Crawford, K. F. King, C. J. Ritchie, and J. D. Godwin. Respiratory compensation in projection imaging using a magnification and displacement model. *IEEE transactions on medical imaging*, 15(3):327–332, 1996.

[45] L. R. Croft, P. W. Goodwill, and S. M. Conolly. Relaxation in x-space magnetic particle imaging. *IEEE transactions on medical imaging*, 31(12):2335–2342, 2012.

[46] A. V. Dalca, G. Balakrishnan, J. Guttag, and M. R. Sabuncu. Unsupervised learning for fast probabilistic diffeomorphic registration. In *Medical Image Computing and Computer Assisted Intervention–MICCAI 2018: 21st International Conference, Granada, Spain, September 16-20, 2018, Proceedings, Part I*, pages 729–738. Springer, 2018.

[47] L. Desbat, S. Roux, and P. Grangeat. Compensation of some time dependent deformations in tomography. *IEEE transactions on medical imaging*, 26(2):261–269, 2007.

[48] H. Dirks. Joint large-scale motion estimation and image reconstruction. *arXiv preprint arXiv:1610.09908*, 2016.

[49] M. Dobrowolski. *Angewandte Funktionalanalysis: Funktionalanalysis, Sobolev-Räume und elliptische Differentialgleichungen*. Masterclass. Springer-Verlag Berlin Heidelberg, 2 edition, 2010.

[50] O. Dössel. *Bildgebende Verfahren in der Medizin*. Springer, 2016.

[51] J. Ehrhardt, M. Ahlborg, H. Uzunova, T. M. Buzug, and H. Handels. Temporal polyrigid registration for patch-based MPI reconstruction of moving objects. *International Journal on Magnetic Particle Imaging*, 5(1-2), 2019.

[52] H. W. Engl, M. Hanke, and A. Neubauer. *Regularization of inverse problems*, volume 375. Springer Science & Business Media, 1996.

[53] M. Erbe. *Field free line magnetic particle imaging*. Springer Science & Business Media, 2014.

[54] M. Erbe, T. Knopp, T. F. Sattel, S. Biederer, and T. M. Buzug. Experimental generation of an arbitrarily rotated field-free line for the use in magnetic particle imaging. *Medical physics*, 38(9):5200–5207, 2011.

[55] L. Feng, R. Grimm, K. T. Block, H. Chandarana, S. Kim, J. Xu, L. Axel, D. K. Sodickson, and R. Otazo. Golden-angle radial sparse parallel MRI: Combination of compressed sensing, parallel imaging, and golden-angle radial sampling for fast and flexible dynamic volumetric MRI. *Magnetic resonance in medicine*, 72(3):707–717, 2014.

[56] R. M. Ferguson, A. P. Khandhar, S. J. Kemp, H. Arami, E. U. Saritas, L. R. Croft, J. Konkle, P. W. Goodwill, A. Halkola, J. Rahmer, J. Borgert, S. M. Conolly, and K. M. Krishnan. Magnetic particle imaging with tailored iron oxide nanoparticle tracers. *IEEE transactions on medical imaging*, 34(5):1077–1084, 2014.

[57] F. Foerger, M. Boberg, M. Möddel, J.-P. Scheel, M. Gräser, and T. Knopp. Low-power iron selection and focus field generator. *International Journal on Magnetic Particle Imaging IJMPI*, 8(1 Suppl 1), 2022.

[58] F. Foerger, N. Hackelberg, M. Boberg, J.-P. Scheel, F. Thieben, L. Mirzojan, F. Mohn, M. Möddel, M. Graeser, and T. Knopp. Flexible selection field generation using iron core coil arrays. *International Journal on Magnetic Particle Imaging IJMPI*, 9(1 Suppl 1), 2023.

[59] J. Franke, U. Heinen, H. Lehr, A. Weber, F. Jaspard, W. Ruhm, M. Heidenreich, and V. Schulz. System characterization of a highly integrated preclinical hybrid MPI-MRI scanner. *IEEE transactions on medical imaging*, 35(9):1993–2004, 2016.

[60] N. Gdaniec, M. Boberg, M. Möddel, P. Szwargulski, and T. Knopp. Suppression of motion artifacts caused by temporally recurring tracer distributions in multi-patch magnetic particle imaging. *IEEE transactions on medical imaging*, 39(11):3548–3558, 2020.

[61] N. Gdaniec, M. Schlüter, M. Möddel, M. G. Kaul, K. M. Krishnan, A. Schlaefer, and T. Knopp. Detection and compensation of periodic motion in magnetic particle imaging. *IEEE transactions on medical imaging*, 36(7):1511–1521, 2017.

[62] S. F. Gilyazov and N. L. Gol'dman. *Regularization of ill-posed problems by iteration methods*, volume 499. Springer Science & Business Media, 2013.

[63] B. Gleich and J. Weizenecker. Tomographic imaging using the nonlinear response of magnetic particles. *Nature*, 435(7046):1214–1217, 2005.

[64] B. Gleich, J. Weizenecker, H. Timminger, C. Bontus, I. Schmale, J. Rahmer, J. Schmidt, J. Kanzenbach, and J. Borgert. Fast MPI demonstrator with enlarged field of view. In *Proc. ISMRM*, volume 18, pages 1920–1970, 2010.

[65] P. W. Goodwill and S. M. Conolly. The x-space formulation of the magnetic particle imaging process: 1-D signal, resolution, bandwidth, SNR, SAR, and magnetostimulation. *IEEE transactions on medical imaging*, 29(11):1851–1859, 2010.

[66] P. W. Goodwill, J. J. Konkle, B. Zheng, E. U. Saritas, and S. M. Conolly. Projection x-space magnetic particle imaging. *IEEE transactions on medical imaging*, 31(5):1076–1085, 2012.

[67] M. Graeser, F. Thieben, P. Szwargulski, F. Werner, N. Gdaniec, M. Boberg, F. Griese, M. Möddel, P. Ludewig, D. Van De Ven, O. M. Weber, O. Woywode, B. Gleich, and T. Knopp. Human-sized magnetic particle imaging for brain applications. *Nature communications*, 10(1):1936, 2019.

[68] M. Grant and S. Boyd. Graph implementations for nonsmooth convex programs. In V. Blondel, S. Boyd, and H. Kimura, editors, *Recent Advances in Learning and Control*, Lecture Notes in Control and Information Sciences, pages 95–110. Springer-Verlag Limited, 2008.

[69] M. Grant and S. Boyd. CVX: Matlab software for disciplined convex programming, version 2.2. build 1148. http://cvxr.com/cvx, 2020.

[70] D. J. Griffiths. Introduction to electrodynamics fourth edition. 2021.

[71] B. Gris, C. Chen, and O. Öktem. Image reconstruction through metamorphosis. *Inverse Problems*, 36(2):025001, 2020.

[72] M. Grüttner, T. Knopp, J. Franke, M. Heidenreich, J. Rahmer, A. Halkola, C. Kaethner, J. Borgert, and T. M. Buzug. On the formulation of the image reconstruction problem in magnetic particle imaging. *Biomedizinische Technik/Biomedical Engineering*, 58(6):583–591, 2013.

[73] J. Hadamard. *Lectures on Cauchy's problem in linear partial differential equations*, volume 15. Yale university press, 1923.

[74] J. Haegele, J. Rahmer, B. Gleich, J. Borgert, H. Wojtczyk, N. Panagiotopoulos, T. M. Buzug, J. Barkhausen, and F. M. Vogt. Magnetic particle imaging: Visualization of instruments for cardiovascular intervention. *Radiology*, 265(3):933–938, 2012.

[75] J. Haegele, T. Sattel, M. Erbe, K. Luedtke-Buzug, M. Taupitz, J. Borgert, T. Buzug, J. Barkhausen, and F. Vogt. Magnetic particle imaging (MPI). In *RöFo-Fortschritte auf dem Gebiet der Röntgenstrahlen und der bildgebenden Verfahren*, pages 420–426. © Georg Thieme Verlag KG, 2011.

[76] B. Hahn. Reconstruction of dynamic objects with affine deformations in computerized tomography. *Journal of Inverse and Ill-posed Problems*, 22(3):323–339, 2014.

[77] B. N. Hahn. Efficient algorithms for linear dynamic inverse problems with known motion. *Inverse Problems*, 30(3):035008, 2014.

[78] B. N. Hahn. Null space and resolution in dynamic computerized tomography. *Inverse Problems*, 32(2):025006, 2016.

[79] B. N. Hahn. Motion estimation and compensation strategies in dynamic computerized tomography. *Sensing and Imaging*, 18(1):1–20, 2017.

[80] B. N. Hahn. Motion compensation strategies in tomography. In *Time-Dependent Problems in Imaging and Parameter Identification*, pages 51–83. Springer, 2021.

[81] B. N. Hahn, M.-L. K. Garrido, and E. T. Quinto. Microlocal properties of dynamic fourier integral operators. In *Time-Dependent Problems in Imaging and Parameter Identification*, pages 85–120. Springer, 2021.

[82] B. N. Hahn, M.-L. Kienle-Garrido, C. Klingenberg, and S. Warnecke. Using the Navier-Cauchy equation for motion estimation in dynamic imaging. *arXiv preprint arXiv:2009.04212*, 2020.

[83] B. N. Hahn and E. T. Quinto. Detectable singularities from dynamic Radon data. *SIAM Journal on Imaging Sciences*, 9(3):1195–1225, 2016.

[84] B. N. Hahn, E. T. Quinto, and G. Rigaud. Foreword to special issue of inverse problems on modern challenges in imaging, 2023.

[85] M. Hanke, A. Neubauer, and O. Scherzer. A convergence analysis of the Landweber iteration for nonlinear ill-posed problems. *Numerische Mathematik*, 72(1):21–37, 1995.

[86] P. C. Hansen. The truncated SVD as a method for regularization. *BIT Numerical Mathematics*, 27:534–553, 1987.

[87] V. Hartung, J. Günther, A. M. Augustin, T. Reichl, P. Gruschwitz, M. Rückert, T. A. Bley, V. Behr, S. Herz, and P. Vogel. Resotran® meets MPI–clinically approved ferucarbotran reintroduced: A major leap towards MPI in humans. *International Journal on Magnetic Particle Imaging IJMPI*, 9(1 Suppl 1), 2023.

[88] A. Hauptmann, S. Arridge, F. Lucka, V. Muthurangu, and J. A. Steeden. Real-time cardiovascular MR with spatio-temporal artifact suppression using deep learning–proof of concept in congenital heart disease. *Magnetic resonance in medicine*, 81(2):1143–1156, 2019.

[89] A. Hauptmann, O. Öktem, and C. Schönlieb. Image reconstruction in dynamic inverse problems with temporal models. *Handbook of Mathematical Models and Algorithms in Computer Vision and Imaging: Mathematical Imaging and Vision*, pages 1–31, 2021.

[90] D. Hensley, Z. W. Tay, R. Dhavalikar, B. Zheng, P. Goodwill, C. Rinaldi, and S. Conolly. Combining magnetic particle imaging and magnetic fluid hyperthermia in a theranostic platform. *Physics in Medicine & Biology*, 62(9):3483, 2017.

[91] B. K. Horn and B. G. Schunck. Determining optical flow. *Artificial intelligence*, 17(1-3):185–203, 1981.

[92] G. N. Hounsfield. Computed medical imaging. nobel lecture, december 8, 1979. *Journal of computer assisted tomography*, 4(5):665–674, 1980.

[93] T. Hytönen, J. Van Neerven, M. Veraar, and L. Weis. Bochner spaces. *Analysis in Banach Spaces: Volume I: Martingales and Littlewood-Paley Theory*, pages 1–66, 2016.

[94] S. Ilbey, C. B. Top, A. Güngör, T. Çukur, E. Ü. Sarıtaş, and H. E. Güven. Comparison of system-matrix-based and projection-based reconstructions for field free line magnetic particle imaging. *International Journal on Magnetic Particle Imaging*, 3(1):1–8, 2017.

[95] A. Isola, A. Ziegler, T. Koehler, W. Niessen, and M. Grass. Motion-compensated iterative cone-beam CT image reconstruction with adapted blobs as basis functions. *Physics in Medicine & Biology*, 53(23):6777, 2008.

[96] K. Ito and B. Jin. *Inverse problems: Tikhonov theory and algorithms*, volume 22. World Scientific, 2014.

[97] C. Jung, J. Salamon, M. Hofmann, M. G. Kaul, G. Adam, H. Ittrich, and T. Knopp. MPI as high temporal resolution imaging technique for in vivo bolus tracking of ferucarbotran in mouse model. In *Medical Imaging 2016: Biomedical Applications in Molecular, Structural, and Functional Imaging*, volume 9788, pages 208–214. SPIE, 2016.

[98] W. A. Kalender. *Computed tomography: Fundamentals, system technology, image quality, applications*. Wiley, 3 edition, 2011.

[99] B. Kaltenbacher. All-at-once versus reduced iterative methods for time dependent inverse problems. *Inverse Problems*, 33(6):064002, 2017.

[100] B. Kaltenbacher, A. Neubauer, and O. Scherzer. *Iterative regularization methods for nonlinear ill-posed problems*. Walter de Gruyter, 2008.

[101] B. Kaltenbacher, T. T. N. Nguyen, A. Wald, and T. Schuster. Parameter identification for the Landau–Lifshitz–Gilbert equation in magnetic particle imaging. In *Time-dependent Problems in Imaging and Parameter Identification*, pages 377–412. Springer, 2021.

[102] B. Kaltenbacher, T. Schuster, and A. Wald. *Time-dependent Problems in Imaging and Parameter Identification*. Springer, 2021.

[103] T. Kampf, M. A. Rückert, V. C. Behr, and P. Vogel. Modular simulation framework for magnetic particle imaging. *International Journal on Magnetic Particle Imaging IJMPI*, 9(1 Suppl 1), 2023.

[104] A. Katsevich. Motion compensated local tomography. *Inverse Problems*, 24(4):045012, 2008.

[105] A. Katsevich. An accurate approximate algorithm for motion compensation in two-dimensional tomography. *Inverse Problems*, 26(6):065007, 2010.

[106] A. Katsevich, M. Silver, and A. Zamyatin. Local tomography and the motion estimation problem. *SIAM Journal on Imaging Sciences*, 4(1):200–219, 2011.

[107] B. Kilic, D. A. Soydan, A. Güngör, and C. B. Top. Inverse Radon transform-based reconstruction with an open-sided magnetic particle imaging prototype. *Signal, Image and Video Processing*, pages 1–8, 2022.

[108] A. Kirsch. *An introduction to the mathematical theory of inverse problems*, volume 120. Springer, 2011.

[109] T. Kluth. Mathematical models for magnetic particle imaging. *Inverse Problems*, 34(8):083001, 2018.

[110] T. Kluth, B. Jin, and G. Li. On the degree of ill-posedness of multi-dimensional magnetic particle imaging. *Inverse Problems*, 34(9):095006, 2018.

[111] T. Kluth, P. Szwargulski, and T. Knopp. Towards accurate modeling of the multidimensional magnetic particle imaging physics. *New journal of physics*, 21(10):103032, 2019.

[112] T. Knopp, S. Biederer, T. Sattel, J. Weizenecker, B. Gleich, J. Borgert, and T. Buzug. Trajectory analysis for magnetic particle imaging. *Physics in Medicine & Biology*, 54(2):385, 2008.

[113] T. Knopp and T. M. Buzug. *Magnetic particle imaging: An introduction to imaging principles and scanner instrumentation*. Springer Science & Business Media, 2012.

[114] T. Knopp, M. Erbe, T. F. Sattel, S. Biederer, and T. M. Buzug. A Fourier slice theorem for magnetic particle imaging using a field-free line. *Inverse Problems*, 27(9):095004, 2011.

[115] T. Knopp, N. Gdaniec, and M. Möddel. Magnetic particle imaging: From proof of principle to preclinical applications. *Physics in Medicine & Biology*, 62(14):R124, 2017.

[116] T. Knopp, J. Rahmer, T. F. Sattel, S. Biederer, J. Weizenecker, B. Gleich, J. Borgert, and T. M. Buzug. Weighted iterative reconstruction for magnetic particle imaging. *Physics in medicine & biology*, 55(6):1577, 2010.

[117] T. Knopp, T. F. Sattel, S. Biederer, J. Rahmer, J. Weizenecker, B. Gleich, J. Borgert, and T. M. Buzug. Model-based reconstruction for magnetic particle imaging. *IEEE Transactions on Medical Imaging*, 29(1):12–18, 2009.

[118] A. Kofler, M. Dewey, T. Schaeffter, C. Wald, and C. Kolbitsch. Spatio-temporal deep learning-based undersampling artefact reduction for 2D radial cine MRI with limited training data. *IEEE transactions on medical imaging*, 39(3):703–717, 2019.

[119] J. J. Konkle, P. W. Goodwill, O. M. Carrasco-Zevallos, and S. M. Conolly. Projection reconstruction magnetic particle imaging. *IEEE transactions on medical imaging*, 32(2):338–347, 2012.

[120] V. P. Krishnan and E. T. Quinto. Microlocal analysis in tomography. *Handbook of mathematical methods in imaging*, 1:3, 2015.

[121] L. Landweber. An iteration formula for Fredholm integral equations of the first kind. *American journal of mathematics*, 73(3):615–624, 1951.

[122] L. F. Lang, N. Dutta, E. Scarpa, B. Sanson, C.-B. Schönlieb, and J. Étienne. Joint motion estimation and source identification using convective regularisation with an application to the analysis of laser nanoablations. *Time-dependent Problems in Imaging and Parameter Identification*, pages 191–227, 2021.

[123] L. F. Lang, S. Neumayer, O. Öktem, and C.-B. Schönlieb. Template-based image reconstruction from sparse tomographic data. *Applied Mathematics & Optimization*, 82:1081–1109, 2020.

[124] A. Lechleiter. Dynamic inverse problems: Modelling—regularization—numerics. *Inverse Problems*, 34(040301):4pp, 2018.

[125] T. Li, E. Schreibmann, Y. Yang, and L. Xing. Motion correction for improved target localization with on-board cone-beam computed tomography. *Physics in Medicine & Biology*, 51(2):253, 2005.

[126] J. Liu, A. I. Aviles-Rivero, H. Ji, and C.-B. Schönlieb. Rethinking medical image reconstruction via shape prior, going deeper and faster: Deep joint indirect registration and reconstruction. *Medical Image Analysis*, 68:101930, 2021.

[127] A. K. Louis. Orthogonal function series expansions and the null space of the Radon transform. *SIAM journal on mathematical analysis*, 15(3):621–633, 1984.

[128] A. K. Louis. Approximate inverse for linear and some nonlinear problems. *Inverse problems*, 12(2):175, 1996.

[129] W. Lu and T. R. Mackie. Tomographic motion detection and correction directly in sinogram space. *Physics in Medicine & Biology*, 47(8):1267, 2002.

[130] F. Lucka, N. Huynh, M. Betcke, E. Zhang, P. Beard, B. Cox, and S. Arridge. Enhancing compressed sensing 4D photoacoustic tomography by simultaneous motion estimation. *SIAM Journal on Imaging Sciences*, 11(4):2224–2253, 2018.

[131] K. Lüdtke-Buzug, J. Haegele, S. Biederer, T. F. Sattel, M. Erbe, R. L. Duschka, J. Barkhausen, and F. M. Vogt. Comparison of commercial iron oxide-based MRI contrast agents with synthesized high-performance MPI tracers. *Biomedizinische Technik/Biomedical Engineering*, 58(6):527–533, 2013.

[132] M. Lustig, J. M. Santos, D. L. Donoho, and J. M. Pauly. kt SPARSE: High frame rate dynamic MRI exploiting spatio-temporal sparsity. In *Proceedings of the 13th annual meeting of ISMRM, Seattle*, volume 2420. Citeseer, 2006.

[133] A. Mang and L. Ruthotto. A Lagrangian Gauss–Newton–Krylov solver for mass- and intensity-preserving diffeomorphic image registration. *SIAM Journal on Scientific Computing*, 39(5):B860–B885, 2017.

[134] D. Markov, H. Boeve, B. Gleich, J. Borgert, A. Antonelli, C. Sfara, and M. Magnani. Human erythrocytes as nanoparticle carriers for magnetic particle imaging. *Physics in Medicine & Biology*, 55(21):6461, 2010.

[135] S. Marsland and C. J. Twining. Constructing diffeomorphic representations for the groupwise analysis of nonrigid registrations of medical images. *IEEE transactions on medical imaging*, 23(8):1006–1020, 2004.

[136] E. Mattingly, E. Mason, K. Herb, M. Śliwiak, K. Brandt, C. Cooley, and L. Wald. OS-MPI: an open-source magnetic particle imaging project. *International Journal on Magnetic Particle Imaging*, 6(2 Suppl 1), 2020.

[137] E. Mattingly, E. E. Mason, K. Herb, M. Śliwiak, J. Drago, M. Graeser, and L. L. Wald. A sensitive, stable, continuously rotating FFL MPI system for functional imaging of the rat brain. *Int. J. Magn. Part. Imaging*, 8:2212001, 2022.

[138] H. Medimagh, P. Weissert, G. Bringout, K. Bente, M. Weber, K. Gräfe, A. Cordes, and T. M. Buzug. Artifacts in field free line magnetic particle imaging in the presence of inhomogeneous and nonlinear magnetic fields. *Current Directions in Biomedical Engineering*, 1(1):245–248, 2015.

[139] M. Möddel, A. Schlömerkemper, T. Knopp, and T. Kluth. Limitations of current MPI models in the context of fluid dynamics. *International Journal on Magnetic Particle Imaging IJMPI*, 9(1 Suppl 1), 2023.

[140] J. Modersitzki. *FAIR: Flexible algorithms for image registration*. SIAM, 2009.

[141] A. Mosek. The MOSEK optimization toolbox for MATLAB manual. version 9.1. 2020. https://docs.mosek.com/9.1/toolbox/index.html.

[142] J. L. Mueller and S. Siltanen. *Linear and nonlinear inverse problems with practical applications*. SIAM, 2012.

[143] K. Murase, M. Aoki, N. Banura, K. Nishimoto, A. Mimura, T. Kuboyabu, and I. Yabata. Usefulness of magnetic particle imaging for predicting the therapeutic effect of magnetic hyperthermia. *Open Journal of Medical Imaging*, 5(02):85, 2015.

[144] F. Natterer. *The Mathematics of Computerized Tomography*. 1986.

[145] E. Niemi, M. Lassas, A. Kallonen, L. Harhanen, K. Hämäläinen, and S. Siltanen. Dynamic multi-source X-ray tomography using a spacetime level set method. *Journal of Computational Physics*, 291:218–237, 2015.

[146] M. Nitzsche, H. Albers, T. Kluth, and B. Hahn. Compensating model imperfections during image reconstruction via RESESOP. *International Journal on Magnetic Particle Imaging IJMPI*, 8(1 Suppl 1), 2022.

[147] O. Öktem, C. Pouchol, and O. Verdier. Spatiotemporal PET reconstruction using ML-EM with learned diffeomorphic deformation. In *Machine Learning for Medical Image Reconstruction: Second International Workshop, MLMIR 2019, Held in Conjunction with MICCAI 2019, Shenzhen, China, October 17, 2019, Proceedings 2*, pages 151–162. Springer, 2019.

[148] J. Pagan, C. McDonough, T. Vo, and A. Tonyushkin. Single-sided magnetic particle imaging device with field-free-line geometry for in vivo imaging applications. *IEEE Transactions on Magnetics*, 57(2):1–5, 2020.

[149] N. Panagiotopoulos, R. L. Duschka, M. Ahlborg, G. Bringout, C. Debbeler, M. Graeser, C. Kaethner, K. Lüdtke-Buzug, H. Medimagh, J. Stelzner, T. M. Buzug, J. Barkhausen, F. M. Vogt, and J. Haegele. Magnetic particle imaging: Current developments and future directions. *International journal of nanomedicine*, pages 3097–3114, 2015.

[150] J. Peypouquet. *Convex optimization in normed spaces: Theory, methods and examples*. Springer, 2015.

[151] C. Qin, W. Bai, J. Schlemper, S. E. Petersen, S. K. Piechnik, S. Neubauer, and D. Rueckert. Joint learning of motion estimation and segmentation for cardiac MR image sequences. In *Medical Image Computing and Computer Assisted Intervention–MICCAI 2018: 21st International Conference, Granada, Spain, September 16-20, 2018, Proceedings, Part II 11*, pages 472–480. Springer, 2018.

[152] J. Radon. Über die Bestimmung von Funktionen durch ihre Integralwerte längs gewisser Mannigfaltigkeiten. *Classic papers in modern diagnostic radiology*, 5(21):124, 2005.

[153] J. Rahmer, A. Antonelli, C. Sfara, B. Tiemann, B. Gleich, M. Magnani, J. Weizenecker, and J. Borgert. Nanoparticle encapsulation in red blood cells enables blood-pool magnetic particle imaging hours after injection. *Physics in Medicine & Biology*, 58(12):3965, 2013.

[154] T. Reichl, M. Rückert, J. Günther, T. Kampf, T. Bley, V. Behr, S. Herz, and P. Vogel. Realistic vascular 3D printed phantom for real-time bolus tracking in a human-sized MPI scanner. *International Journal on Magnetic Particle Imaging IJMPI*, 9(1 Suppl 1), 2023.

[155] A. Rieder. *Keine Probleme mit inversen Problemen: Eine Einführung in ihre stabile Lösung*. Springer-Verlag, 2013.

[156] C. J. Ritchie, J. Hsieh, M. F. Gard, J. D. Godwin, Y. Kim, and C. R. Crawford. Predictive respiratory gating: A new method to reduce motion artifacts on CT scans. *Radiology*, 190(3):847–852, 1994.

[157] T. J. Rivlin. *Chebyshev polynomials*. Courier Dover Publications, 2020.

[158] S. Roux, L. Desbat, A. Koenig, and P. Grangeat. Exact reconstruction in 2D dynamic CT: Compensation of time-dependent affine deformations. *Physics in Medicine & Biology*, 49(11):2169, 2004.

[159] L. I. Rudin, S. Osher, and E. Fatemi. Nonlinear total variation based noise removal algorithms. *Physica D: nonlinear phenomena*, 60(1-4):259–268, 1992.

[160] J. Salamon, M. Hofmann, C. Jung, M. G. Kaul, F. Werner, K. Them, R. Reimer, P. Nielsen, A. Vom Scheidt, G. Adam, T. Knopp, and H. Ittrich. Magnetic particle/magnetic resonance imaging: In-vitro MPI-guided real time catheter tracking and 4D angioplasty using a road map and blood pool tracer approach. *PloS one*, 11(6):e0156899, 2016.

[161] F. Santambrogio. Optimal transport for applied mathematicians. *Birkäuser, NY*, 55(58-63):94, 2015.

[162] E. U. Saritas, P. W. Goodwill, G. Z. Zhang, and S. M. Conolly. Magnetostimulation limits in magnetic particle imaging. *IEEE transactions on medical imaging*, 32(9):1600–1610, 2013.

[163] T. F. Sattel, T. Knopp, S. Biederer, B. Gleich, J. Weizenecker, J. Borgert, and T. M. Buzug. Single-sided device for magnetic particle imaging. *Journal of Physics D: Applied Physics*, 42(2):022001, 2008.

[164] O. Scherzer. *Handbook of mathematical methods in imaging*. Springer Science & Business Media, 2010.

[165] O. Scherzer, M. Grasmair, H. Grossauer, M. Haltmeier, and F. Lenzen. *Variational methods in imaging*, volume 167. Springer, 2009.

[166] I. Schmale, B. Gleich, J. Rahmer, C. Bontus, J. Schmidt, and J. Borgert. MPI safety in the view of MRI safety standards. *IEEE Transactions on Magnetics*, 51(2):1–4, 2015.

[167] I. Schmale, J. Rahmer, B. Gleich, J. Kanzenbach, J. Schmidt, C. Bontus, O. Woywode, and J. Borgert. First phantom and in vivo MPI images with an extended field of view. In *Medical Imaging 2011: Biomedical Applications in Molecular, Structural, and Functional Imaging*, volume 7965, pages 263–268. SPIE, 2011.

[168] U. Schmitt and A. K. Louis. Efficient algorithms for the regularization of dynamic inverse problems: I. theory. *Inverse Problems*, 18(3):645, 2002.

[169] U. Schmitt, A. K. Louis, C. Wolters, and M. Vauhkonen. Efficient algorithms for the regularization of dynamic inverse problems: II. applications. *Inverse Problems*, 18(3):659, 2002.

[170] F. Schöpfer, A. K. Louis, and T. Schuster. Nonlinear iterative methods for linear ill-posed problems in Banach spaces. *Inverse problems*, 22(1):311, 2006.

[171] F. Schöpfer and T. Schuster. Fast regularizing sequential subspace optimization in Banach spaces. *Inverse Problems*, 25(1):015013, 2008.

[172] T. Schuster. *The method of approximate inverse: Theory and applications*, volume 1906. Springer, 2007.

[173] M. Storath, C. Brandt, M. Hofmann, T. Knopp, J. Salamon, A. Weber, and A. Weinmann. Edge preserving and noise reducing reconstruction for magnetic particle imaging. *IEEE transactions on medical imaging*, 36(1):74–85, 2016.

[174] A. N. Tikhonov. On the stability of inverse problems, CR (Doklady) Acad. *Sci. URSS (NS)*, 39:176–179, 1943.

[175] A. N. Tikhonov. On the regularization of ill-posed problems. In *Doklady Akademii Nauk*, volume 153, pages 49–52. Russian Academy of Sciences, 1963.

[176] A. N. Tikhonov. Solution of incorrectly formulated problems and the regularization method. *Sov Dok*, 4:1035–1038, 1963.

[177] A. N. Tikhonov. On the stability of the functional optimization problem. *USSR Computational Mathematics and Mathematical Physics*, 6(4):28–33, 1966.

[178] C. B. Top, A. Güngör, S. Ilbey, and H. E. Güven. Trajectory analysis for field free line magnetic particle imaging. *Medical Physics*, 46(4):1592–1607, 2019.

[179] R. Tovey, M. Benning, C. Brune, M. J. Lagerwerf, S. M. Collins, R. K. Leary, P. A. Midgley, and C.-B. Schönlieb. Directional sinogram inpainting for limited angle tomography. *Inverse Problems*, 35(2):024004, 2019.

[180] G. Van Eyndhoven, J. Sijbers, and J. Batenburg. Combined motion estimation and reconstruction in tomography. In *Computer Vision–ECCV 2012. Workshops and Demonstrations: Florence, Italy, October 7-13, 2012, Proceedings, Part I 12*, pages 12–21. Springer, 2012.

[181] C. L. Vaughan. *Imagining the elephant: A biography of Allan MacLeod Cormack*. Juta and Company Ltd, 2008.

[182] F.-X. Vialard and F. Santambrogio. Extension to BV functions of the large deformation diffeomorphisms matching approach. *Comptes Rendus Mathematique*, 347(1-2):27–32, 2009.

[183] C. Villani et al. *Optimal transport: Old and new*, volume 338. Springer, 2009.

[184] P. Vogel, S. Lother, M. A. Rückert, W. H. Kullmann, P. M. Jakob, F. Fidler, and V. C. Behr. MRI meets MPI: A bimodal MPI-MRI tomograph. *IEEE Transactions on Medical Imaging*, 33(10):1954–1959, 2014.

[185] P. Vogel, J. Markert, M. A. Rückert, S. Herz, B. Keßler, K. Dremel, D. Althoff, M. Weber, T. M. Buzug, T. A. Bley, W. H. Kullmann, R. Hanke, S. Zabler, and V. C. Behr. Magnetic particle imaging meets computed tomography: First simultaneous imaging. *Scientific reports*, 9(1):12627, 2019.

[186] P. Vogel, M. A. Rückert, T. Kampf, S. Herz, A. Stang, L. Wöckel, T. A. Bley, S. Dutz, and V. C. Behr. Superspeed bolus visualization for vascular magnetic particle imaging. *IEEE transactions on medical imaging*, 39(6):2133–2139, 2020.

[187] P. Vogel, M. A. Rückert, P. Klauer, W. H. Kullmann, P. M. Jakob, and V. C. Behr. Traveling wave magnetic particle imaging. *IEEE transactions on medical imaging*, 33(2):400–407, 2013.

[188] A. Wald and T. Schuster. Sequential subspace optimization for nonlinear inverse problems. *Journal of Inverse and Ill-posed Problems*, 25(1):99–117, 2017.

[189] J. Weizenecker. The Fokker–Planck equation for coupled Brown–Néel-rotation. *Physics in Medicine & Biology*, 63(3):035004, 2018.

[190] J. Weizenecker, B. Gleich, and J. Borgert. Magnetic particle imaging using a field free line. *Journal of Physics D: Applied Physics*, 41(10):105009, 2008.

[191] J. Weizenecker, B. Gleich, J. Rahmer, H. Dahnke, and J. Borgert. Three-dimensional real-time in vivo magnetic particle imaging. *Physics in Medicine & Biology*, 54(5):L1, 2009.

[192] E. Yagiz, A. R. Cagil, and E. U. Saritas. Non-ideal selection field induced artifacts in x-space MPI. *International Journal on Magnetic Particle Imaging IJMPI*, 6(2), 2020.

[193] L. Younes. *Shapes and diffeomorphisms*, volume 171. Springer, 2010.

[194] E. Y. Yu, M. Bishop, B. Zheng, R. M. Ferguson, A. P. Khandhar, S. J. Kemp, K. M. Krishnan, P. W. Goodwill, and S. M. Conolly. Magnetic particle imaging: A novel in vivo imaging platform for cancer detection. *Nano letters*, 17(3):1648–1654, 2017.

[195] L. Zdun and C. Brandt. Fast MPI reconstruction with non-smooth priors by stochastic optimization and data-driven splitting. *Physics in Medicine & Biology*, 66(17):175004, 2021.

[196] B. Zheng, T. Vazin, P. W. Goodwill, A. Conway, A. Verma, E. Ulku Saritas, D. Schaffer, and S. M. Conolly. Magnetic particle imaging tracks the long-term fate of in vivo neural cell implants with high image contrast. *Scientific reports*, 5(1):14055, 2015.

List of Figures

List of Tables

A. Appendix

A.1. Expansion of magnetic fields in spherical harmonics

This section summarizes considerations stated in [30] and [31] adapted to our notation. Since in practice every magnetic field is three dimensional, from now on considerations are made in $\mathbb{R}^3$. We further assume the fields to be sufficiently smooth. Starting from the Maxwell conditions, under the assumption that the FOV is free of field sources and has constant permeability μ_0, magnetic fields can be assumed to comply with

$$\nabla \cdot \mathbf{H} = 0 \quad \text{and} \quad \nabla \times \mathbf{H} = 0. \tag{A.1}$$

Thus, the field components H_i fulfill the Laplace equation $\Delta H_i = 0,\ i = 1,2,3$. Adding Dirichlet boundary conditions on the sphere $S_R^2 := \left\{\mathbf{r} \in \mathbb{R}^3 :\ \|\mathbf{r}\| = R\right\}$ with radius $R > 0$

$$\begin{cases} \Delta H_i(\mathbf{r}) = 0, & \mathbf{r} \in B_R, \\ H_i(\mathbf{r}) = H_i^R(\mathbf{r}), & \mathbf{r} \in S_R^2, \end{cases}$$

using continuous functions $H_i^R :\ S_R^2 \to \mathbb{R}$, for $i = 1,2,3$, the magnetic field can be described via spherical harmonics introduced in Section 2.4. The according series expansion in spherical coordinates (r, ϑ, φ) is then determined by

$$H_i(r,\vartheta,\varphi) = \sum_{l=0}^{\infty} \sum_{m=-l}^{l} c_{lm}^{R,i} \left(\frac{r}{R}\right)^l Y_{lm}(\vartheta,\varphi) = \sum_{l=0}^{\infty} \sum_{m=-l}^{l} \frac{c_{lm}^{R,i}}{R^l}\, p_{lm}(\vartheta,\varphi). \tag{A.2}$$

Regarding the normalization (2.6) the coefficients can be computed via

$$c_{lm}^{R,i} = \int_0^{2\pi} \int_0^{\pi} H_i^R(\vartheta,\varphi)\, Y_{lm}(\vartheta,\varphi) \sin\vartheta \,\mathrm{d}\vartheta \,\mathrm{d}\varphi.$$

Alternatively, for the Schmidt quasi-normalization (2.7) the computation transforms to

$$c_{lm}^{R,i} = \frac{1}{\|Y_{lm}\|^2} \int_0^{2\pi} \int_0^{\pi} H_i^R(\vartheta,\varphi)\, Y_{lm}(\vartheta,\varphi) \sin\vartheta \,\mathrm{d}\vartheta \,\mathrm{d}\varphi, \quad \|Y_{lm}\|^2 = \frac{4\pi}{2l+1}.$$

Therewith, the magnetic field within the ball B_R of radius $R > 0$ around the zero point is completely determined by the values on the sphere. Furthermore, in the latter choice of normalization, the coefficients give the maximum amplitude of the spherical harmonics on a sphere, which is advantageous for the assessment of the spatially dependent field amplitude.

Example A.1. *A rotating ideal field-free line, obtained by the composition of five field generating coils, can be described by a few spherical harmonics coefficients. Assume without loss of generality* $R = 1$ *and neglect the according index. Exploiting* (A.2) *and Table 2.1, the resulting magnetic field*

at $\mathbf{r} = (x, y, z)^T$ *can be computed by*

$$\begin{aligned}\mathbf{H}(\mathbf{r}, t) &= \mathbf{H}_{\text{Maxwell}}(\mathbf{r}) + \mathbf{H}_{\text{Quad0}}(\mathbf{r}) \cos(4\pi f_{\text{rot}} t) + \mathbf{H}_{\text{Quad45}}(\mathbf{r}) \sin(4\pi f_{\text{rot}} t) \\ &\quad - \mathbf{H}_{\text{x-Drive}}(\mathbf{r}) \Lambda(t) \sin(2\pi f_{\text{rot}} t) + \mathbf{H}_{\text{y-Drive}}(\mathbf{r}) \Lambda(t) \cos(2\pi f_{\text{rot}} t) \\ &= \frac{G}{2} \begin{pmatrix} -x \\ -y \\ 2z \end{pmatrix} + \frac{G}{2} \begin{pmatrix} x \\ -y \\ 0 \end{pmatrix} \cos(4\pi f_{\text{rot}} t) + \frac{G}{2} \begin{pmatrix} y \\ x \\ 0 \end{pmatrix} \sin(4\pi f_{\text{rot}} t) + A\Lambda(t) \begin{pmatrix} -\sin(2\pi f_{\text{rot}} t) \\ \cos(2\pi f_{\text{rot}} t) \\ 0 \end{pmatrix} \\ &\overset{z=0}{=} (A\Lambda(t) + Gx \sin(2\pi f_{\text{rot}} t) - Gy \cos(2\pi f_{\text{rot}} t)) \begin{pmatrix} -\sin(2\pi f_{\text{rot}} t) \\ \cos(2\pi f_{\text{rot}} t) \\ 0 \end{pmatrix}.\end{aligned}$$

A simple computation using the double angle formulas for trigonometric functions and setting $z = 0$ *therefore yields*

$$\mathbf{H}(\mathbf{r}, t) = (-G\, \mathbf{r} \cdot \mathbf{e}_t - A\Lambda(t))\, \mathbf{e}_t,$$

i.e. the magnetic field for the simultaneously rotating FFL regarded in Chapter 6. When considering piecewise constant angles φ_t*, it transforms into the discrete line rotation that we have considered in the other chapters.*

Table A.1.: Spherical harmonics coefficients for a continuously rotating ideal field-free line.

Coil Name	$\mathbf{H}$			Time-dependent Part
	H_1	H_2	H_3	
Select Maxwell	$2\,c^1_{1,1} = -G$	$2\,c^2_{1,-1} = -G$	$c^3_{1,0} = G$	1
Select Quad0	$2\,c^1_{1,1} = \quad G$	$2\,c^2_{1,-1} = -G$		$\cos(4\pi f_{\text{rot}} t)$
Select Quad45	$2\,c^1_{1,-1} \quad = G$	$2\,c^2_{1,1} \quad = \quad G$		$\sin(4\pi f_{\text{rot}} t)$
x-drive	$c^1_{0,0} = A$			$-\Lambda(t) \sin(2\pi f_{\text{rot}} t)$
y-drive		$c^2_{0,0} = A$		$\Lambda(t) \cos(2\pi f_{\text{rot}} t)$

A.2. Explicit expression of spherical harmonics

Binomial Theorem: $(x+y)^n = \sum_{k=0}^{n} \binom{n}{k} x^{n-k} y^k, \quad \binom{n}{k} = \frac{n!}{(n-k)!\, k!}, \quad n \in \mathbb{N}_0$

We derive a closed-form expression of spherical harmonics, which we have translated into Julia code. Our implementation of spherical harmonics is inspired by `https://github.com/hofmannmartin/SphericalHarmonicExpansions.jl`.

In a first step, we exploit the well-known binomial theorem for the computation of the associated Legendre polynomials (2.5). Let $l \in \mathbb{N}_0$ and $m \in \{-l, \ldots, l\}$. With $\lfloor \cdot \rfloor : \mathbb{R} \to \mathbb{Z}$ denoting the floor function, we obtain

$$\begin{aligned} P_l^m(x) &= \frac{1}{2^l l!} \left(1-x^2\right)^{\frac{m}{2}} \frac{\mathrm{d}^{l+m}}{\mathrm{d}x^{l+m}} \left(x^2-1\right)^l = \frac{1}{2^l l!} \left(1-x^2\right)^{\frac{m}{2}} \sum_{k=0}^{l} (-1)^k \binom{l}{k} \frac{\mathrm{d}^{l+m}}{\mathrm{d}x^{l+m}} x^{2(l-k)} \\ &= \frac{1}{2^l l!} \left(1-x^2\right)^{\frac{m}{2}} \sum_{k=0}^{\lfloor \frac{l-m}{2} \rfloor} (-1)^k \binom{l}{k} \frac{(2(l-k))!}{(2(l-k)-(l+m))!} x^{2(l-k)-(l+m)} \end{aligned}$$

and thus

$$P_l^m(\cos\vartheta) = \frac{1}{2^l l!} \sin^m\vartheta \sum_{k=0}^{\lfloor \frac{l-m}{2} \rfloor} (-1)^k \binom{l}{k} \frac{(2(l-k))!}{(l-2k-m)!} \cos^{l-2k-m}\vartheta.$$

Further, we make use of the *Chebyshev polynomials* of the first T_m and of the second kind U_m. A comprehensive overview on Chebyshev polynomials is given in [157]. We use their following representation

$$\begin{aligned} \cos(m\varphi) &= T_m(\cos\varphi) = \sum_{k=0}^{\lfloor \frac{m}{2} \rfloor} (-1)^k \binom{m}{2k} \sin^{2k}\varphi \cos^{m-2k}\varphi, \\ \sin(m\varphi) &= \sin\varphi U_{m-1}(\cos\varphi) = \sum_{k=0}^{\lfloor \frac{m-1}{2} \rfloor} (-1)^k \binom{m}{2k+1} \sin^{2k+1}\varphi \cos^{m-1-2k}\varphi. \end{aligned}$$

Regard the spherical coordinates $\mathbf{r} = (x,y,z)^T = r(\sin\vartheta\cos\phi, \sin\vartheta\sin\phi, \cos\vartheta)^T$. Moreover, by setting

$$\begin{aligned} A_{lm}^{kk'} &:= \sqrt{2} K_l^m \frac{1}{2^l l!} (-1)^{k+k'} \binom{m}{2k} \binom{l}{k'} \frac{(2(l-k'))!}{(l-2k'-m)!}, \\ B_{l0}^{k'} &:= K_l^0 \frac{1}{2^l l!} (-1)^{k'} \binom{l}{k'} \frac{(2(l-k'))!}{(l-2k')!}, \\ C_{lm}^{kk'} &:= \sqrt{2} K_l^{|m|} \frac{1}{2^l l!} (-1)^{k+k'} \binom{|m|}{2k+1} \binom{l}{k'} \frac{(2(l-k'))!}{(l-2k'-|m|)!} \end{aligned}$$

the spherical harmonics (2.4) can be stated explicitly. For $m > 0$ we obtain

$$\begin{aligned} Y_{lm}(\vartheta,\varphi) &= \sqrt{2} K_l^m \cos(m\varphi) P_l^m(\cos\vartheta) \\ &= \sum_{k=0}^{\lfloor \frac{m}{2} \rfloor} \sum_{k'=0}^{\lfloor \frac{l-m}{2} \rfloor} A_{lm}^{kk'} (\sin\vartheta\sin\varphi)^{2k} (\sin\vartheta\cos\varphi)^{m-2k} (\cos\vartheta)^{l-2k'-m} \\ &= \sum_{k=0}^{\lfloor \frac{m}{2} \rfloor} \sum_{k'=0}^{\lfloor \frac{l-m}{2} \rfloor} A_{lm}^{kk'} y^{2k} x^{m-2k} z^{l-2k'-m} \left(\sqrt{x^2+y^2+z^2}\right)^{2k'-l} = Y_{lm}(\mathbf{r}). \end{aligned}$$

Likewise, we compute for $m = 0$

$$Y_{l0}(\vartheta,\varphi) = K_l^0 P_l^0(\cos\vartheta) = \sum_{k'=0}^{\lfloor \frac{l}{2} \rfloor} B_{l0}^{k'} \cos^{l-2k'}\vartheta = \sum_{k'=0}^{\lfloor \frac{l}{2} \rfloor} B_{l0}^{k'} z^{l-2k'} \left(\sqrt{x^2+y^2+z^2}\right)^{2k'-l} = Y_{l0}(\mathbf{r}),$$

as well as for $m < 0$

$$\begin{aligned} Y_{lm}(\vartheta,\varphi) &= \sqrt{2} K_l^{|m|} \sin(|m|\varphi) P_l^{|m|}(\cos\vartheta) \\ &= \sum_{k=0}^{\lfloor \frac{|m|-1}{2} \rfloor} \sum_{k'=0}^{\lfloor \frac{l-|m|}{2} \rfloor} C_{lm}^{kk'} (\sin\vartheta\sin\varphi)^{2k+1} (\sin\vartheta\cos\varphi)^{|m|-1-2k} (\cos\vartheta)^{l-2k'-|m|} \\ &= \sum_{k=0}^{\lfloor \frac{|m|-1}{2} \rfloor} \sum_{k'=0}^{\lfloor \frac{l-|m|}{2} \rfloor} C_{lm}^{kk'} y^{2k+1} x^{|m|-1-2k} z^{l-2k'-|m|} \left(\sqrt{x^2+y^2+z^2}\right)^{2k'-l} = Y_{lm}(\mathbf{r}). \end{aligned}$$

The above representation of the spherical harmonics can be used to rewrite (A.2)

$$H_i(r,\vartheta,\varphi) = \sum_{l=0}^{\infty} \left(\sum_{m=-l}^{-1} c_{lm}^{R,i} \left(\frac{r}{R}\right)^l Y_{lm}(\vartheta,\varphi) + c_{l0}^{R,i} \left(\frac{r}{R}\right)^l Y_{l0}(\vartheta,\varphi) + \sum_{m=1}^{l} c_{lm}^{R,i} \left(\frac{r}{R}\right)^l Y_{lm}(\vartheta,\varphi) \right).$$

This explicit formulation of the spherical harmonics allows the determination of conditions on the corresponding coefficients to ensure the fulfillment of Maxwell's equations.

Publications derived from this dissertation

Parts of the results of this thesis have been published in

S. Blanke and C. Brandt Radon-based image reconstruction for MPI using a continuously rotating FFL. In *Modeling, Simulation and Optimization of Fluid Dynamic Applications, Springer,* 2023

S. Blanke and C. Brandt Field-free line magnetic particle imaging: Radon-based artifact reduction with motion models. *arXiv preprint*, 2023

S. Blanke and C. Brandt Dealing with field imperfections for field-free line magnetic particle imaging. In *Tomographic Inverse Problems: Mathematical Challenges and Novel Applications*, *Mathemathisches Forschungsinstitut Oberwolfach*, 2023

Eidesstattliche Versicherung / Declaration on oath

Hiermit erkläre ich an Eides statt, dass ich die vorliegende Dissertationsschrift selbst verfasst und keine anderen als die angegebenen Quellen und Hilfsmittel benutzt habe.

I hereby declare upon oath that I have written the present dissertation independently and have not used further resources and aids than those stated.

Ort, Datum | *city, date*

Unterschrift | *signature*

Erklärung zum Eigenanteil bei der Zusammenarbeit

Ausgehend von dem Vorschlag, die Möglichkeit zu untersuchen, Magnetfeldungenauigkeiten mit Methoden der dynamischen CT zu lösen, habe ich die verschiedenen Schritte auf dem Weg dorthin entwickelt und umgesetzt. Die daraus entstandenen Kapitel 6, 7 und 8 basieren auf den entsprechenden Arbeiten [16], [15] und [14]. Von Kapitel 8 wurden der Ansatz und ein Beispiel analog zu dem ersten Beispiel (8.5) in diesem Kapitel in der genannten Quelle präsentiert. Die weiteren Bestandteile sind kein Teil der Veröffentlichung. In Rücksprache mit C. Brandt habe ich eine erste Fassung der jeweiligen Arbeiten erstellt, die theoretischen Aspekte ausgearbeitet, sowie numerische Beispiele konzipiert und ausgeführt. Abschließend habe ich Anmerkungen und Verbesserungsvorschläge von C. Brandt eingearbeitet.

Ort, Datum | *city, date*

Unterschrift | *signature*